Experimental and Numerical Investigation of Turbulence and Wake Effects in Tidal Turbine Arrays

by

Martin Nuernberg

This thesis is presented

for

The Degree of Doctor of Philosophy

School of Marine Science and Technology

Newcastle University

December 2017

Abstract

Experimental and Numerical Investigation of Turbulence and Wake Effects in Tidal Turbine Arrays

The work presented in this thesis investigates the hydrodynamic interaction and resulting wake characteristics of multiple axially aligned and staggered array sections consisting of up to four horizontal axis tidal turbines (HATTs) through experimental and numerical modelling. Experiments with single and multiple devices in array (1-2-1) and in-line configurations with varying longitudinal spacing were conducted in a low ambient turbulence circulating water channel and long, medium turbulence intensity flume respectively using particle image velocimetry for centreline wake characterisation and flow field recordings. Longitudinal variations between two and three turbines aligned in the flume with turbulence intensity of 10% have shown small differences in the wake velocity recovery. The effect of varying longitudinal and transverse spacing of HATT devices on the array wake recovery within and downstream of the array was investigated by varying the position of the middle row of turbines and the transverse spacing between the second row turbines. Numerical simulation of corresponding configurations in the open-source CFD software OpenFOAM are conducted using Reynolds-averaged Navier Stokes models for turbulence closure, namely k - ω SST and Reynolds Stress Model and dynamic mesh capabilities to account for the rotation of each turbine. The numerical simulations are validated against experimental wake characteristics and used for further investigation of the flow field within tidal turbine arrays. Good agreement between numerical and experimental wake characteristics is shown for large parts of the wake domain with biggest differences in areas where the PIV measurements experienced difficulties due to high velocity shear and turbine structures affecting the laser sheet. The wake recovery in closely spaced arrays is strongly determined by the transverse spacing in the second row with close spacing leading to entrapment of large volumes of slow moving fluid in a combined wake of multiple turbines while wide transverse separation increases wake recovery between adjacent wakes through increased mixing with accelerated ambient flow. This effect is more pronounced for increased longitudinal spacing as more mixing occurs for the centreline wake before passing through the second row of turbines. Open source software for numerical simulation and image based flow field measurements were successfully applied for investigation of multiple tidal turbine wake effects and further investigations of the complex flow fields within tidal turbine arrays.

Acknowledgements

I would like to thank my supervisor Prof. Longbin Tao for his academic guidance and support throughout my time at Newcastle University. I am thankful for the opportunities provided and trust placed in me during my time as a PhD student by supporting a six months exchange program to Shanghai Jiao Tong University to conduct my experiments as well as the support for all the numerical work while in Newcastle. I am more than grateful to have worked on this project with Prof. Tao and his influence extends far beyond the academic part of this journey.

I'd like to extend my thanks to the Staff and Students at Shanghai Jiao Tong University who helped me during my stay in Shanghai in organising, preparing and conducting the experiments, specifically Prof. Longfei Xia, Prof. Zhiqiang Hu and Prof. Ma and Mr. Yi Dai. I would like to mention Dr. Liu Zhen and Mr Lan Jian who supported every single step of the experiments and without whom I could not have finished the experiments in the short time period.

At Newcastle University I would like to thank my friends and Colleagues at the school of Marine Science and Technology and our Offshore Engineering Group who were a great deal of help for academic and non-academic life related matters and provided for many good times throughout the years. Personally, I would like to extend my appreciation to Jamie Torres Lopez and Ikenna Okaro for their help and advice and Serena Lim for her help in Shanghai. Special thanks to my friends Yibo Liang, Ralitsa Mihaylova, Sudheesh Ramadasan, Chang Li, and Alessandro Carchen who were always available for advice or a tea during the afternoon. I'd also like to thank Kothar Al Balushi for making our office a nicer place and setting an example for work dedication and how to do early morning and late nights in the office especially during the write-up phase.

Finally, I would like to express my deepest appreciation for my parents and brothers who supported and encouraged me throughout my studies, my honorary British step brother Iman Ramzanpoor, who was always there to discuss details of the project and leave food on the hob when late nights in the office were needed. For her endless love and support, understanding and continuous motivation to work hard, I am most grateful for Helen to have become part of my life and take this and all future journeys together.

Table of Contents

List of Tables

List of Figures

List of Symbols

A	Area
C_T	Thrust Coefficient
C_p	Pressure Coefficient
C_P	Power Coefficient
D	Diameter
D_{k}	Diffusion transport term
E	Wall roughness constant
F_n	Froude Number
F_x	Axial Force
g	Gravity
I	Unit Tensor
I	Turbulence Intensity
I_∞	Ambient Turbulence Intensity
k	Turbulent Kinetic Energy
κ	Von Kármán constant
L	Characteristics Length
P	Pressure
P_∞	Far field Pressure
r	Distance along radius
R	Radius
R_{dim}	Non-dimensional Reynolds Stress
Re	Reynolds Number
S_{m}	Momentum Source Term
$S_\emptyset$	Source Term
S_k	Turbulence Kinetic Energy Source Term
Ti	Turbulence Intensity
u	In stream velocity component
$\overline{u'}$, $\overline{v'}$, $\overline{w'}$	Time averaged velocity fluctuations
u^+	Dimensionless velocity
U	Velocity Vector
U_∞	Ambient Velocity
U_x	In stream velocity component

U_z	Vertical velocity component
v	Transverse velocity component
V_{def}	Velocity Deficit
w	Vertical velocity component
x	In-stream direction
y	Transverse direction
y	Wall spacing
y^+	Dimensionless wall spacing
z	Vertical Direction

Greek Characters

ε	Rate of dissipation
η	Turbulent length scale
λ	Tip Speed Ratio
μ	Dynamic Viscosity
u_τ	Friction velocity
ν	Kinematic Viscosity
v_t	Turbulent viscosity
ρ	Density
τ	Wall shear stress
τ_η	Kolmogorov length scale
$\emptyset$	Scalar Quantity
ω_t	Angular velocity
ω	Specific dissipation rate
Ω	Vorticity Tensor

Abbreviations

AD	Actuator Disk
ADV	Acoustic Doppler Velocimetry
AMI	Arbitrary Mesh Interface
BEMT	Blade Element Momentum Theory
CFD	Computational Fluid Dynamics
CFL	Courant-Friedrichs-Lewy
CPU	Central Processing Unit
CWC	Circulating Water Channel
DES	Detached Eddy Simulations
DNS	Direct Numerical Simulation
FVM	Finite Volume Method
GAMG	Geometric Agglomerated Algebraic Multigrid
GCI	Grid Convergence Index
HATTs	Horizontal Axis Tidal Turbine
LDV	Laser Doppler Velocimetry
LES	Large Eddy Simulation
LRR	Launder, Reece and Rodi RSTM
MPI	Message Passing Interface
MRF	Moving Reference Frame
OBJ	Wavefront Object file
PDE	Partial Differential Equations
PIMPLE	Merged PISO-SIMPLE algorithm
PISO	Pressure-Implicit with Split Operator
PIV	Particle Image Velocimetry
RANS	Reynolds Averaged Navier Stokes

RSTM	Reynolds Stress Transport Model
SIMPLE	Semi-Implicit Method for Pressure Linked Equations
SGS	Sub-Grid Scale
SST	Shear Stress Transport
STL	Stereo Lithography file
TKE	Turbulence Kinetic Energy
TSR	Tip Speed Ratio
TST	Tidal Stream Turbine
V3V	Volumetric Three Component Velocimetry
WWC Flume	Wind Wave Current Flume

List of Publications

Nuernberg, M., Tao, L., 2016. Experimental Study of Flow Field Characteristics in Tidal Stream Turbine Arrays. *Proceedings of the ASME 2016 35th International Conference on Offshore Mechanics and Arctic Engineering - OMAE (49972)*, V006T009A004.

Nuernberg, M., Tao, L., 2017, Accepted. Three-dimensional tidal turbine array simulations using OpenFOAM with dynamic mesh. *Ocean Engineering*. In Press.

Nuernberg, M., Tao, L., 2017, Under Review. Wake Characterisation of Tidal Turbines in Arrays. *Renewable Energy*.

Chapter 1. Introduction

1.1 Background and Motivation

Global energy demand has seen sharp rises over the past three decades and is projected to have doubled in 2040 compared to 1990 (EIA, 2016). Though the global emissions are predicted to continue rising, driven by increases in wealth and living standard of the emerging economies, they do so at a significantly reduced rate compared to the past two decades, reflecting the gains in efficiency and technology as well as the changing fuel mix used to supply energy (BP, 2017). With increasing concerns about the long term effects of greenhouse gas emissions and the resulting climate changes, worldwide efforts and agreements such as the Kyoto Protocol in 1997 (United Nations, 2017b), the EU 2020 targets from 2009 (European Commission, 2017a) and recently the Paris Agreement in 2016 (United Nations, 2017a) have been brought into action with the aim to reduce the share of traditional carbon based non-renewable energy sources, mainly oil and coal, and increase the share of cleaner and renewable energy to supply the rising energy demand.

The global share of renewable energy is predicted to double from about 10% to 20% by 2035 where fastest growth is expected to be seen in China, but the EU will see the highest share of renewables as part of the power generation in 2035, with almost 40% of the energy coming from renewable sources (Figure 1-1). To date, hydroelectric power which mainly stems from the use of dams and reservoirs to generate electricity from the potential energy is the largest contributor of renewable energy generation, accounting for approximately 70% of the total energy supplied from renewable sources. However, due to its large scale and environmental impact leading to a relatively small number of potential installations, the proportion of hydroelectricity is projected to remain relatively stable while other renewable energy sources such as solar, wind, water, geothermal and biomass/fuels experience exponential growth and are expected to provide a larger share of the total energy demand in the near future. The main drivers for the continued decarbonisation of the global energy market are renewable energy sources with wind and solar energy accounting for the largest proportion in growth of renewable energy as shown in Figure 1-2 with an average annual growth of 6% and 8% respectively between 2012-2040 (EIA, 2016). This development is accelerated by increased competitiveness as these sectors mature and significant reductions in cost of energy are seen (ORE CATAPULT, 2016).

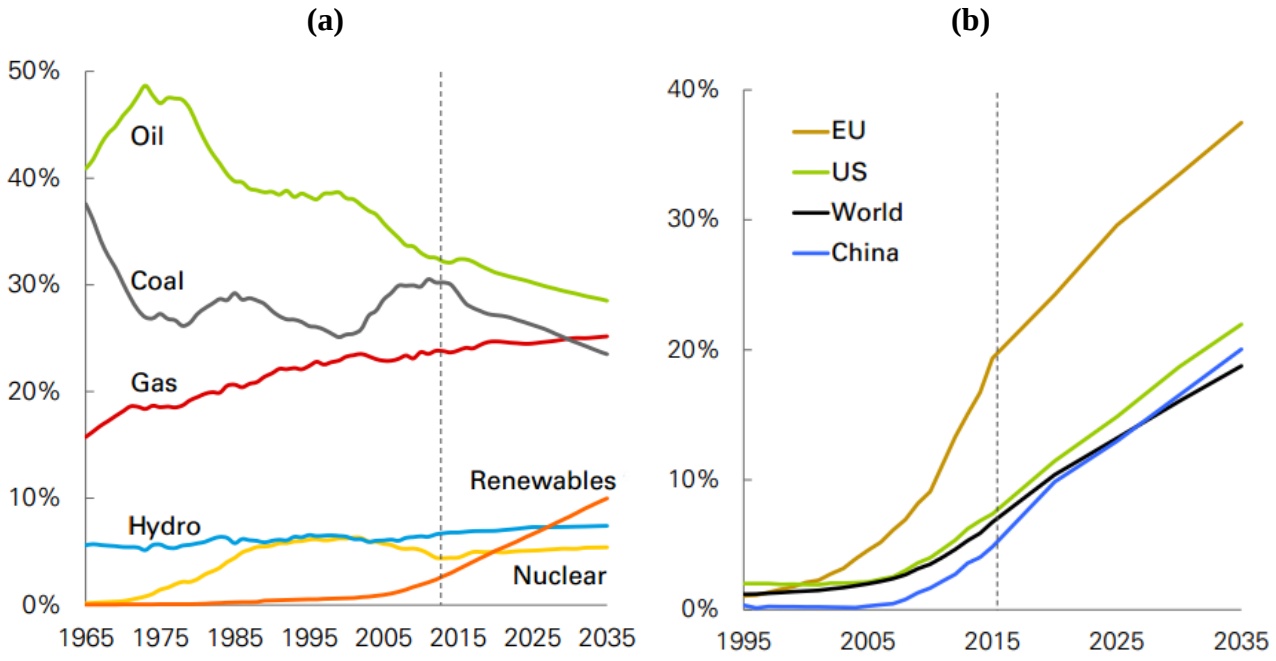

Figure 1-1 - (a) Share of Primary Energy Consumption by Fuel and (b) Detailed Share of Renewable Energy for Selected Areas (BP, 2017).

For the European Union, binding targets (European Commission, 2017a) were set in 2007 and came into force in 2009 to increase the share of energy generated from renewable sources to 20%, reduce greenhouse gas emissions by 20% compared to levels from 1990 and improve energy efficiency by 20%. In 2014 the EU saw 16% of the total energy demand (this includes electricity, transport and heating) and 28% of electricity generation from renewable sources (European Commission, 2017b). The share of wind energy of the installed power generation capacity in the EU rose exponentially from 2% in 2000 to 15% in 2015 (WindEurope, 2016b) with a high number of onshore and offshore wind turbines being installed.

1.1.1 Marine and Ocean Energy

With the increased development of land based renewable energy and the scarcity of appropriate locations for large wind farms in addition to socio-economic concerns such as noise and visual pollution, increased developments of wind farms in coastal areas have been seen over the last decade. Consequently, wind farms have been planned and constructed gradually further offshore (WindEurope, 2016a) and towards deeper waters. The current developments are located in what is considered to be shallow or transitional water depths and near coast locations where the available wind resource is higher and larger rotors can generate more electricity compared to shore based wind turbines. The next anticipated step of development is towards

floating offshore wind structures as deeper waters are reached where the use of bottom fixed foundations becomes uneconomical (WindEurope, 2017). However, due to the complex nature and interactions between wind turbine and floating foundation, the floating offshore wind system development remains at very early stages with first prototypes having been deployed for full scale testing in proposed environment, such as WindFloat in 2011 and the first offshore floating wind farm consisting of five Hywind floating turbines due for start of construction in late 2017 (Statoil, 2017). Both full scale prototypes are shown in Figure 1-3.

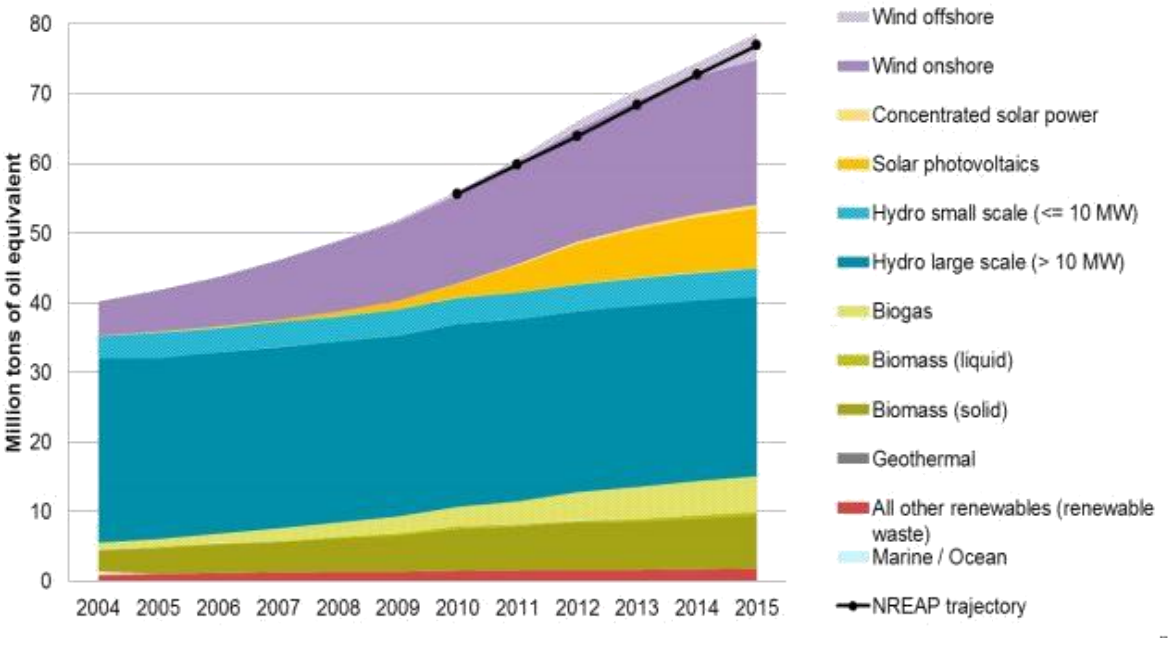

Figure 1-2 - Share of Renewable Energy Sources in EU Electricity Generation (European Commission, 2017b).

While the focus of renewable energy development has largely been on land and near shore areas over the last 30 years due to reduced costs and complexity, the oceans as a direct source of sustainable energy can be a significant contributor to the changing energy fuel mix in the future. About 70% of the planet is covered in water, containing large amounts of energy that could theoretically supply all energy requirements. Energy in the oceans primarily comes in the form of potential and kinetic energy and can be extracted from waves (Wave Energy Converters, WEC), changing water levels due to the tidal flows (Tidal Lagoons or Barrages) and ocean currents directly (Tidal Energy Converter, TEC). Further energy that can be harnessed exists in the form of salinity gradients between sea water and fresh water and temperature across the water depth, however these currently are in very early stages with only a handful of demonstrator and research projects being conducted.

(a)

Source: Untrakdrover (2012)

(b)

Source: OffshoreWIND.biz (2017)

Figure 1-3 - First Large Scale Floating Wind Turbines (a) WindFloat Semi-Submersible (2MW) off the Coast of Portugal from 2012 to 2016, (b) Hywind 5MW Turbine for Installation in the First Floating Wind Farm.

Tidal lagoons and barrages can generate large amounts of electricity from the potential energy across the tidal range when trapping high tides and releasing the water through turbines at low tide, the largest currently operating is the Sihwa Lake Tidal Power station in South Korea with a capacity of 254MW. A large lagoon power station (320MW) is currently under proposal in the UK, with further projects such as the 3GW Cardiff Tidal lagoon, using the second largest tidal range in the world, currently in the design and planning stage (Tidal Lagoon Power, 2017).

Since potential locations are few and capital costs and environmental impact could be high, thus facing increased environmental and societal pressure, recently research interest has focused on developing and commercialising wave and tidal stream energy as methods of generating electricity with reduced visual impact, lower capital costs and environmental impact.

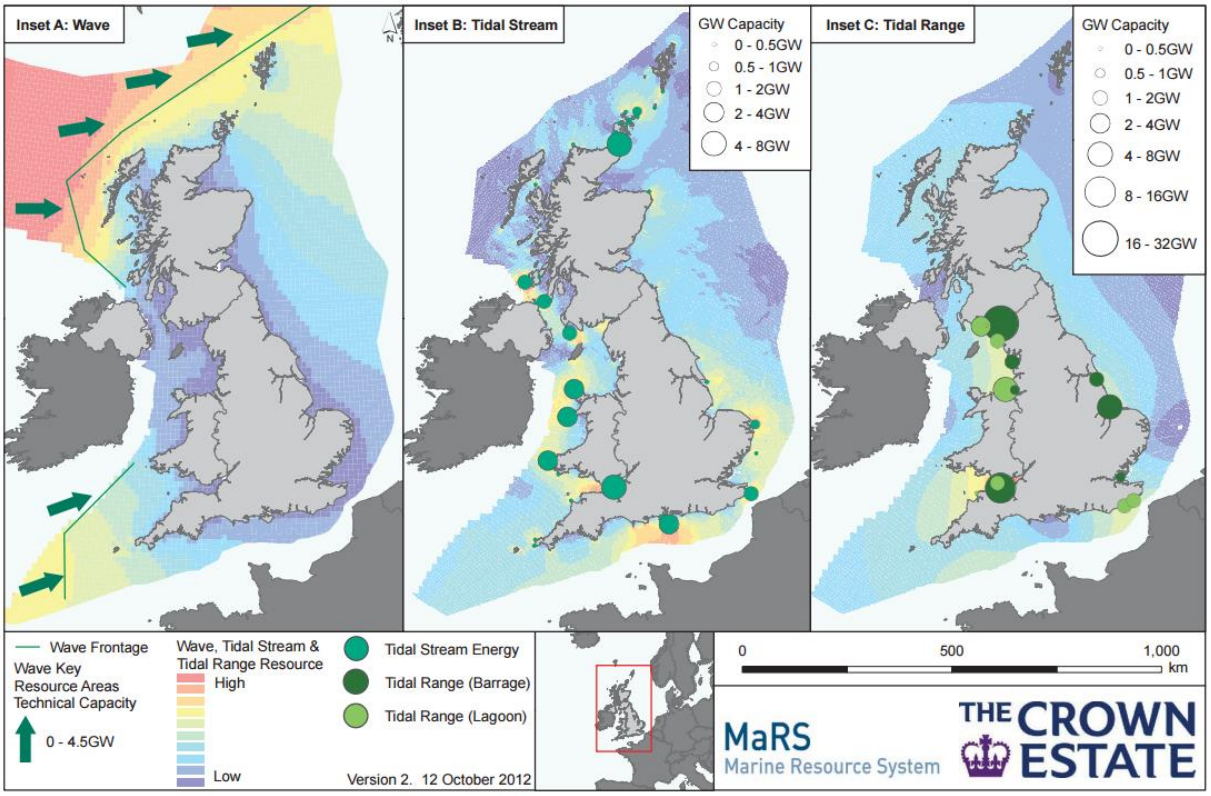

Figure 1-4 – Wave and Tidal Resource Areas and Technical Capacity (Reproduced with Permission from Crown Estate (The Crown Estate, 2012)).

It has been estimated that over the next 35 years, a total of 100GW combined wave and tidal capacity could be installed in Europe, accounting for up 10% of the European Union's demand (OEE, 2017). Areas of significant energy resources are shown in Figure 1-4 highlighting locations for potential large scale energy generation from ocean energy in the UK. The total combined resources for wave and tidal energy in the UK have been predicted to be able to provide about 15% - 20% of the UK's electricity demand in the long term, with half of that generated from tidal currents (Carbon Trust, 2011a; Carbon Trust, 2011b). Current activity and future projects are driving towards further commercialisation as can be seen from Figure 1-5.

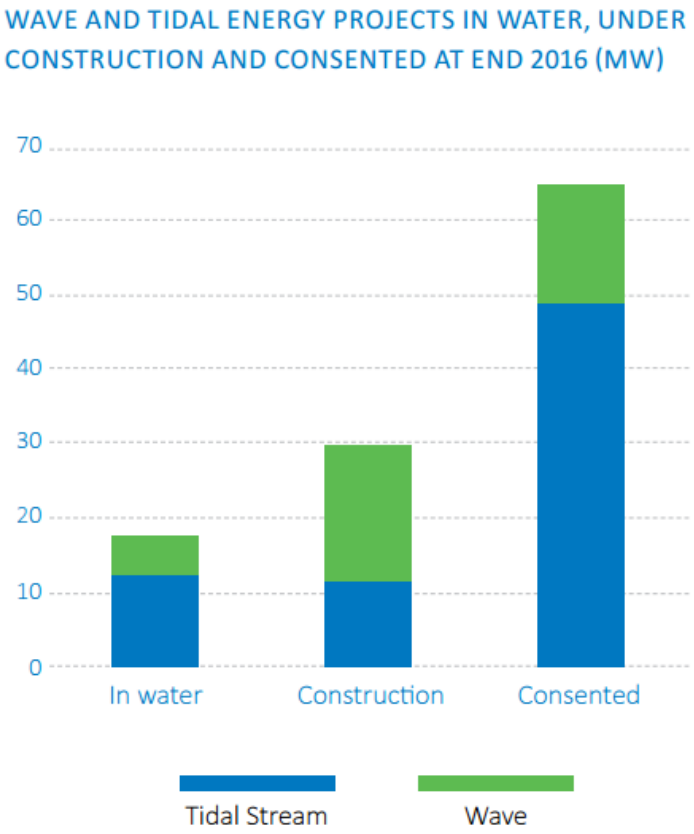

Figure 1-5 - Current and Future Developments (in Rated Capacity, MW) of Wave and Tidal Stream Energy Converters (OEE, 2017).

Therefore as viable alternatives and potential contributor to a sustainable energy mix, energy generation from the oceans is likely to play a significant role in the near future, fuelled by increasing pressure on environmental and climate protection as well as electricity demand and supported by governments to accelerate development and reduce the costs of electricity generation. The two ocean energy sectors with considerable industry investment at this time are wave and tidal stream energy where the current deployment of 10MW is small, however announced projects total at about 2 GW of added capacity, generating electricity for about 1.5 million homes (European Commission, 2014).

1.1.2 Tidal Stream Energy

The tides depend on the gravitational force interaction of sun and moon and the earth's oceans, the timing and extent of these can be predicted accurately and reliably for extended periods of time. Thus tidal stream energy is a very reliable and predictable source of renewable energy with very high energy density due to the increased density of water compared to wind. The available power for extraction is strongly dependent on the current velocity, hence areas where flow accelerations occur, such as between islands, around headlands and in tidal channels are favoured for large scale energy generation. Some of these areas can be seen from the locations highlighted in Figure 1-4. The practicably extractable amount of energy of a fluid such as wind or water is expressed as Power in (1-1),

$$P = 0.5\rho \mathrm{A} {U_\infty}^3 C_P \tag{1-1}$$

where A is the area swept by blades, U_∞ is the incoming velocity, ρ the density of the fluid and C_P the power coefficient which has a theoretical maximum of 0.593, also called the Lanchester-Betz limit. Commonly horizontal axis wind turbines achieve coefficients of about 0.40 to 0.45.

Due to the increased density of sea water, larger amounts of energy are carried within lower current velocities and can be extracted with reduced size of energy converting devices, resulting for example in reduced diameters for similar rated capacities when comparing wind and tidal turbines. Typical 20 metre diameter tidal turbines are rated for 2 MW while the existing WindFloat prototype was rated at 2 MW with a diameter of 80 metres. Overall, tidal stream energy has advantages in terms of planning and grid integration for a changing fuel mix of high proportions of renewable energy over other renewable energy sources such as waves, wind and solar where long terms predictions are less accurate and depending on seasonal variations. Further, by being located under the sea visual impact is minimized which addresses some of the "not in my back yard" concerns expressed over other renewable energy sources.

The extent of environmental impact has yet to be fully understood though some large scale environmental monitoring of prototype devices has not revealed any particular impact on marine flora and fauna (OEE, 2017) and some initial assessment of noise effects during construction and operation have not highlighted a significant risk of damage to marine mammals (NERC, 2013). However with large scale deployment in various locations and to

much larger scale in terms of generating electricity from the available energy, the effects on marine life and environment need to be closely monitored.

With large resources available and many favourable areas around the UK as well as continued support from the EU and UK government, a large proportion of prototype designs for tidal stream turbines (TST) have been developed and/or tested in the dedicated testing facilities such as the European Marine Energy Centre (EMEC) in the Orkney Islands.

To reduce costs and risks for early deployment, methods and knowledge about device development are transferred from the wind energy industry. At this point, the preferred choice of device for commercial development and as such having been the most common design to date for full scale tidal turbines is the horizontal axis tidal turbine (HATT) though alternative designs (Figure 1-6), often focussing on addressing areas with lower current velocities, such as vertical axis (a), cross flow (b), helical screw (c) rotors are being designed and tested. Other concepts such as kites (d) have been proposed to harness the energy of tidal currents, some of which are moving towards commercial scale testing (Minesto, 2017).

(a)

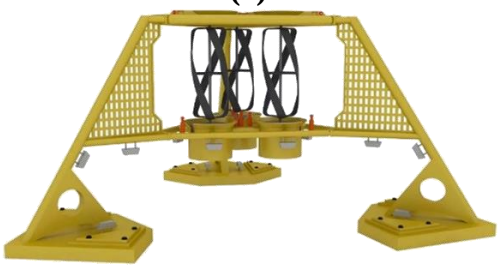

Source: EC-OG, Subsea Power hub (https://i.ytimg.com/vi/4xPMgehG-c4/hqdefault.jpg)

(b)

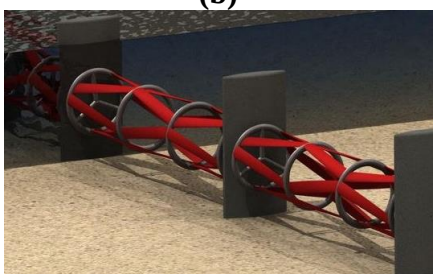

Source: Oxford University, THAWT (http://www.eng.ox.ac.uk/tidal/images/Model-final.jpg/image_large)

(c)

Source: Flumill, Subsea Power hub (https://i.ytimg.com/vi/4xPMgehG-c4/hqdefault.jpg)

(d)

Source: Deep Green, Minesto, (http://renews.biz/105426/minesto-orders-deep-green-wing/

Figure 1-6 – Tidal Energy Converter Prototypes in Scaled and Large Scale Testing.

1.1.3 Developments & Challenges

The UK has been in a leading position for design, construction and testing of tidal stream turbines and saw first full scale commercial turbine generate electricity to a national grid in 2008 (Marine Current Turbines, 2008). Following further development of prototypes and large scale testing of demonstrator devices at dedicated facilities and in open waters, the UK now has the first full scale tidal array with up to 4 operational tidal turbines supplying electricity to the national grid since installation in January 2017. The devices currently deployed in this array are shown in Figure 1-7 and are all bottom fixed horizontal axis tidal turbines with specific support structures to position the turbine within the vertical water column. The MeyGen array Phase 1A, dedicated to test and monitor deployment and initial operational phases is set to be the first of a number of phases for further improvement and evaluation of deployment, foundations and turbine technology to reduce the cost of energy generation, while gradually increasing the capacity of the array towards almost 400MW in the long term (Atlantis Resources Ltd, 2017).

(a)

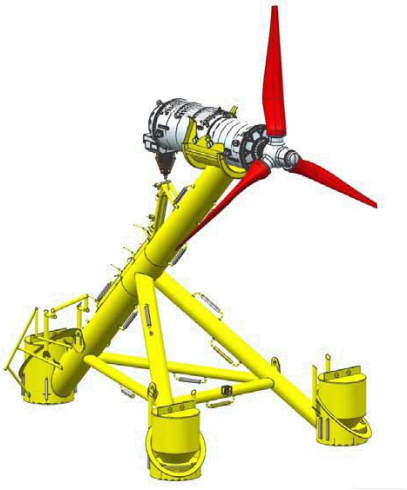

Source:
http://www.andritzhydrohammerfest.co.uk/tidal-turbines/

(b)

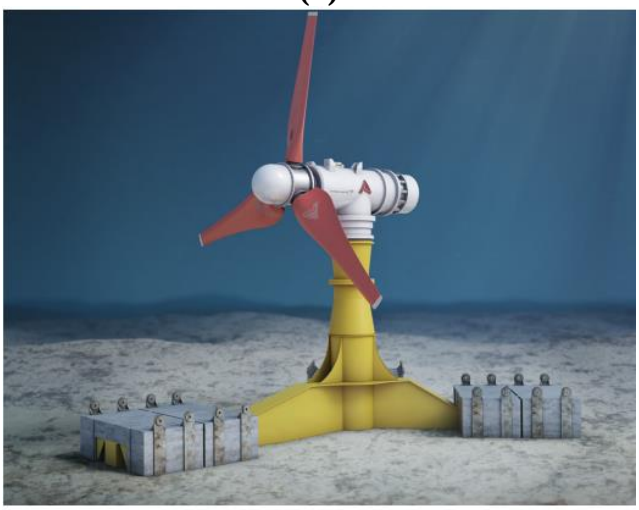

Source:
https://www.atlantisresourcesltd.com/services/turbines/

Figure 1-7 – Currently Installed Large Scale, Commercial Tidal Turbines in the MeyGen Array, (a) AH1000 MK1 (b) AR1500, Both Bottom Fixed Structures.

For full commercialisation and continued and accelerated large scale deployment which is anticipated beyond 2020 (DECC, 2011), further reductions in costs, risk and complexity of offshore installations are vital. The offshore wind energy sector recently passed targets for costs reductions four years ahead of schedule (ORE CATAPULT, 2016) through increased activity and continued improvement in supply chain infrastructure to highlight the potential for cost reduction when large scale development is being actively driven and supported.

For tidal turbines to achieve significant cost reductions in the cost of energy, large scale array deployment needs to be accelerated. Though there are many similarities with energy extraction from large scale wind farms, significant challenges are present in the design, construction, operation and maintenance of large scale tidal farms. The main challenges are summarised here for a brief overview of what has to be overcome to achieve vital cost reduction:

- Present devices have been installed in water depths approximately two to three times the diameter of the turbines. As such, the turbines operate across a varying velocity profile through the entire depth, unlike wind turbines which operate within a much smaller fraction of the boundary layer.
- Offshore wind farms and many on-shore locations are installed with rotors at similar or same vertical position. The seabed bathymetry around the coast makes this much more complex to achieve for tidal turbines.
- Limited locations and varying tidal currents within these require turbines to be installed in close proximity and covering a large proportion of the available tidal flow area, hence interactions between turbines are a vital consideration for array layout. Large scale energy extraction of tidal currents can affect local tidal flows, hence the available resource may be reduced by the presence of large arrays.
- The operating environment is highly turbulent and harsh, constant changes in local conditions with strong saltwater currents require thorough design for structural integrity and lifespan of underwater TSTs adapting to a range of possible conditions met by each individual turbine.
- Given the local conditions, installation and maintenance of complex structures is difficult and expensive and requires careful layout and design of arrays and individual devices.
- Commercial projects to date have relied upon energy extraction using bottom fixed horizontal axis turbines, analogous to the technology widely used to harness energy from winds.

1.2 Literature Review

1.2.1 Methods and Governing Parameters

Due to the high cost involved and complexity of operating in harsh environments with many factors influencing the power performance, wake development and structural integrity of tidal turbines as shown in Figure 1-8, improved understanding and prediction of likely energy yields is needed. This requires comprehensive studies of the complex flow interactions of individual turbine wakes when arranged in close proximity and ultimately power producing performance of tidal turbines when arranged in large arrays.

Tidal turbine devices have been tested extensively over the last decade using experimental and numerical investigations as well as large scale commercial prototype studies in real life operating environments (Atcheson *et al.*, 2015; Jeffcoate *et al.*, 2016). The optimisation of power production through design of devices and device components such as blade sections, support and foundation structures and control systems has been a major focus for development of the first industrial devices by close cooperation of government, academia and industry.

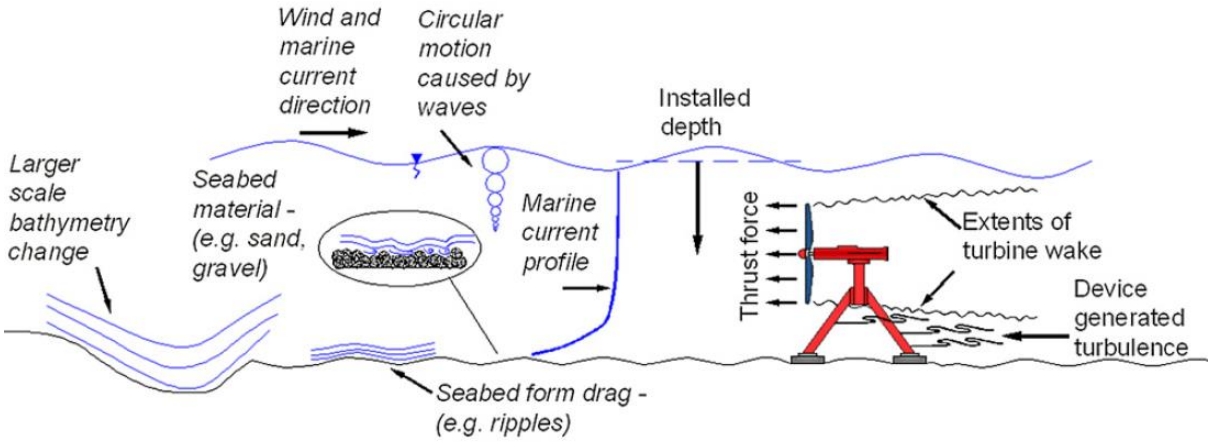

Figure 1-8 – Operating Environment and Influences on Tidal Stream Turbines (Myers and Bahaj, 2012).

Investigation and optimisation of single device performance and resulting flow fields is often performed through numerical modelling, however validation of numerical models is vital and requires experimental studies for comparison of performance and wake characteristics of TSTs. Combined experimental and numerical studies on the flow characteristics within model scale tidal turbine arrays are a vital step towards validation and subsequent application of numerical models for further investigation of array deployment and wake interactions at reduced cost thus providing important insights to the flow conditions faced by devices when arranged in close proximity.

The following sections provide a brief introduction to the methods used for accurate representation of the physics of tidal turbines in experimental as well as numerical methods and comparison to full scale operation. It is essential to maintain similarity of geometry, dynamic and kinematic effects to extrapolate insights gained at small scale to the real life operation. The non-dimensional parameters governing this similarity are briefly introduced here, followed by an overview of recent advances made in investigating the performance as well as flow characteristics of tidal turbines in moving towards large scale electricity generation from tidal current.

The ratio of inertial to viscous forces and gravitational forces respectively defined as Reynolds number (Re) and Froude number (Fn) need to be maintained between experimental as well as numerical scale models to full scale turbines to allow prediction of performance and wake characterisations of full scale devices. For assessment, comparison and investigation of scaled model turbines, non-dimensional parameters are defined that describe the operating conditions in terms of the turbine tip speed and incoming flow (TSR), loading on the turbine and momentum extraction (C_T) and ratio of energy extracted from the energy available in the flow (C_P). The performance and detailed flow conditions around the specific turbine blade section can be investigated and validated for numerical simulation against experimental data, using the pressure coefficient (Cp). Wake characteristics are provided in terms of the velocity deficit (V_{def}) and turbulence intensity (Ti).

Reynolds Number $$Re = \frac{\rho UL}{\mu} = \frac{UL}{\nu} \quad (1\text{-}2)$$

Froude Number $$Fn = \frac{U}{\sqrt{gL}} \quad (1\text{-}3)$$

Tip Speed Ratio $$TSR = \frac{\omega_t R}{U_\infty} \quad (1\text{-}4)$$

Thrust Coefficient $$C_T = \frac{F_x}{0.5\rho A U_\infty^2} \quad (1\text{-}5)$$

Power Coefficient: $$C_P = \frac{Power}{0.5\rho A U_\infty^3} \quad (1\text{-}6)$$

Pressure Coefficient $$Cp = \frac{\mathrm{P} - P_\infty}{0.5\rho[U^2 + (\omega_t r)^2]} \quad (1\text{-}7)$$

Velocity Deficit $$V_{def} = 1 - \left(\frac{u}{U_\infty}\right) \quad (1\text{-}8)$$

Turbulence Intensity $$I = \frac{\sqrt{\frac{1}{3}(u'^2 + v'^2 + w'^2)}}{U_\infty} = \frac{\sqrt{\frac{2}{3}k}}{U_\infty} \quad (1\text{-}9)$$

Where, F_x is the axial force, g is the acceleration due to gravity, L represents a characteristic length, U the characteristic flow velocity, μ is the dynamic viscosity and ν the kinematic viscosity of the fluid. R is the radius of the turbine with r being the distance along the radius and P is the measured/calculated local pressure while P_∞ represents the far field pressure. ω_t is the angular velocity of the turbine. For the velocity deficit, u is defined as the stream wise velocity component, and the turbulence intensity is using u', v' and w', the root mean square values of the turbulence velocity fluctuations and k the turbulent kine tic energy.

Experimental Methods

Experimental testing of tidal turbines for performance estimation or characterisation of the near wake flow, use scaled models operating in controlled conditions in dedicated test facilities such as circulating water channels, cavitation tunnels, flumes and towing tanks. Size and

configuration of scaled models therefore involve choosing an appropriate diameter and turbine design to model the flow characteristics at small scales. Important considerations include the maximisation of Reynolds number to achieve similar classification of turbulent flow, while keeping the size of the rotor within acceptable limits to not incur large blockage of the test facility cross section. This would require correction of the measured coefficients due to the effect of close proximity to boundaries altering the flow around or into the rotors swept area when using large scale rotors in confined test facilities or introduce excessive rotor rotation at very small scale to maintain dynamic similarity (Bahaj *et al.*, 2007b; Myers and Bahaj, 2010). Experiments of tidal turbines arrays are therefore limited by the size of existing test facilities which allow locating multiple devices in close proximity. Thus, while performance investigations have employed scaled rotor models to accurately model the flow in and around the turbine, far wake investigations have been largely conducted using actuator disk (AD) models to represent the momentum extraction, which results in good agreement of wake characteristics where wake recovery is dominated by mixing with ambient flow.

Flow measurements in the wake of experimentally modelled tidal stream turbines require sampling at increased frequency due to the turbulent flow characteristics. Acoustic Doppler velocimetry (ADV), laser Doppler velocimetry (LDV) and to some extent particle image velocimetry (PIV) have been used to examine the flow field downstream of tidal turbines and wind turbines alike. Whereas ADV offers reduced costs and ease of operation, it requires positioning of a probe within the test domain to sample velocity characteristics across a dense grid of measurements points, LDV can provide higher spatial and temporal resolutions with the probe located outside the test area (Maganga *et al.*, 2010; Bahaj and Myers, 2013). PIV can be used for recording larger areas of the flow field by recording illuminated images of a particle seeded flow for calculation of resulting flow vectors based on cross-correlation of particle movement between recordings. PIV has been used more extensively for wind turbine experiments (Whale *et al.*, 2000; Dobrev *et al.*, 2008; Krishnaswami, 2013) to investigate the near wake vortex and wake evolution in water channels and wind tunnel facilities. Some studies have used PIV measurements to characterise the flow in the wake of a tidal turbine showing the vertical velocity profile in the wake of up to 3 tidal turbines at a number of locations (Stelzenmuller, 2013) and showing the horizontal wake field downstream of small scale tidal turbine (Walker, 2014b). Detailed three-dimensional volumetric flow characteristics in the near wake of a miniature tidal turbine are presented by Chamorro *et al.* (2013b).

Numerical Methods

Numerical investigations of tidal stream turbines have the advantage of being low cost and provide the ability for parametric design and optimisation using various methods of estimating the power performance, wake development and interactions between multiple turbines. Performance investigation is primarily conducted using blade element momentum theory (BEMT) while numerical studies investigating wake development and characterisation employ computational fluid dynamics (CFD). A major challenge for CFD simulations is overcoming the requirements on computational resources in resolving the small scale flow passing the blade surfaces and resolving the domain for the highly complex flow field around tidal turbine structures. Structured and unstructured meshing approaches are used across a wide range of numerical investigations. A structured mesh around a three-dimensional turbine blade with chord and twist variations along the radius is difficult to create and takes significant effort and time. The advantage of unstructured mesh generation approaches for complex geometries compared to the simplification of such geometries (through actuator disk modelling for example) to accelerate the generation of structured meshes depends on the available numerical schemes, the accuracy of simplified modelling approaches with empirical source terms and is subjected to a wider range of specific investigations and comparisons for the further development of tidal turbine numerical modelling. Further details and discussion is presented in the following section. Different methods exist to account for the rotation of the turbine blades that introduce the rotational effects to the flow. These methods range from accounting for turbine rotation through additional source terms, using a moving reference frame to introduce rotation to the fluid (MRF) or a dynamic/sliding mesh approach to represent the full rotations in a rotor-stator domain (Liu *et al.*, 2016).

With respect to the turbulence modelling, large eddy simulation (LES) and Reynolds averaged Navier-Stokes (RANS) calculations with a range of available turbulence closure models have been used in previous studies, though their application to tidal flows and identifying appropriate turbulence models for specific investigations is currently a significant challenge across numerical simulations. Eddy-viscosity models such as $k - \varepsilon$ and k - ω SST, which combines the former with the k-ω model within the boundary layer, are widely used to resolve the Reynolds stresses based on the Boussinesq hypothesis due to their computational efficiency. For more complex and anisotropic turbulent flows Reynolds Stress Transport Models (RSTM) calculate the Reynolds stress tensor directly, thus offering improved agreement for certain flows at reduced computational resources compared to LES (McNaughton *et al.*, 2014). Recent

advancements in availability of multi core processing and the ever increasing computational resources available offer a wide range of approaches to investigate the performance, wake and interaction of multiple turbines numerically and are helping to expand the insight gained about the complex flow field characteristics in tidal stream turbine wakes and the interaction of multiple wakes.

1.2.2 Design and Performance of TST

Energy extraction of tidal currents using horizontal axis turbines leads to reduced momentum downstream of the rotor. This flow is defined as wake which consists of two main parts, namely the near wake where the flow field is largely determined by the rotor specific geometry and performance of turbine, and the far wake characterized by wake dissipation and expansion as described by Bahaj *et al.* (2007c) and shown in Figure 1-9. In general, the effect of tidal energy devices on the surrounding flow, or the resulting wake, is a function of the resistance it provides to the flow expressed in terms of C_T, mixing with the ambient flow and type and distance to bounding surfaces (Whelan and Stallard, 2011). The near wake is typically the region dominated by slow moving fluid with strong pressure/shear gradients, high levels of turbulence and swirling flow induced by the rotation and geometry of the rotor and is usually classified to extent up to 7-10 diameters downstream of the rotor. The far wake is usually considered as the wake downstream of the point where the shear layers have reached the centreline of the turbine. The far wake extent, i.e. the downstream distance for velocity recovery towards the free stream velocity in this area is dominated by convection and turbulent mixing with ambient flow. The velocity shear in the vertical profile of ambient flow influences the performance and wake development and dissipation of tidal turbines as large scale rotors are expected to be operating in highly sheared environments.

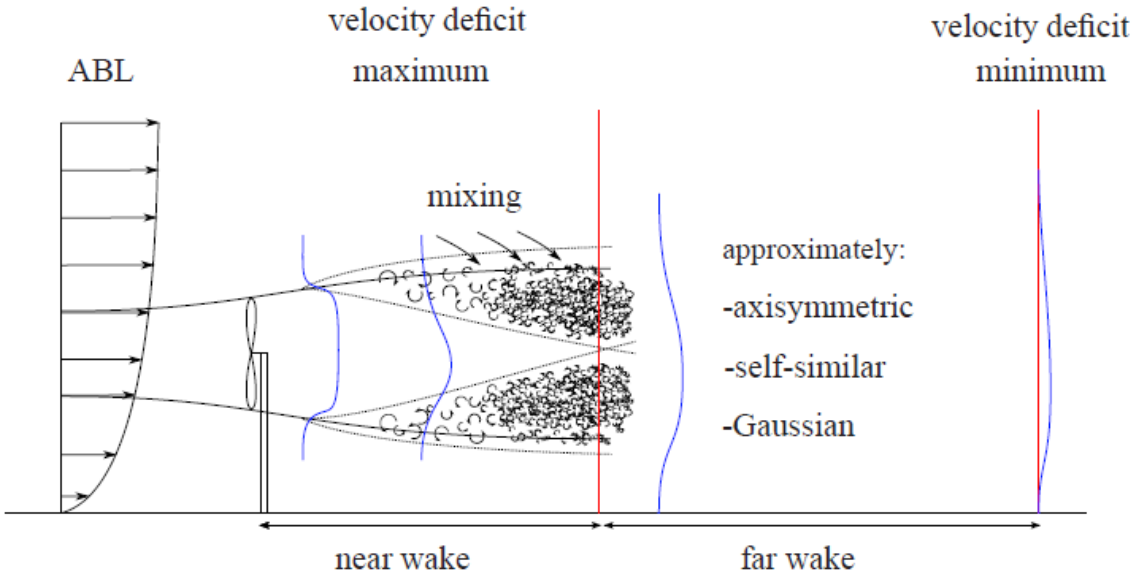

Figure 1-9 - Wake Classification Behind a Wind Turbine (Sanderse, 2009).

While the overall resource potential and extractable power was investigated using large scale one or two dimensional hydrodynamic modelling and analytical models that include the energy extraction of idealised single and multiple turbine arrangements (Garrett and Cummins, 2005; Garrett and Cummins, 2007; Vennell, 2011a; Ahmadian and Falconer, 2012; Funke *et al.*, 2014), assessment of specific turbine performance in tidal currents uses a combination of experiments and numerical methods based on BEMT and increasingly applying RANS and LES CFD modelling for combined performance, wake and array studies.

Initial research activity of detailed tidal turbine devices focused on investigating the hydrodynamic performance prediction of tidal turbines to assess the viability and estimate the extent to which energy can be generated from tidal flows in various operating conditions. Early experimental studies focused primarily on determining power curves of scaled prototype devices based on measured thrust and torque across a range of TSRs and the optimisation of performance in regards to realistic operating conditions such as proximity to bounding surfaces, waves, cavitation, and yawed inflow (Coiro *et al.*, 2006; Bahaj *et al.*, 2007b; Galloway *et al.*, 2014). These showed that in more realistic operating conditions performance predictions depended heavily on the encountered ambient flow conditions. Further optimisation of device specific design through improved blade design and determining optimum blade pitch angles (Jo *et al.*, 2012; Shi *et al.*, 2013) as well as testing of multiple rotors in close proximity (Bahaj *et al.*, 2007b; Clarke *et al.*, 2007) and the effects of foundation design (Giles *et al.*, 2011) have been presented with the aim of maximising the electricity generation capacity.

While a comparison between structured and unstructured mesh generation and two turbulence closure models (k – ε and k - ω SST) by Shi *et al.* (2013) showed little differences in the prediction of thrust loading, the performance differed increasingly with increasing TSR away from the design condition.

Numerical methods to assess the performance characteristics only, have been used in the process of designing blade section and analysing existing airfoil design. BEMT is used to design new, or analyse existing rotors and has been applied for marine propellers, wind turbines and tidal turbine blade design. The analysis matches the fluid momentum changes as determined from axial and angular inflow factors derived from momentum theory with the local lift and drag forces, at the corresponding angle of attack and Reynolds number, acting on the rotor blade elements. This however is isolated from the surrounding flow and the effects of the rotor on the incoming flow are neglected. Existing airfoil lift and drag coefficients from experiments or other numerical methods are required to calculate the resulting forces. Integration along the blade radius then determines the thrust and torque loadings used to determine performance characteristics in terms of C_T and C_P.

Development, validation and application of numerical BEMT methods to design and determine the performance of tidal turbines across a range of operating conditions, with validation from experimental test studies is presented in Batten *et al.* (2007). Additional corrections for the finite number of blades and non-uniform inflow (Turnock *et al.*, 2011) have been included and were used to investigate the effects of realistic tidal inflow and changing blade characteristics such as increased drag due to fouling (Batten *et al.*, 2008). Improved agreement with experiments was shown by Whelan *et al.* (2009) for high blockage cases by including surface deformation to more accurately predict loading on the turbines.

Some full scale performance measurements have been published (Jeffcoate *et al.*, 2015) however are currently, due to the competition in the industry, very limited in number and were according to predictions as stated by the authors. The highly turbulent and fluctuating operating conditions of tidal turbines operating in high current velocities are shown to result in fluctuations of 50% of the mean in terms of power and 30% for thrust highlighting the varying inflow and loading on the turbine and its components. Turbulence intensities measured in close proximity to the rotor across this full scale test have between 17% and 40% across the operational current velocity range of the device.

1.2.3 Numerical and Experimental Wake Characterisation of Single Turbines

Investigation and characterisation of the resulting flow fields due to energy extraction from tidal currents using HATTs have been performed experimentally and numerically by determining the wake formation and recovery towards free stream velocity downstream of the turbine, thereby giving an indication of likely device spacing in multi turbine configurations. In experiments and numerical simulations alike, simplifications are made for the investigation of far wake characteristics. Simplified methods, representing the tidal turbine without fully resolving the geometry by using AD modelling for numerical simulations and experiments to account for the momentum extraction through defining the rotor plane as a porous material thus generating a pressure jump. This has advantages numerically as the geometry and mesh resolution are reduced, therefore increasing computational efficiency. Experimentally scaling to very small scale introduces difficulties in keeping similarity of thrust, power and water surface profile (Myers and Bahaj, 2010; Mason-Jones *et al.*, 2012). However, further modifications, especially numerically to improve the modelling of small scale physics and energy extraction by including blade tip and rotational effects such as swirl, hub and tip vortices through turbulence intensity source terms where the blade geometry is not fully resolved in the numerical analysis are added to actuator disk simulations (Turnock *et al.*, 2011; Batten *et al.*, 2013). In addition, these methods usually ignore any transient effects induced to the flow.

Numerical actuator disk studies showed a strong relation between ambient turbulence levels and the downstream wake extent and rate of recovery (MacLeod *et al.*, 2002), with increased wake recovery seen for higher ambient turbulences. Lartiga and Crawford (2010) showed that actuator disk modelling achieved good agreement at blockage ratios up to 10% in a water channel compared to analytical expressions and used the results to correct experimentally measured values in bounded flow domains. Numerical simulations and a comparison to experimental study of the flow field around porous mesh disks by Myers and Bahaj (2010) are presented by Harrison *et al.* (2010) and show good agreement of wake recovery in the far wake, however under predict the velocity recovery. The simulations use k - ω SST turbulence model stated to be preferred to the k - ε for boundary layer and surface flows. The experiments investigated wake recovery as a function of the ambient flow turbulence observing convergence of wake deficit values across a range of thrust values. Increased sea bed roughness and varying flow velocities above and below the turbine wake in a non-central position within the vertical flow domain led to increased wake extent and lower flow velocities further downstream due to

merging of the sea bed and turbine wakes as well as a downshift in wake centreline. The resulting velocity and turbulence intensity contours are shown in Figure 1-10.

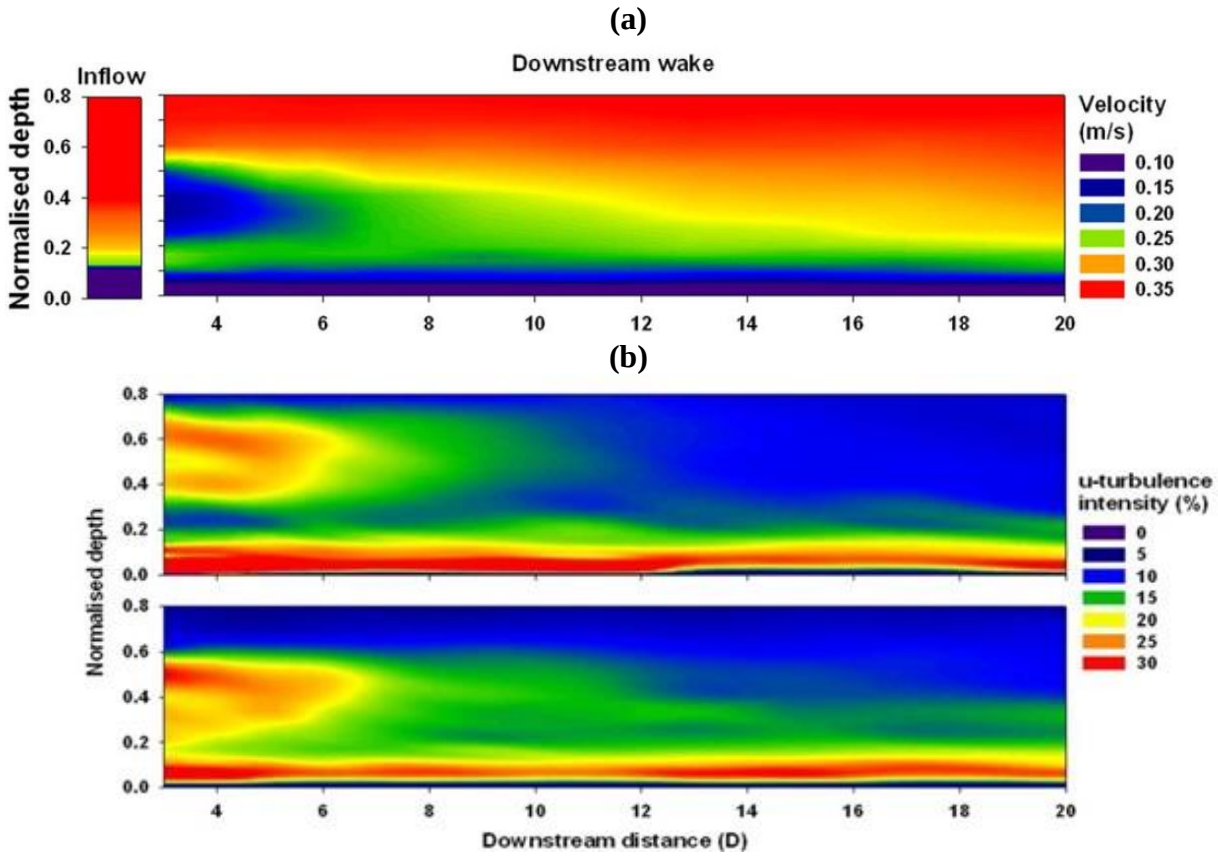

Figure 1-10 – Velocity Contours (a) for Close Proximity to Seabed (0.33D) and Turbulence Intensity (b) for Two Different Actuator Disk Locations (0.5D and 0.33D) from Experiments by Myers and Bahaj (2010). All Distances Normalised with the Turbine/Disk Diameter (D).

This shows that a number of factors regarding local bathymetry and turbine installation can affect the wake recovery. An important consideration stated by the authors is that increased turbulence intensities alone, especially at low current velocities may not accelerate and describe the wake recovery as expected. Differences in thrust coefficient of the porous mesh disks on the resulting wake velocity deficit have been shown to be small especially in the far wake 5 diameters (D) downstream and beyond. The authors highlight the need to account for improved turbulence modelling in the near wake to achieve better agreement of the wake characteristics in the near and medium wake. Far wake turbulence intensities show good agreement from 7D downstream of the disk in these low ambient turbulence level cases.

Combination of BEMT and RANS simulations offer a computationally efficient methodology of including blade forces in the prediction of resulting wakes without modelling the turbine geometry to a detailed level. This allows for efficient calculation of blade performance characteristics as well as wake characteristics. Improved modelling of the resulting velocity and turbulence intensity close to the disk without the use of empirical source terms otherwise included in AD modelling is shown in Figure 1-11. The flow velocities and turbulence in close proximity to the disk show improved wake modelling up to 3D downstream due to the blade induced forces.

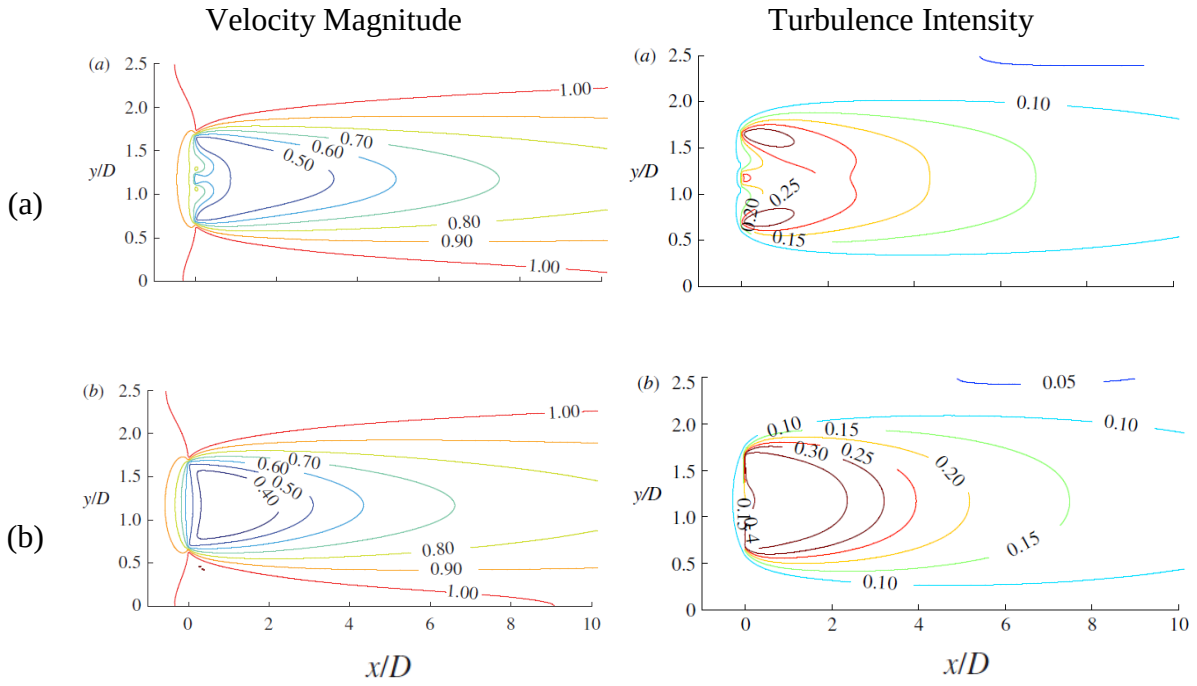

Figure 1-11 – Comparison of RANS+BEMT (a) and RANS (b) Actuator Disk Simulations for Velocity Magnitude (Left) and Turbulence Intensity (Right) from Batten *et al.* (2013) .

Agreement with experiments of actuator disk modelling including BEMT to determine the blade forces was shown to be improved by Batten *et al.* (2013) over Harrison *et al.* (2010) in comparison with the experiments from Bahaj *et al.* (2007b) in terms of performance and the medium wake characteristics between 5D and 10D as shown in Figure 1-12. The wake measurements are compared to the same turbine presented by Myers and Bahaj (2009) without including additional turbulence terms at turbine location for the numerical simulation as turbulence is generated by the velocity shear in the wake. In this RANS-BEMT modelling the *k*-ε turbulence closure model was used as eddy-viscosity was found to be under predicted for uniform actuator disk RANS modelling in previous studies using the *k*-ω SST closure model. The velocity and turbulence intensity characteristics downstream of the disk are shown in

Figure 1-12. Additionally the vertical velocity and turbulence intensity presented by the authors show improved agreement with increasing distance, and for both, better agreement over the top half of the wake than the bottom part.

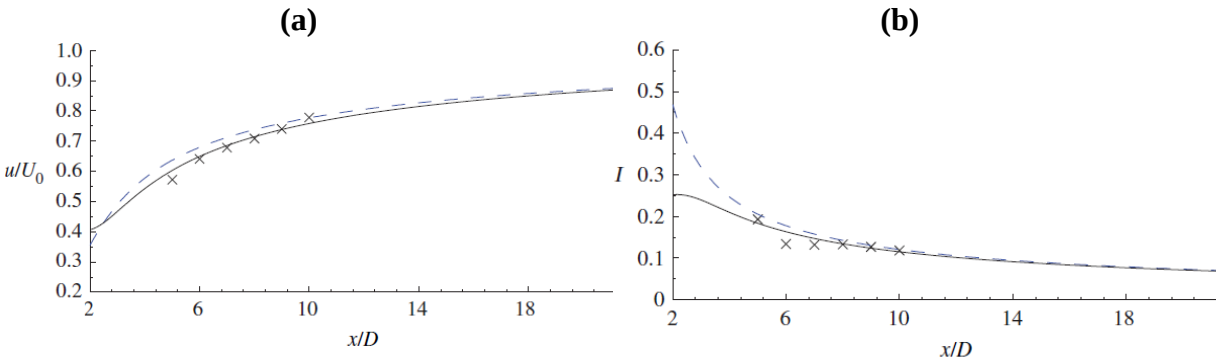

Figure 1-12 – Comparison of Normalised Wake Velocity from Batten *et al.* (2013) for (a) Normalised Velocity and (b) Turbulence Intensity for RANS+BEMT (Solid), RANS+AD (Dashed) and Experiments by Myers and Bahaj (2009) (Cross).

By accounting for blade induced swirl, Turnock *et al.* (2011) show good agreement of predicted power coefficient with Bahaj *et al.* (2007b). For the wake characteristics it is shown that accounting for swirl slows down the wake recovery processes, however no comparison to experimentally measured wakes is shown. The importance of adding turbulence intensity terms to account for the mechanical turbulence arising from turbine blades, and the sensitivity of wake spread in the near wake (x/D < 2) is shown by comparison of the wake growth downstream of the actuator disk to theoretical predictions. Malki *et al.* (2013) used a coupled RANS-BEMT approach to show the significance of free surface proximity and blockage effects on the development of the wake and characteristics of rotor performance, however these can be avoided by adapting the size of the numerical domain as well as considering the proposed method for deep immersion of tidal turbines where free surface effects are not expected and the turbine is located deeper within the water channel.

Fully resolved simulations and experiments investigating the resulting flow field of large and small scale experimental devices have been conducted to validate numerical models and gain detailed knowledge of the resulting flow field.

Myers and Bahaj (2009) present near wake measurements using ADV, downstream of a 0.8m diameter tidal turbine in a circulating water channel. The effect of a vertical support structure located downstream of the rotor on the downstream flow field was investigated and led to recommendation of highly streamlined and narrow support geometries as the resulting wakes influenced the downstream flow field of the rotor up to 6D, with a difference of about 10% at 3D in terms of velocity deficit when taking the upstream flow without support structure wake into account. The velocity deficit for the combined case is shown to reduce from approximately 50% to 22% between 3D and 10D. Comparison between a scaled turbine and actuator disk approach (Bahaj and Myers, 2013) show that wake recovery in the far wake (x/D > 8) can be modelled accurately by actuator disks. However, simplifications in numerical models of the near wake flow before transition to far wake recovery dominated by ambient flow conditions have to consider the rotor and support structure turbulence that plays a significant role in the wake evolution downstream of the turbine.

A combination of experiments and numerical simulation for detailed investigation and validation of numerical methods is presented by O'Doherty *et al.* (2009) and Javaherchi *et al.* (2013) including a comparison of isotropic and anisotropic turbulence models and one and two equation models respectively. Best agreement is found using Reynolds Stress Models (RSM) as turbulence closure model. The simulations used quasi-static three-dimensional RANS calculations with moving reference frame (MRF) to account for the turbine rotation. This was extended by investigating dimensional scaling of performance characteristics by conducting a range of simulations with increasing diameters and velocities (Mason-Jones *et al.*, 2012) determining a Reynolds number threshold of $\mathrm{Re} = 5 \times 10^5$ (based on turbine diameter and ambient flow conditions) for independent scaling of performance characteristics of the specific geometry tested. This was followed by investigation of sheared velocity profile and support structure by Mason-Jones *et al.* (2013) showing that both increased wake asymmetry and cyclic loading over the blade rotation. Utilising the same validated approach with a k - ω SST turbulence model, the performance of a tidal turbine design with support located either upstream or downstream of the rotor is evaluated (Frost *et al.*, 2015) and suggest increasing the distance between rotor and support to the maximum that is economically and mechanically viable.

It is also suggested that reduced loading is seen for upstream rotor location which may significantly increase fatigue life time thus justifying the concepts with mechanisms to face the incoming flow in both tidal current directions.

Detailed three-dimensional near wake characterisation of the turbine described in Mason-Jones (2010) in a confined flume environment with high blockage ratio of 16% and ambient turbulence levels of 2% is presented by Tedds *et al.* (2014). Vertical asymmetry in the wake due to free surface effects, with rotor top tip to free surface distance of 0.25D, is observed and could be influenced by the blunt shape of turbine support downstream of the rotor shifting the wake upwards, as observed and accounted for by Myers and Bahaj (2009). Experiments showed a strong anisotropy of turbulence due to the rotating blades and states that approaches with actuator disks neglecting the effects of swirl (Harrison *et al.*, 2010) over predict the reduction in turbulent kinetic energy (TKE) in the near wake. Contours of all three velocity components show that effects of turbine blade rotation are significant up to 5D downstream of the rotor and can be observed across the entire domain where measurements have been conducted (x/D < 7).

Different levels of ambient turbulence levels, ranging from 3% to 25%, have been investigated experimentally by Maganga *et al.* (2010) and Mycek *et al.* (2014a) showing significantly accelerated wake recovery horizontally and reduced vertical wake expansion for the flow field up to 10D downstream of the turbine. In general, a more diffuse wake shape and slight shift of the wake centreline towards the free surface resulting from the flow around the turbine support structure can be observed with higher turbulence intensities as shown in Figure 1-13. Areas of highest turbulence are recorded where shear layers reach the centreline and the location of this is further downstream with decreased turbulence intensity in both experiments. The mean performance of tidal turbines has been shown to not heavily depend on ambient turbulent levels, however larger fluctuations occur and impact the fatigue life and structural design of tidal turbines.

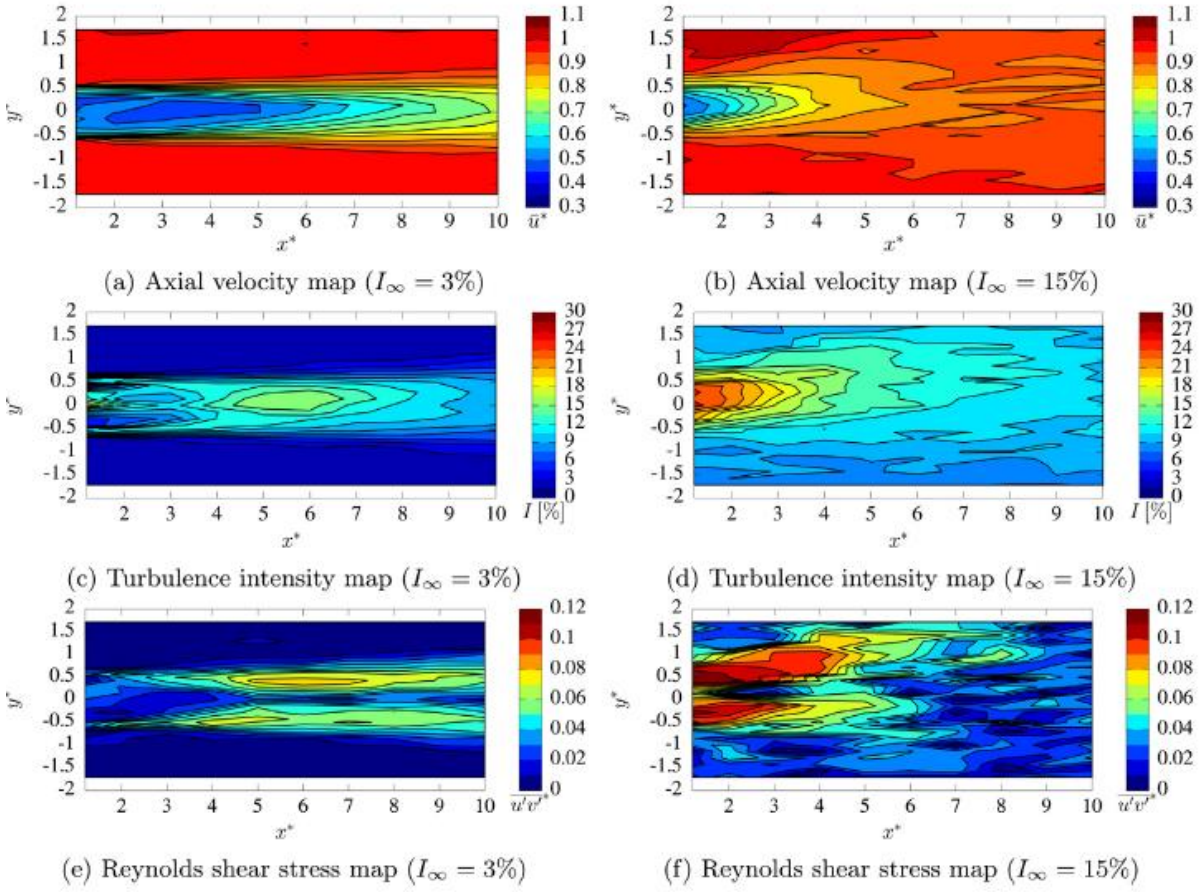

Figure 1-13 – Comparison of Different Ambient Turbulence Levels and the Effects on Wake Characteristics in Terms of Velocity, Turbulence and Reynolds Stress, as Presented by Mycek *et al.* (2014a).

Investigations conducted by Chamorro *et al.* (2013a) on the turbulent fluctuations of incoming flow and the effect on turbine power show a strong correlation at low frequency and provide a critical frequency above which the performance is decoupled from the turbulent fluctuations in the approaching flow. Three-dimensional wake measurements identified a velocity deficit of 10% remaining at 15D downstream and areas of high turbulence intensity persisting in the near wake. The maximum intensity is observed at the turbine top tip at locations linked to the breakdown of tip vortices (x/D < 3) and where wake rotation effects become insignificant at x/D < 4 which also relates to the onset of low frequency wake meandering. Further volumetric three component velocimetry (V3V) in the wake of a miniature tidal turbine (Chamorro *et al.*, 2013b) linked the breakdown tip vortices and onset of wake instability to the interaction between subsequent vortices shed of the blade tip from 2D downstream of the rotor. Numerical simulations of the aforementioned experiments by Kang *et al.* (2012), using a curvilinear immersed boundary method, show good agreement between LES and experiments for near and

far wake characteristics and comparison to actuator line and disk modelling highlights the physical effects of including hub and support geometry in fully resolved simulations as these allow for accurate prediction of device specific flow field including the dynamic effects of wake rotation and hub vortices in predicting wake meandering.

McNaughton *et al.* (2014) and Afgan *et al.* (2013) showed performance indicators for a three bladed tidal turbine including a vertical support structure and also presented information on the flow field within the wake up to 10D. RANS and LES are used and performance prediction is found to be in good agreement for most turbulence closure models tested (k - ε, k - ω SST and LRR RSTM) at optimum turbine TSR. The combination of RANS and k - ω SST turbulence model resulted in comparable performance characteristics at significantly lower computational resource requirement than LES, matching the LES results for the optimum design condition. The k-ε turbulence closure model performed noticeably worse in off-design conditions. Wake characteristics are shown but there is no comparison to experimental data available. The computational effort to complete a single turbine simulation using LES with sliding mesh to account for the rotation of the blades, reaching to at least 25 turbine rotations, was stated to be in the order of millions of CPU hours. Further discussion of LES and RANS approaches presented in McNaughton (2013), especially for wake modelling is presented and the authors suggest further investigation and comparison between experimental and numerical simulations for the accuracy of RANS approaches as fully resolved LES simulations are deemed infeasible.

A comparison between modelling tidal turbines using the approaches (AD, MRF and Sliding mesh) described above is shown by Liu *et al.* (2016) and the authors argue that the most realistic wake representation is achieved by fully resolving the turbine geometry and there is still limited information about comparison of simplified, resolved and experimental investigations of tidal turbine wakes. The most significant advantage of AD modelling is the generation of high quality structured meshes throughout the domain. The study showed that sliding mesh technique presents the wake characteristics most accurately in the near and far wake and captures realistic transient behaviour in the wake and comparison of normalized mean velocity to experiments conducted by Mycek *et al.* (2013) showed close agreement.

1.2.4 Numerical and Experimental Methodologies for Tidal Turbine Arrays

Some of the "key" factors determining the macro and micro array level design have been discussed by Vennell *et al.* (2015) including the influence of array sections on the ambient and large scale flow and available power characteristics. On a micro design level, the turbulence generated from devices and the wake mixing and velocity recovery of a small number of turbines in close proximity has a significant impact on the device spacing within the array as well as the optimised design of support structures to maximise power output and reduce risk of operating tidal turbines in these complex and challenging environments.

Theoretical models have shown that power generation of turbines operating in a tidal channel is improved by increasing the blockage ratio (Garrett and Cummins, 2007) and where it is practically infeasible to occupy the entire width of a channel by a tidal fence, the energy produced reduces to 1/3 of the tidal fence for turbines occupying a large fraction of the channel cross-section and to 2/3 of the tidal fence for turbines covering a small section of the cross-section. Assuming individual tuning of turbines placed within an array, Vennell (2010) shows that power potential can be maximised by maximising the area of the channels cross-section occupied by tidal turbines.

Extending the work of Garrett and Cummins (2007) to tidal turbine arrays has shown that with increasing local blockage efficiency is increased up to a level where total array efficiency is reduced due to array scale chocking effects reducing the flow through the entire array (Nishino and Willden, 2012). Investigations of centred and staggered arrays using theoretical linear momentum actuator disk theory (Draper and Nishino, 2013) showed that for multi-row arrays the device spacing within each row is a function of the number of rows, reducing the optimum blockage from 0.4 for one fence to 0.12 for two fences with a distance downstream between both of the order of the fence width. With additional rows this trend continues, thus recommendations for large spacing within each row to maximize power per turbine similar to offshore wind farms are made. Arrays with staggered rows of turbines to maximise the amount of energy generated by an entire farm are shown in Figure 1-14. The actual amount of energy extracted and optimisation of array and individual turbine performance is further investigated by considering multiple closely spaced rows as presented by Vennell (2011b). This work accounts for channel and flow characteristics and it was found that farm efficiency can be maximised by accounting for the effects of adding additional rows of turbines on the ambient flow and tuning of individual turbines and rows of turbines in array.

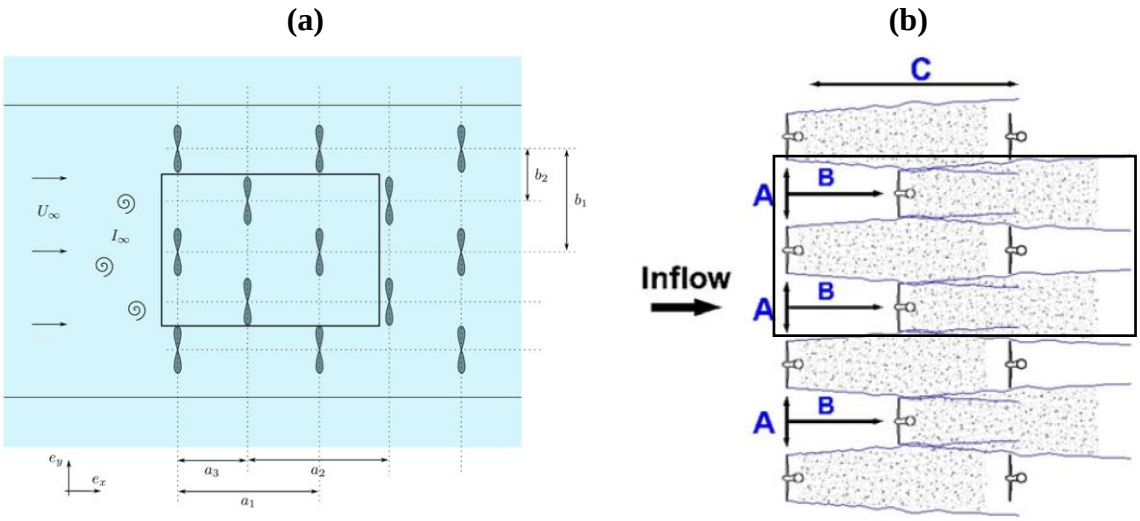

Figure 1-14 – Typical Array Description for Tidal Turbine Arrangement as Shown by (a) Mycek *et al*. (2014b) and (b) Myers and Bahaj (2012) for Classifying Inter Device Spacing with Additional Box to Show Staggered Array Section.

Large scale hydraulic investigations with non-stationary shallow water equations (Funke *et al.*, 2014) of tidal turbines have aimed to optimise specific designs for proposed tidal farms , shown in Figure 1-15. The optimum design for a previously rectangular aligned array consisting of 8 rows with 4 turbines each, for constant and sinusoidal inflow conditions are shown in (a) and for ebb tide in (b) respectively, and the resulting velocity fields in (c) and (d). Turbines are modelled as friction coefficient derived according to a single turbine study that resulted in maximum energy extraction. Further improvements include realistic modelling of local seabed conditions and inclusion of turbulence closure models for improved wake modelling.

Similar mathematical methods of accounting for individual turbines are used in the optimisation of offshore wind farm layouts (Pérez *et al.*, 2013), accounting for the wake development and interactions in a wide range of models from analytical solutions to resolved numerical simulations. An overview of the current wake modelling approaches in presented by Vermeer *et al.* (2003), Barthelmie *et al.* (2009) and Sanderse *et al.* (2011). The requirement for validation of simplified models is highlighted in these, stating reducing performance of wake models with increasing size of wind farms.

Typical inter device spacings in the offshore wind farms used for validation of numerical models range from 4D to 10D in longitudinal direction (Barthelmie *et al.*, 2009) and approximately 3D in transverse direction (Raúl Bayoán *et al.*, 2010). The main differences in the array design for tidal stream turbines lie in the strong bi-directional currents compared to a

wider range of wind directions faced in offshore wind farms where averaged power losses of downstream turbines offshore were 12%, while operation in full wakes led to power losses of up to 40% (Barthelmie *et al.*, 2009). Furthermore, large scale extraction of energy from tidal currents can affect the tidal flows while wind farms are too small to affect the weather systems and in addition beneficial blockage effects may be exploited in tidal channels where optimum levels of vertical and cross sectional blockage can be identified for specific locations (Vennell *et al.*, 2015).

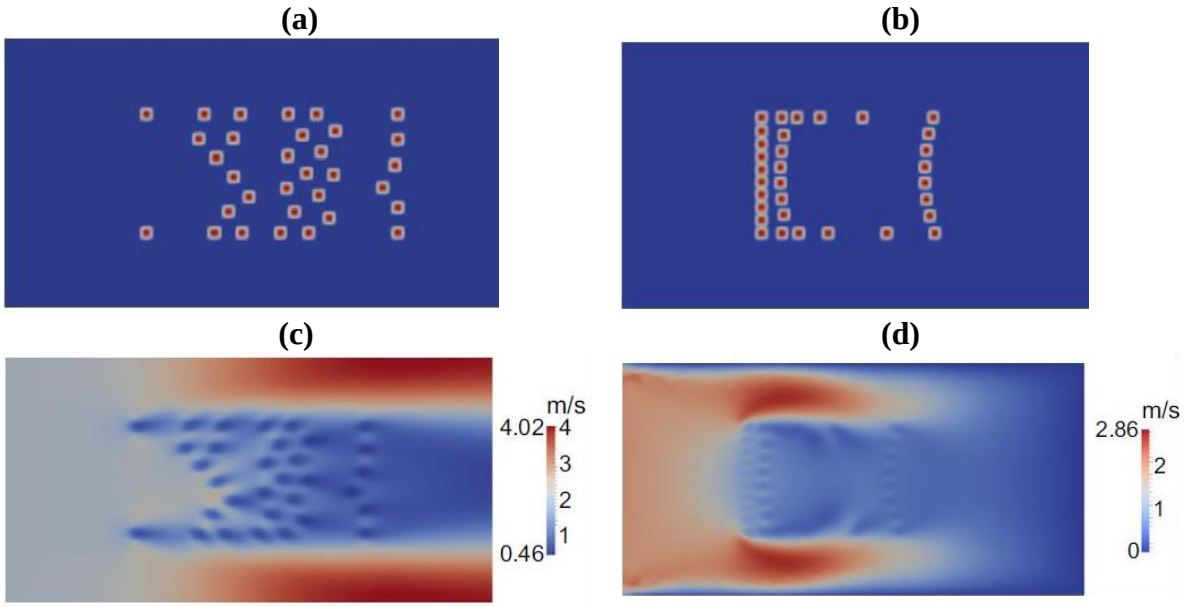

Figure 1-15 – Array Optimization by Funke *et al.* (2014) Showing Array Turbine Arrangement (Top) with Constant Inflow (a) and (c) and Sinusoidal Flow (b) and (d). Contours Show the Resulting Velocity Magnitude In and Around the Array (c) and (d).

Experimental studies of tidal turbines arrays presented by Myers and Bahaj (2012) used up to three actuator disks to investigate wake interaction with varying transverse separation (0.5D to 1.5D) between two disks in a single row array, and a two-row array with a third actuator disk being located 3D downstream of the first row. Use of mesh disks enables testing at very small scale by achieving similarity of thrust coefficient through different levels of disk porosity and avoids scaling effects of mechanical rotors at very small scale requiring excessive rotation rates to achieve required tip-speed ratios. Optimum transverse spacing was shown to increase flow velocity between adjacent disks with 1.5D spacing, where smaller spacing showed combined wakes of each individual disk and increased thrust coefficients. By placing a third disk in the accelerated jet between the two upstream disks, near wake deficit of the first row turbines was reduced as these were diverted around the downstream disk.

The combined wakes further downstream of the array showed increased width and higher centreline velocity deficits due to reduced ambient flow mixing reaching the wake centreline. No increase in thrust of the upstream disks was recorded when placing a third disk downstream and the thrust coefficient of the downstream disk is equivalent to the upstream disk with $C_T \cong 0.92$, using the inflow velocity at the position of the disk in its absence.

Mycek *et al.* (2014b) investigated the effects of axially aligning multiple turbines with the flow direction on the wake characteristics and performance of tidal turbines at different inter-device spacing (2D to 10D) and ambient turbulence levels (3% and 15%). With increasing turbulence intensity, the wakes of the upstream and the downstream turbines are more alike and recovery of wake characteristics to ambient levels occurs much closer to the turbine than in a low ambient turbulence environment where wake effects are more pronounced throughout the downstream area. Evolution of TSR, C_P and C_T are provided with reference to the array inflow condition to determine array efficiency when knowing only the inflow to the section of an array. Experiments showed reductions in C_P up to 50% for the downstream turbine operating in the wake of the upstream turbine. Downstream distance between devices can be significantly reduced for locations with higher ambient turbulence intensity due to the accelerated wake recovery.

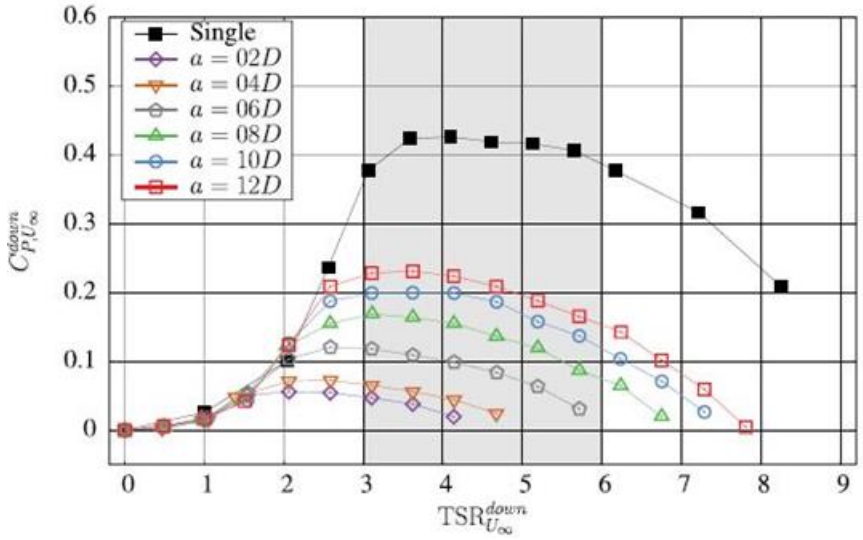

Figure 1-16 - Power Curves for Tidal Turbine Operating the Wake of an Upstream Turbine at 3% Ambient Turbulence Intensity for Different Distances Downstream and Comparison to an Isolated Turbine from Experiments Presented by Mycek *et al.* (2014b).

Horizontal wake field measurements in the near wake of small scale tidal stream turbines have been shown for two axially aligned turbines by Walker (2014a) using two dimensional PIV measurements. Small differences in wake structure are observed but turbulence of upstream turbine wakes is reported in terms of increased vorticity in the wake of the downstream turbine influencing the wake of the downstream turbine for 5D and 10D downstream spacing. The power performance of downstream turbines is reduced and differences of 40% are observed between 5D and 10D location of the downstream turbine.

Multiple 3-bladed tidal turbines were used by Stallard *et al.* (2013) in various configurations and inter device-spacing to investigate the wake characteristics and interactions of turbines in transversely bounded flow where the side wakes are bound by tank walls and centre wakes by adjacent wakes. Longitudinal, transverse and vertical velocity profiles and turbulence intensities are presented for several arrangements of multiple turbines located in a single row. For transverse separation of 2D and less, wake merging between adjacent wakes was observed resulting in nearly constant velocity deficit across the wake width by 8D downstream.

For these configurations, thinner wake shapes and faster wake recovery are seen in areas between wakes due to increased turbulence levels. Comparisons between RANS - BEMT and experimental measurements of thrust and wake velocities are reported by Olczak *et al.* (2016) showing that inclusion of device generated turbulence improved agreement between experiments and numerical simulations especially in the near wake region where $x/D < 4$. It was also found that the velocity deficit between adjacent wakes is under predicted for $x/D < 8$. The predictions of thrust coefficients on the actuator disks compared to experiments show variations of less than 10% for the front row, 20% for second and 38% for the third row. The differences to experimentally measured thrust are increased especially on the centre turbines operating in the wake of upstream turbines.

Comparison of 3D actuator disk simulations with different versions of the *k*-w SST model using an adaptive dynamic mesh by Abolghasemi *et al.* (2016) showed good agreement with side-by-side and in-line experiments as presented by Stallard *et al.* (2013) and Mycek *et al.* (2014b) respectively. Accurate predictions of the numerical model were observed in the far wake. For in-line configurations with lower ambient turbulent intensity the agreement was improved in the near wake compared to higher turbulent inflow and close transverse spacing of turbines. Shives and Crawford (2016) considered the standard *k*-ω SST model to be appropriate for

modelling with actuator disks. Empirical tuning of the turbulent kinetic energy production with an additional source term to include the effects of blade tip vortex breakdown across a pre-defined region downstream of the turbine is shown to achieve improved agreement with the experimental array studies mentioned. The additional source term varies between experimental conditions, most significantly the ambient turbulence levels and rotor geometry, and is thus tuned to available experimental data for comparison. Accounting for tip vortex turbulence in AD modelling is shown to improve the predictions made by the numerical model and improvements are more significant for closely spaced arrays of turbines.

To model tidal turbine arrays with reduced computational resource requirements, tidal fence simulations have been compared to experiments along with numerical considerations for defining an experimental inflow profile and the prediction of flow near boundaries. Results of this study by Daly *et al.* (2013) showed that an $1/8^{th}$ power law gave best agreement with experimental results for the downstream wake characteristics and constrained flow around the fence.

Further numerical simulations of tidal arrays with fully resolved turbines have been conducted using steady state solutions with MRF to simulate the blade induced rotational flow by Lee *et al.* (2010). The study was investigating the distance between 6 tidal turbines arranged in a generic sea side and lake environment. Optimum spacing of turbines was found to be three turbine diameters to maximise efficiency and wake asymmetry due to turbine rotation could be observed in the flow field data presented. Further modelling of the flow field within a small tidal turbine array using LES in combination with actuator lines to represent the rotation of turbine blades is presented by Churchfield *et al.* (2013) to investigate the structure of unsteady wakes and determined staggered arrays to have higher efficiencies. Additionally rotating downstream rows of turbines in opposite direction was found to show small benefits. The importance of including tangential forces in simplified representations of tidal turbine in simulations was highlighted by the existence of asymmetric wake structures.

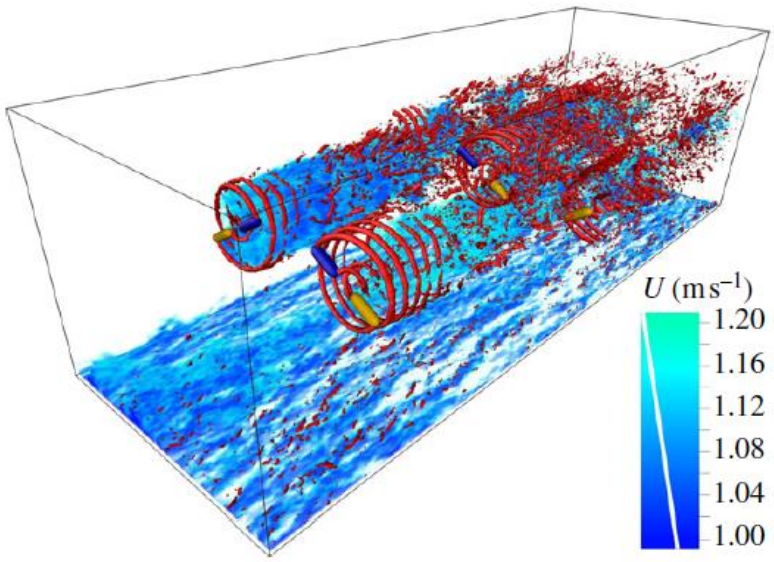

Figure 1-17 – Resulting Array Flow Field from LES with Actuator Line Modelling as Presented by Churchfield *et al.* (2013).

A fully resolved numerical simulation with two tidal turbines arranged in line has been presented by Liu *et al.* (2016) with a second turbine being located 8D downstream of the first. The velocity contours show the downstream turbine operating with significantly reduced wake velocities, most pronounced at the centreline, and very slow moving fluid in the near wake of the downstream turbine. The contours also highlight areas of significantly increased turbulence intensity about 4D downstream of the second turbine due to accumulation of turbulent effects in the wake and increased wake recovery downstream of this area. Performance of the downstream turbine is significantly affected while loading on the structure is increased as a result of the increasingly turbulent inflow. The comparison of different modelling techniques for tidal turbine arrays showed that AD modelling is sensitive to the definition of input parameters, especially turbulence length scales, and result in different wake profiles. This leads the authors to suggest further investigations on the reliability of AD modelling for array simulations. The authors also suggest using C_P rather than C_T for derivation of the axial induction factor when using actuator disk, though both approaches show the weakness of near wake modelling up to 10D with agreement of wake velocity deficit with experiments from (Mycek *et al.*, 2013) improving further downstream.

1.3 Aims & Objectives

With the previous work carried out and future outlook of marine energy introduced, specifically the development of large scale tidal turbine arrays, the aim of this project is to investigate the wake characteristics and turbulence effects of single turbines and small arrays through a combined experimental and numerical study. This will provide insight into the effects of arrangements of multiple turbines in close proximity and provide guidance on positioning of tidal turbines in closely spaced arrays as well as showing the applicability of open source software to the numerical modelling of tidal turbine arrays.

Correctly scaled and conducted measurements in physical experiments can provide detailed information of the resulting flow field. However, experiments are very time consuming and expensive to conduct. Recording detailed information on complex, three-dimensional flows such as those investigated herein is difficult and can be intrusive to the flow features investigated, especially for tidal turbine arrays. Although experiments investigating the operation of tidal turbines in the wake of upstream turbines have been discussed in the literature review, the effect of varying close transverse and longitudinal spacing in staggered arrays is yet to be experimentally investigated.

Numerical simulations provide an alternative and enable detailed investigations of specific areas of flow of interest at reduced cost. Existing uncertainties and challenges of numerical modelling have been highlighted and displayed a range of numerical methodologies used to account for important characteristics such as the inflow conditions, turbulence modelling, and inclusion of turbine geometry as well as blade rotation induced effects. While the computational resources required can be very significant, availability of open source software and increasing computational power at reduced prices will aid in accurately modelling the flow within tidal turbine arrays.

However, a combination of both allows to gain an insight into the resulting flow fields and provides reliable data for numerical validation that allows for further investigation using numerical models. Therefore a comprehensive experimental study is carried out to investigate the array effects within an axially aligned and staggered section of a second generation array, thus providing experimental data for comparison with numerical predictions of the resulting wake characteristics. Following validation of the application of open source codes for the simulation of tidal turbine arrays, the numerical model is then used to further investigate the

complex three-dimensional flow resulting from energy extraction in closely spaced array sections.

Experiments with small scale tidal turbine devices are conducted to gather data of the array centreline wake recovery using PIV measurements. Numerical simulations are configured and carried out using openly available open source software packages, investigating the suitability of automated mesh generation and multi-core processing for the simulation of tidal turbine arrays with dynamic mesh features to take into account the blade rotation, thus representing the experimental conditions.

The specific objectives of this thesis can be summarized as follows:

1. To conduct experiments investigating the effect of varying spacing on the wake characteristics in tidal turbine arrays. This requires:
    a. Designing a model tidal turbine device for experiments in a circulating water channel and a long water flume.
    b. Defining an experimental set-up in terms of operating conditions, flow field measurements and test matrix aimed at representing a realistic commercial array arrangement.
    c. To process and investigate the resulting wake characteristics for different in-line and array configurations with varying longitudinal and transverse spacing of individual devices.

2. To investigate numerically the resulting flow field within tidal turbine arrays. This requires:
    a. Conducting automated mesh generation and pre-processing of numerical simulations in open source software.
    b. Simulating the flow field within and downstream of tidal turbine arrays with varying longitudinal and transverse device spacing.
    c. Validating the numerical predictions with the experimental results.
    d. Further investigating the complex three-dimensional flow field.

1.4 Thesis Outline

Chapter 1 introduced the field of tidal stream energy and highlighted its importance and potential to play a significant role in the decarbonisation of electricity production. The current state of research of experimental and numerical investigations of tidal stream turbines has been reviewed and the need for detailed studies of array flow fields has been highlighted.

Chapter 2 describes the objectives and design considerations of the employed model turbines characteristics. In addition, the specifications for experimental studies in the circulating water channel (CWC) as well as wind wave and current flume (WWC Flume) are provided. An introduction of the test facilities and their flow characterisation is presented along with further details of the equipment and processing of the obtained measurements.

Chapter 3 provides insight into the numerical methodology applied to model the wake flow field of tidal turbine arrays using OpenFOAM with dynamic mesh capabilities. Specifications of the numerical set-up are introduced to model the flow according to the experimental study and a thorough validation of the numerical set-up is performed for performance and wake modelling.

Chapter 4 presents the results of the experimental tidal turbine study and a comparison between numerical and experimental wake characteristics is shown as validation of the applied numerical methodology. Results are presented for single and multiple turbine configurations with axial alignment (WWC Flume Test) and single as well as multiple turbines in a staggered array arrangement (CWC Test). Further numerical and experimental results are presented to investigate the flow field and take advantage of the applied measurement and simulation methods for investigation of complex flow fields.

Chapter 5 provides a synthesis and summary of the obtained results and highlights the main findings and considerations. Further research potential is identified and presented.

Chapter 2. Experimental Investigation

Testing large scale prototypes of tidal turbines requires significant capital investment and is primarily done by device developers to confirm performance objectives of developed designs as these are the vital parameters governing economic performance and justify long term investments. Wake characterisation becomes vital when moving towards installations of multiple turbines in close proximity as this can significantly alter the operational conditions faced by a device, in turn affecting the performance and lifespan of devices and their equipment. Full scale measurements at turbine location introduce a number of uncertainties due to environmental and geographical features, thus studies in controlled environments will provide insight of the wake characteristics due to changing array layout and inter-device distances at reduced costs and risks, while allowing a greater number of conditions to be investigated.

Additionally, results from experimental studies can be used for validation of numerical models further decreasing the costs and expanding the opportunities for investigating a wide range of parameters determining the power extraction and wake development. This is especially of importance where full scale data measurements for validation are not yet available in great numbers, as is the case for the tidal energy industry.

Comprehensive experiments have been conducted in two different test facilities at Shanghai Jiao Tong University. Scaled tidal turbine models were used to investigate the interactions of multiple turbines operating in a number of configurations. A long wind, wave and current flume (WWC Flume) was used to investigate the varying wake recovery for multiple turbines axially aligned and a circulating water channel (CWC) with a wide test section area was used to investigate the array centreline flow field and its variations due to the transverse and longitudinal changes in inter-device spacing.

This chapter will introduce the experimental design and testing objectives and characteristics of the model turbines used across all experiments. The characteristics of test facilities and configurations tested in each, as well as the flow measurement equipment and analysis procedure are outlined.

2.1 Design of Model Turbine

Four small scale (1/70th), three bladed tidal turbine models with bottom mounted support have been designed and built to conduct experiments in two experimental test facilities. The model (Figure 2-1) was designed to allow for change in rotor centreline height and included a mechanism that allows for variation of the blade pitch angle. The connection of blades and rotor hub is designed to accommodate increased blade diameters if required for further studies. The specific details of the scaled model are described in the following section.

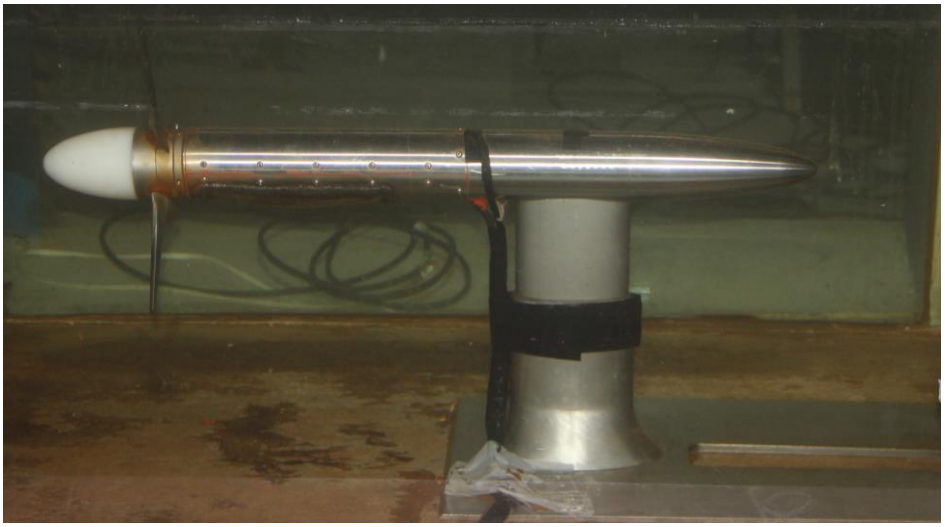

Figure 2-1 - Scaled Tidal Turbine Model in Long Wind Wave Current Flume.

2.1.1 Blade Section Details

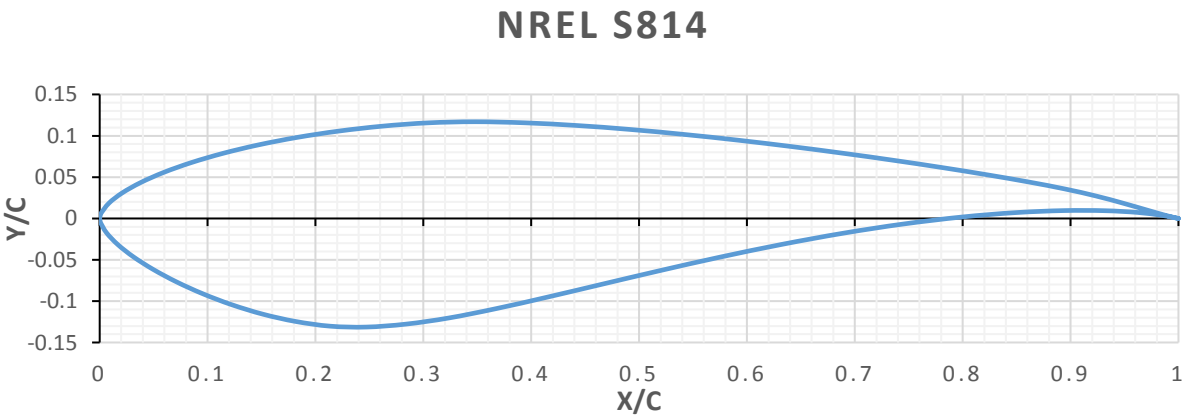

Figure 2-2 – NREL S814 Blade Profile.

The blade design is based on the thick NREL S814 airfoil section as shown in Figure 2-2 and has been geometrically scaled to a diameter of 0.28m with chord and pitch distribution as shown in Table 2-1. The blade section was chosen because of its robust performance characteristics in terms of maximum lift coefficient and has been designed to be less sensitive to surface roughness and operation in unsteady inflow conditions (Somers, 1992). Based on these blade design considerations, the presented blade sections are seen as a robust basis for generalised wake characterisation in tidal turbine arrays where changes in surface roughness due to abrasion may play a significant role in reducing the performance of tidal turbine blades. Further, due to the thick blade characteristics, the blades provide structural stiffness for tidal turbine application (Milne *et al.*, 2013; Milne *et al.*, 2015). The initial design objectives and wind tunnel tests of the airfoil section are presented, along with further information about the performance by Somers (1992) and Somers and Tangler (1996). The performance of the applied rotor design has been previously investigated experimentally in a cavitation tunnel and numerically by Shi *et al.* (2013) for a slightly larger model turbine with a diameter of 0.4m. The resulting C_P vs TSR curves for various numerical modelling approaches and experiments at optimised pitch angle of 8.33° in Figure 2-3 show optimum performance with a highest power coefficient of approximately 0.44 for tip speed ratios ranging from approximately 3.2 to 4 during experiments in a cavitation tunnel and a thrust coefficient of approximately 0.95 over a wider range of tip speed ratios.

Table 2-1 - Geometry of Scaled NREL S814 Rotor.

r/R	**0.3**	**0.4**	**0.5**	**0.6**	**0.7**	**0.8**	**0.9**	**1**
Chord length (mm)	42.04	39.05	36.03	33.03	29.53	27.01	24	21
Pitch Angle (Degree)	23.33	15.83	12.33	10.33	8.33	7.93	7.03	6.33

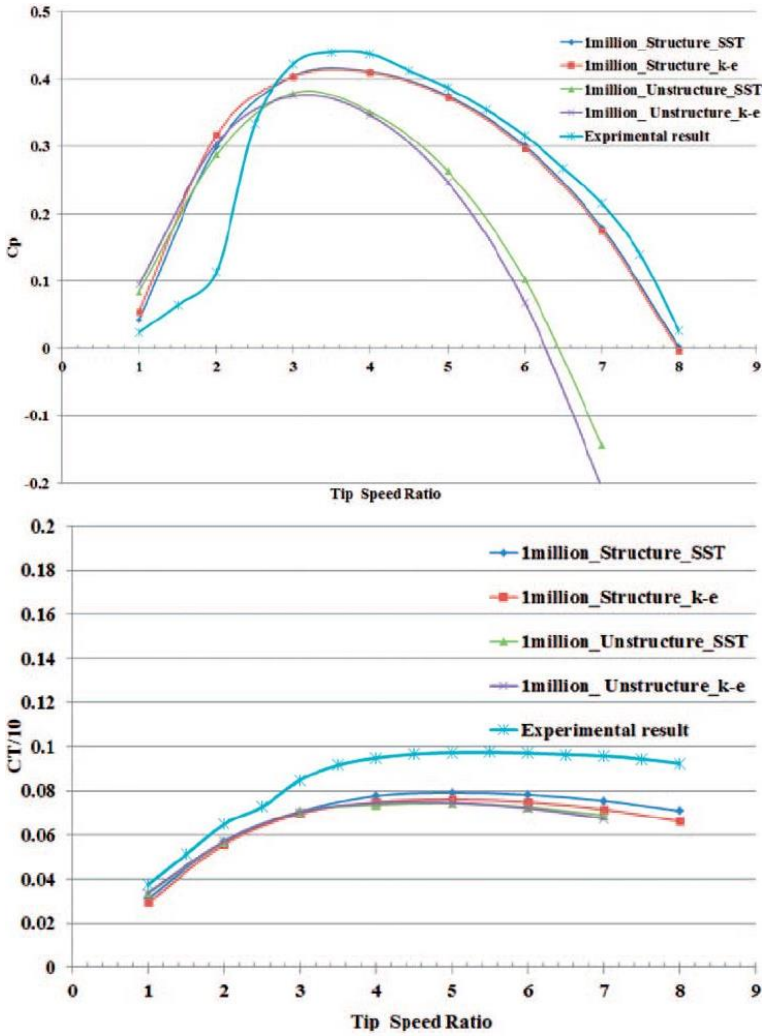

Figure 2-3 – Experimental and Numerical C_P and C_T for NREL S814 Blade Design from Shi *et al.* (2013).

For the experiments presented here, the blade diameter has been constrained by the use of a long wave-current flume with a water depth of 0.56m hence was chosen to represent the typical depth to diameter ratio of about 2. For experiments in the large test section of the CWC the diameter of 0.28m led to small blockage of the cross section for the incoming flow in multi turbine arrangements. The blades were precision fabricated from stainless steel with additional smoothing of all surfaces prior to the experiments. One of the manufactured blades with a circular root for connection to the rotor hub and the local chord and twist distribution is shown in Figure 2-4.

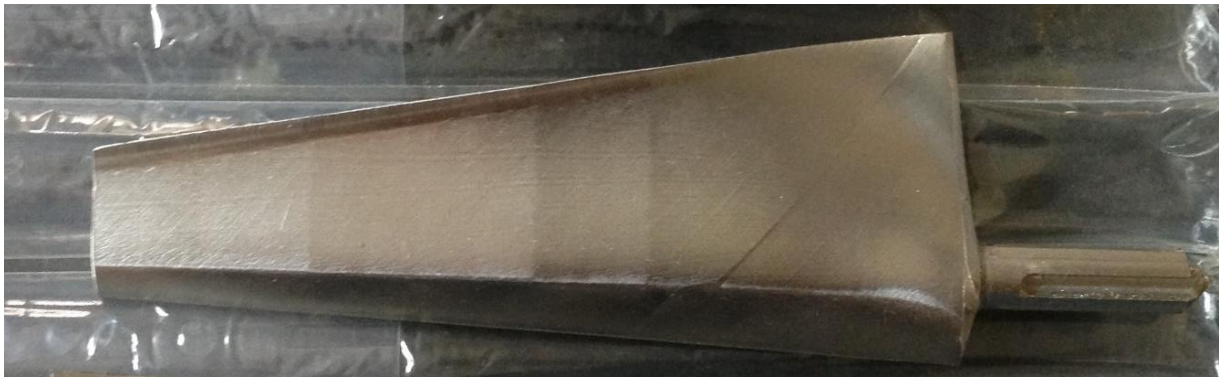

Figure 2-4 - Stainless Steel Turbine Blade with NREL S814 Section Details and Chord and Twist Variations.

2.1.2 Nacelle, Hub and Vertical Support Structure

The nacelle was designed to contain the AC motor for control of rotational rate of the turbine and for some of the turbines a load cell for thrust measurement. Due to the location on the floor of the respective test section, the compartments were made watertight to allow for the control of the individual turbines through an external control system only. A design objective was to not require any type of external drives or shafts thus disturbances to the flow field are reduced to the vertical support and support frame near the bottom of the test section only. This resembles the design of first and second generation commercial turbines as outlined earlier, which are primarily bottom support horizontal axis devices.

To minimise the size and effects on the resulting flow field, streamlined front and back cones are designed for the upstream and downstream end of the cylindrical main body of the nacelle. The CAD design of the rotor hub and front cone are shown in Figure 2-5. The cone was fabricated of plastic to reduce the weight of the rotating parts thus loading on the motor shaft. No transitional blade sections were used in the root region close to the hub, hence the front cone diameter was chosen to correspond to the first blade section located at r/R = 0.23 with a diameter of 6.4cm. This allows for a wide range of pitch angles to be tested, as well as the possibility to test increased rotor diameters due to the flexible attachment mechanism. Additionally, the incoming flow is directed towards the blade section reducing the impact of the cylindrical blade to rotor hub connection.

(a) **(b)**

Figure 2-5 – (a) CAD Design of Rotor Hub and Cone and (b) Fabricated Cone and Rotor Hub

The distance between rotor centre and location of the vertical support was maximised by locating the centre of the rotor hub one diameter upstream of the support leg based on the findings from previous experimental and numerical studies investigating the effect of support structure to rotor spacing (Walker (2014a), Frost *et al.* (2015) and Mason-Jones *et al.* (2013)). Similarly, the shape of the support structure facing the incoming flow was designed with an elliptical shape to reduce the impact on the flow field by minimizing the cross flow dimension. The vertical support was designed in two parts to allow for changes of the operating height of the model turbine to investigate different distances to bounding surfaces and various positions within the vertical water column. For smooth connection to the nacelle, the vertical support was built with a width of 6cm and length of 11cm for the fixed external part on the bottom while the dimensions of the adjustable part are reduced by 1cm to slide within the external support structure as shown in Figure 2-6 (a). A CAD model of the turbine assembly at its maximum rotor height is shown in Figure 2-6 (b) where both the inner and outer part of the vertical support are shown.

Figure 2-6 – (a) Photo of Constructed Support Plate and Outer Vertical Support, (b) CAD Model of Tidal Turbine at Maximum Height.

The main dimensions of the turbine nacelle are shown in Figure 2-7 showing the small increase of nacelle diameter directly downstream of the rotor to accommodate the motor assembly. The vertical distance can be varied from a centreline height of the rotor of 20cm, thus a rotor bottom tip to sea bed separation of 0.2D, up to 35cm corresponding to a distance between the test section floor and the rotor tip of 0.75D. All efforts have been made to minimise the diameter of the nacelle (6cm), and a nacelle to rotor diameter ratio of 21.5% was achieved, comparable to other tidal turbine devices tested experimentally, usually with hub diameters ranging from 10% to 20% of the rotor. The size of the AC motor and especially the wiring of the motor and thrust sensor required parts of the nacelle to be slightly increased in diameter (6.7cm at maximum) over a short distance downstream of the rotor hub. The effects of this increase are kept minimal by locating the cable connection on the bottom side between the rotor and vertical support structure as can be seen in Figure 2-7.

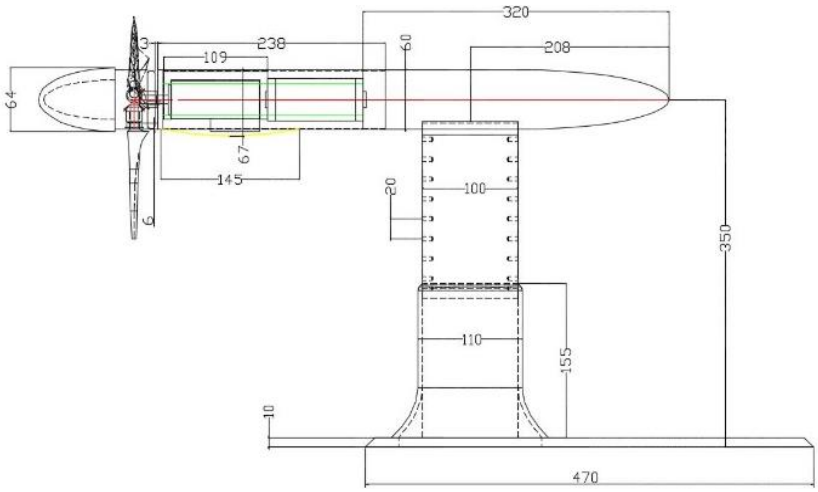

Figure 2-7 – Schematic of Location of Motor and Thrust Sensor with Main Dimensions (mm).

(a) **(b)**

Figure 2-8 – (a) Blade Pitch Mechanism of Scaled Tidal Turbine Model and (b) Rotor Blades Assembled into the Hub and Blade Pitch Mechanism.

The blade pitch mechanism shown in Figure 2-8 allows to rotate the blades in 0.5° steps over a total range of 10°. For all experiments presented here, the blade pitch angle was kept constant at the previously identified (Shi *et al.*, 2013) optimum pitch angle of 8.33° to investigate the wake characteristics at optimum power generating operating condition.

2.1.3 Support Plate and Frame

Each of the tidal turbine models was placed on a rectangular support plate, as shown in Figure 2-6, to provide additional stability during experiments. The support plate was cut to allow the laser light to reach to the endpoint of the nacelle for PIV recordings in the Circulating Water Channel. The leading edge of the support plate was cut at an angle of 45° based on findings by Giles *et al.* (2011) and Giles (2013) showing that increased velocities and reduced effect of the boundary layer can be achieved by using ramp foundations for tidal stream turbines. In this configuration however, a flat plate extending downstream of the rotor was used to minimise the effects on the incoming flow and reduce interference with the downstream flow.

The support frame shown in Figure 2-9 was designed to accommodate all array configurations and allowed for quick repositioning of the second row turbines in transverse and longitudinal direction for all experiments conducted within the CWC. The first and last turbine in array were installed at the centre of the front and back row while the two turbines of the second row could be moved longitudinally from a location corresponding to 3D downstream spacing between rotors in first and second row to 5D spacing as shown in Figure 2-9 (a). In the transverse direction turbines were located along the rail using the fixing mechanism shown in Figure 2-9 (b). The leading edge profile of the support frame was again designed with a 45 degree sharp ramp design, matching the ramp profile of the individual turbine support plates to minimize the flow disruption caused by the supporting members used to locate the combined turbine device and support plate on.

(a)

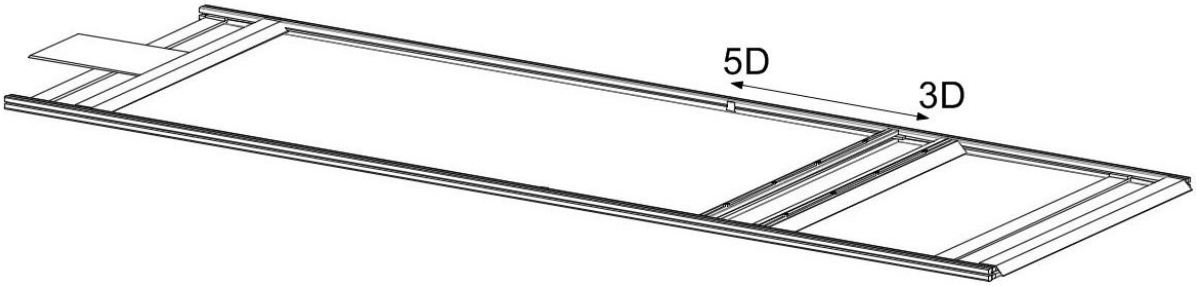

(b)

Figure 2-9 – (a) Design of Turbine Support Frame Showing the Three Rows used to Install Model Turbines on (b) Support Frame with Detail of Turbine Model Mounted on Second Row.

2.1.4 Scaling for Operation and Ambient Flow conditions

Scaling of model turbines for experiments and numerical simulations is important to maintain geometric, kinematic and dynamic similarity for results to be extrapolated to the full scale design and operation. Geometric similarity is maintained by scaling the blade section details according to the size of the rotor blades required for testing the model turbines in the experimental facilities used in this study as outlined previously. Kinematic similarity is achieved by scaling the ambient current velocities and rotation of the rotor blades defined by the tip speed ratio (TSR), $\lambda = \omega_t R / U_\infty$, where U_∞ is defined as the ambient velocity upstream of the tidal turbine array, R is the radius of the rotor and ω_t the angular velocity (rad/s).

Dynamic similarity, i.e. matching the Reynolds Number (Re) between scaled experiments and full scale tidal turbines, is inherently difficult to maintain as high rotational speeds and current velocities are required at small scale. When exact similarity cannot be maintained it is essential to achieve turbulent flow regimes of the same classification, thus in this study Reynolds numbers have exceeded the laminar-turbulent threshold of approximately 2×10^3 for all reference lengths as shown in Table 2-2.

Table 2-2 - Reynolds Number Based on Different Characteristics and Inflow Velocity Specifications.

	CWC - 0.44m/s		**WWC Flume - 0.275m/s**	
Characteristic Length	Re (U_∞)	Re (U_{tip})	Re (U_∞)	Re (U_{tip})
Diameter	1.23E+05	4.93E+05	7.70E+04	2.80E+05
Radius	6.16E+04	2.46E+05	3.85E+04	1.40E+05
Chord (0.5R)	1.58E+04	6.34E+04	9.90E+03	3.60E+04
Chord (0.7R)	1.30E+04	5.19E+04	8.11E+03	2.95E+04
Chord (tip)	9.24E+03	3.70E+04	5.78E+03	2.10E+04

For improved accuracy and extrapolation to large scale, it is important to achieve Reynolds numbers that exceed thresholds that have previously been identified above which the performance and wake development become independent of the observed range of Re. The choice of characteristic length for calculation of Reynolds numbers varies across previous tidal turbine and wind turbine experiments as shown in Table 2-3. Reynolds numbers have been calculated using the free stream current velocity as well as tip speed of the rotor and the turbine diameter by Chamorro *et al.* (2013b), radius (Mycek *et al.* (2014a); Tedds *et al.* (2014)) and chord length (Stelzenmuller, 2013) at different stations along the blade radius as characteristic length.

Further investigations have aimed to determine the Reynolds number independence of flow characteristics and performance of tidal turbines through numerical and experimental investigations. The Reynolds independence threshold for main flow statistics was reported from experimental wind turbine tests to be 4.8×10^4 for mean velocity and 9.3×10^4 for higher order statistics (Chamorro *et al.*, 2012) which has been exceeded based on the turbine diameter and current inflow in all but one CWC test case presented herein. It was also highlighted that the sensitivity to Reynolds number decreases with increasing distance from the turbine. Previous tests using 3 bladed wind turbine in a water channel (McTavish *et al.*, 2014) have shown little changes of wake expansion for Reynolds number ranging from 2×10^4 to 3×10^4 based on the chord length, diameter and tip speed as shown in Table 2-3. From numerical investigation of non-dimensional scaling of tidal turbine devices, a Reynolds number independence threshold was identified above Re = 5×10^5 by Mason-Jones *et al.* (2012) for the specific tidal turbine geometry and pitch angle.

Based on the above, the Reynolds number is maximised to achieve the required turbulent flow classification while maintaining similarity of the non-dimensional kinematic scaling parameters, i.e. Froude scaling the approach flow and matching TSR at rotational speeds within the range of previous experiments of small tidal turbine rotors (Chamorro *et al.*, 2013b; Doman *et al.*, 2015).

Table 2-3 - Comparison of Experimental Studies and Their Reynolds Number Definition and Range. Reference Length as Diameter (D), Chord Length (C) and Blade Section in Terms of Radius (R). Reference Velocity other than Approach, or Free Stream Velocity are Provided.

References	Wind (W) or Tidal (T)	Diameter (m)	Re Definition	Re
Whale *et al.* (2000)	W	0.175	C & Rel. Vel.	6400 to 1.6×10^4
Chamorro *et al.* (2012)	W	0.128	D	1.66×10^4 to 1.73×10^5
Bahaj and Myers (2013)	T	0.8	D	1.56×10^6
McTavish *et al.* (2014)	W	0.2 – 0.4	C & Tip Speed	Re (tip) 2.26 – 2.4×10^4 Re(D) 4.62 – 4.85×10^4
Chamorro *et al.* (2013a)	T	0.5	D C at 0.5r	Re(D) 1.7×10^5 Re(C) 1.5×10^4
Chamorro *et al.* (2013b)	T	0.126	D	2.5×10^4
Stallard et al. (2013)	T	0.27	C at 0.75r	3.0×10^4
Stelzenmuller (2013)	T	0.45	C	Up to 1.0×10^5
Tedds *et al.* (2014)	T	0.5	R	2.22×10^5
Mycek *et al.* (2014b)	T	0.7	R	$1.4 – 4.2 \times 10^5$
This Study	T	0.28	D	7.70×10^4 to 1.23×10^5

2.1.5 Control System and Force Measurements

To maintain kinematic similarity and to ensure the rotor is operating at its optimum operating point in terms of power generation, as has been found in previous experiments and numerical studies by Shi *et al.* (2013), each model of the tidal turbine array is equipped with a Panasonic Minas A5 II Servo AC motor and driver to ensure rotational speeds of the rotor corresponding to the desired TSR. The motors are placed in the watertight nacelle of each model, connected to the rotor hub through a short shaft (Figure 2-10). A control unit (Figure 2-11) with software for individual control of each rotor and logging of rotational rate across the testing period was used to adapt the rotational rate to each inflow velocity used across the experiments.

A force sensor was placed within the turbines to measure the thrust acting on the rotor. However, during submerged operation it failed to provide the intended thrust measurements acting on the turbine rotor. The monitoring of the turbine operating condition was thus adopted by estimating the performance of the turbines from the mechanical torque supplied to the rotor by the AC motor to maintain a constant rotation. Calculation of the supplied torque was based on the electrical power and rotational rate of the turbine and directly extracted from the driver and control system supplied and integrated into the graphical user interface where rotation of each turbine is set. Torque recordings were taken across a small number of tests to confirm the operating condition in the ambient flow conditions of the upstream turbine. Further comparison was made between the motor data from the control software for the upstream and downstream turbine to quantify the loss in performance of a turbine operating in the wake of an upstream turbine. This allowed for basic validation of the turbines' operating condition and the performance of the upstream and downstream turbines have been quantified for some of the array cases.

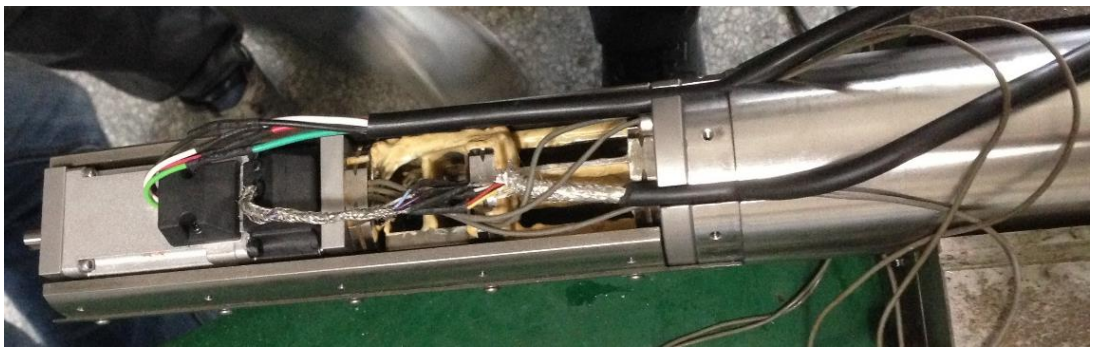

Figure 2-10 - Assembly of AC Motor and Load Cell in Nacelle of the Tidal Turbine Model.

(a) **(b)**

Figure 2-11 – Control System for Tidal Turbine Array Showing in (a) Control Interface and (b) Motor Driver Unit Assembly at Experimental Facility. The Control Unit was Later Updated to Include Torque Calculation from the Driver Control Software.

To estimate the performance of the tidal turbine rotors, the torque supplied to achieve constant rotation corresponding to the rotational speed required to match the TSR was recorded without any current flowing. This was then compared to the torque required to maintain the same rate of rotation with the current acting on the turbine blades to allow for a basic estimation of the torque provided by the current flowing over the blades. Similar methods, using supplied torque with and without blade connected were used to derive the power performance by Walker (2014a) as part of the MARINET-TEDSSWIP project (MARINET, 2017).

A time series of the percentage of torque generated from the current flowing over the blades is shown in Figure 2-12. The upstream turbine average is approximately 44% of the required torque without current flowing whereas the downstream turbine sees about 30% of the required torque generated by the current flowing past the turbine. It can also be seen that the fluctuations in torque supplied to the motor are larger for the downstream turbine, as would be expected for a turbine operating in the resulting wake of another turbine where higher variations in the inflow exists compared to an upstream turbine operating in undisturbed flow.

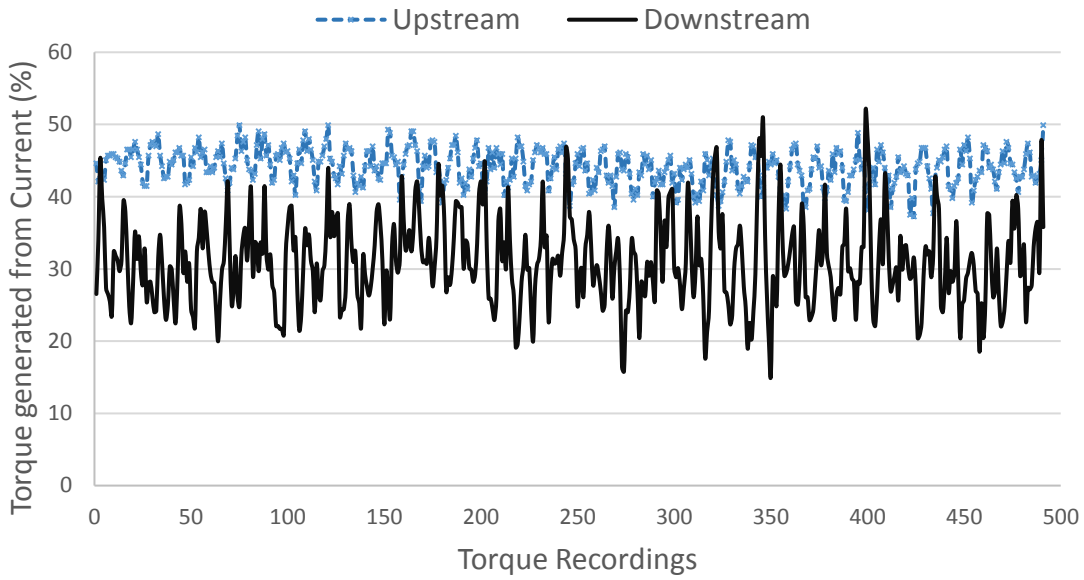

Figure 2-12 – Comparison of Torque Generated from the Current between Upstream (Dashed) and Downstream (Solid) Turbine Operating in Array for a Downstream Spacing of 12D.

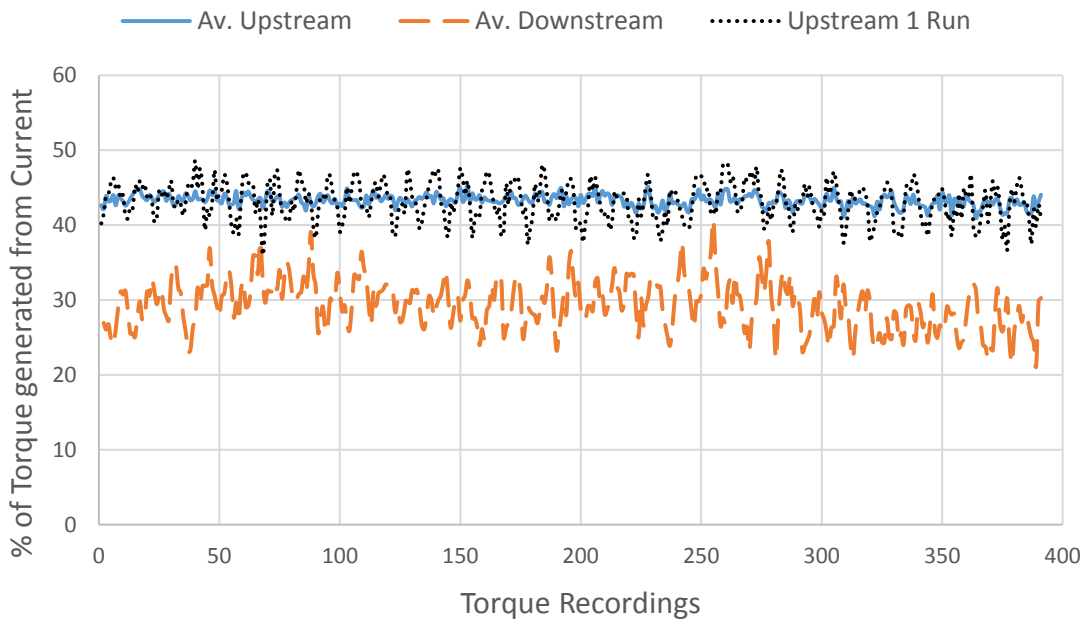

Figure 2-13 - Averaged Torque Contributions from Current Across Six Instances of Data Recording. Upstream Turbine instantaneous (Dotted) and Averaged (Solid) and Downstream Turbine Averaged (Dashed) Values are Shown.

Repeatability of measurements, shown here by comparison of control data for the upstream and downstream turbine averaged over six different instances of data logging are shown in Figure 2-13, showed that the operating conditions for the upstream turbine were constant across the tests presented here. Larger fluctuations are observed for the downstream turbine across instantaneous runs and averaged over six measurements.

Since the main objective of this experiment was to investigate the centreline array flow field, the outer rotors in the array formation were configured to run at constant RPM by modifying control values set in the motor driver software for gain adjustment to ensure constant operating conditions through all experiments (Panasonic, 2014). The performance shown for the tidal turbine model here matches results presented in previously conducted experiments in terms of the calculated power coefficient. The thrust coefficient which governs the momentum extraction and wake development was shown to be relatively constant for the range of TSR values expected for all turbines, including the downstream turbine operating in the slow flow velocities within the wake of the upstream turbine, operating of the turbines was judged to be within the expected range. Therefore the performance of these rotors has not been further investigated experimentally but will be included in the discussion of numerical results.

2.2 Test Facilities

The following section introduces the facilities used for the experimental investigation of tidal turbine wakes. The characteristics of the two experimental water channels, namely the Circulating Water Channel (CWC) used for multiple turbine arranged in a staggered array, as well as a long Wind Wave Current Flume (WWC Flume) used for characterisation of turbine wakes in axially aligned configurations are provided. The Particle Image Velocimetry (PIV) system used for measurement and analysis of flow field within the array is introduced here along with a brief introduction of the most critical aspects of the calibration, recording and analysis procedures. The PIV system used for the long WWC flume consisted of a single laser and high speed camera, which due to the set up and viewing direction resembles a more straight forward application without the need for comprehensive image correction. Analysis for calculation of flow vectors of the flume recordings is done using an open source software code PIVlab1.4.1 (Thielicke and Stamhuis, 2014; Thielicke, 2016) in Matlab R2014a.

2.2.1 Circulating Water Channel

The Circulating Water Channel (CWC) at Shanghai Jiao Tong University (SJTU), shown in Figure 2-14 with a working section of 8m length, 3m width and 1.6m water depth was used to conduct array experiments. The specified water depth had to be used for all experiments as required for the operation of the CWC. The wide cross section allows for placing multiple turbine models without incurring significant blockage ratios based on the cross-sectional area of the test section. Current velocities tested with the scaled model turbines ranged from 0.25m/s to 0.8m/s. The water channel capacities in terms of current velocities are rated from 0.2m/s to 3.0m/s with a step configuration of 0.01m/s. Figure 2-15 shows the CWC test section and current velocity control panel.

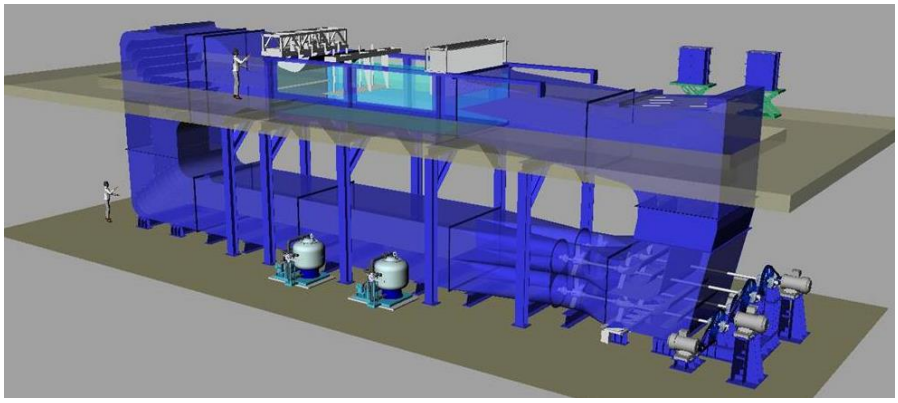

Figure 2-14 – Impression of Circulating Water Channel at Shanghai Jiao Tong University.

(a) **(b)**

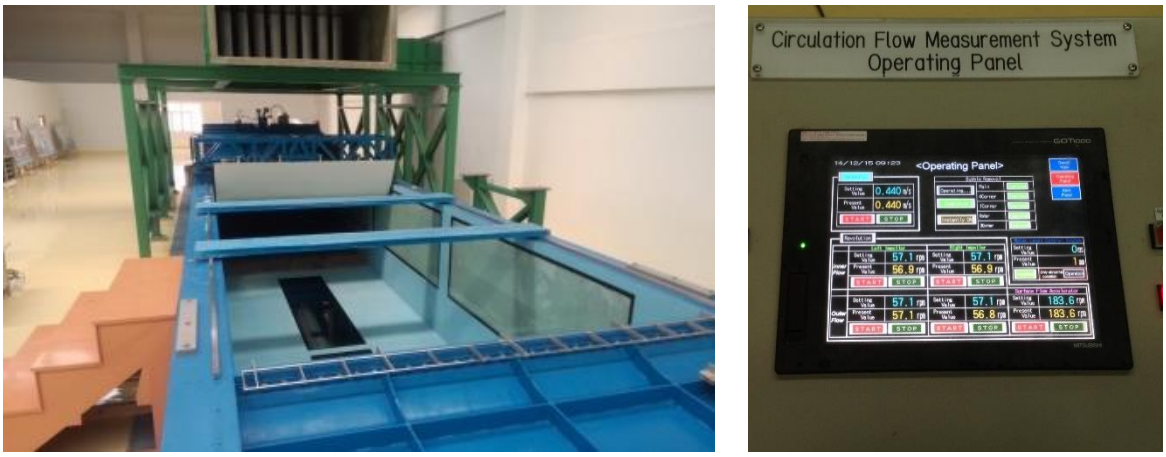

Figure 2-15 – (a) Top View of CWC Test Section and (b) Control Panel for Current Velocities.

The free stream ambient current velocity has a low turbulence intensity of 2% based on the specification of the test facility and PIV measurements conducted. Undisturbed flow measurements have been taken at several positions through the test-section to confirm ambient current and turbulence conditions prior to conducting experiments. The vertical profiles of the ambient flow in Figure 2-16 (a) show small velocity variations across the lower part of the rotor and constant velocities above the rotor hub height. The deviations through the bottom half of the rotor show a maximum reduction of the in-stream velocity of 2.3%. On average, the velocity across the rotor plane (-0.5z/D to 0.5z/D) is within 0.45% of the set value for 0.44m/s and 0.58% for 0.52m/s. A vertical profile of the turbulence intensity for the lower part of the CWC is shown in Figure 2-16 (b).

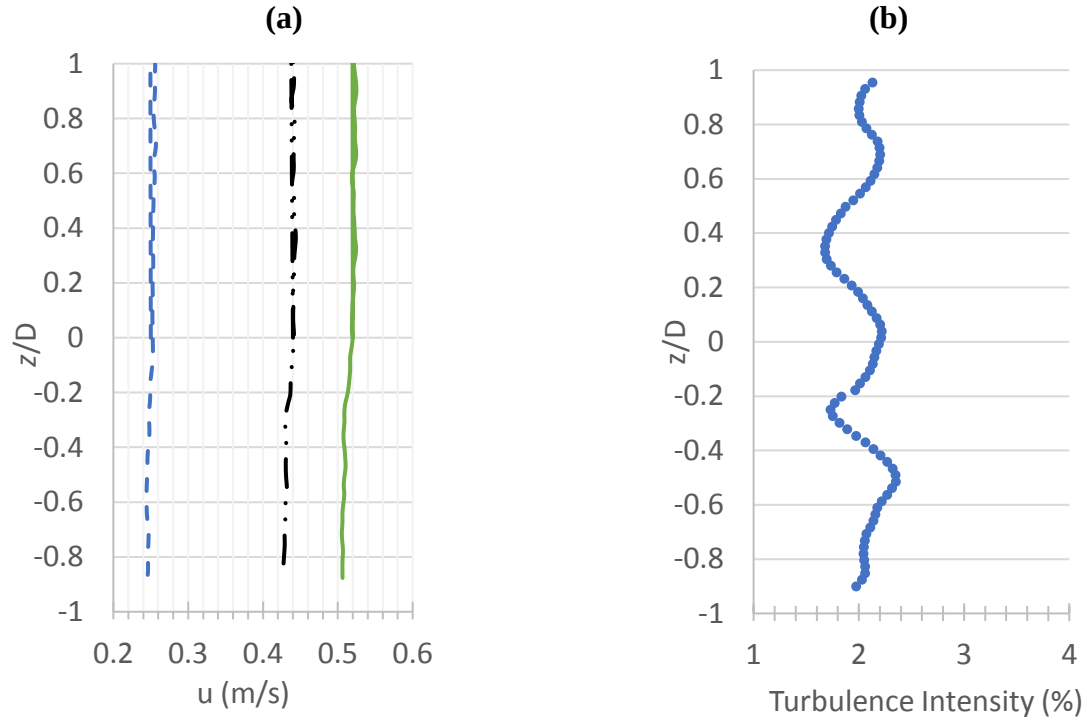

Figure 2-16 – (a) Vertical Current Profile in the CWC for 0.25m/s (Dashed), 0.44m/s (Dash Dot) and 0.52m/s (Solid) and (b) Ambient Turbulence Intensity at 0.44m/s.

2.2.2 Wind, Wave Current Flume

The Wind, Wave and Current flume at Shanghai Jiao Tong University (Figure 2-17) is 60m long, 0.8m wide and 1.2m high with a maximum operating water depth of 0.8m. For the experiments presented here, currents of 0.275m/s were used with a water depth of 0.56m, corresponding to two times the diameter of the model turbine. The ambient flow characterisation was performed using a Nortek Vectrino+ ADV to determine the vertical velocity profile at the set velocity and calculate the turbulence intensity within the WWC Flume. The ambient inflow velocity and turbulence intensity profile are shown in Figure 2-18 with an additional comparison of the inflow measurements as obtained from the PIV wake characterisation downstream of the turbines and ambient flow characterisation upstream of the turbine. The flume provided a sufficiently long test section to investigate spacing of tidal turbines arranged in-line with varying spacing between multiple turbines and allowed for further tests using waves and different operating heights with respect to the bottom and free surface distance.

Figure 2-17 – Long Wind, Wave, Current (WWC) Flume at Shanghai Jiao Tong University.

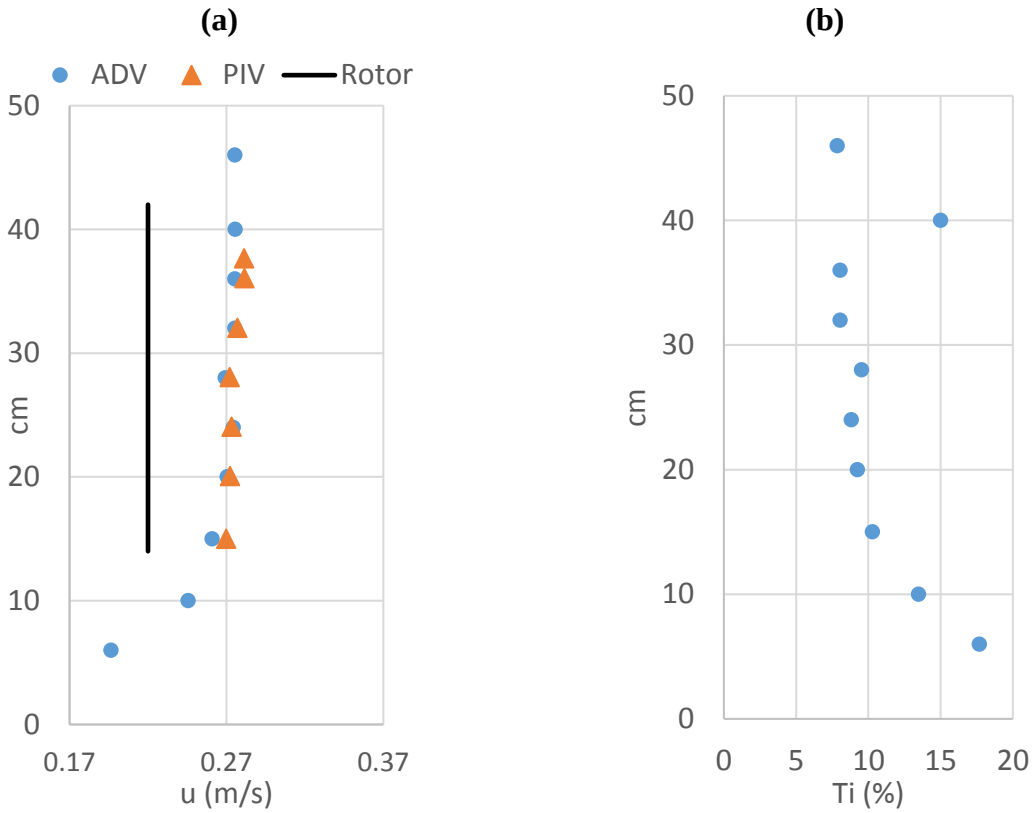

Figure 2-18 - (a) Vertical Flow Profile of Flume with ADV Measurements (Circle) and PIV Measurements Across Turbine Diameter (Triangle) with the Turbine Rotor Location Shown (Solid) and (b) Turbulence Intensity from ADV Measurements.

2.2.3 Particle Image Velocimetry

Particle Image Velocimetry (PIV) provides a non-intrusive, optical method of recording instantaneous flow fields and provide flow visualisations across an extended area of a flow field. The flow is seeded with neutrally buoyant particles, which are illuminated using laser light, and images are recorded with a known pulse separation that allows calculation of local flow vectors using cross-correlation techniques. This section describes the particular PIV system as used in the CWC utilising two cameras and a pulsed laser while the WWC Flume PIV was conducted using a single laser sheet and high speed camera set-up without the need for strong image correction.

The LaVision GmbH PIV system used to record images of illuminated seeding particles in the wake of the tidal turbine array included a double pulsed Nd: YAG laser, located on a traversing unit below the centreline of the test section for accurate positioning, with output energy of 425mJ/pulse at 532nm wavelength to illuminate the particles. The double pulsed laser illuminates the particles twice within a small time interval to record the scattered light from the first and second exposure in two separate images. Two LaVision ImagerProX11M CCD cameras were used in a stereoscopic arrangement to record double frame/ double exposure images of the illuminated field of view at the maximum frequency of 4.52Hz. A brief overview of the characteristics of laser and camera is shown in Table 2-4. The recordings and positioning for each measurement location of the laser sheet optics below the array centreline were controlled using the DaVis 8.2.2 software.

The integrated software was used for all stages of the PIV recording process including calibration, control of measurements and analysis of the recorded images to yield flow field vector maps of the calculated velocities for further analysis. Analysis has been performed for stereo and mono PIV applying image correction based on the PIV system's calibration conducted beforehand using a three-dimensional calibration plate located at the reference location for measurements in the wake of the turbines at array centreline. Images are corrected based on the calibration, accounting for distortions due to different fluids and the glass of the observation windows as well as the viewing angle.

The laser sheet optics provided a large laser sheet at the measurement location, centred at the hub height of the tidal turbine models with an approximate thickness of 2-3cm to allow analysis in stereoscopic mode. The cameras were located at the outside of the test section observation windows, slightly elevated from the measurement locations which required the cameras to point downwards through the glass windows. The arrangement used corresponds to the schematic shown in Figure 2-19 classified as backward-forward scattering where one camera is recording light scattered in forward direction while the other one records light scattered in the backward direction. Using the same lenses on both cameras requires camera1 to have larger aperture due to the lower light intensities for the backward scattered light recorded.

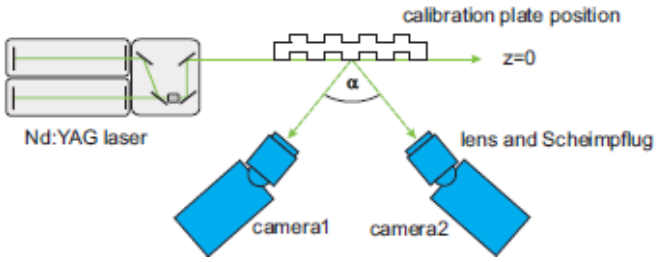

Figure 2-19 - Schematic of Camera Arrangement from LaVision GmbH (2014b).

In the experiments the laser sheet was projected vertically upwards as the laser optics were set up at the bottom of the test facility, projecting a laser sheet upwards at the centreline of the array parallel to the in-stream flow direction. The arrangement of laser sheet optics below the tank and cameras on the side of the test section is shown in Figure 2-23. To overcome the requirements of the Scheimpflug criterion (shown in Figure 2-20) when measuring in- and out of plane components in a stereoscopic arrangement, which introduces a perspective distortion with non-constant factor of magnification across the field of view (LaVision GmbH, 2014c), corrections are made by use of an adapter to increase the range of focused field of view and is done empirically until the required field appears focused, an example of this is shown in Figure 2-21.

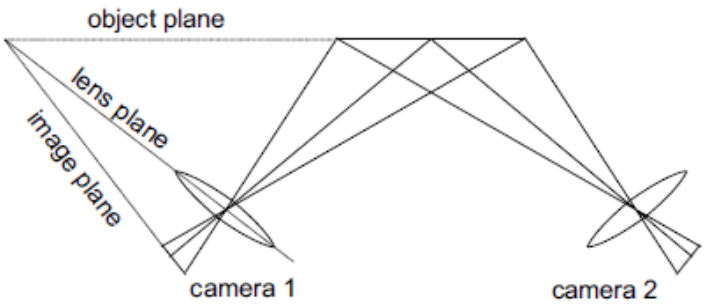

Figure 2-20 - Scheimpflug Criterion (LaVision GmbH, 2014a) where Image Plane, Lens Plane and Object Plane are to Intersect in a Common Line.

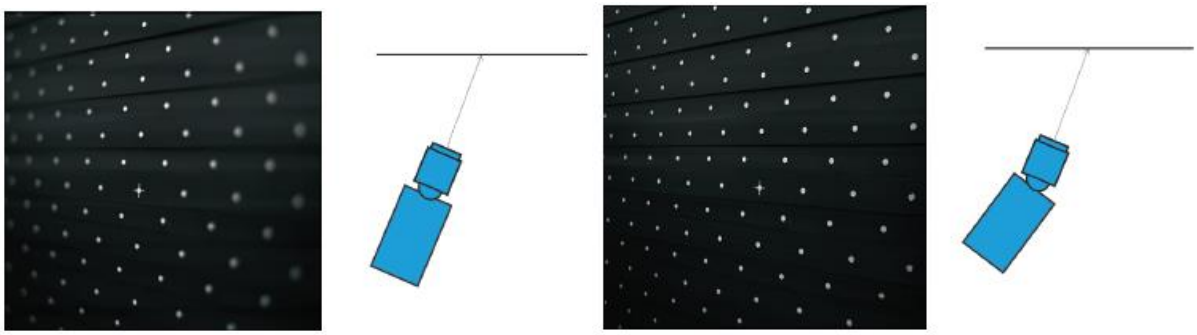

Figure 2-21 – Use of Scheimpflug Adapter to Increase Focused Field of View (LaVision GmbH, 2014a).

A thorough calibration was conducted accounting for the oblique viewing direction and distortion of the observation windows to apply a correction on all recorded images for accurate calculation of flow velocities. With the supplied calibration plate, automated search for calibration mark is conducted within the software system after marking corresponding locations for all camera views. To configure the coordination system used for subsequent analysis, three different locations specifying the centre point, point in *x* direction (here in stream direction) and a point in *z* direction (vertical direction) are marked as shown from the example in the DaVis manual in Figure 2-22.

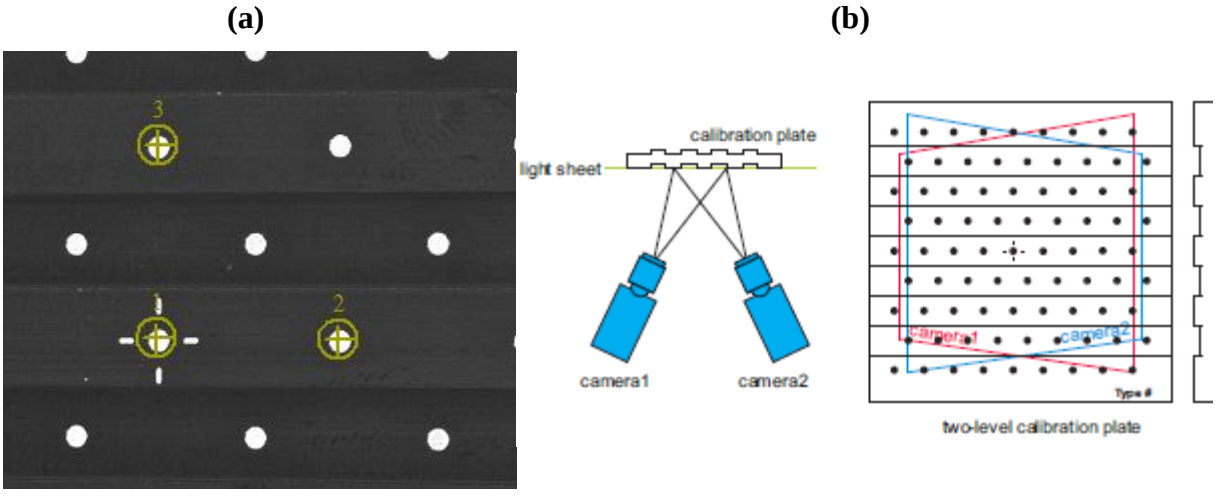

Figure 2-22 – (a) Specification of Coordinate System on DaVis Calibration Plate and (b) Arrangement of Cameras for Stereoscopic Calibration (LaVision GmbH, 2014a).

The obtained mapping function, a polynomial (3rd order) fit is then applied as image correction. The calibration is then used at all measurement locations throughout the array tests. The average deviation of the de-warped mark, are 0.7 pixel for a good calibration and smaller than 0.3 for an excellent fit (LaVision GmbH, 2014b). Further visual checks are performed as described in LaVision GmbH (2014c) to ensure that the corrected images coincide and that the ideal regular grid passes through the marks on the calibration plate. In the calibration used here deviations were kept below 1 pixel for both cameras with values between 0.3 and 0.7 pixel respectively for each camera calibration.

Following the calibration, the coordinate system was set to coincide with reference locations within the wake downstream, i.e. the hub height location at integers of the distance in metres divided by the turbine diameter. Camera placement along the test section was then set-up so that the reference point in the images was located at 3D, 6D, 8D, 15D, 17D and 19D downstream of the upstream turbine rotor centre point.

Validation of the calibration and applied PIV measurements is performed by comparison to the channel flow velocity characteristics as presented in Section 2.2.1 which were found to be within less than 2% of the expected velocities in the CWC.

Table 2-4 - LaVision PIV System Details for Laser and Camera.

Laser

Manufacturer	Litron Lasers
Laser	Nano TRL PIV
Type	Double Pulsed Nd:YAG
Output Energy @ 532nm (specified)	425mJ
Repetition Rate (Hz)	0-10

CCD Cameras

Cameras	2 x ImagerProX11M (1GB)
Resolution	4008 x 2672
Buffer	2 x 2 (2004 x 1336)
Max. acquisition rate	4.52Hz
Picture Mode	Double Frame/Double Exposure
dt (μs)	2500-6500
No. of image pairs	500

(a) **(b)**

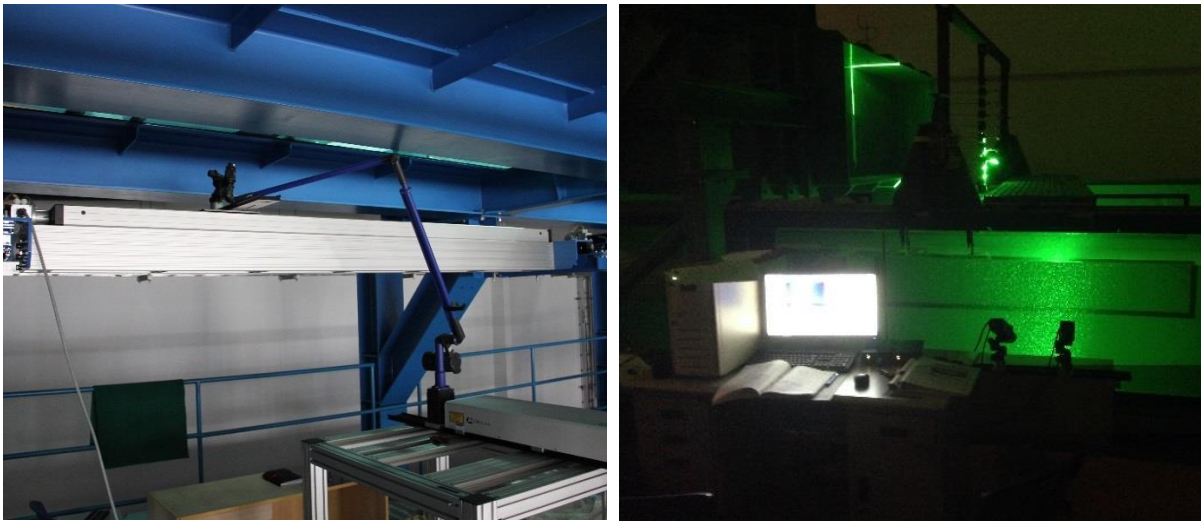

Figure 2-23 – (a) Laser Sheet Optics on Translation Unit at Array Centreline below Test Section and (b) View from Side of Channel Showing Illuminated Centreline and Control Unit of PIV System.

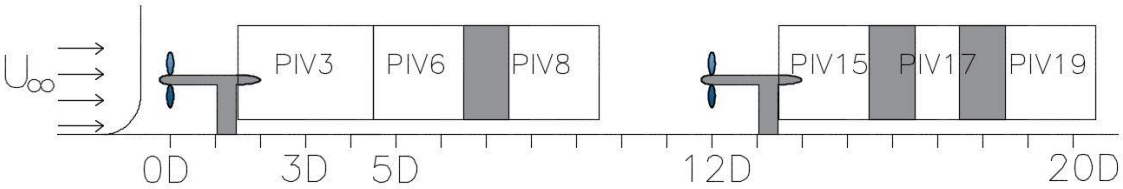

Figure 2-24 - Measurement Locations at Array Centreline (Overlapping Areas Shaded).

2.2.4 PIV Analysis

Images were pre-processed using a sliding background filter to remove large intensity fluctuations due to reflections in the background of the image and particle intensity normalisation to achieve more homogeneous particle intensities, allowing smaller particles to contribute to the cross-correlation. Cross correlation is used to determine the displacement of particle ensembles within an interrogation window between the two recorded image frames, shown as an example case in Figure 2-25. A correlation peak obtained during the analysis for recordings of the tidal turbine wake is shown in Figure 2-26. Further information on the cross-correlation method can be found in Raffel *et al.* (2013) and Westerweel (1997).

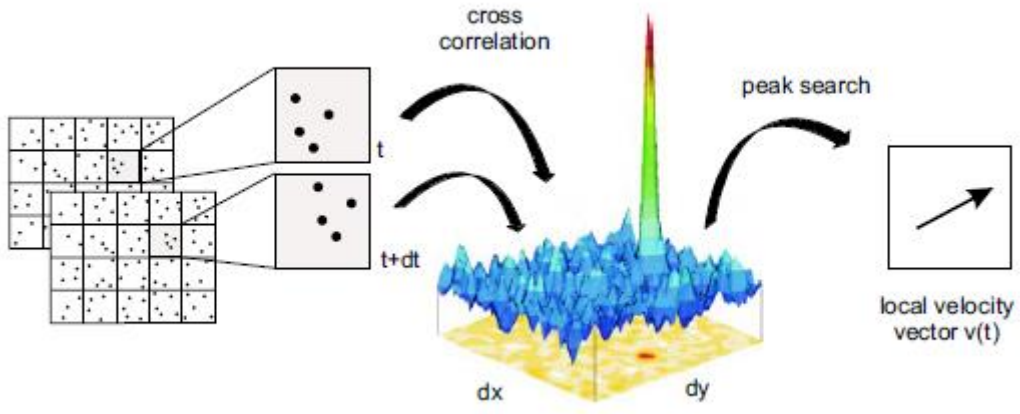

Figure 2-25 - Cross Correlation Showing Movement of Particle Ensemble between Two Frames of a Recording and Correlation Peak which Provides the Local Velocity Vector (LaVision GmbH, 2014a).

Table 2-5 – Summary of PIV Analysis Settings for Pre-Processing, Vector Calculation and Post Processing in DaVis 8.2.2.

Image Pre-Processing	
Sliding background scale length	8 pixel
Particle Intensity normalization	6 pixel
Vector Calculation	
Cross Correlation Mode	Stereo and Mono
Interrogation Window Size (Pixel)	64 x 64 (1st Pass)
Shape	Square
Overlap	50%
Final Pass	32 x 32, Adaptive PIV, 2 passes
Post-Processing	
Median Filter	3 iterations
Smoothing	1 x Smoothing 3 x 3

To improve vector calculation in areas with large velocity fluctuations vertically across the wake of tidal turbines, calculations are performed using multiple iterations with decreasing interrogation window size (64 x 64 to 32 x 32 pixel) and on the final iteration an adaptive gaussian weighting function, automatically adjusting window size and shape to local seeding density and flow gradients. The resulting vector fields have then been post processed to remove spurious vectors by applying a median filter and smoothing to eliminate high frequency noise. The analysis settings are summarized in Table 2-5 and an example of pre-processing and vector calculation on a single image taken during the experiment is shown in Figure 2-27.

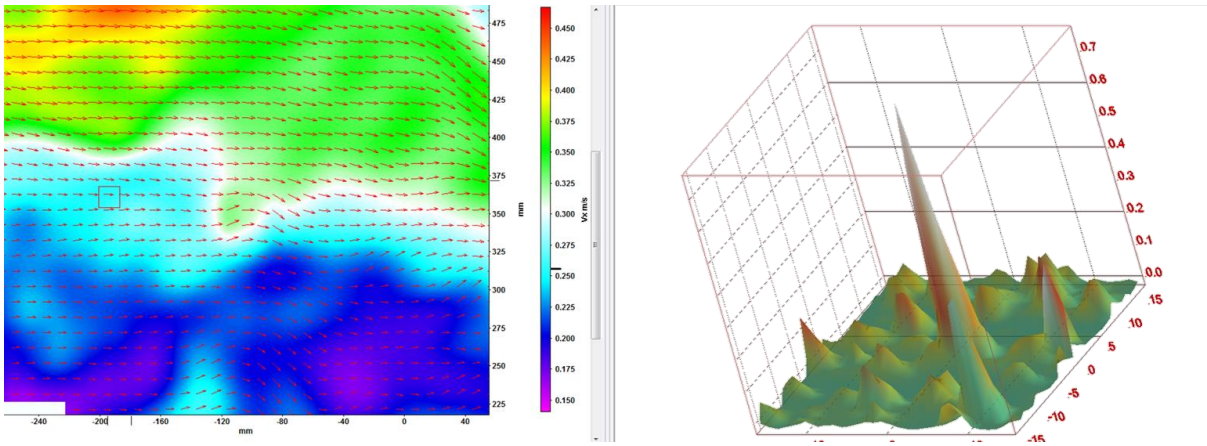

Figure 2-26 - Correlation Peak from Instantaneous Wake Measurements.

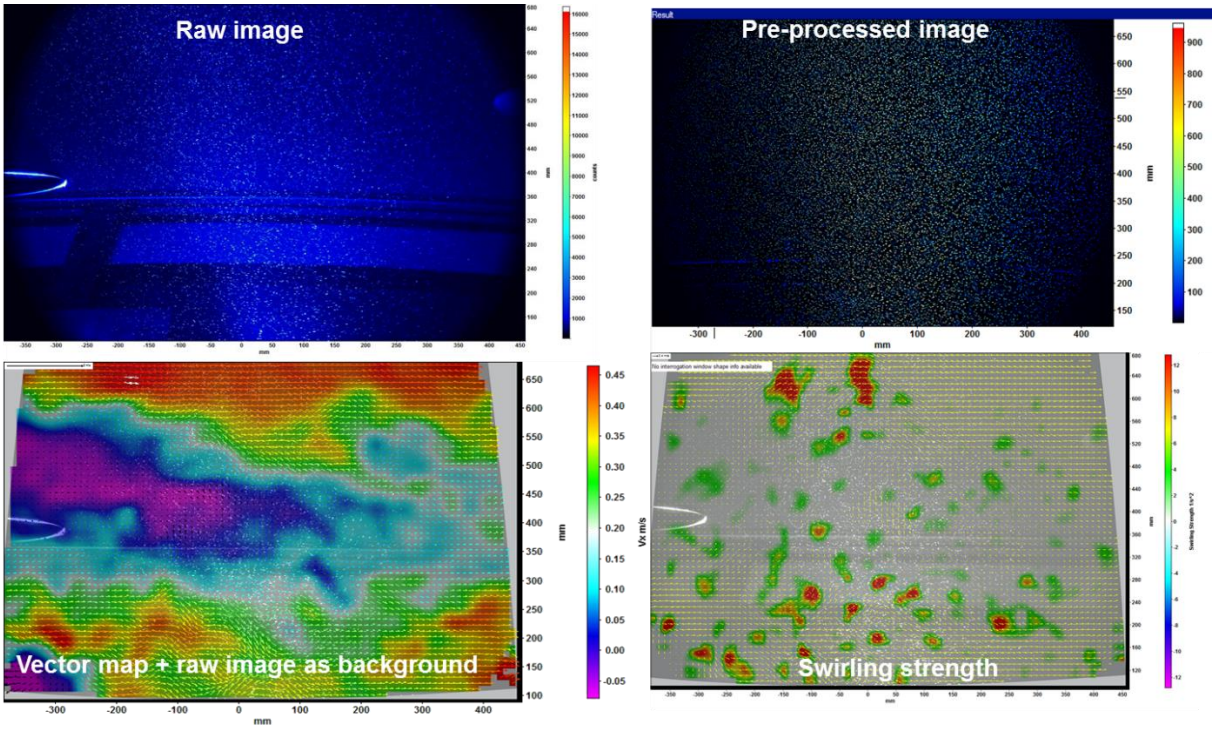

Figure 2-27 - PIV Analysis Process in DaVis 8.2.2 Showing Sequence from Raw Image to Flow Field Characteristics.

2.3 Experiment Set-up

The exact configurations and arrangements of turbines in the test facilities are described in the following section. Brief discussion of the parameters governing the experimental tests which are specific to each facility is presented with regards to the ambient conditions in terms of water depth and blockage ratio. For both facilities the location of wake measurements as well the configuration of turbines are detailed and test matrices are shown.

All distances along the test facility are given in terms of the distance in metres divided by the turbine diameter with reference to the location of the rotor centre of the upstream turbine. The origin for each experimental study is placed at 0D and wake extents are reported up to 20D downstream.

2.3.1 CWC Array Test

Due to the large water depth in relation to the turbine diameter (Depth/Diameter = 5.71) the set-up does not represent a likely deployment of actual turbines in first/second generation array environment in shallow waters. However, it does represent bottom fixed turbines with support structure operating in the lower part of the water column, where velocity shear of the ambient flow across the turbine diameter exists. The proximity to the seabed is therefore maintained while free surface effects are ignored, similar to previous experiments that maintained Froude numbers of less than 0.25, therefore stating independence of the water surface elevation (Bahaj and Myers, 2013). The effect of varying device spacing can therefore be investigated with a fixed vertical separation from turbine to sea-bed. Further, the study will provide some insight whether the support structure wake is affected by close spacing of a number of tidal turbine devices in transverse and longitudinal configurations.

Locations similar to those reported here, within the bottom part of the tidal domain, have previously shown to affect the wake shape downstream of tidal turbines by shifting the wake centreline downwards. This is caused by the velocity shear in ambient flow and the resulting reduced wake re-energisation on the lower part of the wake which is exacerbated especially for increased roughness on the seabed and has been shown through tests with actuator disks by Myers and Bahaj (2010). A summary of previous experimental studies, including their blockage ratio and distances to surrounding surfaces is presented in Table 2-6. All four models are operating at the same centreline height of 0.34cm from the test section bottom. This results in

a rotor-tip to seabed separation of 0.71D, while turbine tip-free surface separation is 4D. The minimum distance between the outer tip of the rotor blades and the side walls of the test section is 3.36D.

Table 2-6 - Table of Experiments with Blockage and Distance to Bounding Surfaces.

Study	Blockage	Depth (D)	Distance To		
			Free Surface (D)	Bed (D)	Side (D)
Bahaj and Myers, (2013)	6.3%	2.45	0.825	0.625	2
Myers and Bahaj (2007)	12%	2.1	0.55	0.55	1.25
Bahaj *et al.* (2007a)*	CT: 17.45% TT: 7.55%	CT:1.5 TT:2.25	CT: 0.25 TT:0.19, 0.55	CT:0.25 TT: 1.06,0.7	1.8
Mycek *et al.* (2014a)	4.8%	2.86	0.93	0.93	2.35
Tedds *et al.* (2014)	16%	1.6	0.25	0.35	0.9
Stallard *et al.* (2013)	12.7%	1.6	0.3	0.3	5.75
Good *et al.* (2011)	3.95%	3.7	1.35	1.35	2.18
Chamorro *et al.* (2013a)	6%	2.3	0.95	0.35	2.25
Chamorro *et al.* (2013b)	9.98%	1.98	0.61	0.37	1.48
Whale *et al.* (2000)	8%	4.3	1.714	1.536	0.64
McTavish *et al.* (2014)	6.3% - 25.4%	2.025 - 4.05	0.5125 - 1.525	0.5125 - 1.525	0.26
Stelzenmuller (2013)	20%	1.7	0.35	0.35	0.55
WWC Flume	16%	2	0.25	0.75	0.925
CWC	4%	5.7	4	0.71	3.36

*CT – Cavitation Tunnel, TT – Towing Tank

For the purpose of wake measurements and characterisation of the local flow within the array, the origin of the coordinate system is placed at the position of the first rotor, with the in stream direction denoted by x, the cross-stream direction as y and the vertical position by z. The corresponding velocity components are denoted as Ux or (u) and Uz or (w) for the instream and vertical flow components respectively.

Blockage ratio of a single turbine facing the incoming flow are very low due to the high water depth required to run the experimental facility. The blockage ratio in this experiment for an isolated turbine is 1.3% and for the full array, with the projected area of three turbines facing the incoming flow, occupying less than 4% of the channels cross section, thus no further blockage correction is applied.

The experimental arrangement is taken as a section of a staggered tidal turbine array of four turbines and highlighted by the box in Figure 2-28 (a) from Mycek *et al.* (2014b). For investigation of the initial array effects, the focus will be the centreline array wake characterisation across a number of device spacings in longitudinal (constant a1 with varying a3 & a2) and transverse (variation of b1) direction. The distance between upstream and downstream turbine (a1) is kept constant as 12D. The measurement area covers the downstream distance ranging from 2D – 20D on the array centreline as shown in Figure 2-28 (b) and Figure 2-29.

(a)

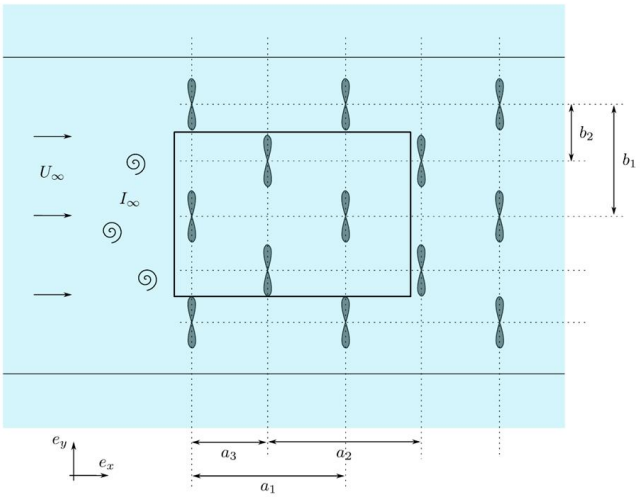

(b)

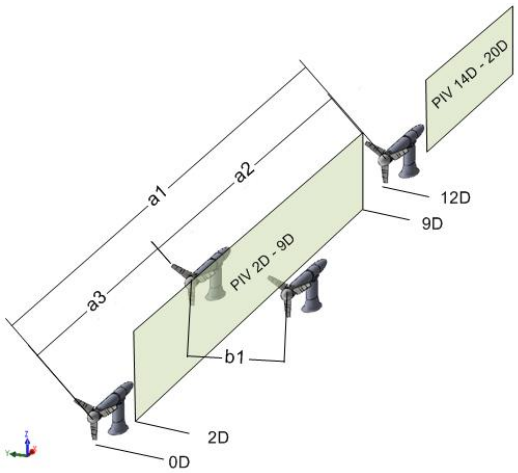

Figure 2-28 - (a) Typical Array Formation from Mycek *et al.* (2014b) with Experimentally Tested Array Section Highlighted (Box), (b) Experiment Configuration and Location of Laser Sheet at Array Centreline for PIV Measurements.

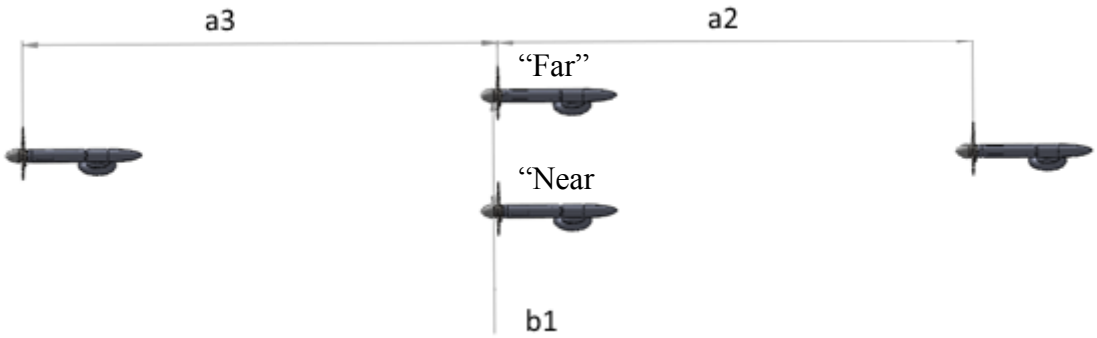

Figure 2-29 - Definition of Array Cases: a3 is Denoted as L3 or L5 to Describe the Longitudinal Spacing Whereas b1 will be given either T15, T2 or T3 to Represent the Transverse Spacing.

The support frame placed on the floor of the test section to allow variation in inter-device spacing for both, transverse (b1) and longitudinal (a3) spacing between individual turbines and turbine rows respectively. Arrays are named according to their longitudinal and transverse spacing denoted by L(a3) and T(b1) respectively and individual turbines are referred to as shown in Figure 2-29, thus the array in Figure 2-30 is denoted L5T3.

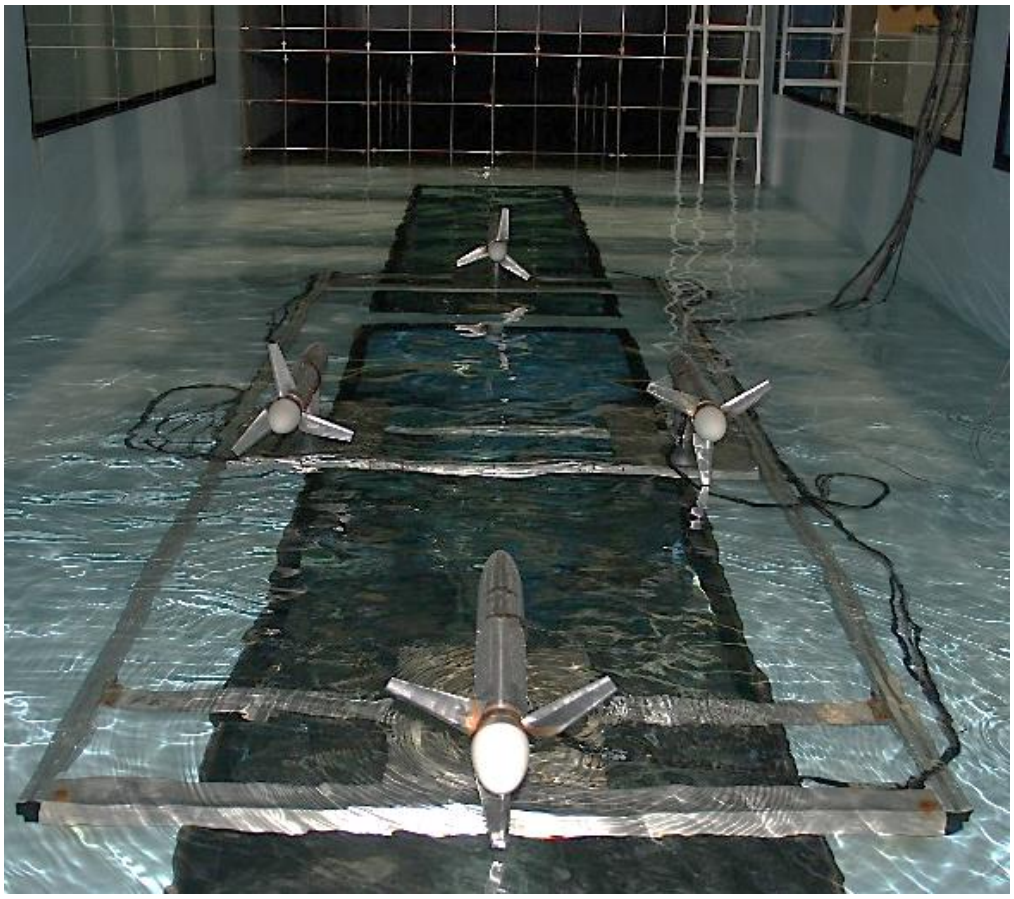

Figure 2-30 - L5T3 Array Set-Up in Test Section of CWC.

The location of the array frame within the test section and thus the placing of the experimental coordinate system fixed at the upstream rotor location was performed using the translational stage below the centreline window to ensure all distances set for placing of laser sheet and camera are accurate and is shown in Figure 2-31.

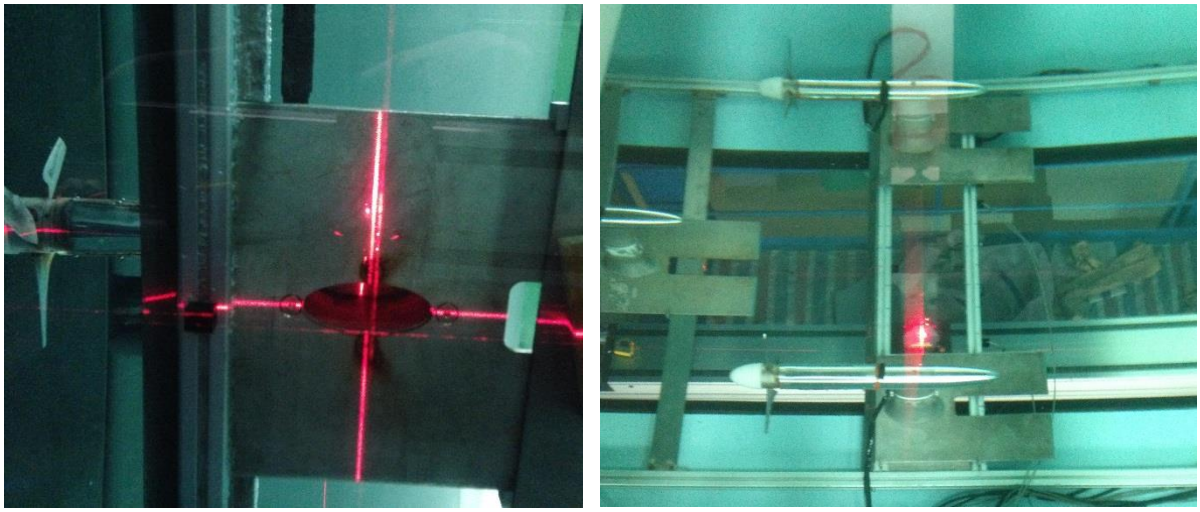

Figure 2-31 - Positioning of Upstream Turbine and Confirming Location of Second Row within the CWC Test Section.

Flow measurements are taken along the array centreline as indicated in Figure 2-28 (b) for a duration of 110 seconds with the maximum sampling rate of the camera in double frame-double exposure mode, resulting in 500 image pairs per measurement location. To ensure 500 images are sufficient for the time averaging of flow characteristics the moving average of the streamwise and vertical velocity components and RMS values has been monitored and are presented in Figure 2-32. Periodic fluctuations such as vortex shedding at three times rotor frequency are neglected as the primary focus was to gather time averaged flow field characteristics of the larger scale flow in terms of velocity recovery and turbulence intensity within the wake.

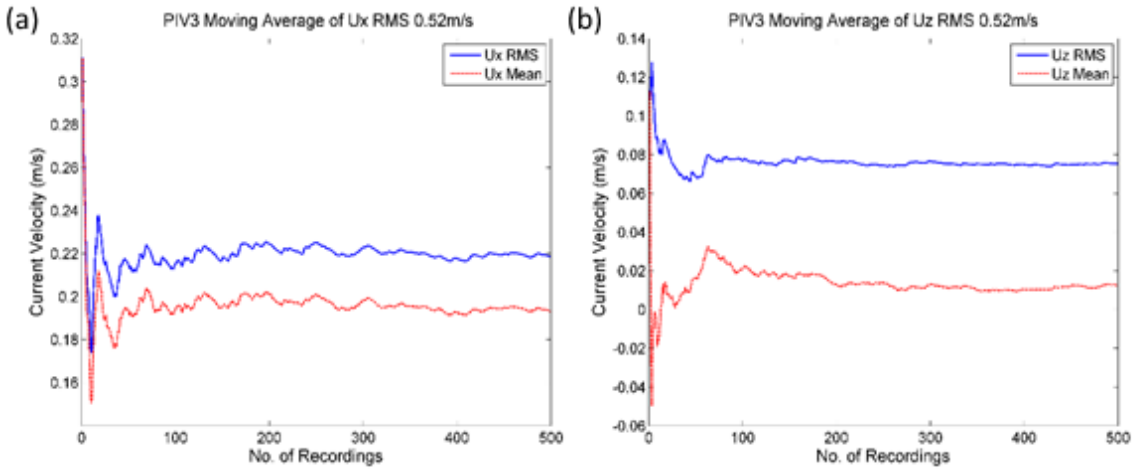

Figure 2-32 - Moving Average of (a) Ux and (b) Uz and RMS Value at 3D for L3T15 Array.

Data extraction for comparison is done along the wake centreline at hub height as indicated in Figure 2-33 (a), showing the array centreline passing between the second row turbines for the array configuration L3T15. The missing data in the corners of the recording window due to the camera lens and intensity of the laser light can be clearly seen here and in resulting areas within the overlap in the combined wake plots. The location of the second row for all L5 arrays is shown in Figure 2-34, where an obstruction to the laser sheet was created by the position of the laser optics under the test section of the CWC. Those points have been excluded from the results discussion. Table 2-7 shows the overview and naming of each of the tests conducted in the CWC with the inter-device spacings and current velocities provided as well.

Flow measurements were conducted for three different velocities at several stations across the empty test section of the experimental facility and showed very good agreement with the set velocity (< 2% difference). Accuracy of the PIV measurements in the very near wake of the tidal turbine is affected due to the high gradients across the vertical wake and stagnating flow behind the turbine structure (2D - 3D). This is especially relevant for the turbulence intensity calculations at very low velocities immediately downstream of the rotor and nacelle support stucture, affecting the flow measurements up to 4D downstream of the rotor. Further downstream of this very slow moving region, the recording settings of the PIV were adjusted to the estimated velocity deficit and analysis with adaptive interrogation windows based on local flow gradients was applied, with reducing shear across the flow field, analysis was improved.

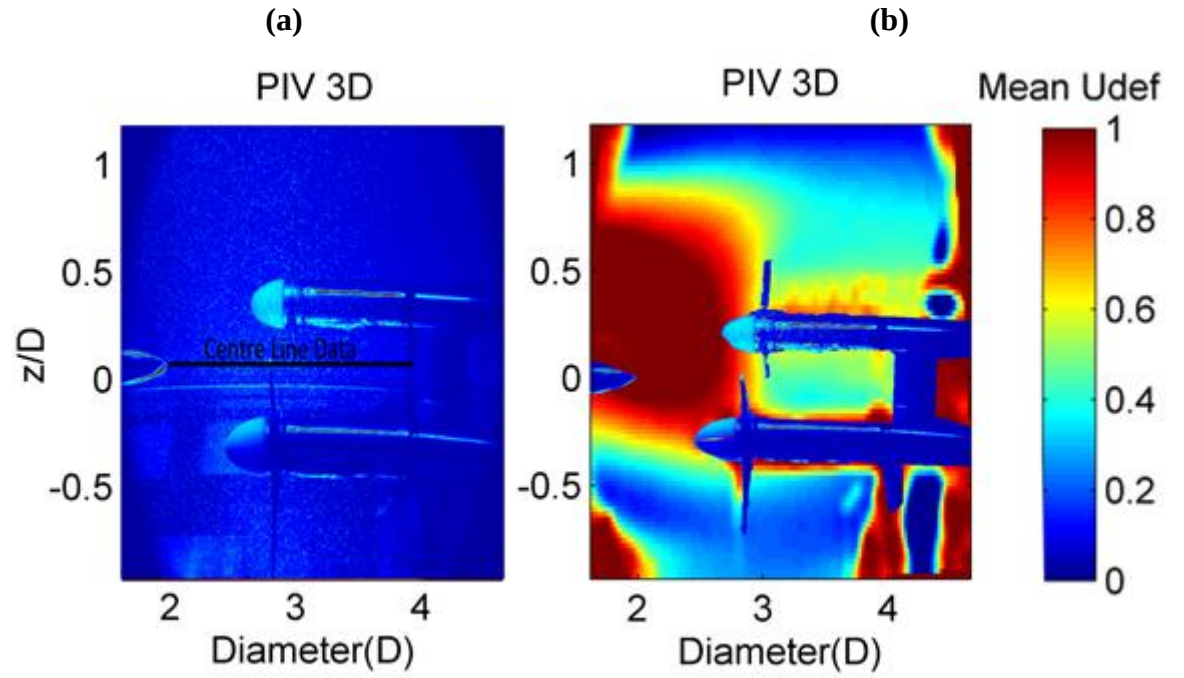

Figure 2-33 – (a) Raw Image, and (b) Contour Plot of Velocity Deficit Showing the Influence of the Turbine Devices Located Offset from the Array Centreline in Row Two for L3T15.

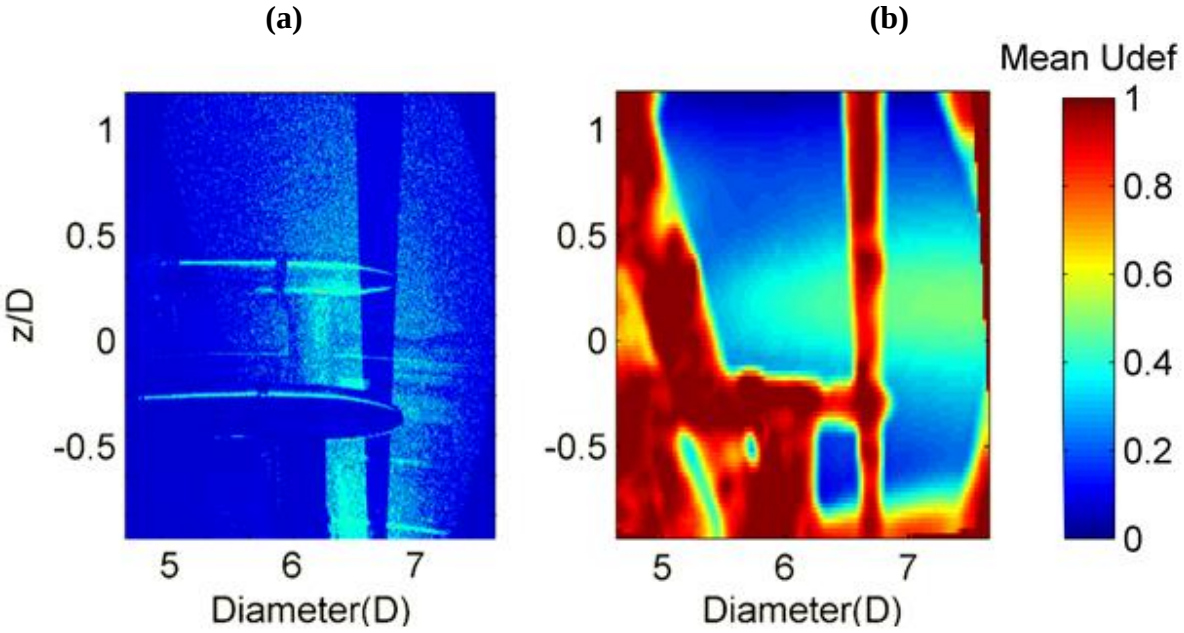

Figure 2-34 – Location of Row Two Turbines in L5 Array Tests Shown are (a) Raw Image and (b) Resulting Contour Plot of Velocity Deficit Shown to Highlight the Interference with the Support Structure.

Table 2-7 - Experiment Overview CWC Array Tests.

Experiment	a2 (D)	a3 (D)	b1 (D)	Current (m/s)
Single				0.25, 0.44, 0.52
3 Turbines		3	3	0.44, 0.52, 0.80
L3T15	3	9	1.5	
L3T2			2	
L3T3			3	
L5T15	5	7	1.5	
L5T2			2	
L5T3			3	

2.3.2 Flume Test

The WWC flume provides a test section of 60 metre length which is used for characterising the velocity recovery across a number of axially aligned experimental configurations of up to three turbines. Wake measurements at a number of locations downstream of the turbines are conducted to investigate the varying wake recovery of multiple turbines operating within the wake of one and two upstream turbines.

The blockage of a single rotor operating in the flume with a width of 0.8m and water depth of 0.56 metres is approximately 14%, similar to experiments by Myers and Bahaj (2007), Stallard *et al.* (2013) and Tedds *et al.* (2014). Galloway *et al.* (2014) found unsatisfactory results using previously applied blockage corrections and stated missing consensus of ranges where corrections should be applied, thus no blockage correction is applied for determining the wake characteristics.

For all turbines presented here, the operating height of the rotor centreline was at half the water depth corresponding to 0.28 metres. The inflow current was kept constant across all tests, hence the same turbine rotation was used for all experiments using a TSR of 4. Wake measurements were conducted for a single turbine, downstream of a second turbine for two different downstream distances (a1) and in the wake of the third of three turbines with varying spacing between first and second (a1), and second and third (a4) turbine with respective distances as shown in Figure 2-35. An overview of the tests included here and the names used to refer to the specific arrangements is shown in Table 2-9.

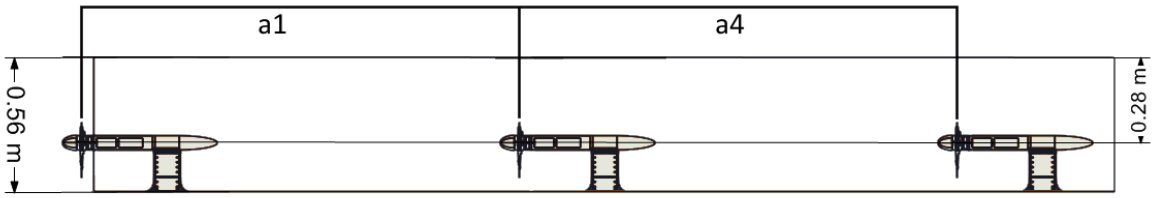

Figure 2-35 - Axially Aligned Multiple Turbine Tests in WWC Flume.

PIV measurements in the wake were taken using a high speed, 10 bit CMOS camera and particles within the flume were illuminated using a laser sheet at the centreline of the tank directed into the flume through a mirror situated on top of the tank frame as shown in Figure 2-36. Due to the internal memory (4 GB) and time interval between image recordings (7ms) a total of 2860 images were recorded and transferred to the control computer. This corresponds to a measuring period of 20 seconds and at the ambient current velocity and applied TSR to approximately 15 rotor revolutions. To minimize the effect of any fluctuations within the flume and ensure full development of the wake, each configuration was set-up and run for up to 10 minutes before recording of the wake characteristics commenced. No synchronisation between the rotor position and wake measurements is applied.

Table 2-8 – High Speed Camera Characteristics used for WWC Flume Experiments.

Camera	
Camera	Pco. 1200s
Resolution (Pixel)	1280 x 1024
Buffer	1 x 1
Internal Memory	4GB
Time Step	7ms
Acquisition rate	≈143 fps

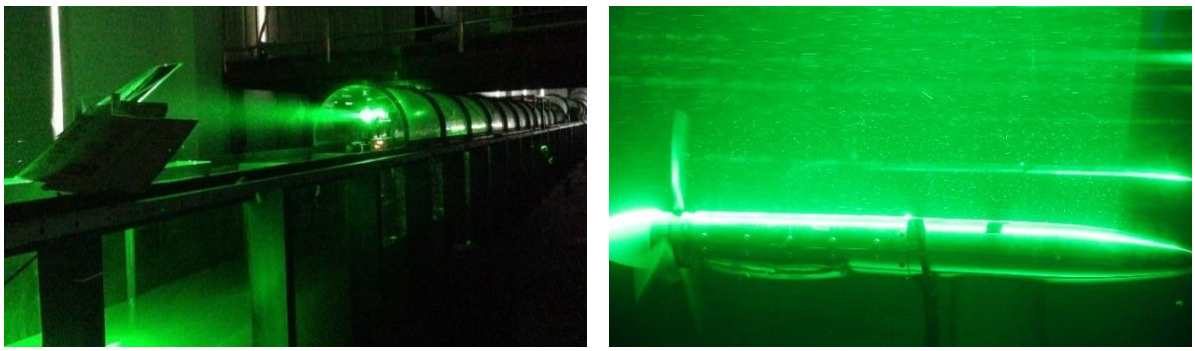

Figure 2-36 – PIV Measurements in CCW Flume showing Laser Sheet Set-Up and View of Flow on Top Part of Model Turbine.

The tests conducted in the WWC Flume are presented in Table 2-9 with the respective spacing between turbines for multi-turbine arrangements. The downstream distances are represented by a1 for first and second turbine axially aligned, equivalent to the distance from upstream to downstream turbine in the array cases, and a4 the distance between the second and third turbine within the flume. The models located in the test section are shown in Figure 2-37. Additional data has been collected from a test simulating the effect of waves on the wake centreline characteristics for shallow water operation with the rotor in the centre of the vertical water column. The wave height and period used are representative of a full scale wave with a height of 1.5m and a period of 3.5 seconds. Figure 2-38 shows the tidal turbine model in the tank with a larger wave during calibration of the wave maker and Figure 2-39 shows the approximate crest and through of the wave as for the described wave condition taken from a video that was recorded during the test.

Table 2-9 – WWC Flume Test Matrix Overview.

Multiple-Turbine Experiments				
No of Turbine	**Test**	**a1**	**a4**	**Name**
1	Single Wake			**Single**
2	In-line Wake	**12**		**2T 12D**
	In-line Wake	**16**		**2T 16D**
3	In-line Wake	**16**	**12**	**3T**
Wave Experiment				
No of Turbine	**Test**	**Period (s)**	**Amplitude (cm)**	**Name**
1	Wave	0.42	2	**Wave**

(a)

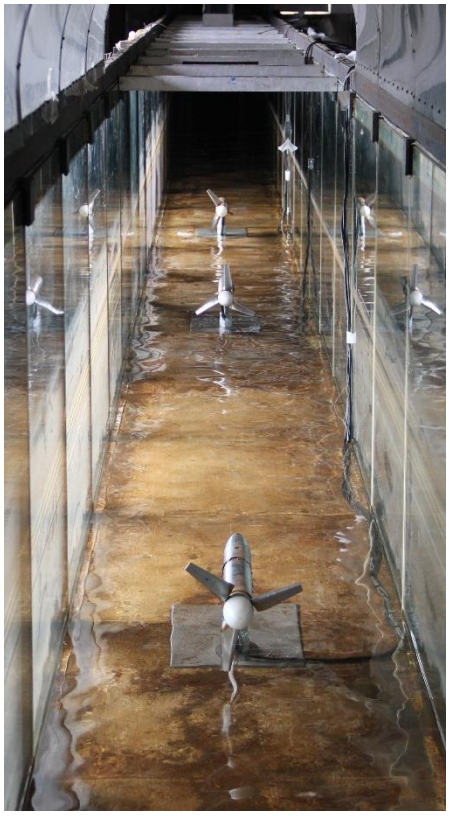

(b)

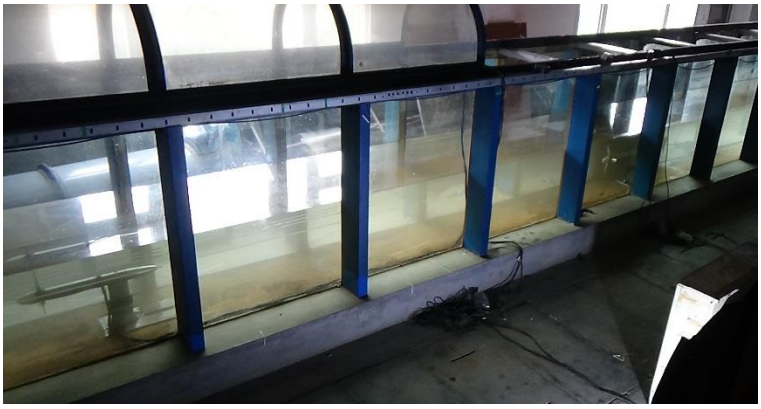

Figure 2-37 - Tidal Turbine Models in WWC Flume, Three Turbine Configuration and Overview of Test Section with Turbines Placed in the Flume.

Figure 2-38 - Tidal Turbine Model with Model Equivalent of a 5m Wave in Full Scale.

Figure 2-39 – 4cm Wave Height with Period of 0.42 Seconds, Two Screenshots from Video Recorded, the Values Do Not Show Actual Water Depth.

Chapter 3. Numerical Modelling

This chapter introduces the numerical methodology applied to predict the flow field within and downstream of staggered tidal turbine arrays. The numerical model presented herein is validated using the results from experiments described in Chapter 2 and used to further investigate the complex, three-dimensional flow field. To make use of increasing computational resources at reduced costs by avoiding large license fees normally incurred by commercial solvers, the open source CFD software package OpenFOAM was chosen to solve the governing fluid flow equations. Numerical simulations of tidal turbine arrays are able to provide more detailed, three-dimensional insights into the inherently complex flow field within tidal turbine arrays and the interactions of multiple wakes as a function of micro spacing between turbine devices in arrays. The computational resources have seen considerable improvements recently with access to multi-core processing becoming less cost intensive and more widely available hence allowing detailed modelling of complex structures and flows on reasonable computational resources.

This chapter will introduce the underlying principles of the applied numerical simulations and the numerical methods used to investigate the flow in and around a tidal turbine array. The description of the numerical tidal turbine arrays is presented followed by validation of the applied numerical model resolution.

3.1 Numerical Methodologies

Computational Fluid Dynamics (CFD) describes the analysis of fluid flow phenomena through simulations, applying different numerical techniques in order to find a close approximation of a solution to a mathematical problem. Finding the analytical solution for fluid flow problems is possible only for a very limited number of flow scenarios and for complex flows still requires infeasible computational resources for most applications. Conducting a numerical investigation of particular flow problems requires the fluid domain under investigation to be divided into a finite number of control elements, referred to as computational mesh consisting of volumetric cells. The fundamental fluid flow characteristics are governed by the conservation laws of physics regarding mass, momentum and energy and expressed through the continuity, momentum and energy equation. At the scales of fluid flow under investigation here, fluids are

described by their macroscopic properties such as velocity, pressure, density and temperature and their derivatives in space and time (Versteeg and Malalasekera, 2007).

3.1.1 OpenFOAM

OpenFOAM (Open Field Operation and Manipulation) is an object orientated library for numerical simulation in continuum mechanics written in C++ programming language (Weller *et al.*, 1998). Recognising common interfaces and interchangeable functionalities, for example in the application of RANS turbulence models where all models effectively evaluate the Reynolds stress tensor, breaks down the complexity of software codes and in combination with the openly available source code allows for an unlimited amount of algorithms, models or boundary conditions to be implemented de-coupled from specific solvers and the software package as a whole. These design objectives and advantages of the object orientated approach are further described by Jasak *et al.* (2007). OpenFOAM provides a framework including all aspects of numerical simulation from geometry handling, pre-processing including arbitrarily unstructured meshes with polyhedral mesh support, solving of governing flow physics using known numerical models as well as post processing and further data analysis capabilities as stated by Jasak *et al.* (2007), one of the principal developers of OpenFOAM. This, in combination with its support for high performance computing without incurring large licence fees for parallel, multiprocessor computations makes OpenFOAM a viable alternative to commercial CFD software programs.

The version used in this Thesis is OpenFOAM 2.3.0, a major release with updated and new functionalities for automated mesh generation (snappyHexMesh), sliding mesh capability (AMI) and general improvements to numerical performance. Further details of the main functionalities and utilities used in the simulation of tidal turbine arrays are presented in the following section and for specific details of the used software version and its capabilities and contents, the reader is referred to the release notes and software documentation (The OpenFOAM Foundation, 2014).

3.1.2 Computational Fluid Dynamics with the Finite Volume Method

OpenFOAM uses a cell-centred Finite Volume Method (FVM) to solve the governing Navier-Stokes equations for viscous flows, here shown in the continuity (3-1) and momentum equation in general form (3-2) and the generalised form of the scalar transport (3-3) equation, usually taken as the starting point for computational methods using FVM. The following introduction is provided with reference to Versteeg and Malalasekera (2007). Continuity and momentum equation are:

$$\frac{\partial \rho}{\partial t} + \nabla \cdot (\rho \mathbf{U}) = 0 \quad , \tag{3-1}$$

$$\frac{\partial (\rho \mathbf{U})}{\partial t} + \nabla \cdot (\rho \mathbf{U}\mathrm{u}) - \nabla \cdot (\mu \nabla \mathrm{u}) = -\nabla p + S_m \quad , \tag{3-2}$$

where **U** represents the three-dimensional velocity vector with components (*u*, *v*, *w*), $\nabla \boldsymbol{U}$ is the gradient and $\nabla \cdot \boldsymbol{U}$ the divergence respectively, S_m represents a momentum source term including the body force and the viscous terms not expressed by the diffusive term $\nabla \cdot (\mu \nabla u)$.

The physical processes governed by the above equations are expressed in the general scalar transport equations for $\emptyset$, defined in (3-3) where D is the diffusion coefficient. This generalised equation can be used to derive all forms of the governing equations by selecting an appropriate value for $\emptyset$ (i.e. 1, *u*, *v*, *w*) such that the resulting equation obtained represents one of the four governing partial differential equations (PDE).

$$\frac{\partial (\rho \emptyset)}{\partial t} + \nabla \cdot (\rho \emptyset \mathbf{U}) = \nabla \cdot D \nabla \emptyset + S_{\emptyset} \tag{3-3}$$

Where each term signifies physical properties described as:

Rate of Increase of $\emptyset$ inside control volume	+	Net rate of decrease of $\emptyset$ due to convection across the control volume boundaries	=	Net rate of increase of $\emptyset$ due to diffusion across the control volume boundaries	+	Net rate of creation of $\emptyset$ inside the control volume due to Sources

By integrating Equation (3-3) over a finite control volume and applying Gauss's divergence theorem, the convective term and diffusive term are expressed as integrals over the bounding surface of the control volume representing the net rate of decrease of ∅ due to convection across the control volume boundary and net increase of ∅ due to diffusion across the control boundaries. The first term on the LHS represents the rate of increase of ∅ inside the volume while the source term signifies the rate of creation of ∅ inside the control volume. Thus for each cell of the system, the conservation of relevant physical properties is expressed.

To obtain a solution to the resulting system of partial differential equations, the governing equations are integrated over a three-dimensional control volume and discretized at each nodal point. The system of PDEs is thus replaced by a system of non-linear algebraic equations, evaluated at discrete positions within the domain that can be solved using iterative methods for which a range of numerical schemes exists.

OpenFOAM offers a number of discretisation schemes used in combination with interpolation of values from cell centres to face centres. In OpenFOAM, numerical schemes have to be specified for each mathematical term in the scalar transport equation (time derivative, gradient, divergence and Laplacian operators and the time derivative for transient simulations), further a correction for non-orthogonal cells is used for the gradient and Laplacian operations. Gaussian finite volume integration with central differencing interpolation are the standard schemes used in OpenFOAM though choice is practically unlimited on the applied numerical schemes. Further information about the available schemes can be found in the programmer's guide (The OpenFOAM Foundation, 2015). The application and details of FVM are well documented in the existing literature, for example Versteeg and Malalasekera (2007) and Ferziger and Peric (2012).

Due to the non-linearity of the convective term and the coupling of momentum and continuity equation through velocity-pressure linkage for incompressible flows, computing the entire flow field requires application of iterative solution algorithms that ensure the correct pressure field is used for calculation of the velocity field to satisfy continuity. The coupling can be treated in two ways, by solving the complete system of equations simultaneously, which becomes impractical for problems with a large number of computational points, or by applying a segregated approach solving the discretised governing equations in sequence. Further details of the velocity-pressure coupling of the discretised Navier-Stokes equations and linearization of

the non-linear convection term with reference to the implementation in OpenFOAM are presented by Jasak (1996).

The most popular algorithms for solving steady state and transient flow simulations are the Semi-Implicit Method for Pressure Linked Equations (SIMPLE) using under relaxation to correct pressure and velocity fields to ensure stable computation when the initial field is differing from the final solution and Pressure-Implicit with Split Operator (PISO) algorithm. The non-iterative transient PISO algorithm is an extension of the SIMPLE with an additional corrector step and no under-relaxation required, as for a sufficiently small time step the velocity and pressure field calculated from the second corrector step satisfy continuity. For further details the reader is referred to Patankar and Spalding (1972) and Issa (1986) respectively or to Versteeg and Malalasekera (2007) and Ferziger and Peric (2012) providing overviews of the most commonly used algorithms for pressure-velocity coupling.

In OpenFOAM the PIMPLE (merged PISO-SIMPLE) solver provides a method of increasing the time step for implicit transient simulations by a introducing the idea of relaxation from the SIMPLE algorithm in combination with PISO algorithm. PIMPLE effectively wraps a SIMPLE algorithm around the PISO algorithm, calculating at each time step the required number of SIMPLE and PISO loops until convergence of residuals, under consideration of the applied relaxation factors and residual tolerances is achieved before moving on in time. The last loop is calculated without relaxation (or a relaxation factor = 1) to ensure time consistency.

The combination of SIMPLE and PISO allows for increased time steps compared to the PISO algorithm for which the CFL number has to be < 1 for convergence. For dynamic meshes with small cells around a tidal turbine blade, this requirement dramatically increases the computational efforts for maintaining a stable solution.

3.1.3 Mesh Generation

Automated mesh generation addresses some of the main drawbacks of discretizing the fluid and complex geometries as being extremely time intensive, hence the use of SnappyHexMesh, a fully automated mesh generator that comes within the OpenFOAM software environment is presented in this study. Geometries for external flow simulations can be supplied as triangulated surface files such as in Stereo lithography (STL) or Wavefront Object (OBJ) format and will be used to generate a three-dimensional mesh that conforms to the surface of the supplied geometry through iterative refinement, by splitting the cells, and under consideration of pre-

specified final mesh quality measures as detailed in OpenFOAM 2.3.0 (2014). The mesh generation utility operates in five basic steps, briefly introduced in Figure 3-1 to show the general methodology applied for automatic mesh generation for external flows (CFD Direct, 2017).

Further details of the specific meshing procedure of a tidal turbine geometry and tidal turbine arrays are outlined in Section 3.2.

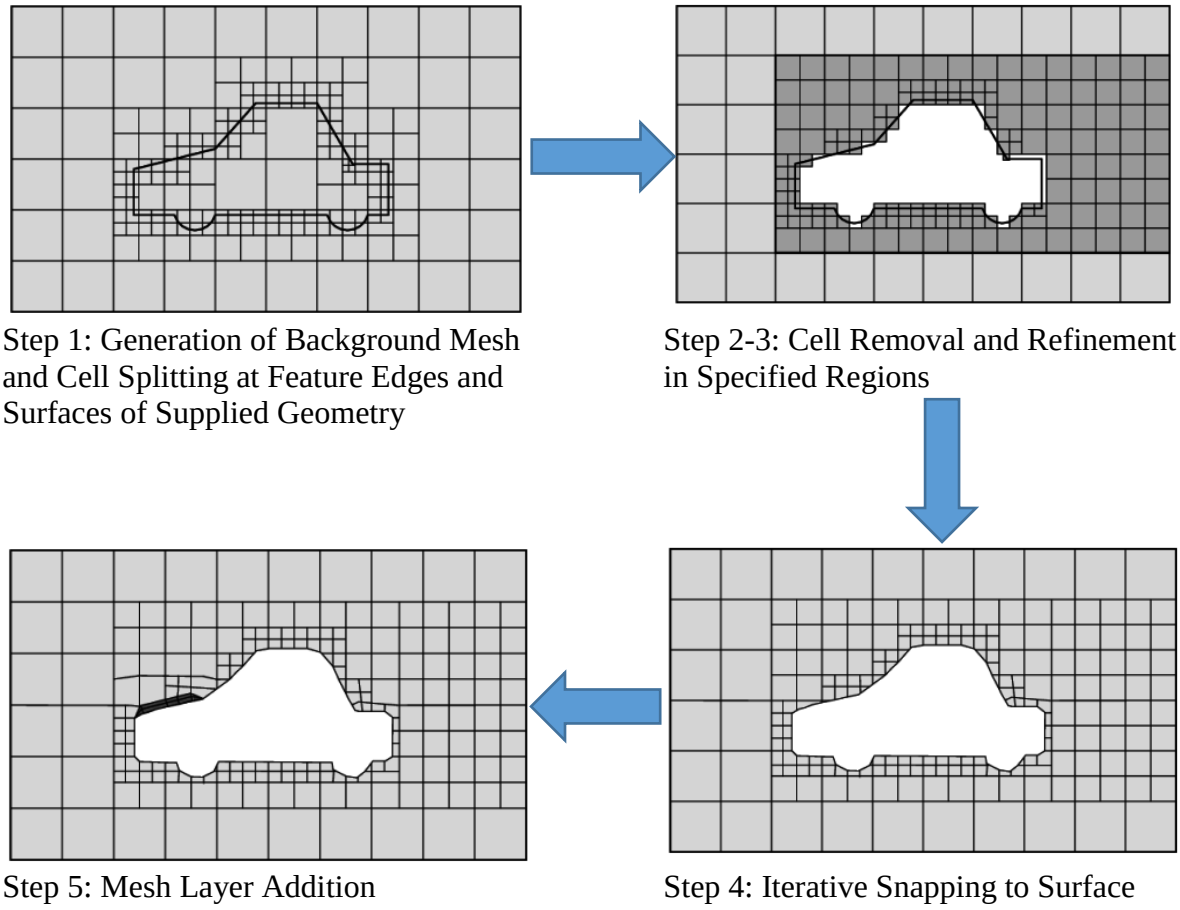

Step 1: Generation of Background Mesh and Cell Splitting at Feature Edges and Surfaces of Supplied Geometry

Step 2-3: Cell Removal and Refinement in Specified Regions

Step 5: Mesh Layer Addition

Step 4: Iterative Snapping to Surface

Figure 3-1 – Illustration of Mesh Generation Process in snappyHexMesh (Images from CFD Direct (2017)).

The meshes generated with OpenFOAM automated mesh generation utility snappyHexMesh, are based on a 3D structured hexahedral background mesh, iteratively refined and morphed onto the tidal turbine structure surface by splitting hex-cells that intersect the feature edges and surfaces until the mesh conforms to the boundary. This is followed by removal of all cells within the specified geometry. The final stage snaps the cell vertices onto the surfaces under consideration of mesh quality parameters.

Often for CFD simulations of blade sections, the trailing edge of the blade is thickened to allow for generation of block structured meshes. For unstructured meshes this is not required, however snappyHexMesh showed some difficulties in generating a mesh conforming to the trailing edge of the tidal turbine blade geometry which can be seen in Figure 3-2 (a) and the improved modelling of the final blade section in (b) by manually multiplying the vertices defining the trailing edge prior to the snapping process.

The mesh generation and snapping process is shown for the tidal turbine blade geometry in (c) and (d) respectively before and snapping of the surface mesh to the surface of the supplied geometry. Publications using SnappyHexMesh for 3D airfoil applications are limited, however Liu *et al.* (2017) recently validated the aerodynamic performance of a NREL 5MW wind turbine in a SnappyHexMesh generated domain, featuring a sliding mesh interface, against experimental data.

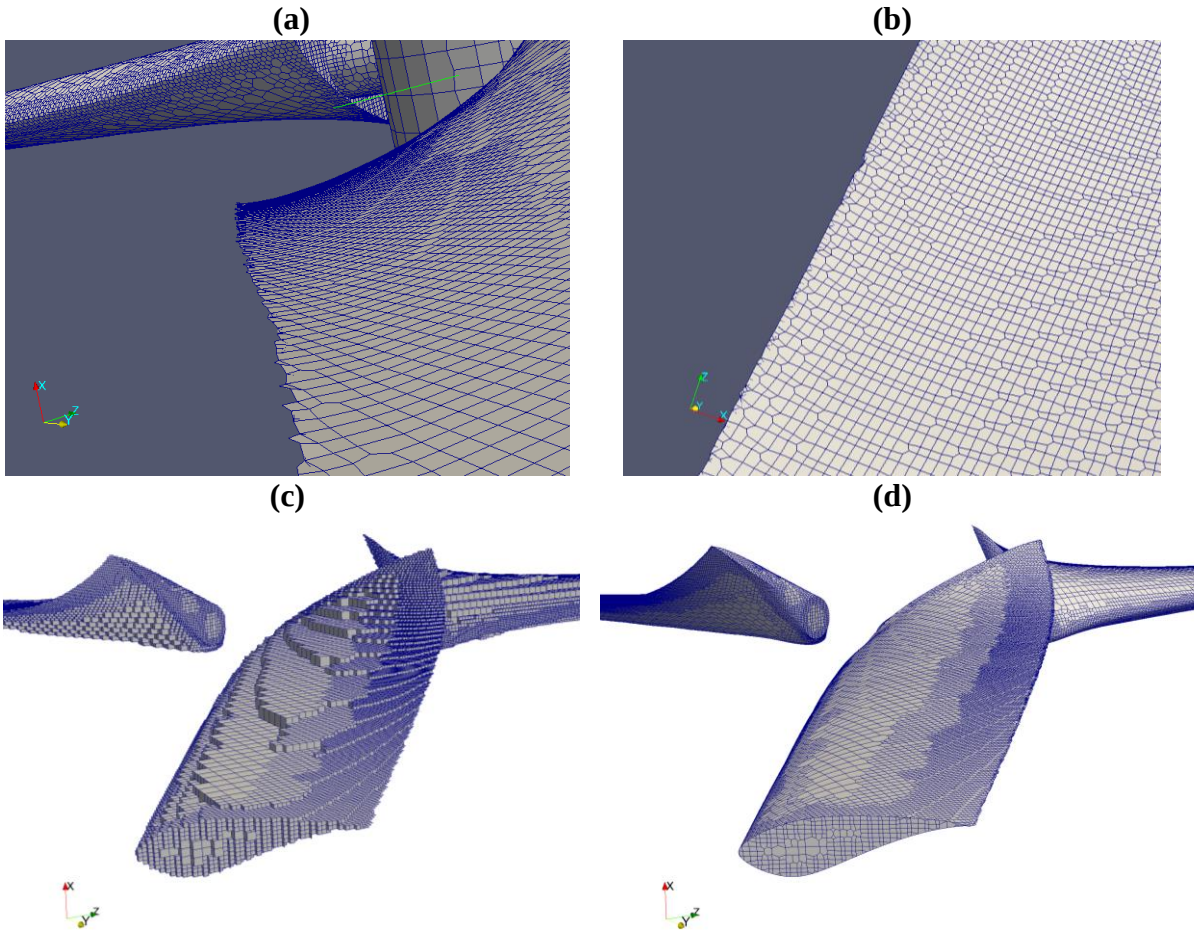

Figure 3-2 – (a) Trailing Edge of Turbine Blade Before Improved Snapping for Thin Features and (b) Improved Trailing Edge Snapping (c) Castellated Mesh (Step 1 & 2) of the Turbine Blade Geometry and (d) Mesh Snapped to the Surface of the STL Geometry.

3.1.4 Turbulence Modelling

Modelling of complex, three-dimensional turbulent flows, i.e. flows with unstable, chaotic motions expressed through velocity and pressure variations across time and space is one of the most significant challenges in modern CFD application (Wilcox, 2010). Turbulent flows are often described as containing rotational flow structures, so called eddies, of a wide range of scales from the largest being of similar length and velocity scale as the mean flow where inertia effects dominate and viscous effects are negligible, down to the Kolmogorov microscales where inertia and viscous effects are of equal strength (Re = 1). Unsteady flow causes the large eddies to break down and turbulent kinetic energy is passed on to smaller and smaller eddies through the energy cascade until the energy is dissipated and converted into heat due to the viscous forces (Versteeg and Malalasekera, 2007). The length (η) and time (τ_η) scales expressed in terms of the rate of dissipation of turbulent energy (ε) and kinematic viscosity (υ) as shown in (3-4) from Wilcox (2010) for the flow considered here are approximated as:

$$\eta \equiv \left(\frac{\upsilon^3}{\varepsilon}\right)^{\frac{1}{4}} \quad \text{and} \quad \tau_\eta \equiv \left(\frac{\upsilon}{\varepsilon}\right)^{\frac{1}{2}} \tag{3-4}$$

$$\text{resulting in} \quad \eta \equiv 2.2 \times 10^{-5}\text{m} \quad \text{and} \quad \tau_\eta \equiv 2.34 \times 10^{-7}\text{s} \tag{3-5}$$

Thus, resolving all such turbulent structures numerically requires cell size and time steps according to the Kolmogorov length and time scales, shown in Equation (3 4) with estimates for the presented flow conditions in Equation (3-5). This approach would be classified as Direct Numerical Simulation (DNS) where the Navier Stokes Equations are numerically solved without any further modelling required to account for the mean flow and all velocity fluctuations. However, this approach is extremely computationally expensive even for flows at low turbulence (i.e Reynolds Numbers) and for the phenomena investigated here would be unfeasible.

Large Eddy Simulations (LES) provide an intermediate model of accounting for the turbulent flow through spatially filtered Navier Stokes equation, rejecting smaller eddies but accounting for their effect on the resolved flow (mean flow and larger eddies) and are accounted for through so called sub-grid scale models of which a wider variety has been developed. Examples of SGS models include the models described by Smagorinsky (1963) and Kim and Menon (1995) based on the kinetic energy closure.

For most applications mean flow properties and the effects of turbulence on the mean flow are of interest and thus Reynolds Averaging is applied to the governing Navier-Stokes equations. The Reynolds Averaged Navier Stokes equations are obtained by decomposing the instantaneous velocity component into a mean and fluctuating component and averaging the governing equations, shown for incompressible flow in Equation (3-6) and (3-7) from Jasak (1996):

$$\nabla \cdot (\overline{\mathbf{U}}) = 0 \ , \tag{3-6}$$

$$\frac{\partial(\overline{\mathbf{U}})}{\partial t} + \nabla \cdot (\overline{\mathbf{U}}\overline{\mathbf{U}}) = g - \nabla \bar{P} + \nabla \cdot (\upsilon \nabla \overline{\mathbf{U}}) + \overline{\mathbf{U}'\mathbf{U}'} \ , \tag{3-7}$$

Where υ is the kinematic viscosity and $\overline{\mathbf{U}'\mathbf{U}'}$ is called the Reynolds Stress Tensor, introducing extra terms (six additional stress components (three normal and three shear stress components) in combination with the velocity components and the pressure, thus resulting in ten unknowns and four equations (the continuity equation (3-6) and three Navier Stokes Equations (3-7)). Hence the resulting system is not closed and requires additional modelling.

Formulating and solving the additional Reynolds stress transport equations, due to the additional six components, namely the three normal and three shear stresses, requires additional modelling to close the above system of equations. Including the exact Reynolds stress transport equations, plus additional modelling of the scalar dissipation rate, thus adding seven partial differential equations to the system of equations increases the computational resource requirement substantially. Turbulence closure models using the exact Reynolds Stress transport equation are usually collected under the term Reynolds Stress Modelling (RSM) or Reynolds Stress Transport Modelling (RSTM) for which a number of various formulations have been presented such as the LRR model by Launder *et al.* (1975) or SSG model by Speziale *et al.* (1991).

The most commonly used approach to solve the closure problem is assuming that the Reynolds stress tensor can be modelled as the product of an eddy viscosity and the mean strain rate tensor. Applying the Boussinesq assumption, originally proposed by Boussinesq in 1877 and discussed in Schmitt (2007) a linear relation for the Reynolds Stress tensor is presented in the same form used by Jasak (1996) as:

$$\overline{\mathbf{U}'\mathbf{U}'} = \nu_t(\nabla\mathbf{U} + (\nabla\mathbf{U})^T) + \frac{2}{3}k\mathbf{I} \ , \tag{3-8}$$

and

$$k = \frac{1}{2}\,\overline{\mathbf{U}'.\mathbf{U}'} \ , \tag{3-9}$$

where ν_t is the kinematic eddy viscosity, *k* the turbulence kinetic energy and **I** is the unit tensor.

The kinematic eddy viscosity or turbulence viscosity is evaluated in a number of ways which represent the classification of eddy-viscosity turbulence models according to the number of additional transport equations introduced (Versteeg and Malalasekera, 2007). Dimensional analysis yields that the turbulence viscosity is proportional to a characteristic velocity and a mixing length, with the difference between zero, one or two equation models being the way these are computed (Argyropoulos and Markatos, 2015). Starting from zero equation models such as Prandtl's Mixing length hypothesis using algebraic expressions, computational advances have led to two equation models that compute the turbulence kinetic energy as well as the turbulence length or equivalent terms to determine the length scales for flows where an algebraic prescription for the mixing length is no longer feasible (Versteeg and Malalasekera, 2007).

The most commonly applied turbulence models that introduce two model equations are the k – ε (Launder and Spalding, 1974) and k – ω (Wilcox, 2010) turbulence closure models where ε is the rate of dissipation of turbulence kinetic energy and ω the specific dissipation rate (or turbulence frequency) which are defined in (3-10) for k – ε and (3-11) for k- ω which are obtained by solution of their respective transport equations. The transport equation for *k* as formulated within OpenFOAM (OpenCFD Ltd., 2017) is shown in (3-12) as both models use the same formulation.

$$\varepsilon = \upsilon\overline{\mathbf{U}'\mathbf{U}':\nabla\mathbf{U}'} \ , \tag{3-10}$$

$$\omega = \frac{\varepsilon}{k} \tag{3-11}$$

$$\frac{\partial(\rho k)}{\partial t} + \nabla\cdot(\rho k\boldsymbol{U}) = \nabla\cdot(\rho \mathrm{D_k}\nabla k) + \rho \mathrm{G} - \frac{2}{3}\rho k(\nabla\cdot\mathbf{U}) - \rho\beta^*\omega \mathrm{k} + \mathrm{S}_k \tag{3-12}$$

A combination of the above mentioned two equation turbulence closure models has been introduced by Menter (1994) and modified for performance improvements as presented in Menter *et al.* (2003) which is the version implemented in OpenFOAM. The principle of the modified version is that the original k – ω is sensitive to the applied free-stream values of ω, yet performs better in near wall areas with adverse pressure gradients, while the k - ε performs better for the fully turbulent flow in the region far from the wall. In the shear stress transport model, a cross diffusion term is added to the model through transforming the ε equation using $\varepsilon = k\omega$ (Versteeg and Malalasekera, 2007) and the inclusion of stress limiters on the eddy viscosity when turbulence kinetic energy production exceeds its dissipation (Wilcox, 2010).

Applying the Boussinesq assumption for turbulence models in these two equation turbulence closure models provides the advantage of very reasonable computational efficiency and accuracy over a wide range of turbulent flow problems, however at a cost of simplifying the prevailing turbulence by implying isotropy. These models thus fail to predict interactions between the turbulent stresses and the mean flow caused by anisotropy of the normal stresses as well as the effects of extra strains and stresses on the turbulence. Further difficulties lie in the modelling of rotational flow (Versteeg and Malalasekera, 2007). While RSM turbulence closure takes these effects into account directly, the additional computational overhead required is significant. LES simulations past complex geometry on arbitrarily unstructured meshes with polyhedral cells introduce further difficulty for the definition of the filter cut-off in the near wall regions (Versteeg and Malalasekera, 2007).

3.1.5 Solving

All pre-processing and solving of governing RANS equations is performed in the Open Source software OpenFOAM. The systems of linear equations are solved iteratively using Gauss-Seidel and Geometric Agglomerated Algebraic Multigrid (GAMG) solvers.

The pressure – momentum coupling algorithm used from the OpenFOAM library, PimpleDyMFoam, is a combination of PISO - SIMPLE algorithm allowing for larger time steps (Courant-Friedrichs-Lewy (CFL) > 1) in incompressible, unsteady viscous flows as well as dynamic mesh features such as the rotation of turbine blades with a user defined mesh interface between the rotor and stator part of the domain.

The solver uses the SIMPLE algorithm to converge the steady state solution within time steps while the number of PISO calculations for each SIMPLE iterations is a combination of the number of pressure corrector steps and additional corrections applied such as for non-orthogonality of the mesh. Advancement to the next time step is controlled by defining tolerances on the residuals thus the number of outer correctors is set to a high maximum and the final iteration is carried out without any relaxation factors. Due to the combination of the two algorithms, the strict time step requirements for the PISO pressure velocity coupling are relaxed and the time step can be significantly increased, which presents a huge advantage for large simulation problems where a small time step would led to excessive simulation times.

The time step itself is dynamically controlled by a maximum Courant (CFL) number depending on the flow velocity and a measure of the local cell size. The adaptive time step control ensures that the CFL number is kept below a set maximum and changes according to changes in flow velocity which, in combination with a moving mesh interface presents significant advantages in ensuring the influence of time step settings are minimal. A flow chart of the main parts of the applied pressure-velocity coupling used is shown in Figure 3-3.

OpenFOAM supports parallel computations without restrictions on the number of processor cores, using message passing interface (openMPI) for communication between all processes. The computational domain is decomposed using scotch decomposition method minimizing the number of processor boundaries and divided into a number of domains corresponding to the number of CPU cores allocated. This study employed between 16 and 48 cores for the simulation of tidal turbine arrays.

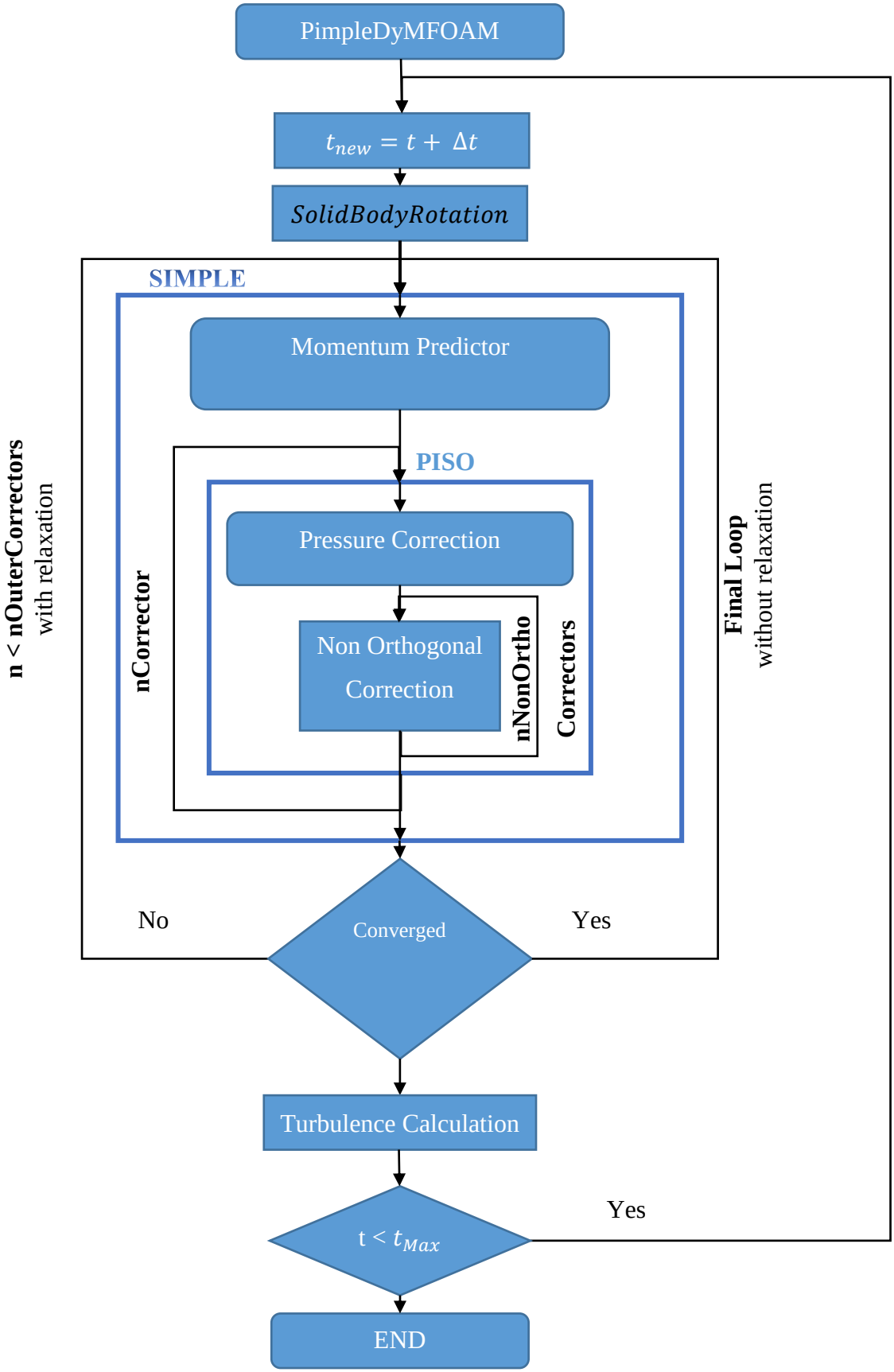

Figure 3-3 – PimpleDyMFoam with Residual Control.

3.2 Modelling of Tidal Turbines

The co-ordinate system used for numerical modelling corresponds to the co-ordinate system presented in the experiment set-up with the rotor of the upstream turbine located at (0, 0, 0) as can be seen in Figure 3-4. In accordance with distances reported throughout the experiment study, all distances are given in terms of the turbine diameter (D).

To represent the tidal turbine models used in experiments, the CAD models were exported and surface meshes created in the open source software SALOME (OPEN CASCADE, 2013) to provide unstructured triangulated surface representation defined by unit vectors and vertices (STereoLithography, STL files). These were used in snappyHexMesh for the generation of arbitrarily unstructured three-dimensional mesh within the test domain.

3.2.1 Experiment Conditions

The computational domain (Figure 3-4) represents the dimensions of the Circulating Water Channel (CWC) at Shanghai Jiao Tong University with a test section extending from -5D upstream of the first turbine location to 22D downstream. Vertically the domain extends 4D from the top-tip of the rotor while the rotor bottom tip to seabed distance is 0.75D. For additional comparison of wake recovery with higher ambulant turbulence intensities, a single turbine is modelled with 10% ambient turbulence intensity.

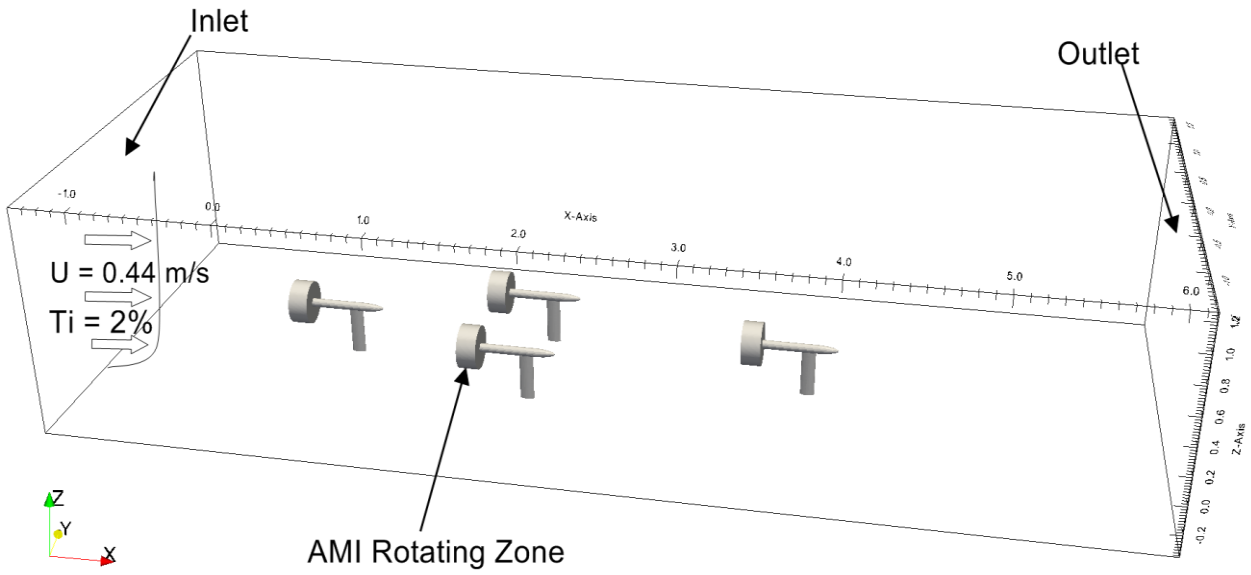

Figure 3-4 – Computational Domain with Array Configuration for Numerical Simulations.

Due to the distance between rotor tip and free surface, and a Froude number of less than 0.2, the computations do not account for the free surface, hence top, side and bottom of the test channel are modelled as walls, this is also applied to the static parts of the turbine structure. The rotor blades, hub and cone are modelled as walls with a moving wall condition to account for the rotation according to the operating condition. The current velocity is specified upstream of the array as a velocity inlet on the left and a pressure-outlet is defined on the right, downstream of the array.

To model the ambient flow conditions used during the experiment, the inflow was set to a velocity of 0.44m/s and an ambient turbulence intensity of 2%. This was defined through a turbulent kinetic energy (TKE) condition on the inlet patch based on the mean flow velocity and turbulence intensity representative of the CWC. A comparison between the numerically achieved velocity profile upstream of the turbine, and the free stream velocity profile measured across the turbine diameter without any devices located in the CWC are shown in Figure 3-5. Variations between numerical and experimental inflow velocity are small, indicating the present numerical resolution is satisfactory.

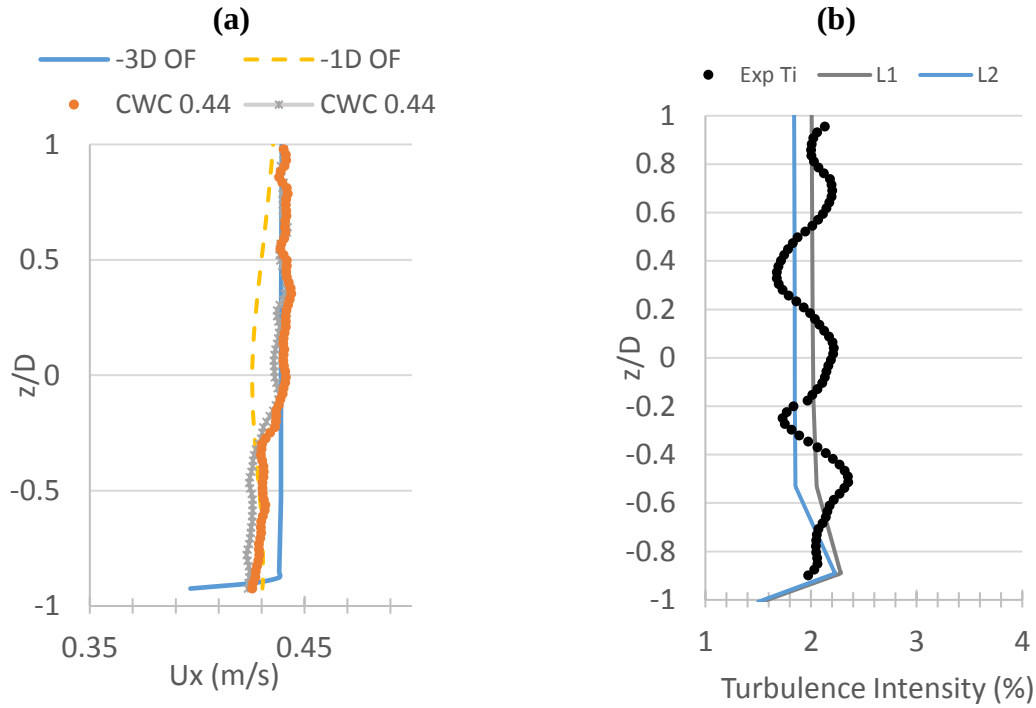

Figure 3-5 – (a) Inflow Velocity Comparison between Numerical Simulation and Experiment for 0.44m/s Ambient Current and (b) Turbulence Intensity from Experiments (Dotted) vs Various Mixing Lengths used in OpenFOAM at 2D Upstream of the Turbine.

3.2.2 Turbine and Rotation

Modelling the rotation of the hub, cone and blades is achieved by using the arbitrary mesh interface (AMI) a sliding mesh interface where all cells within the rotational zone rotate at a specified, constant rotation which for the simulation presented here is set according to the turbine TSR of 4. AMI allows for simulation of mesh patches that are disconnected but adjacent, stationary or with relative movement between the two interfaces.

The AMI algorithm used for the conservative interpolation between non-conformal mesh patches is implemented based on the Galerkin projection presented by Farrell and Maddison (2011) in OpenFOAM 2.1.0 and has been improved by implementation of a zero gradient condition applied on cell weights between source and target patched below user-defined thresholds in OpenFOAM 2.3.0. Further information about the implementation of a sliding mesh interface in an earlier version of OpenFOAM using weighting factors to allow for coupling of non-conformal meshes can be found in Beaudoin and Jasak (2008).

The AMI zone extends from 0.12m upstream of the rotor centre to 0.02m downstream (a total length of 0.5D) with a diameter of 1.4D. The clearance between upstream AMI interface and tip of the nose cone is 2cm, similarly the clearance downstream is 2cm from the rotor blade to the downstream interface.

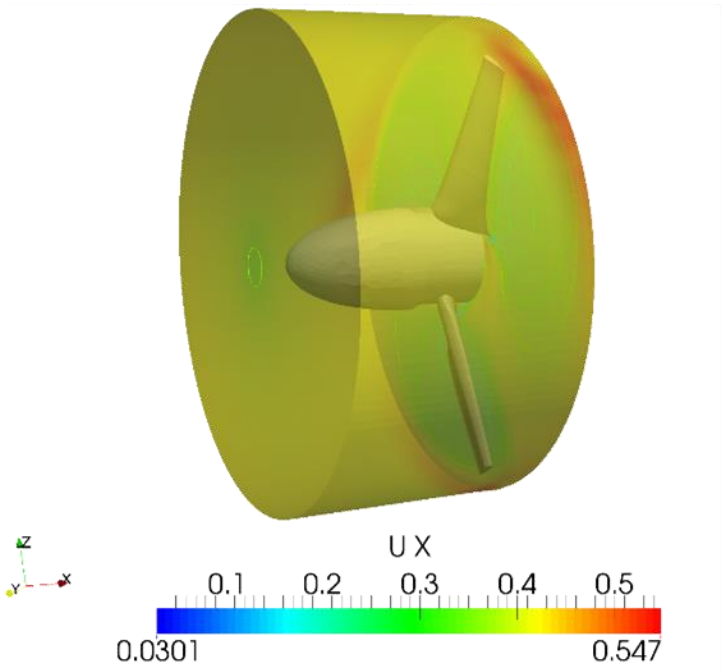

Figure 3-6 – Rotating AMI Zone to Model Turbine Rotor and Rotation.

Care has been taken in the generation of the rotor-stator interface to ensure good overlapping of the source and target patches by generating two identically resolved cylinder surfaces between which the flow information is passed axially and radially. An image of the rotating zone with stream-wise velocity component contours is shown in Figure 3-6. Figure 3-7 shows the AMI interface from an upstream direction (a) and a side view (b) with the mesh resolution inside and downstream of the rotational zone. The downstream extent of the AMI zone has been modelled according to the experimental turbine where the rotor hub and cone rotated at a set rotation rate and upstream of the static turbine nacelle.

At each rotational step, information is passed between rotor and stator patch interfaces through a cyclic boundary condition with contributions from overlapping cells weighted corresponding to the fraction of overlapping areas. Additionally, the source and target face weights are monitored to avoid introducing conservation errors due to non-conforming patch geometries (where sum of weights does not equal 1) and monitored and show an average source and target weight sum of 0.99. A zero gradient condition is applied for patch faces where the weight contribution lies below 0.2.

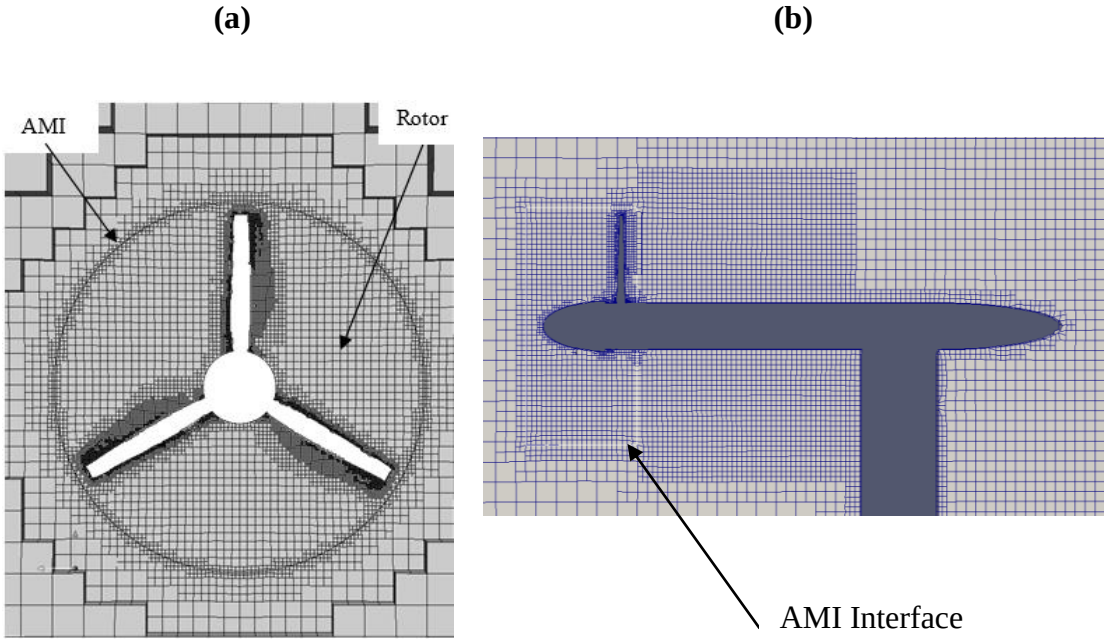

Figure 3-7 - (a) Rotor-Stator Interface for Rotating AMI Zone and (b) Mesh Density for Rotor and Stator Regions with AMI Interface Shown Around the Rotor.

The support structure was designed to minimize the influence on the resulting wake and the flow field around the tower within the turbine blade wake is shown in Figure 3-8 (a) with the average wake velocity deficit below the rotor wake shown in (b). The rotor impacts on the flow in the wake but due to the rotation of the wake in the immediate near wake downstream of the rotor (the vertical support is located between 1D and 2D) the most significant impact is seen in the transverse, not downstream direction. However in this area the flow is highly turbulent and very slow moving thus the wake extent of the support is reduced as can be seen. Below the turbine wake, the support structure causes a thin wake with a low wake velocity deficit that reduces to less than 5% within 3D downstream of the rotor thus the effect on the ambient flow on the lower part of the wake is minimal.

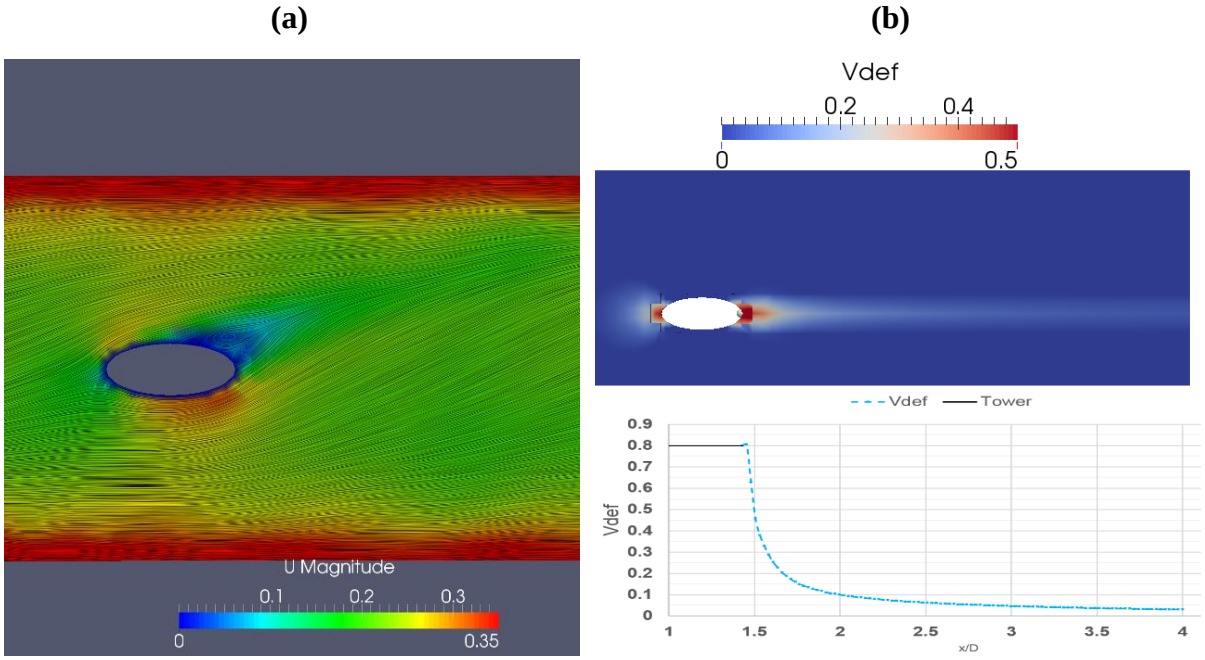

Figure 3-8 – Influence of the Vertical Support Structure on the Resulting Wake at (a) z/D = -0.25 for Instantaneous Velocity Magnitude and Surface Streamlines (LICs) and (b) Time Averaged Wake Velocity Deficit at z/D = -0.75 Contour and Line Plot at Centreline of the Wake.

3.2.3 Turbulence

A comparison of grid resolution estimations between different turbulence modelling strategies by Spalart (2000) stated that by moving from three-dimensional unsteady RANS calculations to LES, the grid count increases by approximately 4 orders of magnitude. The computationally more economical RANS approach with the $k - \omega$ SST turbulence closure model was chosen based on the previous comparison of RANS and LES simulations with sliding mesh interface by McNaughton *et al.* (2014) for investigations of tidal turbine performance and wake characteristics. The authors stated that a single calculation of a tidal turbine LES with dynamic mesh requiring CPU resources in the order of millions of hours to achieve 25 complete rotations. Previous studies (Apsley and Leschziner, 2000) have stated improved prediction of velocity and Reynolds stress profiles for the $k - \omega$ SST model compared to $k - \omega$ and $k - \varepsilon$ turbulence closure models. Comparison of linear and non-linear eddy-viscosity turbulence closure models for three-dimensional aerodynamic flows around a number of wing sections and stated the $k - \omega$ SST model provided results similar to those achieved with higher order (non-linear) k - ε models at reduced computational expenses (Catalano and Amato, 2003).

Based on the characteristics of turbulence modelling presented in Section 3.1.4 and the discussion above combined with the computational resource requirements for a multi-turbine array and dynamic modelling of the turbine rotor rotations, the $k - \omega$ SST model (Menter *et al.*, 2003) was chosen for the turbulence closure in the presented study. A comparison of $k - \omega$ SST and Reynolds stress model, specifically the LRR model developed by Launder *et al.* (1975) is conducted for a single turbine operating in the CWC test section at reduced computational requirements compared to the array cases for additional comparison.

To solve the fluid flow problems, initial and boundary conditions are needed to solve the integrated forms of the transport equations in the finite volume approach summarised as below by Versteeg and Malalasekera (2007). Boundary conditions are classified as Dirichlet (fixed value) and Neumann (fixed gradient) and applied to the physical boundaries modelled in the computational domain. For external flows such as presented here, these usually include an inlet and outlet, solid impermeable walls and in the case of mesh rotation also moving walls.

In addition to all initial flow variables, the distribution of all variables has to be supplied at all inlets to the flow domain under investigation. The pressure has to be specified at one location inside the flow domain and all variables have a zero gradient applied in the flow direction at the outlets of the domain. In addition, at solid walls the values of flow variables or normal gradients have to be supplied.

The application of these boundary conditions for the numerical modelling presented here is shown in tabulated form in Table 3-1. While the velocity is set according to the experiment conditions, turbulence kinetic energy and dissipation frequency are approximated for initial conditions to represent the ambient flow with a turbulence intensity of 2%.

In addition to the boundary conditions above, an additional condition is introduced to connect the rotor and stator part in the simulations featuring an arbitrary mesh interface. The patches of the AMI are described as cyclic (periodic) interfaces and corrections for low overlapping weights due to partial overlap between static and rotating patches during the AMI rotation can be applied.

Table 3-1 - Boundary Conditions used for Numerical Simulation and Wall Functions (WF) applied, where I is the Ambient Turbulence Intensity (2% and 10%) and L the Inlet Mixing Length, Taken as 0.7 Times the Axis Immersion Depth (L_1) and Chord Length (L_2).

Domain Patch	**Velocity**	**Pressure**	***k***	***ω***
Inlet	0.44 m/s	Zero Gradient	$k = 1.5 * (U_\infty * I)^2$	$\omega = \sqrt{k}/(C_\mu^{0.25} * L)$
Outlet	Zero Gradient	0	Zero Gradient	Zero Gradient
Walls	(0, 0, 0)	Zero Gradient	Zero Grad (WF)	WF (3-22)
Rotational Parts	12.57 rad/s	Zero Gradient	Zero Grad (WF)	WF (3-22)
AMI	Cyclic Boundary			

The k – ω SST model requires initialisation at the domain boundaries of the turbulence kinetic energy k and specific dissipation rate ω according to the following formulations:

$$k = \frac{3}{2}(I\,|U_\infty|)^2\,, \tag{3-13}$$

$$\omega = \frac{\sqrt{k}}{C_\mu{}^{0.25} L}\,, \tag{3-14}$$

$$L_1 = 0.7\ \times Immersion\ Depth\,, \qquad L_2 = Chord\ Length\,, \tag{3-15}$$

where I is the ambient turbulence intensity, U_∞ is the ambient or reference current velocity, C_μ = 0.09 and L is the mixing length scale defined using (3-15).

The definition of the mixing length scale used to initialise the turbulence models varies considerably across previous numerical simulations. The representative length used to calculate the mixing length scale varies from the diameter of the turbine and chord length at tip (Olczak *et al.*, 2016), to the depth or immersion depth (Afgan *et al.*, 2013; McNaughton *et al.*, 2014) to a fraction of the wake (from mixing length models (Versteeg and Malalasekera, 2007)). A comparison of the obtained inflow turbulence intensity obtained for a range of omega (specific dissipation rate) values is shown in Figure 3-5 (b).

The simulations presented here used the mixing length definition based on the turbine immersion depth (L_1) and blade chord length (L_2) for initial comparison to experiments and determine the most suitable definition based on the agreement for wake recovery of a single turbine.

A single turbine has been simulated using the LRR Turbulence model as described in Launder *et al.* (1975) with the OpenFOAM specific implementation including a generalised gradient diffusion model and wall reflection terms as defined in OpenCFD Ltd. (2017). The inlet distribution of Reynolds stress term is approximated as stated in (3-16) and Versteeg and Malalasekera (2007).

$$\overline{u'^2} = k, \qquad \overline{v'^2} = \overline{w'^2} = \frac{1}{2}k, \qquad \overline{u_i' u_j'} = 0\ \ (i \neq j) \tag{3-16}$$

3.2.4 Wall Modelling

Turbulent flows in proximity to solid walls are affected by their presence and the flow behaves differently from the free stream flow. This region is called the boundary layer and is further divided into the outer part where the flow behaviour is influenced by the wall shear stress and the free stream flow is important and the inner part, which itself is divided into a further three areas.

The boundary layer close to the wall is dependent on the turbulent kinematic viscosity (υ_t) and wall shear stress which are used to define non-dimensional parameters such as the friction velocity u_τ (3-17), dimensionless velocity (u^+) and dimensionless wall distance (y^+) in (3-18).

$$u_\tau = \sqrt{\frac{\tau}{\rho}} \tag{3-17}$$

$$u^+ = \frac{U}{u_\tau} \quad \text{and} \quad y^+ = \frac{y u_\tau}{\upsilon_t} \tag{3-18}$$

$$u^+ = \frac{1}{\kappa}\ln(E y^+) \tag{3-19}$$

Where τ is the wall shear stress and y is the distance to the wall, κ is the von Kármán constant (κ = 0.41) and E an integration constant for the roughness of the wall (E = 9.8 for smooth walls).

The thin layer closest to the solid wall is called the viscous (or linear) sub-layer where $u^+ = y^+$ which is considered true for $y^+ < 5$. For $30 < y^+ < 500$ viscous and turbulent effects are both important and the wall shear stress is assumed to be constant. The non-dimensional velocity and distance are thus related by the logarithmic function (3-19) and the layer between 30 and 500 is called the log-layer. The two equations intercept at $y^+ \approx 11$ and the region from 5 to 30 is called the buffer layer where viscous and turbulent stresses are of similar magnitude (Versteeg and Malalasekera, 2007).

Capturing the flow and turbulence characteristics in the viscous boundary layer near to a wall introduces strong requirements on the mesh resolution, i.e. $y^+ < 1$, especially for high Reynolds number flows thus increasing the computational time significantly. To reduce this, the flow near a wall can be modelled using so called wall-functions that place the first grid in the log layer and model the near wall flow.

The turbulent kinematic viscosity wall function is defined in Spalding (1961) with the calculation of local y^+ based on the velocity field in the boundary layer using u^+ as shown in (3-20), and in the OpenFOAM set-up here used to provide an adaptive wall function that calculates the friction velocity (u_τ) and y^+, based on the Newton – Raphson method with the definitions provided in (3-21). These are then used for calculation of turbulence coefficients in the omegaWallFunction (Menter and Esch, 2001), providing omega for viscous (ω_{vis}) and log layer (ω_{log}) and blending in the buffer layer as shown in (3-22). This procedure reduces the meshing requirements of resolving the viscous-sub layer or ensuring placing of the first cell within the log layer, which is beneficial when using automated mesh generation for such complex geometries as a tidal turbine rotor. The OpenFOAM wall functions used for numerical simulation were listed in Table 3-1.

$$y^+ = u^+ + \frac{1}{E}\left[e^{ku^2} - 1 - ku^+ - \frac{1}{2}(ku^+)^2 - \frac{1}{6}(ku^+)^3\right] \tag{3-20}$$

$$v_t = \frac{(u_\tau)^2}{\partial U/\partial y} - v \quad \text{and} \quad y^+ = \frac{u_\tau y}{v} \quad \text{and} \quad u_\tau = \sqrt{(v_t + v)} \tag{3-21}$$

$$\omega_{vis} = \frac{6v}{0.075y^2} \text{ and } \omega_{log} = \frac{1}{0.3k}\frac{u_\tau}{y} \text{ and } \omega = \sqrt{{\omega_{vis}}^2 + {\omega_{log}}^2} \tag{3-22}$$

Similar to the modelling of a single tidal turbine with sliding mesh by Afgan *et al.* (2013) average y^+values across the tidal turbine blades are less than 5 while vertical support and tower are kept above 30. A contour plot of the y^+ values across the turbine blades is shown in Figure 3-9.

3.3 Validation

Validation of the computational methodologies is required to ensure that numerical simulations are independent of the computational grid employed. Further, the resolution of surfaces such as the turbine support structure and more importantly for the wake characterisation, the turbine blades, must allow to accurately resolve the flow in order to account for the blade induced effects on the wake flow field. In addition to the spatial discretisation, the temporal discretisation, i.e. the time step used to advance the transient simulations has to be fine enough for the flow phenomena under investigation to be represented.

This presents a significant challenge in achieving the required mesh resolution (minimising the cell sizes) to reduce the variations of flow field characteristics while maximising the time step. The main objective is to ensure sufficient simulation time for the flow to reach a converged status thus allowing for comparison to the flow field characteristics measured during the experiments. In this study, the time step is controlled by convergence of residuals within the combined SIMPLE and PISO loops, with a convergence criterion for residuals of 1×10^{-6}.

The following section presents the validation of the numerical model for the performance coefficients of the numerical model as well as the wake characteristics. The grid convergence index (GCI) as described in Celik *et al.* (2008) is used as well as comparison to previous numerical and experimental studies using the same blade section profile (NREL S814) in terms of performance data. Furthermore, to validate the blade scale flow, quantitative and qualitative comparison of the blade scale flow is presented. The flow through the rotor-stator interface is monitored to ensure that the sliding mesh interface does not induce non-physical effects to the flow through the numerical tidal turbine rotor. The final mesh configuration used for the array test is then chosen based on the obtained validation and comparison with experiments, with the increased resolution resulting from automated mesh refinement and the increased computational requirements for the simulation of multiple rotating tidal turbines in mind. For further comparison and investigation of the resulting wake field, the in-stream velocity component is monitored using the GCI. As final validation of the numerical resolution applied, the in-stream velocity characteristics are compared to those obtained from the experiments.

A number of meshes with increasing numbers of cells for regional wake refinement have been generated (see Figure 3-10 & Table 3-2). To decrease the computational time for this study, a single turbine mesh configuration was tested in a smaller domain covering a large enough time period to reach at least 20 revolutions of the turbine blades. The different refinement zones of the turbine wake can be seen in Figure 3-10 where different cell sizes are used to resolve the wake domain at different distances downstream, with smaller elements used near the turbine where the flow is expected to show increased fluctuations.

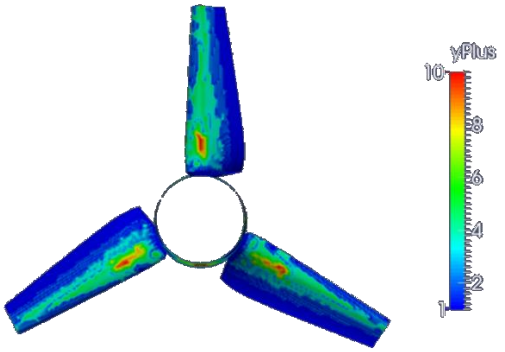

Figure 3-9 - Average y^+ Distribution on Tidal Turbine Rotor.

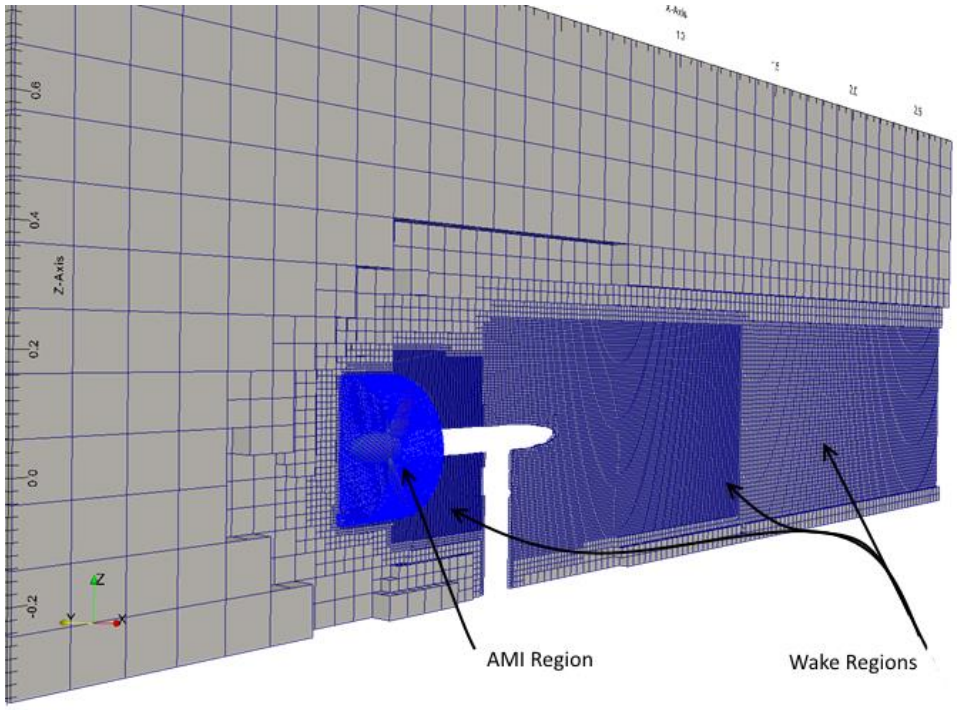

Figure 3-10 - Tidal Turbine CFD Domain, the Vertical Slice at the Centreline Showing the Different Wake Refinement Zones Downstream of the Turbine.

Table 3-2 - Mesh Characteristics for Convergence Study.

Mesh	No. of Cells	Refinement Ratio	Approximate Cell Resolution near Blade	Wake Cell Resolution
Coarse	343698		5.58×10^{-3} D	0.089D
Medium	819607	C - M: 1.34	2.79×10^{-3} D	0.044D
Fine	2959484	M - F: 1.53	0.69×10^{-3} D	0.02D

3.3.1 Loading and Performance

The time averaged thrust and torque over a period of 20 seconds have been used with constant sampling rate between all simulations to determine grid convergence, showing oscillating convergence in the GCI as shown in Table 3-3 (a). The extent of loading on the vertical support structure is less than 5% of the thrust experienced by the entire device. The numerically obtained mean thrust and power coefficients are compared to numerical experiments and simulations with tidal turbines using a NREL S814 blade section design at TSR = 4 in Table 3-3 (b). Experiments with same chord and twist distribution with a diameter of 0.4m presented in Shi *et al.* (2013) were conducted at a blockage ratio of approximately 13% compared to approximately 5% in Milne *et al.* (2013) & (2015) with near identical chord distribution, and twist angles differing by less than 5 degrees except at 0.2r/R where a 10 degrees higher blade pitch angle was used by Shi *et al.* (2013). Details of the twist and chord distribution are shown in Figure 3-11. No blockage correction has been applied. Previous estimates of the effect of blockage in Bahaj *et al.* (2007b) stated a 5% increase of thrust at 8% blockage compared to unbounded flow. The thrust and power coefficients based on calculated torque acting on the turbine blades have been used to determine the discretisation error based on the grid convergence index (CGI) as described in Celik *et al.* (2008) and shown in Table 3-3.

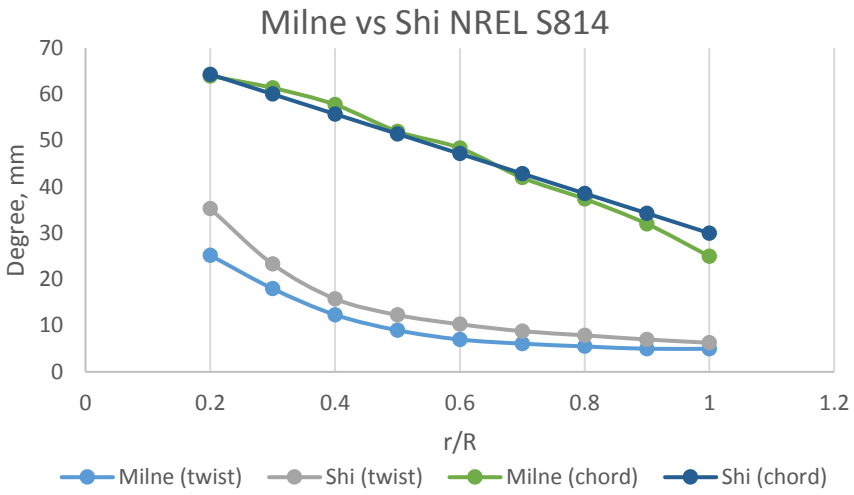

Figure 3-11 - Comparison of Twist (Degrees) and Chord (mm) to Previous Experiments Using NREL S814 Blade Section Details.

Table 3-3 – (a) GCI of Thrust (C_T) and Power Coefficient (C_P) of the Modelled Tidal Turbine and (b) Comparison to Previous Numerical and Experimental Investigations.

(a)

	Coefficients	
Mesh	**C_T**	**C_P**
Fine	0.709	0.353
Medium	0.698	0.336
Coarse	0.704	0.341
Extr.(Fine)	0.711	0.342
GCI (%, Med)	2.9	1.57
GCI (%, Fine)	2.5	3.12

(b)

	This Study Num/Exp	Shi (2013) Num/Exp	Milne (2013 / 2015)	Mycek (2014)
Blockage ratio	1.3 %	13 %	5 %	4.8%
C_P	0.34/0.43*	0.35 / 0.43	0.38 / 0.35	0.43
C_T	0.70/0.94*	0.72 / 0.95	0.77 / 0.56	0.79

*C_P calculated during experiment from Torque supplied by Motor, *C_T calculated using C_P and axial induction factor (Neary et al., 2013)

3.3.2 Blade Scale Flow

To validate the blade scale flow further, and with the limited experimental and numerical data available from previous studies, the pressure coefficient is compared to experiments conducted by Janiszewska *et al.* (1996) and qualitatively with the blade scale flow presented by Shi *et al.* (2013). The Numerically obtained blade scale flow is presented for different operating conditions (TSR = 5 for Shi *et al.* (2013)) in terms of velocity streamline and pressure field around the blade section at the reference section r/R = 0.7. The presented comparison of the pressure field around the blade in Figure 3-12 is performed based on the reasoning that the obtained power and thrust coefficient for the employed blade section show small variations between TSR 4 and 5. The colour scale used for the pressure field of this study shown in (a) covers the same range of pressure values and approximately corresponds to the colour-band used in (b). Agreement between the two pressure fields is reasonable considering the section in (b) is not operating at the same TSR which does not result in the highest power coefficient.

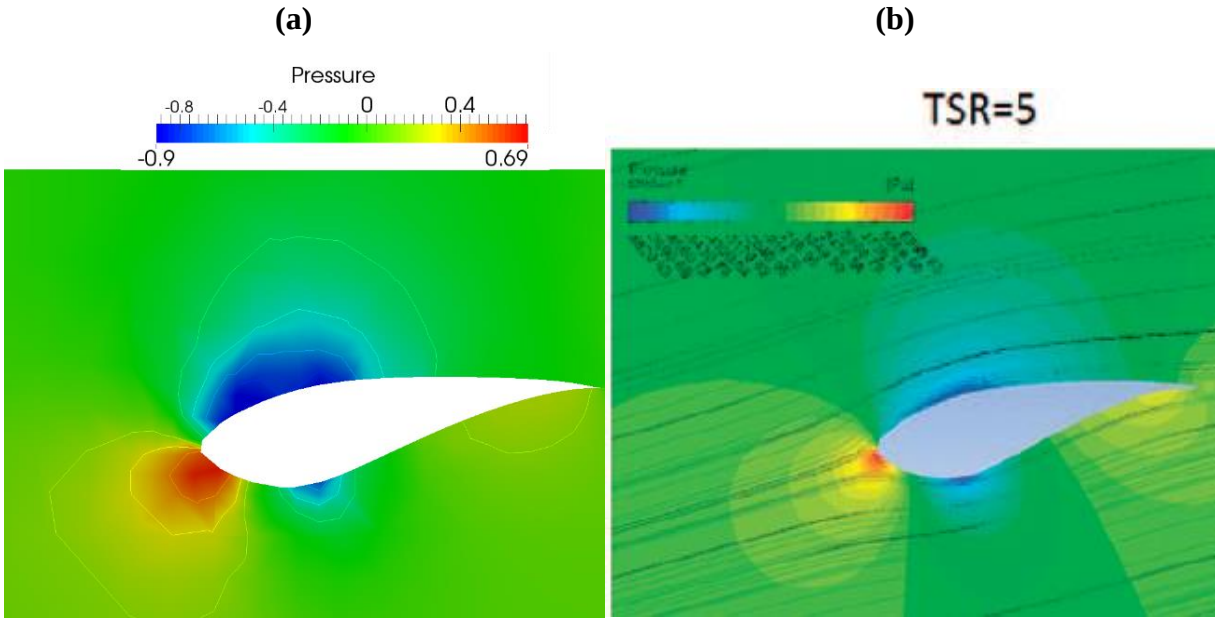

Figure 3-12 – (a) Pressure Over Blade at Reference Pitch Angle Location (r/R = 0.7) in this Study (at TSR 4) and (b) Pressure Contours Including Streamlines in Shi *et al.* (2013) using Identical Chord and Twist Distribution and Ambient Turbulence Levels. The Color Band is Closely Reproduced to Match between the Two Plots.

Due to the lack of experimental data at similar operating conditions in terms of ambient flow conditions, experimental data of the pressure coefficient for varying angles of attack in steady flow at increased Reynolds number by Janiszewska *et al.* (1996) is used to compare the pressure field around the blade for a rough surface NREL S814 airfoil. For comparison of the pressure coefficient calculated as in Liu *et al.* (2017), the resulting angle of attack of the tidal turbine blade has been calculated based on the procedure proposed by Johansen and Sørensen (2004), using the averaged flow field at the rotor plane to calculate the local angle of attack distribution along the twisted blade. Comparison of the pressure coefficient was then made where the experimental data presented by Janiszewska *et al.* (1996) presented data for the same angle of attack.

Following the procedure outlined, the resulting pressure coefficient at r/R = 0.67, corresponding to a local angle of attack of 8.1°, was compared between the numerical study and experiments. Both profiles are shown in Figure 3-13 and good agreement over most of the blade section profile can be seen with the numerical simulation showing slightly lower pressure coefficients on the top surface of the blade. Bearing in mind that experiments where conducted at steady inflow conditions with a constant blade profile along the blade radius, the transient numerical results are judged as agreeing well with the published data.

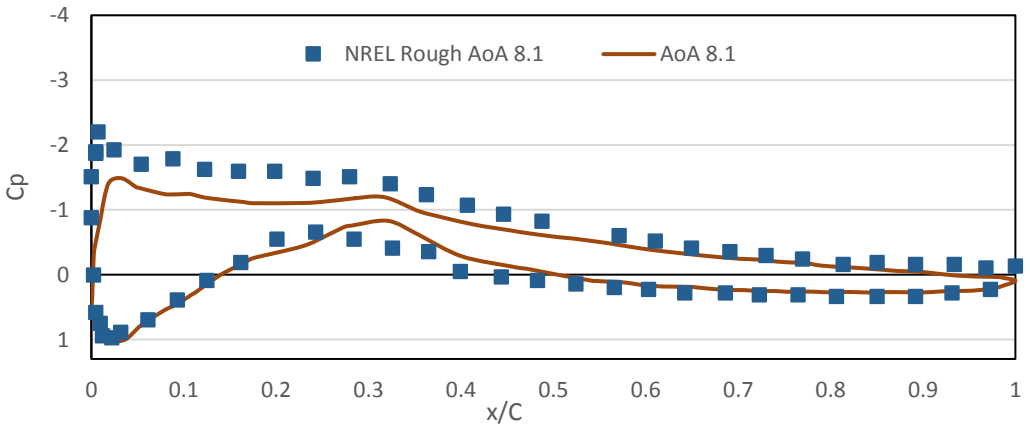

Figure 3-13 – Comparison of Pressure Coefficient at Angle of Attack of 8.1 Degrees from Janiszewska *et al.* (1996) Conducted with Steady Inflow and at Re = 750,000 (Box) with Numerical Results (Solid Line).

3.3.3 Arbitrary Mesh Interface (AMI)

Flow across the AMI boundaries is monitored to ensure the flow passes unaffected through the applied rotor stator interface. The interface is modelled as a cyclic boundary condition which passes information from the corresponding rotating cell to the overlapping cells of the stator interface. The instantaneous velocity components and pressure are monitored to ensure the flow across the cylindrical circumference is not adversely affected by the sliding motion of the interfaces. A plot of the flow variables passing through the rotating zone and AMI interface at half rotor radius off the centreline is shown in Figure 3-14.

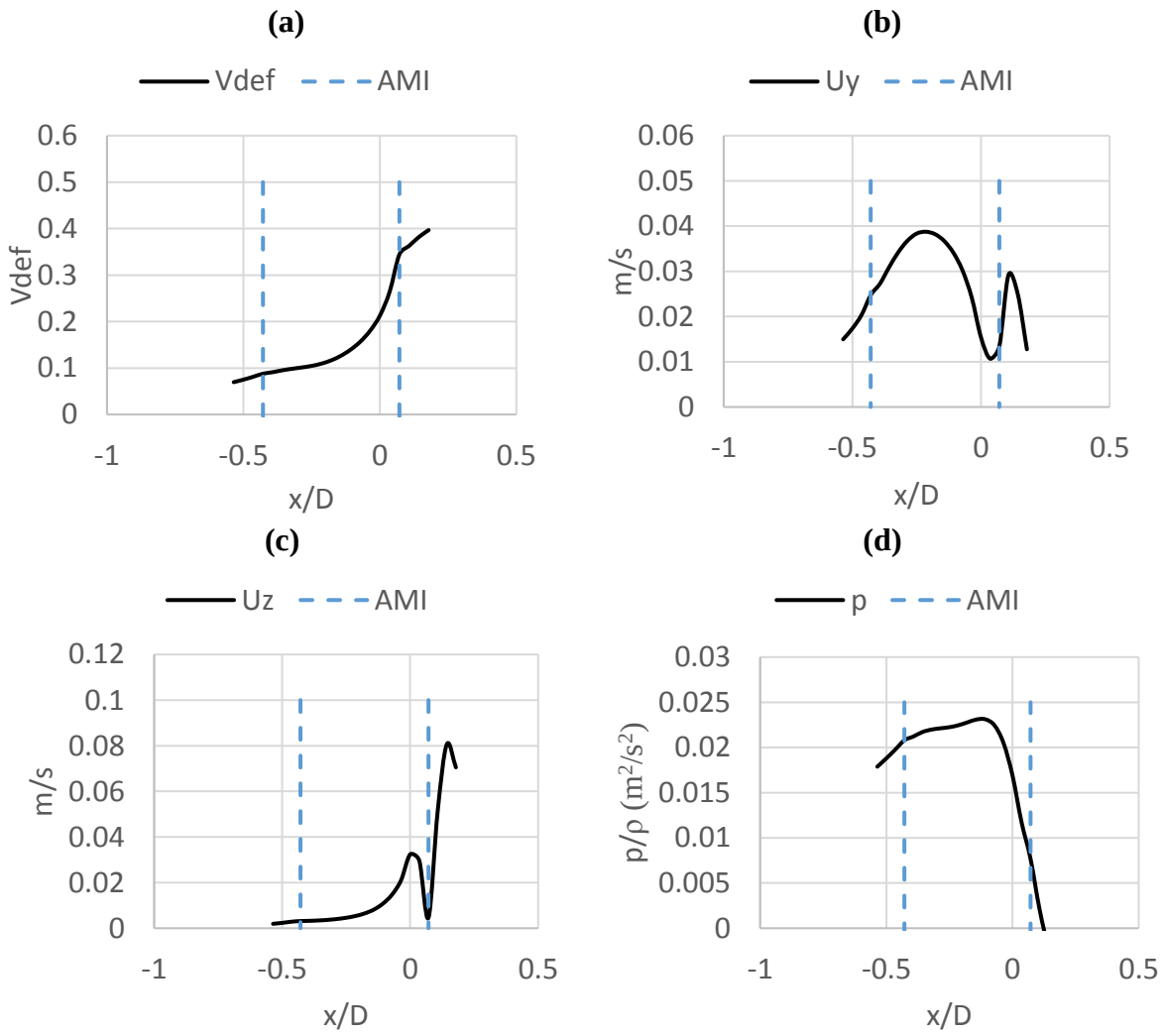

Figure 3-14 – At Half Radius (r/R = 0.5): (a) In-Stream Velocity Deficit (b) Transverse Velocity and (c) Vertical Velocity Component, (b) Pressure Evolution. Showing Flow Through Arbitrary Mesh Interface with the Upstream ($x < 0$) and Downstream ($x/D > 0$) Interface (Dashed Line).

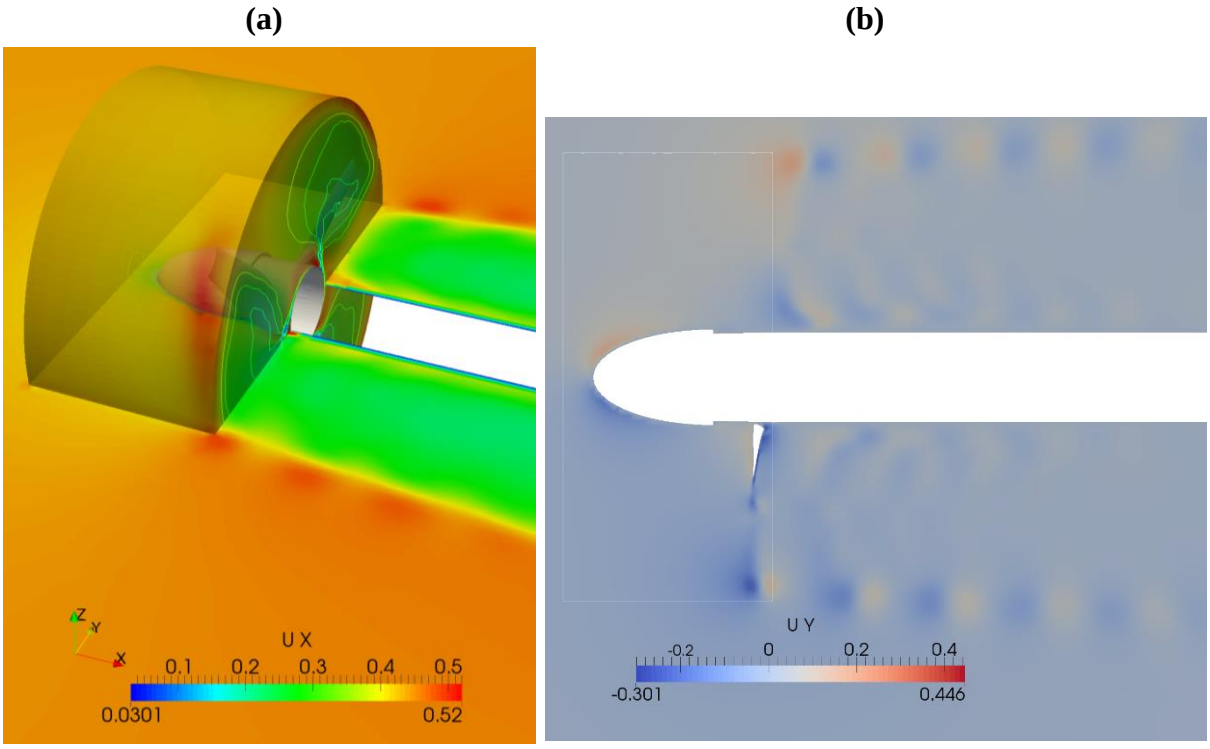

Figure 3-15 – (a) Stream-Wise Velocity Component at AMI Interface and Wake Downstream and in (b) Transverse Velocity Component at AMI Interface.

The influence of the sliding mesh interface on the wake and flow characteristics has been considered by investigating the resulting flow field for in-stream and transverse velocity component and their evolution through the AMI interface which is shown in Figure 3-15. It can be seen that the velocity components are not affected by the interface and flow features stemming from the blade rotation can be seen travelling through the interface without any imminent distortion.

Further indication of the flow field travelling through the sliding interface is provided by using higher order flow field visualisations such as Iso-Q surfaces (Figure 4-39) and normalised Reynolds Stresses (Figure 3-16) which show that the velocity field and its gradients pass through the interface without being disrupted as previously shown in McNaughton *et al.* (2014).

3.3.4 Flow Field Comparison

For comparison of wake characteristics to experiment, and study of mesh convergence, time averaging of all flow characteristics is performed at run-time for each time step (in the order of 1.5 to 3×10^{-3} seconds), this way the averaged data sampled here includes effects of all periodic fluctuations occurring at higher frequencies.

Error estimates for the wake velocity presented in Table 3-4, show similar trend to those presented for the wake downstream of an actuator disk modelled in combination with BEMT by Batten *et al.* (2013) between 4D and 10D, however a much higher GCI is observed at 6D and 7D. Since the calculated GCI values across the wake downstream of the turbine showed high numerical errors at some locations (6D - 9D) between the tested mesh configurations further investigations comparing the resulting flow field with previous experimental studies to investigate the possible cause of the high variations are presented. Similar differences in the turbulent flow field were identified by McNaughton (2013), highlighting as well that detailed description of mesh independence for the wake region of tidal stream turbine modelling has not been reported in great detail before. Thus, including a comparison with experiments will provide further insight into the mesh generation and independence for numerical investigations of tidal turbine array flow fields.

It is difficult to conduct systematic grid convergence studies of unstructured meshes, which is further amplified through the use of automatic mesh refinement applied in combination with transient simulations, which results in different flow field evolution thus affecting convergence observed at specific locations within the mesh. Hence, additional comparison of non-dimensionalised Reynolds shear stress maps, as defined in (3-23), is performed between the medium and fine mesh configuration and to experiments conducted at C_T = 0.79, C_P = 0.43 and TSR = 3.67 with ambient turbulence intensity of 3% by Mycek *et al.* (2014a) where detailed higher order flow characteristics have been presented for the near wake of a tidal turbine model. The experiments provide detailed flow field information at similar low ambient turbulence conditions, however with a different blade section profile, to investigate the approximate location of the merging of the upper and lower mixing layers.

Table 3-4 - Discretisation Error Estimation using GCI, Flow of 0.44m/s and TSR 4.

	Time-Averaged In-Stream Velocity Ux (m/s)								
	2D	**3D**	**4D**	**5D**	**6D**	**7D**	**8D**	**9D**	**10D**
Fine	0.0241	0.220	0.234	0.267	0.296	0.317	0.332	0.342	0.350
Medium	0.0254	0.211	0.211	0.231	0.262	0.290	0.312	0.327	0.339
Coarse	0.0245	0.235	0.220	0.232	0.248	0.265	0.280	0.293	0.303
Extrapolated (Fine)	0.0206	0.237	0.253	0.336	0.36	0.367	0.343	0.371	0.352
GCI (%, Med)	10.12	0.03	7.52	0.18	18.85	38	12.5	7.6	4.74
GCI (%, Fine)	1.42	0.19	10.4	1.54	25.9	25	4.2	1.73	0.66

$$R_{dim} = \sqrt{\frac{|\overline{u'w'}|}{(\bar{u}^2 + \bar{w}^2)}} \tag{3-23}$$

Figure 3-16 shows the interaction of the upper and lower mixing layer between 4D and 7D comparing well to those reported in experiments. By comparing the medium (top) and fine (bottom) mesh, it can be seen that the medium mesh shows good agreement with the fine mesh in most regions of the wake, more detailed mixing can be observed in the near wake of the fine mesh. Around 6D and 7D the shape of the mixing layers in the averaged contour plots shows more variations in the medium mesh than the fine mesh, which could be a reason for the varying GCI values obtained. Differences in resulting velocities between the two meshes are around 10% in the near wake reducing to 6% by 8D, however with a 100% increase in computation time for the fine mesh leading to an increase in simulation from 1900 to 3800 CPU hours to achieve a simulation time of 30 seconds for a single turbine.

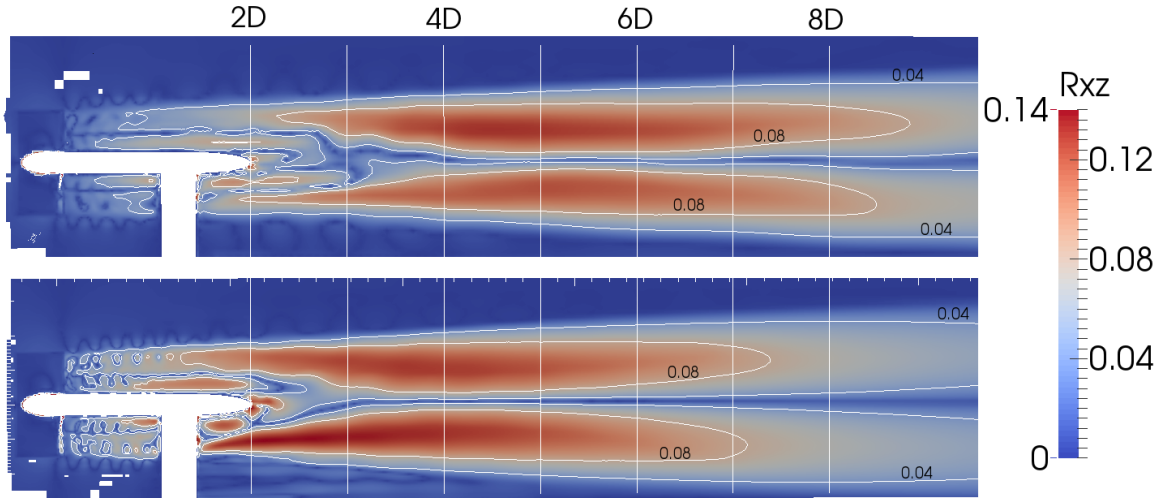

Figure 3-16 - Normalised Reynolds Shear Stress Map Comparison of Medium (Top) and Fine (Bottom) Mesh for the Evolution of the Mixing Layer Downstream of the Simulated Turbine.

3.3.5 Comparison with Experimental Wake Characteristics

Initial comparison between different mesh resolutions was performed at the lowest current velocity to give an indication of the convergence of velocity characteristics downstream of a single turbine. The instantaneous wake velocity at the centreline up to 10D downstream of the turbine is shown in Figure 3-17 for a simulation using 0.25m/s inflow current. The coarse mesh did not capture the area downstream of the turbine where upper and lower layer of the mesh merge, leading to a reduction of the centreline velocity as observed for the medium and fine mesh between 2.5D and 5D. For low current velocities, the velocity recovery between the fine and medium mesh is almost identical.

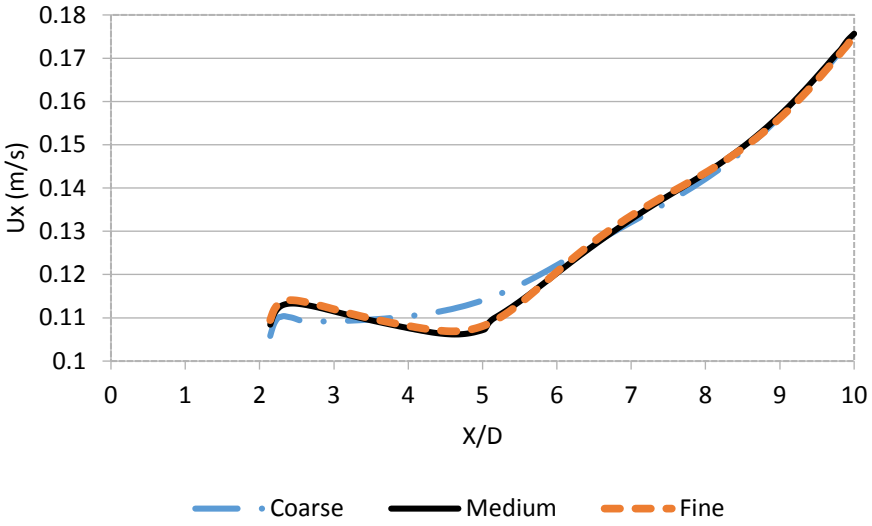

Figure 3-17 – Comparison Between Instantaneous Velocity Downstream of a Single Turbine for Different Mesh Resolution in the Wake of the Turbine at 0.25m/s Ambient Current Velocity.

The current velocity presented here represents the current used across the Flume and a Single turbine experiment conducted in the CWC for comparison of the wake between the two different facilities, including differing water depth and distances to bounding surfaces. A separate comparison was conducted for the array cases and is presented in the following.

The mesh configuration for turbine structure and flow domain for the CWC array simulations was investigated by comparing the time-averaged in-stream velocity at different downstream stations along the rotor centreline to the values recorded in the experimental study as shown in Figure 3-18. Improved wall modelling led to all mesh configurations showing a stagnating or reducing velocity in the near wake downstream of the turbine nacelle compared to the low current velocity case. Comparison to experimentally measured flow values shows the medium and fine mesh have best agreement along the wake centreline. The experimental velocity recordings are within less than 10% difference to the numerical values obtained during the mesh sensitivity study. The fine mesh approximately over predicts the wake recovery by 8% through the wake region tested. The medium mesh under predicts the recovery up to 7D (1.96m) downstream of the turbine and slightly over predicts in-stream velocity component thereafter. The rate of recovery between fine, medium mesh and the experiments are showing good agreement, especially from 7D downstream.

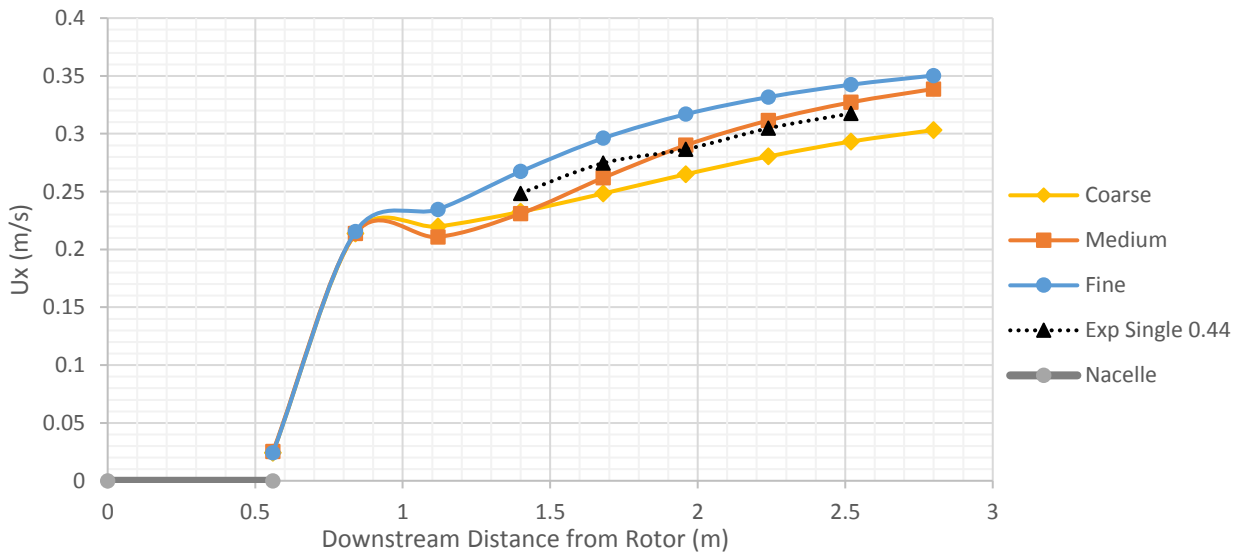

Figure 3-18 - Time Averaged Numerical vs Time Averaged Experiment Data for In-Stream Velocity Component Comparison across a Number of Meshes with Varying Resolution for Ambient Flow of 0.44m/s.

3.3.6 Further Remarks on Numerical Model Validation

Convergence and agreement with previous studies of the performance characteristics (C_T & C_P) gives confidence in the applied rotor mesh resolution as well as the wall modelling applied to avoid very small cells around the rotating turbine blades. The blade scale flow has been shown to be resolved with a good degree of accuracy by comparing qualitatively the pressure field around the blade sections from previous numerical investigations and additionally the pressure coefficient at a local angle of attack with that obtained from experiments. Comparison is made and agreement is achieved over most of the blade section, however some of the differences may be accounted for by the differing ambient flow and test conditions within the experiments where a constant blade section was used in steady flow, while the simulations see the blade section rotating and only a specific section of the blade corresponds to the angle of attack used for comparison.

The near wake resolution shows highest variations between the different mesh configurations and is affected by the resolution immediately downstream of the turbine as can be seen Figure 3-16. Previous tidal turbine modelling McNaughton (2013) has reported similar trends of convergence, especially for turbulence characteristics, throughout tidal turbine mesh domain and the inclusion of experimentally measured wake characteristics gives additional confidence in the mesh being sufficiently resolved for the investigations presented herein. With increasing distance from the turbine, the mesh characteristics in terms of velocity converge between the experiment and the two finest mesh resolutions. The velocity and higher order flow statistics such as the Reynolds stresses presented previously are within 10% between the medium and fine mesh configurations while the increase in computational time was almost 100%.

Based on the presented investigation and discussion, the medium mesh is chosen to reduce the computational cost when applying the mesh settings on full array configurations with four individual turbines where domain sizes varied from 1.5 million to 4.2 million cells, with closer transverse spacing leading to higher number of cells during the automated mesh generation. Experimental measurements are judged to provide sufficient accuracy by showing flow velocities within 2% - 5% of those expected in the newly calibrated CWC test facility.

The presented validation highlights the difficulties of determining optimum grid resolution with automated unstructured mesh generation especially in combination with transient mesh motion as a large simulated time period is needed before comparisons can be made, allowing for the flow to travel through the entire domain beforehand as previously reported in McNaughton (2013). This results in inherently different flow fields downstream of the turbine which affect the grid sensitivity study.

Further improvements to the numerical modelling in terms of boundary conditions and numerical schemes resulted in improved agreement with the experiments as will be shown in Chapter 4. Comparison with experimental measurements presented in this section and further in Section 4.2.1 show good agreement of the main wake flow, however the near wake modelling close to the rotor and support structure requires further investigation.

Chapter 4. Results and Discussion

This chapter presents the wake characterisation of tidal turbines for a number of configurations across two different experimental facilities, namely the CWC described in 2.3.1 and the WWC Flume introduced in 2.3.2 as well as the results of the numerical investigation for the corresponding array configurations of the CWC. Wake characterisation for a single turbine is presented for a low (2%) and high (10%) ambient turbulence and velocity deficits are presented throughout the wake domain up to 20D downstream.

Wake characterisation is presented mainly in terms of the measured velocity deficit in Equation (1-8) and the turbulence intensity defined in Equation (1-9) for three-dimensional flow. For all cases presented herein, the velocity deficit is defined with the upstream ambient flow. For multiple turbine configurations this means the velocity deficit is not specified with respect to the actual turbine inflow velocity as this could not be measured while conducting the experiments but with reference to the flow velocity upstream of the initial turbine. For the WWC Flume experiments, the location of the second turbine was decided after monitoring of the resulting wake downstream of a single turbine and turbines were placed where the flow was recovered to about 90% of the free stream velocity.

The downstream distance for array configurations tested in the CWC remained constant for all tests thus the changes in wake recovery downstream of the array are attributed to the effects of longitudinal and transverse spacing of the second row of turbines.

Firstly, the wake characteristics of an isolated tidal turbine and up to three tidal turbines in axially aligned configurations with varying downstream spacings are presented for flow with close proximity to bounding surfaces at higher turbulence intensities. Additionally a brief investigation of the effects of surface waves on the wake recovery is presented for an isolated turbine in the WWC flume.

Secondly, the centreline wake characteristics for single and multiple turbine array arrangements in the low ambient turbulence intensity CWC are presented and compared between numerical and experimental investigation for validation of the numerical method and characterisation of the array wakes (see also Nuernberg and Tao (2016) and Nuernberg and Tao (2017, Submitted for Publication)). The effect of varying longitudinal and transverse spacing in a staggered array arrangement is investigated through the velocity recovery and turbulence intensities within the

array and downstream of the array section containing four tidal turbines. Further investigation of the resulting flow field in tidal turbine arrays based on the PIV measurements are presented to highlight some of the advantages and disadvantages of non-intrusive flow field measurements.

Finally, further numerical investigation of the complex flow fields within and downstream of the array sections is presented based on the three-dimensional numerical simulations that have been conducted. Detailed information on the velocity and turbulence intensities within the flow field is presented in addition to further investigation of the resulting flow field (Nuernberg and Tao (2017)) furthermore, two numerical methods for the simulation of turbulent flow ($k - \omega$ SST and RSM closure models) in tidal turbine arrays have been compared.

4.1 Wind Wave Current Flume Experiments

Experiments with an isolated turbine and multiple turbine configurations with up to three turbines axially aligned have been conducted in the long wind wave current flume (Section 2.3.2 at an ambient flow velocity of 0.275m/s and turbulence intensity of approximately 10%. The wake velocity characteristics are presented herein and compared among the different experimental conditions to investigate the effect of inter-device spacing on the velocity recovery downstream of multiple tidal turbines. Measurements have been conducted on top of the nacelle for rotor plane and 1D downstream distances and at the rotor centerline for a wide range of locations throughout the wake up to 20D downstream of the rotor. Vertical profiles of the velocity characteristics are presented for the wake of the single turbine configuration.

4.1.1 Single Turbine Wake Characterisation

The wake recovery towards ambient current velocities is shown by the velocity deficit for the wake of a single turbine in Figure 4-1. Wake recovery is accelerated in the near wake downstream of the turbine with a rapid decrease of velocity deficit shown between 2D and 4D. A deficit of 86% is measured indicating stagnating flow due to the presence of the rotor and nacelle. The recovery further downstream shows a rapid decrease in the velocity deficit from about 60% at 3D to 18% at 8D. From 12D to 20D the velocity recovery slows down and the hub height deficit remains at 5% at 20D downstream of the turbine rotor.

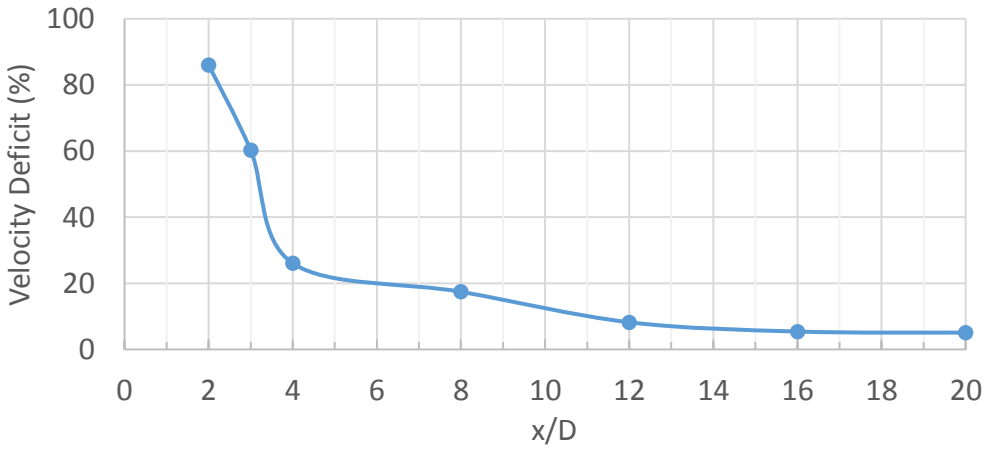

Figure 4-1 - Wake Velocity Deficit for Single Turbine in Flume with U_∞= 0.275m/s and Ti = 10%.

The wake velocity deficit characteristics are comparable to those reported in other studies with similar ambient turbulence conditions. Actuator disk experiments by Bahaj and Myers (2003) with an ambient turbulence of about 8% and thrust coefficients comparable to those achieved by the turbine design used in this study ($C_T \approx 0.9$), showed higher velocity deficits persisting further in the near wake from approximately 60% at 3D to 40% at 5D, but similar deficits are reported from 10D downstream of the turbine with 15% at 10D down to between 7-13% at 20D. The accelerated near wake recovery could thus be attributed to the inclusion of the turbine structure and blades specifically, compared to the actuator disk modelling with porous mesh disk, especially the introduction of blade induced turbulence. Experiments with an ambient turbulent intensity of 10% - 12% by Stallard *et al.* (2013) and Stallard *et al.* (2015) conducted in a wide flume showed velocity deficits in the near wake of 40% at 4D recovering to 20% at 10D and 12% at 20D downstream of the turbine. Here the vertical blockage was smaller (depth to diameter of 1.67D) while the cross sectional blockage ratio was only 2.5%.

Vertical velocity deficit profiles of the single turbine wake for a number of positions are presented in Figure 4-2. The vertical profiles have been merged from three overlapping, individual time averaged flow measurements taken across the height of the WWC Flume. Some areas, where calculation of the local flow vectors was affected by reflection of laser light from the floor of the test section, the turbine structure and the free surface have been removed and are excluded from the plots. The accelerated flow between the upper part of the wake and the free surface can be seen through the negative velocity deficit above 0.75 z/D. Towards the test section floor the velocity deficit increases up to a maximum of 0.8 within the domain where calculation of flow vectors was possible.

Close to the turbine structure the wake shows slower flow on the lower part of the rotor (z/D < 0), this is attributed to the additional wake of the turbine support structure influencing the rotor wake as well as the free stream shear. The recovery of the wake shows that by 12D the maximum deficit is located approximately 0.25D below the rotor axis which is an increase in velocity deficit at this particular height compared to 8D indicating a vertical shift downwards of the slowest part of the wake. This shift of the wake downwards is most likely caused by the increased flow velocities above the turbine and the slower moving fluid on the lower part of the wake. In addition to the rotor wake and the velocity shear in the ambient flow, the wake of the support structure influences the wake recovery on the lower part of the wake.

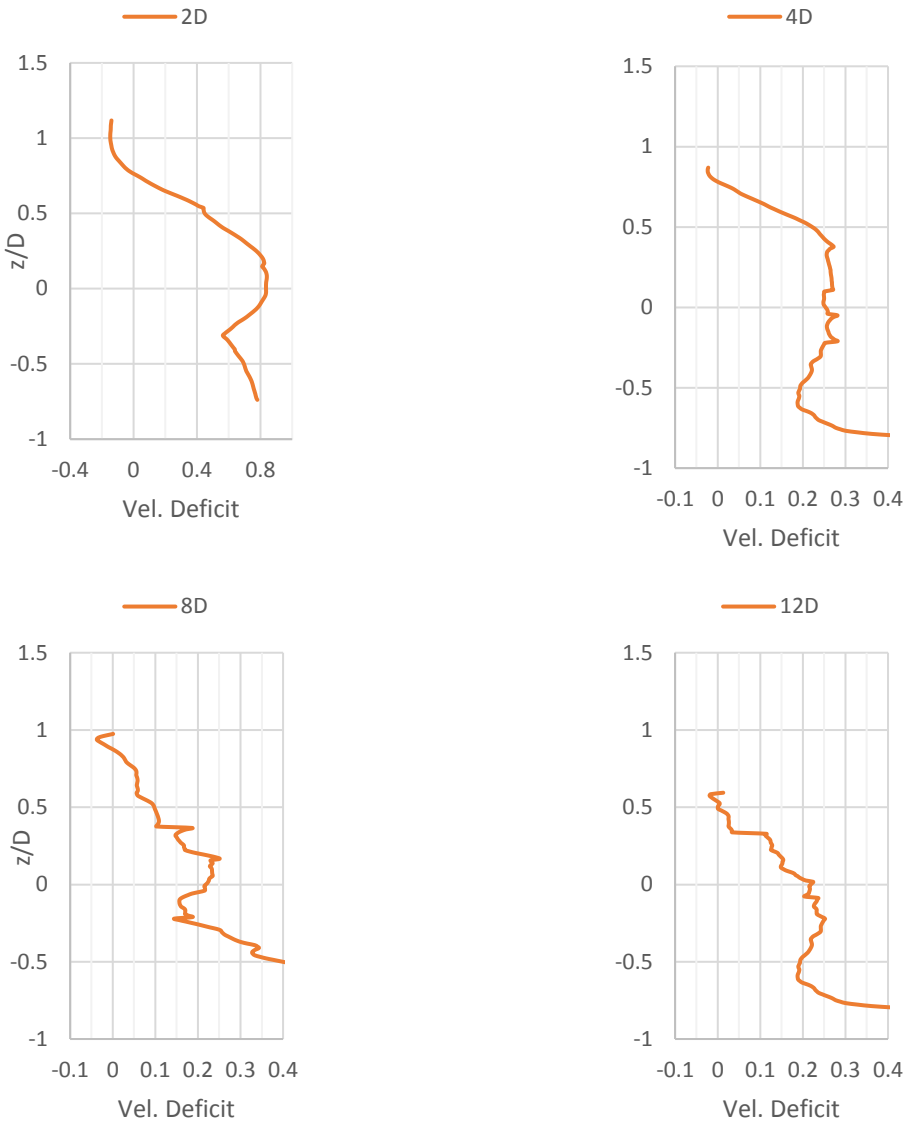

Figure 4-2 – Single Turbine Wake Velocity Deficit Profiles from WWC Flume Experiments.

Investigation of the flow around the tidal turbine rotor from the obtained PIV measurements is shown in Figure 4-3. From the instantaneous flow field recordings shown in (a) - (d), it can be seen how the passing blade, at the top position in (b) leads to an area of very slow moving directly behind the rotor blade and an area of increased flow velocity above it. With the blade passing further (c), the ambient flow travels through at the centreline (d) and an area of flow of ambient velocity can be observed between the next turbine blade and the slow wake downstream (a).

The time averaged flow field in (e) clearly shows the area of very slow moving fluid downstream of the blade, at the top position perpendicular to the nacelle and the accelerated flow above the turbine wake. In all of the presented flow field contours, a layer of undisturbed flow is recorded to flow between the turbine hub and the blades. This could not be recorded further downstream where the laser sheet leads to strong reflections on the upper part of the nacelle, thus explaining the increased layer of slow moving fluid in the downstream flow. The area upstream of the rotor where ambient flow is slightly slowed down before being accelerated and diverted around the turbine is also seen. In Figure 4-3 (e) the expansion of the wake and mixing with the ambient flow on the top part of the wake can be observed as well as the shear layer expanding towards the wake centreline. Wake expansion occurs shortly downstream of the rotor plane but appears to be very limited in this case with close proximity to the free surface as the wake extent remains approximately constant in the area where the ambient flow is accelerated.

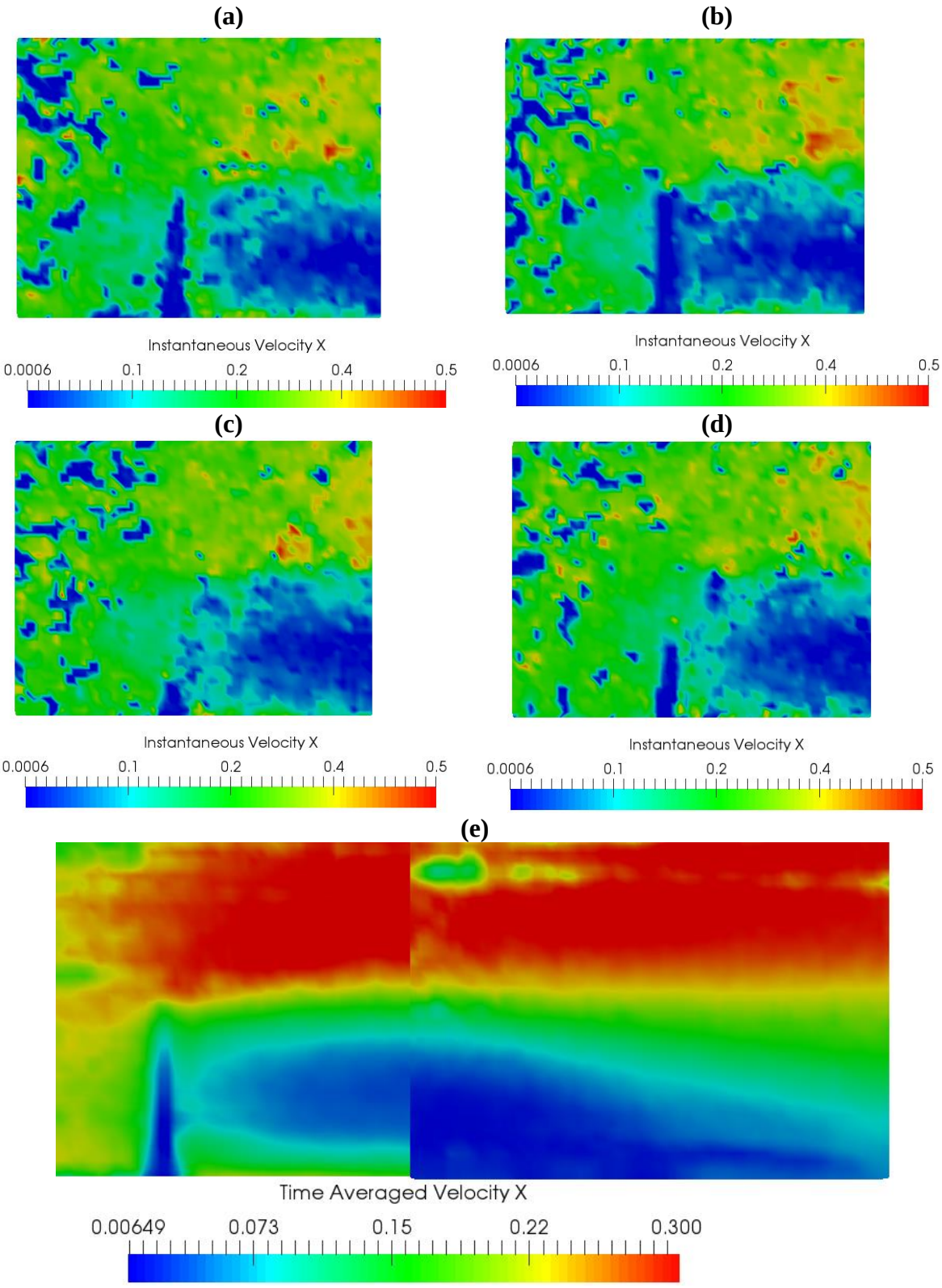

Figure 4-3 - Flow Past Tidal Turbine Rotor in WWC Flume with the Rotor Blade Position Visible in the Centre Showing (a) - (d) Snapshots of Instantaneous Flow as the Turbine Rotates and (e) the Time Averaged Flow Field around the Rotor from Two Measurement Locations Combined.

4.1.2 Axially Aligned Turbines

Additional configurations have been tested with two to three turbines placed in the WWC flume at the same time. The test included two configurations with two turbines with a downstream spacing of 12D and 16D, named as T2 12D and T2 16D respectively, and three turbines arranged with a spacing between turbine one and two of 16D and 12D between the second and third turbine (3T). An additional test was conducted to investigate the wake evolution with surface waves present (Wave) for which further insights of the resulting flow field are presented in Section 4.1.3.

Wake measurements were conducted for the downstream turbine and the resulting wakes are used to investigate the wake recovery for turbines operating axially aligned downstream of another turbine. The centreline wake recovery is shown as well as vertical profiles across the turbine diameter downstream of the turbine to compare the evolution of the centre part of the wake with different configurations of turbines being located upstream of the tested turbine.

From the obtained wake characteristics in Figure 4-4, it can be seen that the differences between all formations tested here are small but most significant between 2D - 5D. The single turbine configuration shows the highest velocity deficit remaining at 20D at approximately 5% while for the three turbine and wave test cases the centreline velocity has virtually recovered to ambient flow velocities at 20D. For higher ambient turbulence intensity flow such as the 10% turbulence in the approach flow in the flume, small variations for the wake recovery for two turbines have been recorded previously by Mycek *et al.* (2014b) with ambient turbulent intensities of 15%. Wake characteristics were presented up to 10D downstream of the downstream turbine and showed remaining velocity deficit of approximately 7.5% at 10D when calculated using the upstream ambient flow velocity. The most pronounced differences can be seen in the near wake of the turbine between 3D and 6D with a maximum difference of 25% between the three turbine wake recovery and the single turbine wake recovery at 3D. From 12D downstream the differences between the multi-turbine configurations are very small with all tests showing a velocity deficit of less than 10% at 12D.

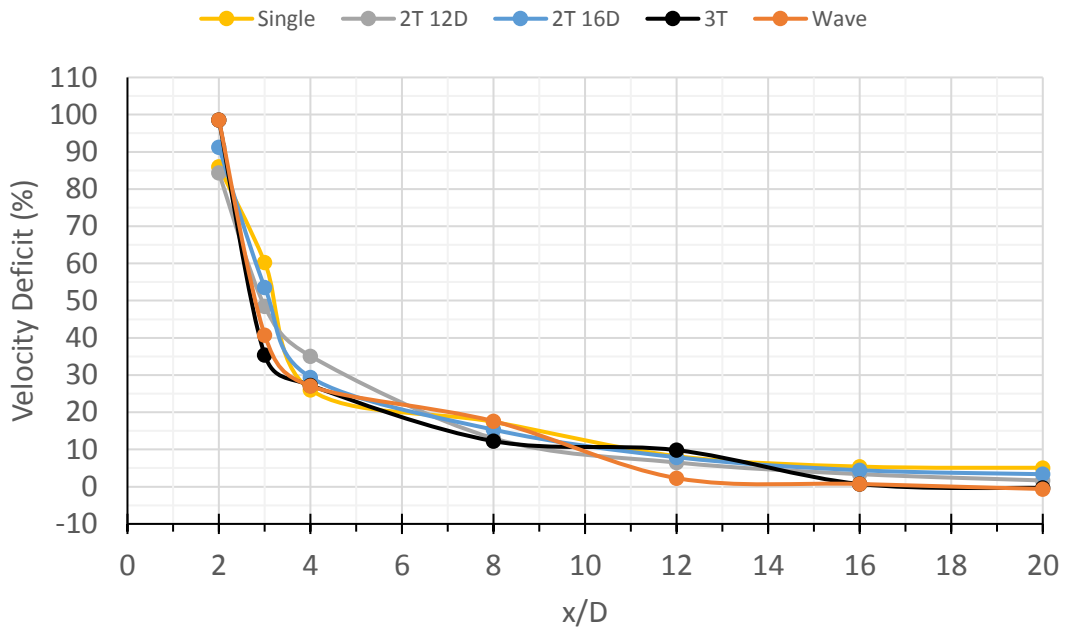

Figure 4-4 – Comparison of Wake Velocity Deficit for Single and Multiple Axially Aligned Turbine Arrangements in the Wake of the Downstream Turbine.

The vertical profiles shown in Figure 4-5 compare the wake recovery at the centre part of the wake ($-0.5 < z/D < 0.5$) among all tested multiple turbine experiments. Immediately behind the turbine nacelle, all experiment configurations show very similar velocity deficits between 85% and 95% and a vertical distribution that is very similar across all tests, indicating the flow at this position to be dominated by effects of the rotor and support structure.

At 3D downstream, the vertical profile shows a higher degree of asymmetry in the wake recovery for the single turbine wake while the recovery behind the rotor is quite constant across the rotor plane for all multiple turbine and wave experiments. Between 8D and 20D the wake for all configuration recover gradually with the 3T and Wave showing lowest velocity deficits.

At 20D the upper part of the wake domain ($0.2 < z/D < 0.4$) shows a lower deficit for the single turbine than for the 2T 16D configuration. This may be a result of the single turbine wake recovery being largely a function of the ambient flow being directed above the turbine. For the 2T 16D case, the wake of the upstream turbine is expected to have spread vertically, and higher turbulence inflow is expected for the downstream turbine which results in a wake recovery that is less dominated by the mixing with the accelerated flow between the turbine tip and the free surface and thus shows a more constant profile across the rotor plane.

With increasing distance downstream, wake recovery of the lower part of the wake is improved for the higher turbulent flow conditions involving 3 turbines axially aligned than for the two turbine cases and the single turbine. At 20D the profiles for 3T and Wave show fully recovered flow velocities on the lower part of the wake where $z/D < 0$ and small flow accelerations on the upper part, whereas for 2T configurations the velocity deficit is between 3% and 10% and for a single turbine reaches up to 15%.

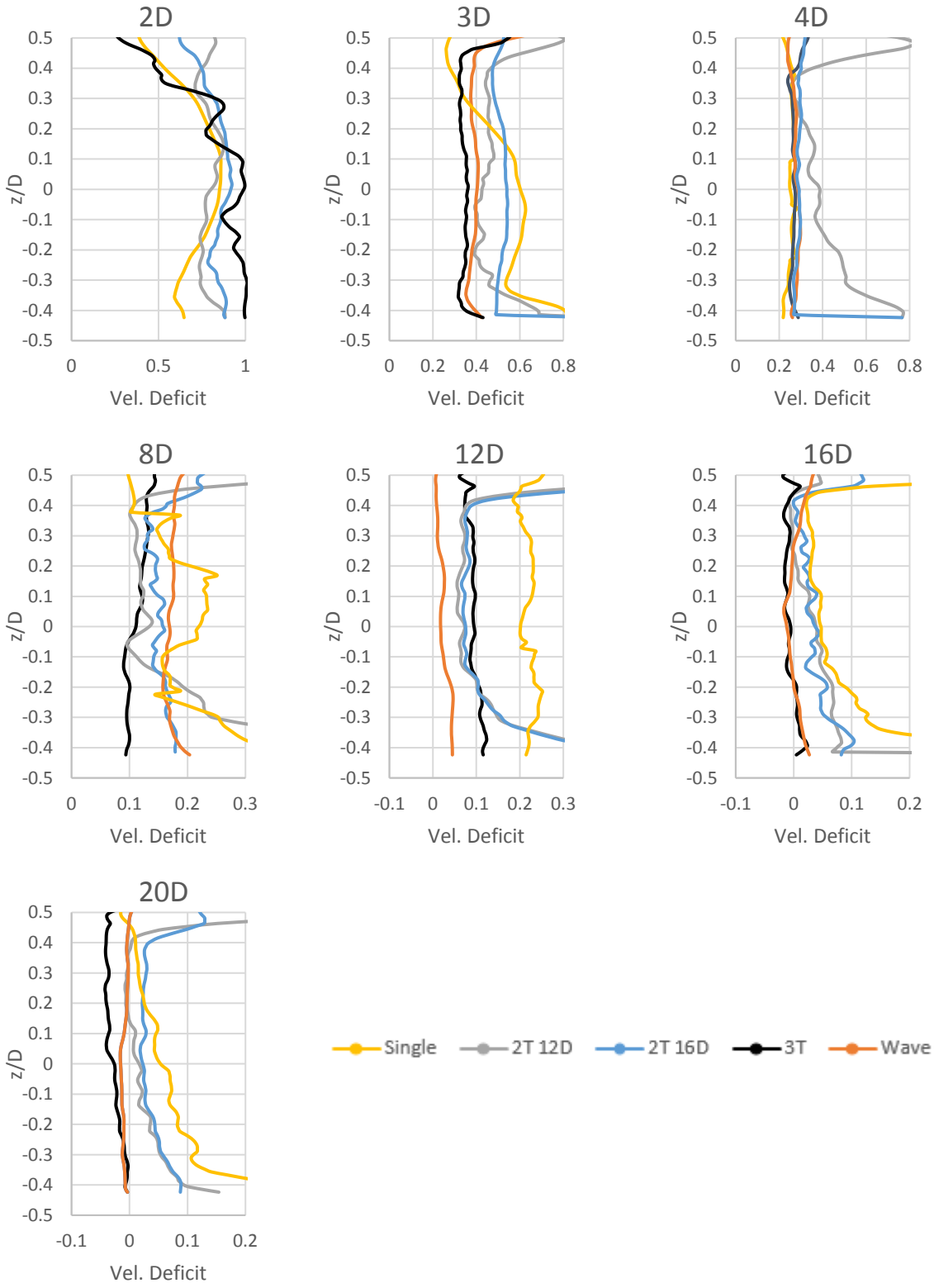

Figure 4-5 – Vertical Profiles of Velocity Deficit Comparison Across the Rotor Height at Several Positions in the Wake of the Downstream Turbine.

4.1.3 Proximity to Waves

The influence of ambient waves on the centreline velocity deficit is shown to be small in Figure 4-4. Wake recovery at the centreline and across the rotor height has been shown to be similar to the 3T in Figure 4-5 for the near and far wake, however differences are observed between 8D and 12D where the recovery is accelerated for the Wave case. Recovery of the velocity is similar to the multiple turbine arrangements but a lower velocity deficit remains at 20D downstream for the 3T configuration, especially on the top half of the wake, the lower half of the wake shows similar remaining deficits. To further investigate the velocity deficit under influence of surface waves, instantaneous flow field recordings above the turbine nacelle, at 0D to 2D downstream of the turbine have been conducted. The time averaged flow field over the nacelle is shown in Figure 4-6 and instantaneous as well as time averaged velocity contours and streamlines at 2D downstream are shown in Figure 4-7.

The time averaged wake shows slightly increased wake expansion towards the free surface and a further distance downstream of the rotor where the extremely slow moving fluid behind the rotor shifts towards the wake centre. A small area of accelerated flow can be seen between the turbine nacelle and blade section with increased in-stream flow velocities.

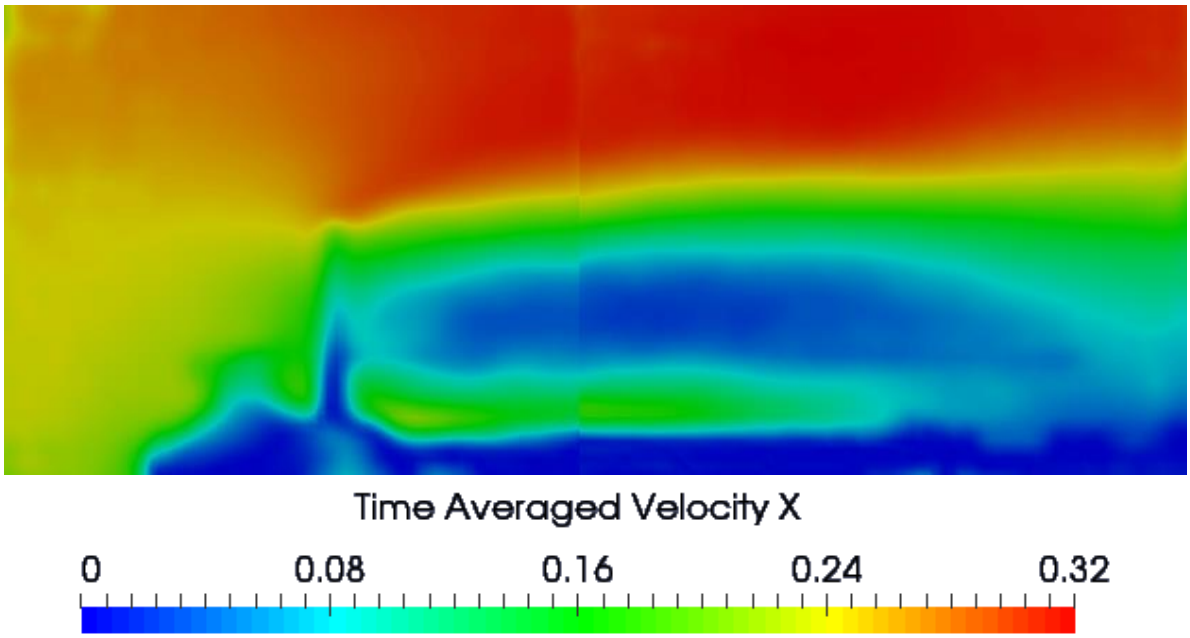

Figure 4-6 - Time Averaged and Merged Flow Field on Top of Turbine Nacelle for Wave Experiment.

From the recordings in Figure 4-7, it can be clearly seen how the surface waves influence the wake behaviour above the turbine nacelle, just downstream of the rotor, by comparing the flow field of a turbine operating without waves (left) with the resulting flow field when waves are passing over the turbine (right).

The velocity contours and streamlines in Figure 4-7 show that the wave passing over the wake leads to the slow moving fluid within the wake being moved upwards and downwards depending on the position of the wave. The streamlines and velocity contours for the single turbine without waves show a more constant flow field at the position investigated, indicating a small extent of downward moving flow. The time averaged flow field results in a wider spread of the area of slowest flow downstream of the turbine nacelle while the combined current and wave also lead to increased flow velocities in the wave experiment near the surface of the Flume.

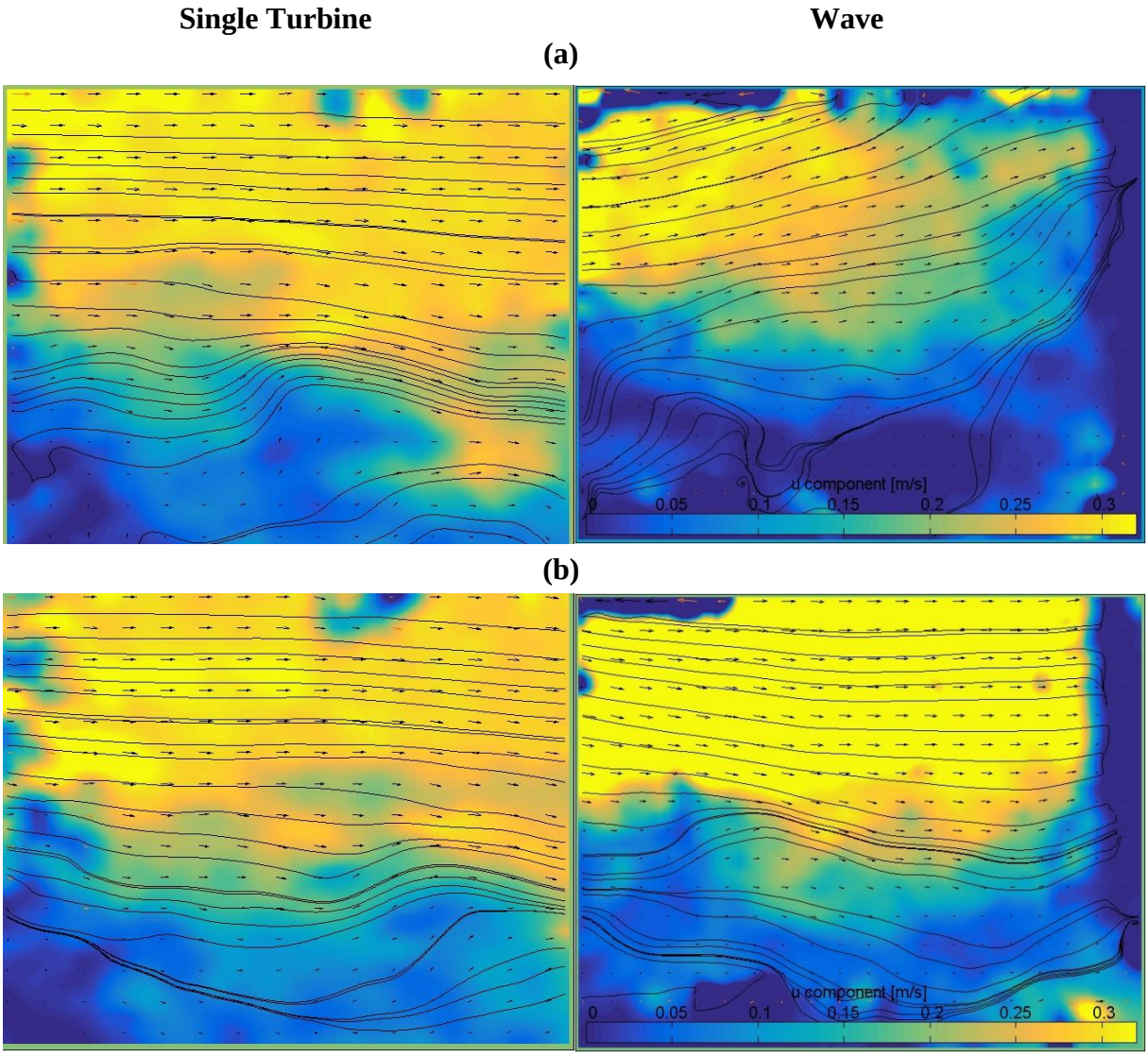

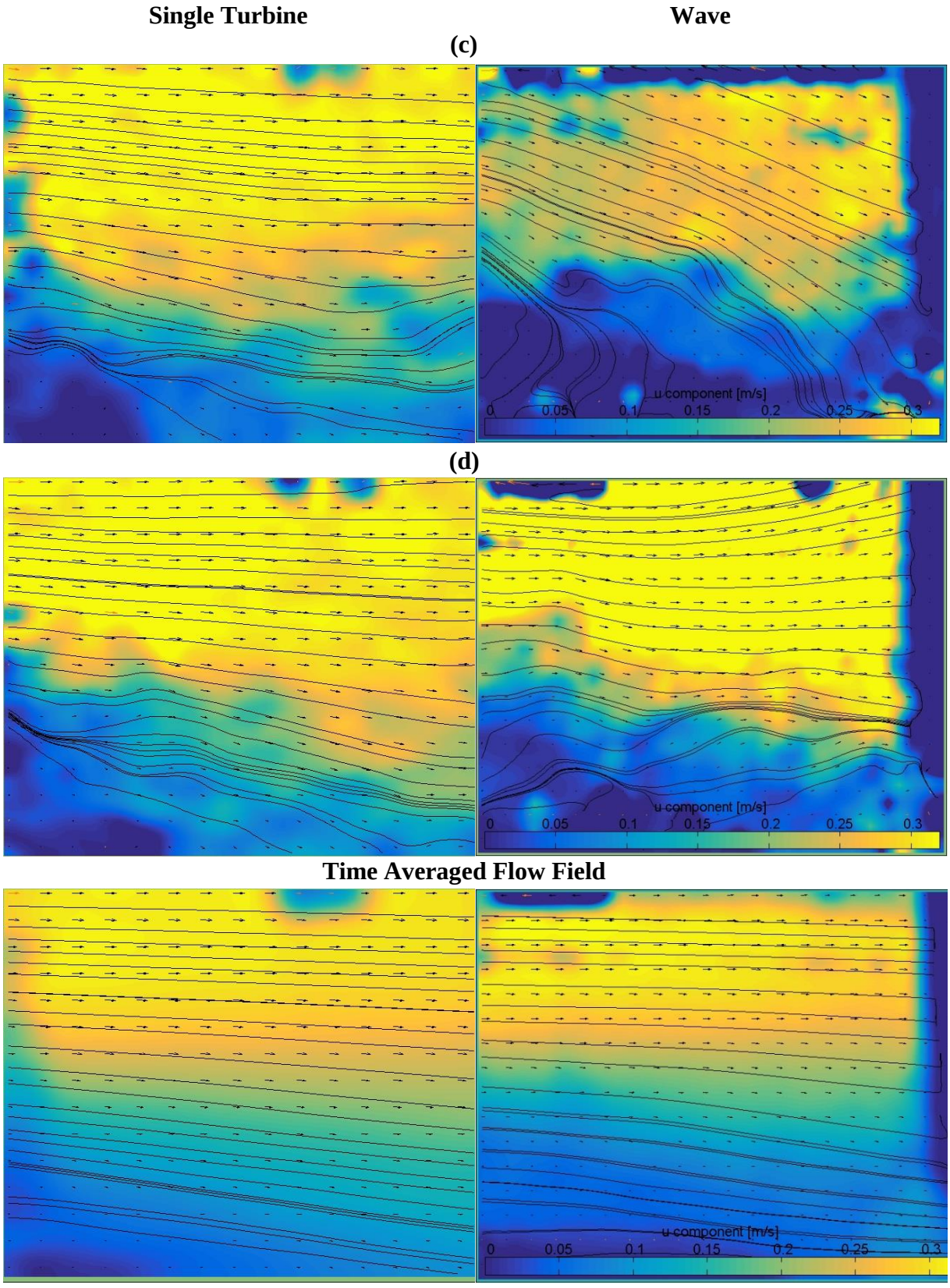

Figure 4-7 – Comparison of the Instantaneous and Time Averaged Flow Fields 2D Downstream of the Turbine Rotor for Ambient Flow without Waves (Single Turbine) and with Ambient Waves (Wave) Showing the Influence of Waves Passing Over the Wake Area.

4.1.4 Summary of Experimental Study in WWC Flume

Wake velocity deficits are presented for a number of experiments conducted at 10% ambient turbulence intensity in a flume of water depth two times the turbine diameter. Wake characterisation was performed primarily for comparison to array studies and to investigate the effects of turbine spacing when axially aligned. Turbine performance has not been investigated experimentally due to the focus on wake development and characteristics of the turbine with near constant thrust coefficients across a wide range of operating conditions.

The single turbine wake velocity deficit is shown for up to 20D downstream of the turbine and shows that:

- Accelerated wake recovery is observed at higher ambient turbulence intensity and small deficits of about 5% remain at 20D.
- Vertical shifts in the velocity deficits have been observed and are attributed to the sheared velocity profile and increased flow velocities between the rotor top and free surface.
- Surface waves influence the flow field on the upper half of the wake, while the centreline wake recovery shows little change. Insignificant velocity deficits remain at 20D thus implying that improved recovery is observed.

In-line downstream spacings of 12D and 16D were tested for two and three turbine configurations. Comparison with the wake characteristics downstream of the downstream turbine for arrangements of up to 3 turbines axially aligned showed little differences among all configurations tested. The measurements revealed:

- Initial wake recovery is increased for three turbine arrangement and two turbines where the inter-device spacing upstream of the last turbine is 12D suggesting the higher turbulence in the wake aids faster recovery in the wake of the downstream turbine.
- Far wake recovery shows lower velocity deficits for all multiple turbine arrangements than for the single turbine.
- The closer spacing of 12D in both two and three turbine arrangement and ambient wave tests showed the smallest wake deficits and fastest wake recovery through most of the domain.

4.2 CWC Experimental and Numerical Results

This section presents a comparison between the experimentally and numerically obtained wake characterstics for a single turbine and array configurations as well as the experimetal wake characterisation of a three turbine configuration in the CWC. This is followed by further investigation of the array flow field from the experiments by presenting the resulting wake field contours obtained from the PIV measurements.

Results are presented using the velocity vectors obtained from the PIV analysis and calculated 2-dimensional turbulence intensity (3D Turbulence Intensity shown in Equation (1-9) along the wake centreline. The axial wake velocity deficit defined in Equation (1-8) is used for single turbine, 3 turbine and all array experiments. The velocity deficit is also used for turbine arrays to compare the reduction and recovery of the flow velocity within the wake with reference to the entire array section and the undisturbed upstream flow. The inflow conditions upstream of the array are used for determining operating conditions of multiple in-line arranged turbines as applied in Mycek *et al.* (2014b), hence describing the overall array behaviour and thus showing increased velocity deficits within the wake of the downstream turbine. Trends in the velocity deficit recovery however will reflect the local flow re-energisation within the wake of downstream turbines. The velocity deficit shown downstream of the array thus represents the resulting array wake of the tested section.

This notation does also affect the actual TSR the downstream turbine is run at, which will be increased due to being located in the wake of the upstream turbine thus experiencing flow of reduced velocity. The selected airfoil sections as described earlier and pitch degree of 8.33° have been shown to have small variations in the turbine performance across a range of operating conditions with a C_P exceeding 0.4 for TSR ranging from 2.8 to 4.75 and exceeding 0.3 up to a TSR of 6. C_T is remaining virtually constant between TSR 4 -7 (Shi *et al.*, 2013; Shi *et al.*, 2017) which lies within the expected TSR for the downstream turbine when operating in the wake of the upstream turbine for the configurations tested in this study.

For all measurements in the CWC, between 9D and 14D no data was recorded during the experiment due to obstruction of the PIV equipment by a steel frame between the observation windows of the test section. Furthermore, for all array tests where the centreline measurements were taken at the position of the second row (at 3D and 5D downstream respectively) no measurements could be obtained for the close transverse spacing of 1.5D in the PIV due to the

presence of the tidal turbine model as discussed in Section 2.3.1. No data is obtained in the numerical simulation between 0D and 2D as well as 11.5D and 14D due to the location of the upstream and downstream turbine nacelle respectively.

4.2.1 Single Turbine Wake

Prior to assessing the wake within an array of four tidal turbines, a single turbine has been tested in a range of currents with a constant TSR. The centreline axial wake velocity deficit for a single turbine model operating at three different current settings in the CWC with ambient turbulence intensity of 2% is shown in Figure 4-8, including a comparison to the wake recovery as measured in the WWC Flume with ambient turbulence intensity of 10%.

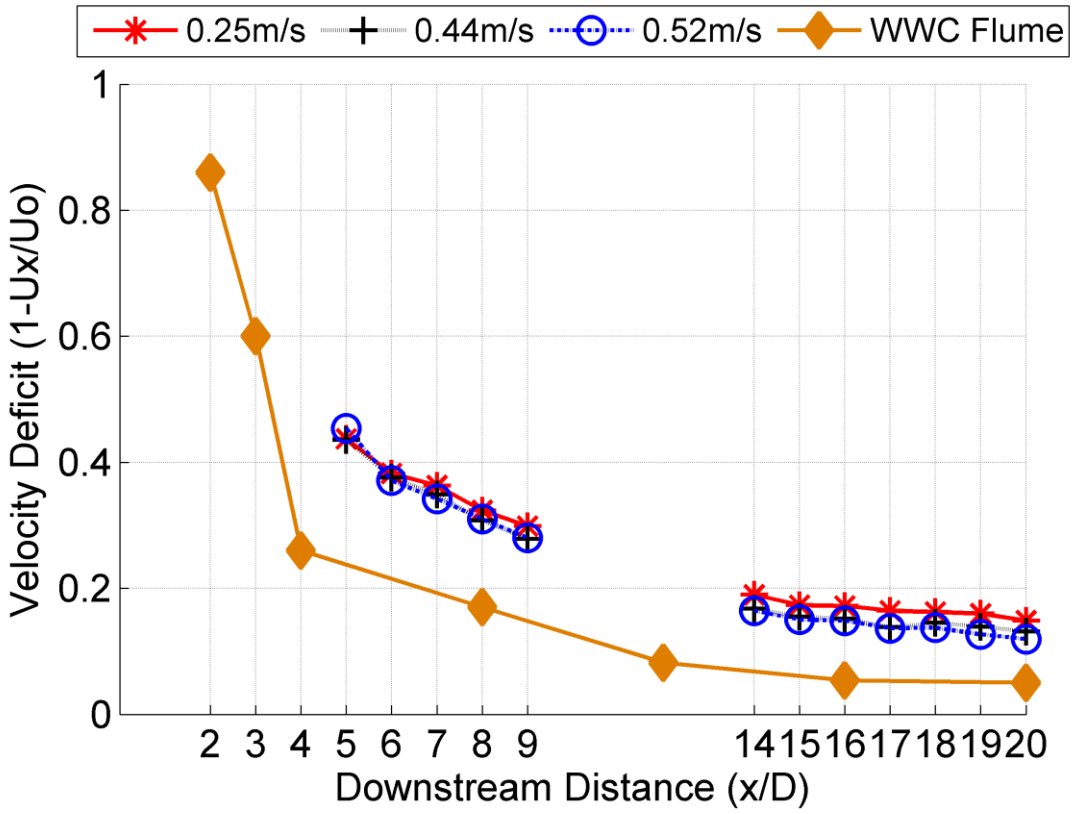

Figure 4-8 – Centreline Wake Velocity Deficit for a Single Turbine in the CWC at Different Current Velocities and Ti = 2% and Comparison to Wake Recovery in WWC Flume where Ti = 10%.

The velocity recovery in the WWC Flume shows the significant impact of increased ambience turbulence intensity levels on the wake recovery of an isolated turbine. Wake recovery is accelerated throughout the tested wake domain and a significantly lower velocity deficit remains at 20D downstream of the rotor for the WWC Flume experiment. The impact of the increased blockage ratio in the WWC Flume is considered to be small, though may aid in the initial recovery of the velocity in close proximity to the rotor and ambient flow is accelerated between the rotor and the free surface. Velocity deficits of 5% at 20D were measured in the WWC Flume while the remaining velocity deficits at 20D ranged from 11% to 15% in the low ambient turbulence CWC.

The velocity deficit shows small variation across the different current velocities in the CWC of a single turbine operating at constant tip-speed ratio for currents of 0.44m/s to 0.52m/s. With a current velocity of 0.25m/s the resulting Reynolds number is below the independence threshold of 4.8×10^4 for mean velocity and 9.3×10^4 for higher order statistics (Chamorro *et al.*, 2012), therefore the deviation of the resulting wake velocity deficit could be attributed to this. Differences in thrust coefficients are expected to be small due to the performance of the used tidal turbine blade section as discussed in Section 2.1.1.

The measured wake velocity deficit (Figure 4-9 (a)) recovers at a higher rate in the near wake of the turbine, where turbulence levels are high (b) due to the combined presence of rotor and support structure. With increasing distance downstream of the rotor, the velocity recovery at the centreline slows down due to dissipation of turbulent kinetic energy. In the far wake of the single turbine configuration, the wake centreline velocity recovery slows and reaches approximately 85% of the free stream velocity at 20D downstream of the rotor. The evolution of velocity deficit through the wake, from 44% at 5D to 28% at 9D is comparable to previous single turbine experiments conducted at similar ambient conditions. Mycek *et al.* (2014a) showed a reduction in centreline velocity deficit from 50% at 5D to 25% at 10D for a slightly higher ambient turbulence intensity flow (3%). Other experiments at slightly higher ambient turbulence intensities by Maganga *et al.* (2010) and Stallard *et al.* (2013) of 10% and 8% respectively have shown recovery of the deficit by about 20% between 5D and 10D.

The calculated centreline turbulence levels (Figure 4-9(b)) in the near wake up to 10D decrease from 22% to 12.5%, showing almost identical dissipation of turbulence to those measured in Mycek *et al.* (2014a). With increasing distance from the rotor (14D - 20D), recovery towards

ambient conditions slows down, and turbulence intensity at hub-height of the turbines remains at considerably higher levels of approximately 3-4 times the ambient upstream conditions of 2%.

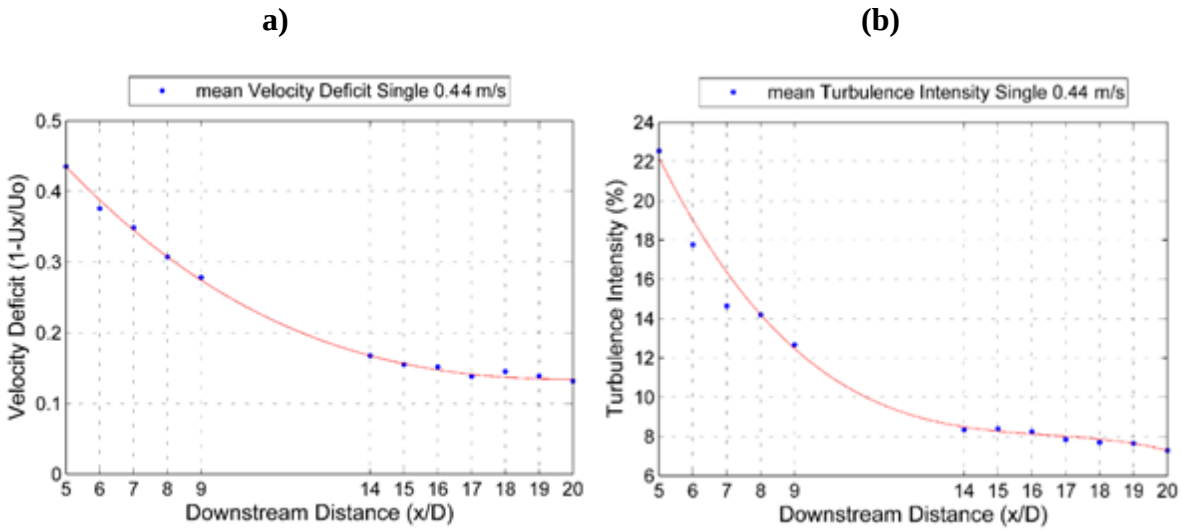

Figure 4-9 – (a) Velocity Deficit and (b) Turbulence Intensity Downstream of a Single Turbine.

The velocity and turbulence characteristics obtained from the numerical simulation are compared to those recorded during the experimental study. The agreement of wake characteristics between numerical models and experimental study is shown for an isolated turbine operating in the CWC with an ambient current velocity of 0.44m/s. All simulations are performed at the same current velocity based on the small differences observed between the current velocities tested experimentally. Comparison in Figure 4-10 (a) and (b) shows that the reference length used to define the mixing length for turbulence modelling, based on turbine blade chord length, (L_2) in Equation (3-15) in Section 3.2.3 shows significantly better agreement with experiments while the length based on immersion depth (L_1) results in significantly under predicted wake recovery and turbulence intensity. Based on this, the reference length $L_2$was chosen for all numerical simulations.

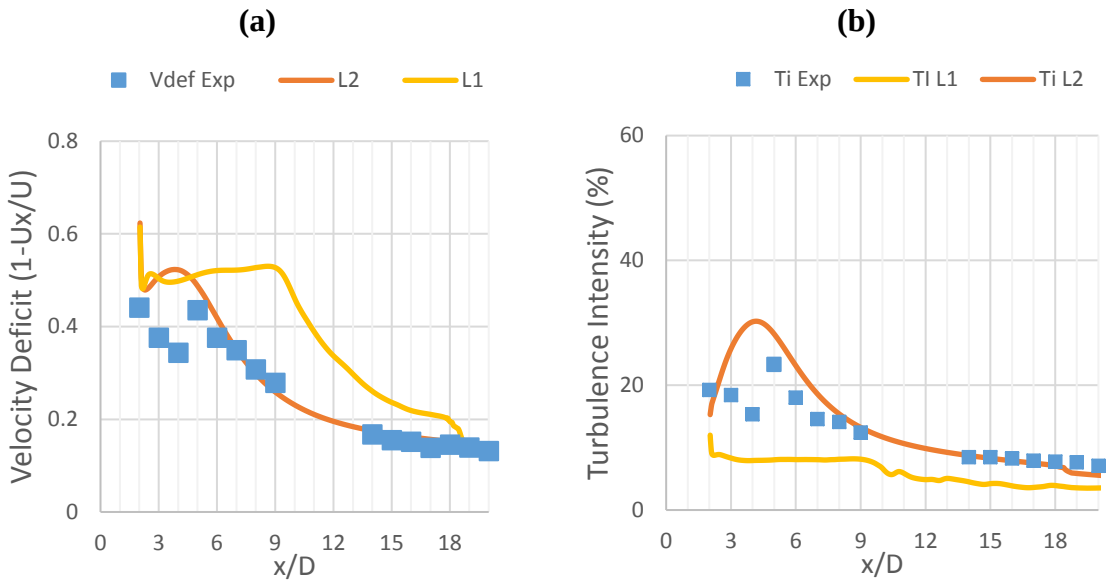

Figure 4-10 - Comparison Between Numerical Simulations (Solid Lines) and Experiment Measurements (Box) for a Single Turbine Operating in Ambient Flow of 0.44m/s: (a) Velocity Deficit and (b) Turbulence Intensity Including Both Reference Length Definitions.

The agreement between numerical simulations and experimental measurements varies depending on the location and configuration of the conducted tests and corresponding numerical simulation (Figure 4-10 & Figure 4-18). The wake characteristics of a single turbine presented in Figure 4-10 (a) show good agreement between 5D and 9D, thus within the range of intended locations of the second row turbine for further simulations. The velocity deficit further downstream, between 14D and 20D matches well with that measured during experiments. The rate of velocity recovery observed between 7D and 15D is very similar and a remaining velocity deficit of 13% is observed for experiments and simulation at 20D at the rotor hub height.

The turbulence intensity is calculated higher in the near wake of the tidal turbine (x/D < 5) than measured from the experiments, where the experimental values obtained between 2D and 4D have to be treated with care due to the limitations in the PIV analysis as stated in Section 2.3.1. The trend of dissipation of turbulence towards free stream levels as well as the location of maximum turbulence intensity are similar, yet differ in magnitude by approximately 7%. In the far wake region between 15D – 20D good agreement is shown, with a remaining turbulence intensity between 5% - 7% at the centreline height of the tidal turbine thus not recovering towards free stream levels of 2% within 20D.

Far downstream, at the end of the numerical and experimental test section domain, the numerical turbulence intensity remains slightly higher than ambient turbulence levels of 5% at 20D, whereas in the experiment the turbulence intensity recovers to about 7% at 20D. The increase in turbulence intensity observed in both cases, reaching a peak between 4D and 5D shows the location where centreline wake recovery accelerates. Differences are most pronounced in the near wake close to the support structure where high velocity gradients and stagnating flow were observed in the experiment, thus increasing the difficulty of ensuring appropriate time stepping and simultaneous analysis of highly sheared flow within the PIV measurements.

The numerical wake flow field in Figure 4-11 shows the accelerated flow around the turbine hub (a) and above the turbine wake 3D downstream of the rotor (b) which is followed by the slow moving fluid downstream of the rotor blades moving towards the centreline (a). Immediately downstream of the turbine nacelle, accelerated flow is observed along the cylindrical main body before the upper and lower layer of the slow moving fluid in the shear layer reach to the rotor centreline further downstream. This flow information from the numerical simulations is thus showing the reasons for the increase in velocity deficit between 2D and 4D observed in the experiments. Further characterisation of the tidal turbine wake from numerical simulations is presented in Section 4.3.1.

(a)

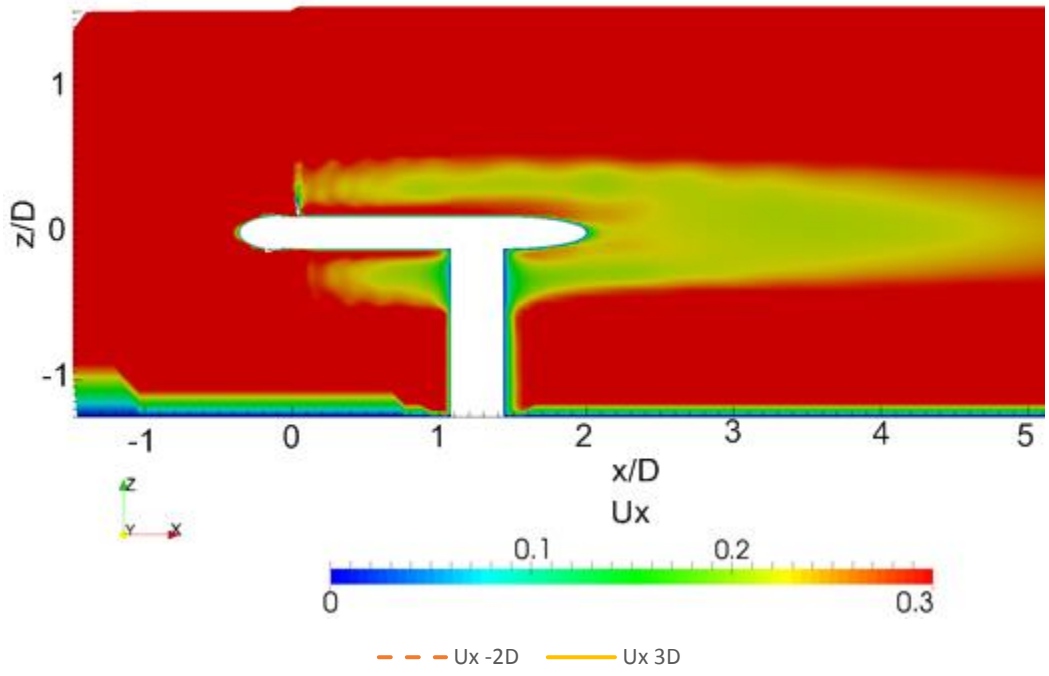

(b)

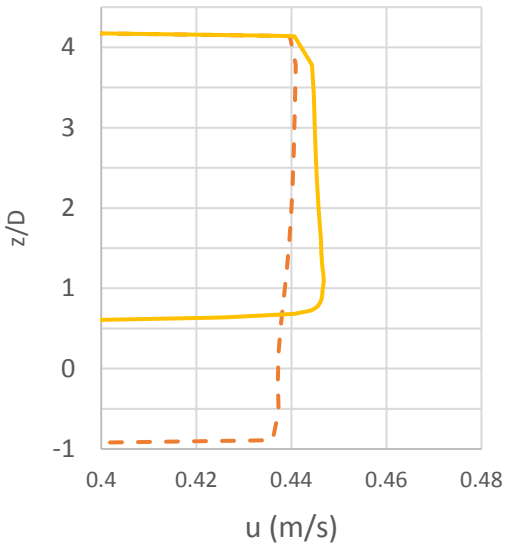

Figure 4-11 – (a) In-Stream Velocity Component Around the Tidal Turbine Support Structure and (b) Velocity Profile Above the Wake ($z/D > 0.5$) for 2D Upstream of the Rotor and 3D Downstream of the Rotor from Numerical Simulations of an Isolated Tidal Turbine at 0.44m/s Ambient Current Velocity.

4.2.2 Two-row Tidal Turbine Array

The effect of adding an additional row of turbines to the single turbine configuration, with a centreline offset of ±3D and downstream spacing of 3D, on the centreline wake is investigated experimentally. The measured time-averaged velocity deficit (Figure 4-12) at 5D is lower for the 3 turbine arrangement (30%) than the single turbine velocity deficit of 40%, however trends in recovery are very similar to the single turbine arrangement in the region from 5-10D. By adding a second row of turbines, the near wake characteristics (between 5D and 9D) show a lower velocity deficit compared to the single turbine case (29% recovering to 18% compared to 43% recovering to 28%) which could be explained by the ambient flow being diverted towards the array centreline due to the presence of the turbines located 3D downstream of the first turbine with a transverse separation of 3D.

An increase in velocity deficit is observed at 0.44m/s between 15D and 19D along with turbulence intensity (Figure 4-13) that increases slightly between 16D and 18D. At 0.52m/s ambient current velocity, this effect is less pronounced and the velocity deficit remains virtually constant between 15D and 18D and continues recovering further downstream where a slight increase in turbulence intensity at 18D can be observed at 0.52m/s which corresponds to the increased rate of velocity recovery seen in Figure 4-12.

The wake further downstream is therefore experiencing a reduction in wake recovery, which may indicate the positions where the outer turbine wakes reach the array centreline, hence slowing down mixing with the ambient flow as these wakes have significantly lower velocities. This evolution of the wake downstream would most significantly affect further positioning of additional tidal turbines in large-scale arrays, however the evolution of the centreline wake may be affected by the positioning of a fourth turbine axially aligned with the upstream turbine and this will be investigated in the following section.

The contour plot of the velocity deficit evolution at the centreline of the test section in Figure 4-14 shows increased velocity deficits downstream of the rotor blades and a slightly reduced velocity deficit in the centre of the wake. The top part of the wake ($y/D > 0$) shows increased recovery of the wake velocity compared to the bottom part of the wake and a small deflection of the wake towards the bottom of the test section is observed and this is caused by the small shear present in the onset flow (Figure 2-16) and increased mixing on the top half on the wake compared to the bottom half.

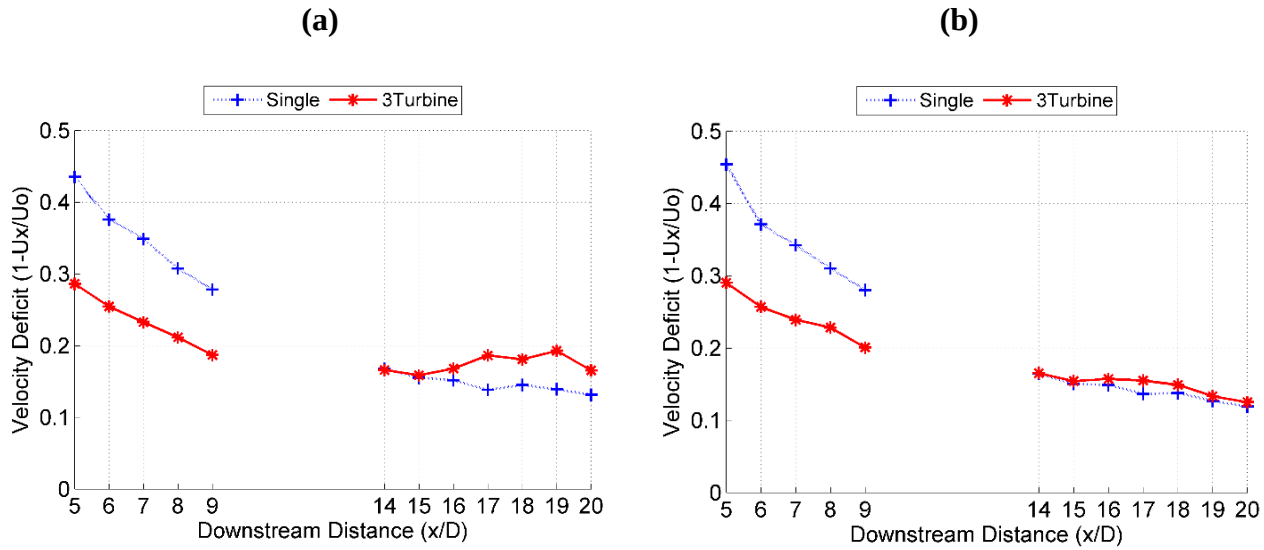

Figure 4-12 - Velocity Deficit Comparison between a Single Turbine and 3 Turbine Arrangement at (a) 0.44m/s and (b) 0.52m/s Ambient Current Velocity.

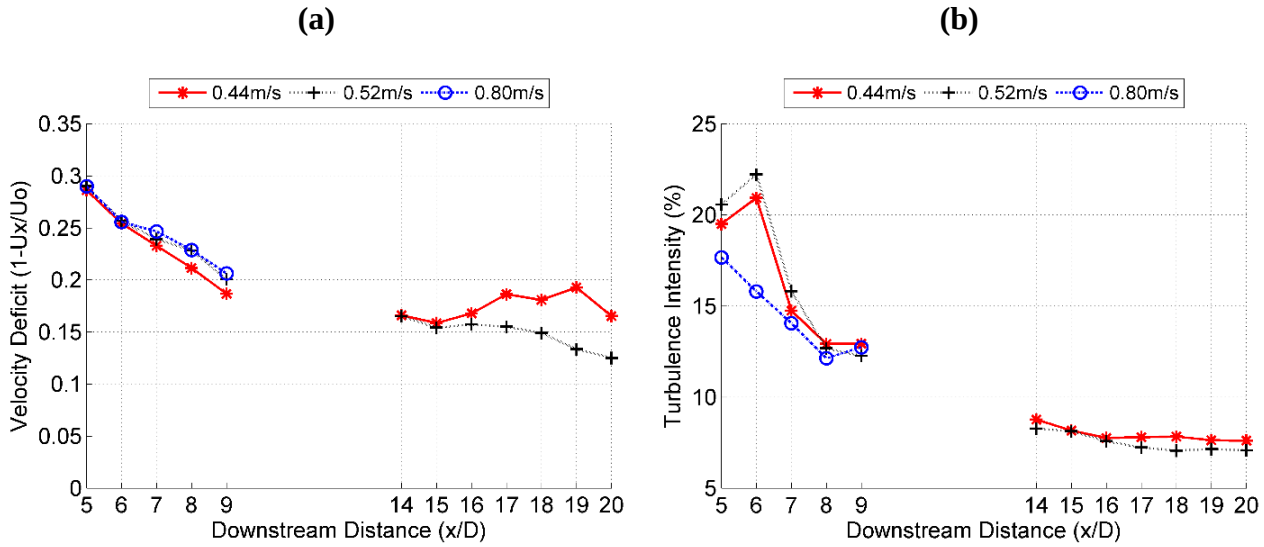

Figure 4-13 – (a) Velocity Deficit and (b) Turbulence Intensity Comparison of 3 Turbine Arrangement at Different Current Velocities.

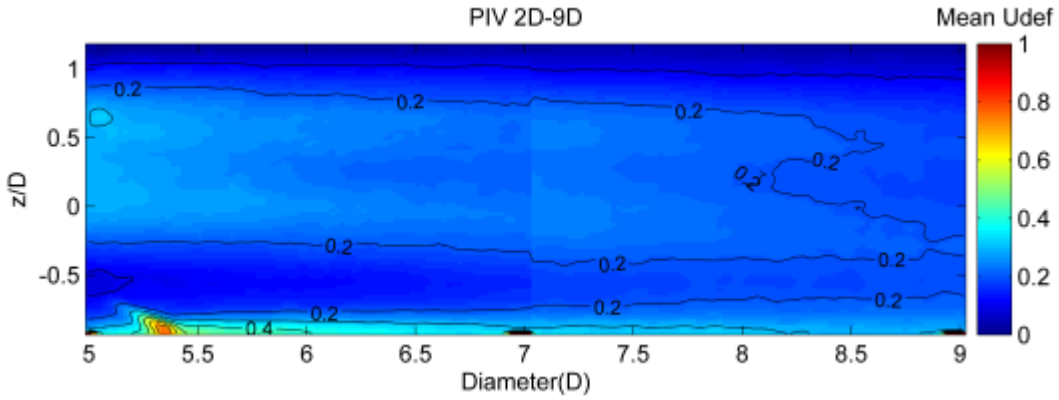

Figure 4-14 - 3 Turbines Velocity Deficit (0.44m/s Current) Downstream of Second Row.

4.2.3 Staggered Tidal Turbine Arrays

To determine the effects of multiple turbines operating in close proximity, measurements have been taken at the centreline of the proposed array sections. Within the array, measurements are conducted from the downstream end of the nacelle of the first turbine located at the array centreline up to 3D upstream of the third row turbine located axially aligned with the upstream turbines with 12D spacing thus representing downstream distances of 2D – 9D. Measurements downstream of the array to the end of the test section (14D - 20D) are used to investigate velocity and turbulence characteristics across a number of array configurations, the experimental set-up is shown in Figure 2-28. Data points between 2D and 5D for close transverse spacing are affected by the presence of support structure in the PIV recordings, as highlighted in Section 2.3.1 (Figure 2-33 & Figure 2-34).

Figure 4-15 shows a comparison of time averaged velocity deficits for both longitudinal spacings tested. There is a clear correlation between the transverse spacing of the second row turbines and the evolution of the velocity deficit as smaller transverse spacing leads to higher velocity deficits remaining in the wake, as well as slower recovery towards free- stream velocity especially between 5D – 9D. The velocity deficit levels observed for array tests have been considerably higher, especially for close transverse spacing of 1.5D between the middle row turbines. For both longitudinal distances velocity recovery slows down approximately 2D - 3D downstream of the second row turbines. An increase of centreline velocity deficit is observed between 5D and 9D for the close transverse and increased longitudinal spacing of L5T15 array. These indicate that the close transverse spacing reduces wake recovery at the centreline and could be explained with the combination of adjacent wakes to form a wide, single wake reducing the mixing with ambient flow at the centreline for wake re-energization, this is shown from the numerical results in Figure 4-36.

The wake downstream of the array shows smaller variations between the different configurations, however with larger transverse spacing between the second row turbines, the rate of velocity recovery of the array wake is increased and velocity deficit remain smaller for a transverse spacing of 3D. Slightly increased velocity deficits remain for transverse spacings of less than 3D in the L5 arrays with a deficit of 35% for T3 and 39% at L5 respectively (Figure 4-15b). For a longitudinal spacing of 3D, the velocity deficit is almost identical between 1.5D and 2D transverse spacing cases. The highest velocity deficit at L5 arrays is seen for transverse

spacing of 1.5D. Comparing the array wake velocity recovery downstream of the array to the 3 Turbine arrangement shown previously indicates that the influence of the middle row turbines on the wake recovery is less pronounced. This could be attributed to the overall high velocity deficit, changes in turbine inflow conditions and the outer turbine wakes preventing ambient flow from reaching the array centreline as rapidly as in the case without turbine D. Increased velocity recovery for large spacing, inside the array section and downstream of the array indicate increased mixing with ambient flow and could point towards ambient flow penetrating between the individual wakes. This will be further investigated in 3D numerical simulations.

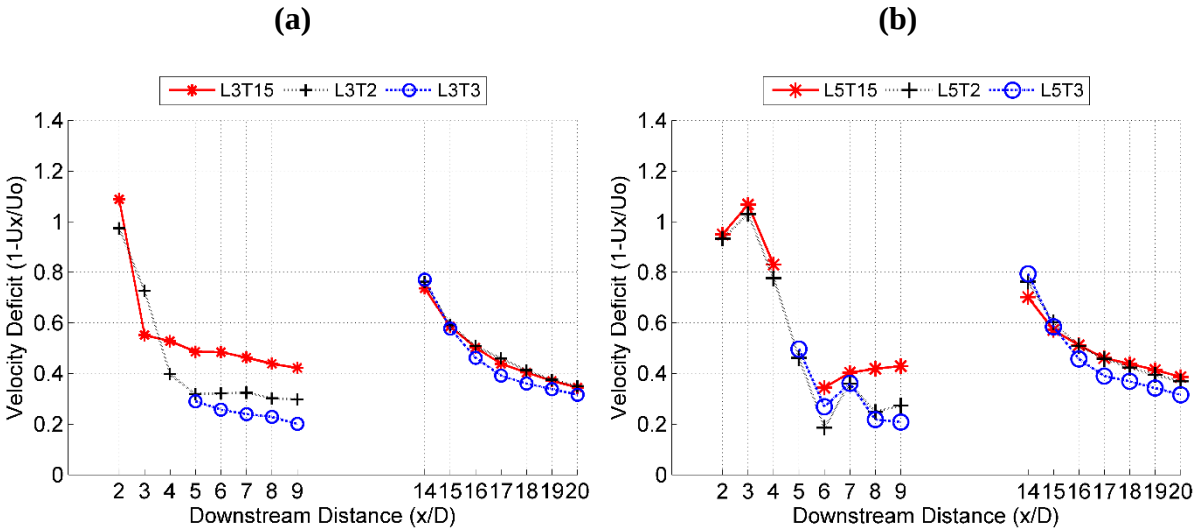

Figure 4-15 - Centreline Array Wake Velocity Deficit Comparison at 0.52m/s for (a) L3 Arrays and (b) L5 Arrays.

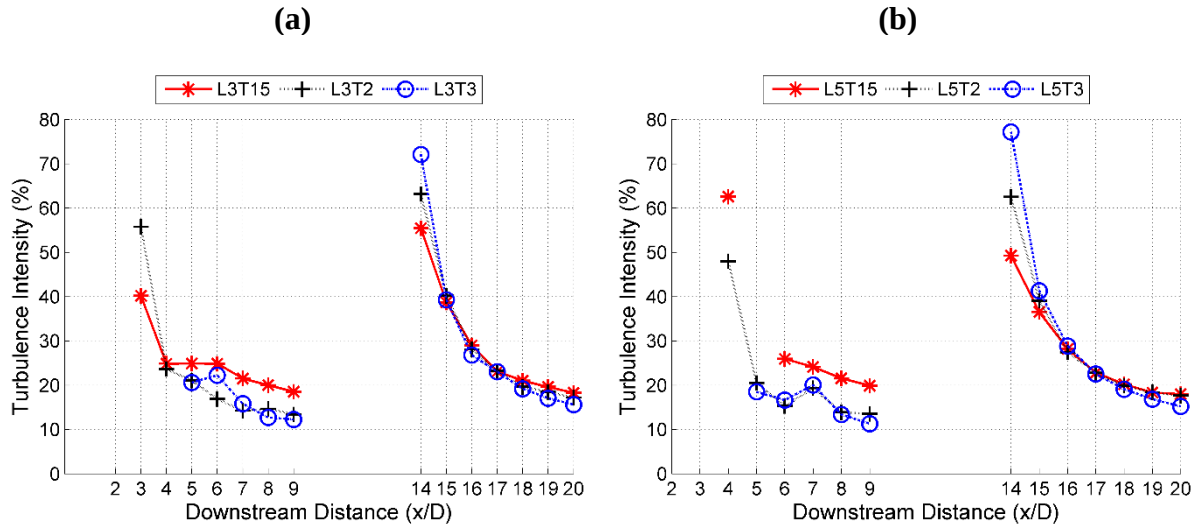

Figure 4-16 - Centreline Array Wake Turbulence Intensity Comparison at 0.52m/s for (a) L3 Arrays and (b) L5 Arrays.

From the wake characteristics presented in Figure 4-15, it can be seen that increasing transverse spacing leads to significantly improved recovery within the array section tested, hence increasing inflow velocity to the first in-line turbine (the downstream turbine) in such arrangements. For 3D longitudinal spacing, differences in velocity deficit of 13% between L3T15 and L3T2 (15% for L5) compared to 9% between T2 and T3 (7% for L5) show a reducing influence of transverse spacing. The wake downstream of the array section is less influenced by the transverse spacing tested and shows small variations only in terms of wake recovery far downstream, however with the trend of slightly increasing differences between the different formations with increasing transverse spacing. Figure 4-16 shows that high turbulence intensities recorded in the inner array field do not translate into accelerated recovery at the array centre line as the L3T15 and L5T15 show highest velocity deficit despite having recorded the highest turbulence intensity.

Comparison of the wake velocity deficits downstream of the arrays show improved recovery for increased transverse spacing of the middle row turbines. Some benefits of very close spacing in both longitudinal and transverse direction can be seen in the wake recovery for L3T15 array (Figure 4-17) showing improved wake recovery at 20D downstream. The influence of longitudinal spacing reduces with wider transverse spacing of the middle-row turbines when comparing the velocity deficit downstream of the array for the both T3 cases.

The downstream turbine operated at increased TSR due to the reduced inflow velocity showed lower performance with higher variations (Figure 2-12 & Figure 2-13). However, the turbine blade design was shown previously to maintain high and practically constant C_T values over a range of TSR expected to be encountered by the upstream and downstream turbine (Shi et al., 2013). The detailed performance of array turbines will be investigated further numerically.

The wake recovery for larger transverse spacing could hence be related to more of the ambient flow travelling through the array at higher velocities and being pushed towards the array centreline without entrapping a large volume of slow moving fluid as for the close transverse configurations which effectively creates a single wake with slowed velocity recovery at the centreline as shown for close spacing in Myers and Bahaj (2012). This can be a particular area of interest for the initial rows in large scale arrays where device generated turbulence levels are lower, hence wake recovery would be influenced more by the characteristics of the ambient flow.

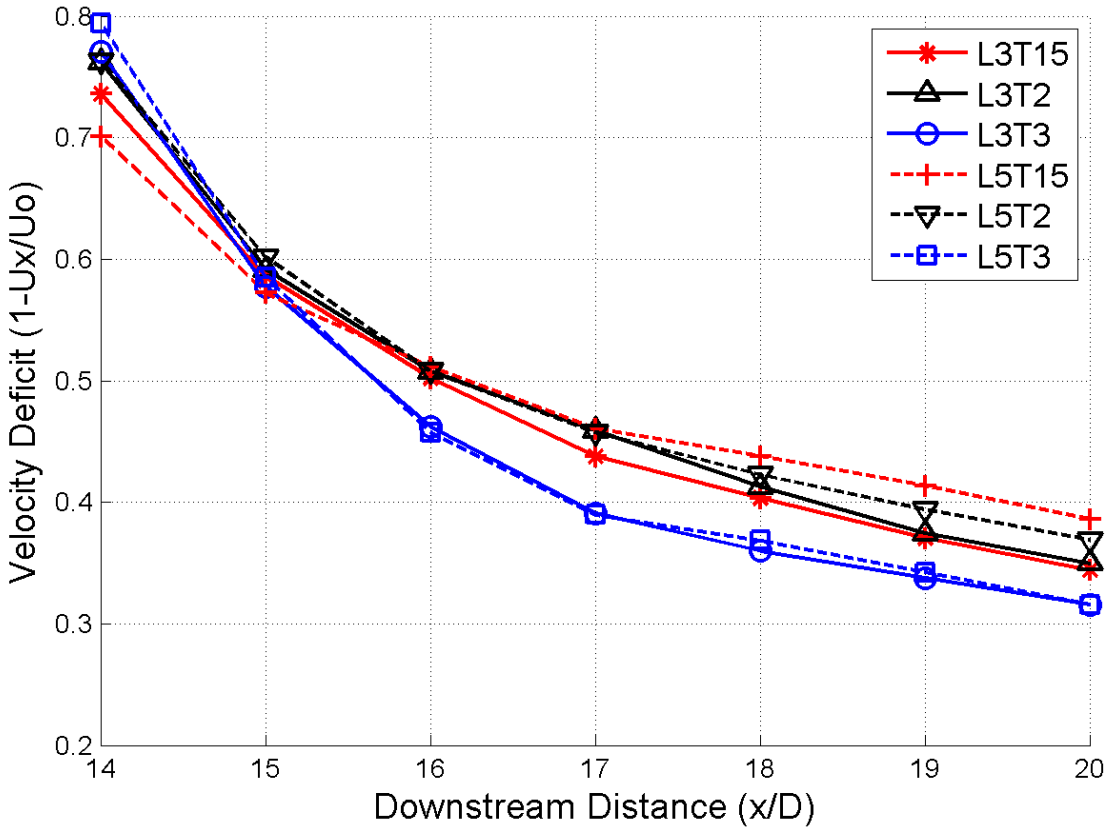

Figure 4-17 – Comparison of Wake Velocity Deficit Downstream of Various Array Configurations with Ambient Flow of 0.52m/s.

Comparison of the experimental results presented here with the prediction of wake characteristics from numerical simulation (Figure 4-18 & Figure 4-19) shows that some significant differences between experiment and numerical simulation are observed immediately downstream of the turbine, where due to high velocity shear across the wake, calculation of flow vectors using PIV was difficult and further calculation of turbulence intensity for very slow flow velocities resulted in high values compared to the numerical solution. The velocity deficit (a) shows good agreement in the array wake and downstream of last row of turbines whereas the turbulence intensity (b) for the close arrangement of tidal turbines in a staggered array agrees well downstream of the array section and matches trends within the array itself. The increasing velocity deficit downstream of the second row of turbines is observed in experiments and numerical simulation for both array cases. For L3T15, the experiments show a near constant velocity deficit between 5D and 7D and numerical results (Figure 4-18(a)) indicate an increase in velocity deficit by 8% for L3T15 between 4D and 6D.

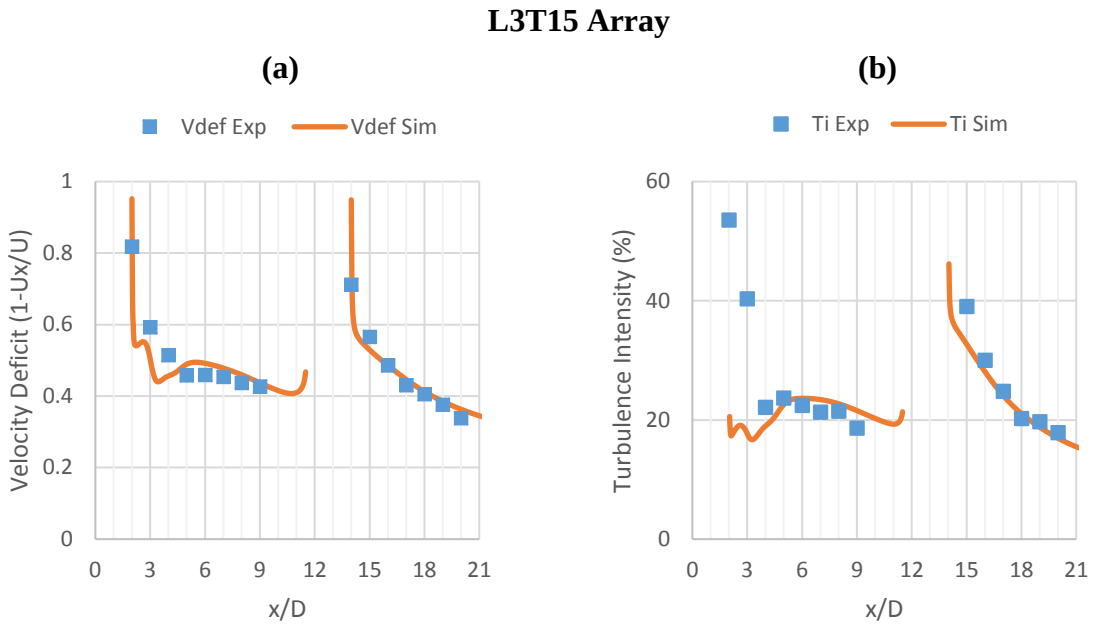

Figure 4-18 - Velocity Deficit (a) and Turbulence Intensity (b) Comparison Between Numerical Simulations (Solid Line) and Experimental Measurements (Box) for the L3T15 Array Operating in Ambient Flow of 0.44m/s.

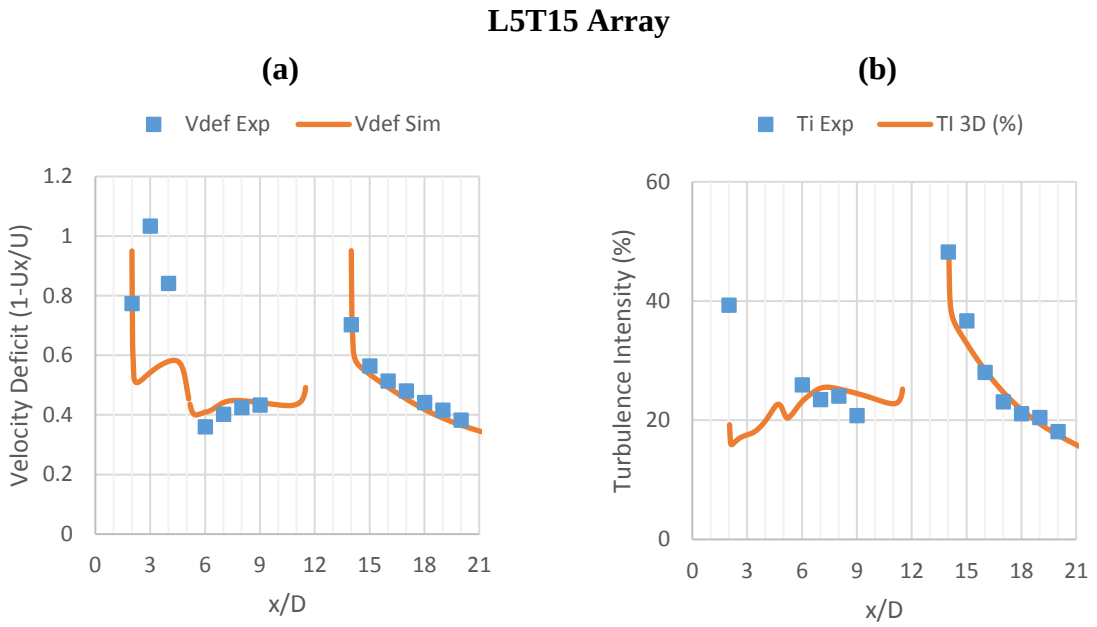

Figure 4-19 - Velocity Deficit and Turbulence Intensity Comparison between Numerical Simulations (Solid Line) and Experimental Measurements (Box) for the L5T15 Array in Ambient Flow of 0.44m/s.

The wake recovery downstream of the last row of turbine is increased for L3T15 in the experiments between 15D and 18D however, the final velocity deficit remaining in the wake at 20D downstream differs by only 3%. For the increased longitudinal spacing shown in Figure 4-19, the velocity deficits agree very well within the combined array wake downstream of the last turbine. The increase in velocity deficit downstream of the second row turbines is also observed for the longitudinal spacing of 5D as can be seen in Figure 4-19 (a) between 6D and 9D. Flow recovery downstream of the last row is almost identical with differences in the velocity deficit of approximately 2%. The turbulence intensity within the array is predicted well within (4D - 9D) the array as seen in Figure 4-19 (b). The dissipation of downstream turbulence is slower in the numerical simulation than in the experiments recorded and a higher turbulence remains at 20D.

One reason for the differences is an observed shift in the wake centreline due to higher shear at the upper wake boundary in the experiments. This has not been shown in the numerical simulation and could be influenced by the omission of the small support frame used in the experiment that effectively increased the roughness of the test section floor which led to less mass flow at the underside of the wake as was shown by Myers and Bahaj (2010) for actuator disk experiments. In a low ambient turbulence environment the developing wake from the support structure reduced wake mixing on the lower part of the wake, thus slowing down recovery of velocity when compared to numerical modelling where flow is passing between the bed and turbine.

While the velocity deficit is matched well in the inner array section, the turbulence intensity shows better agreement for the downstream wake region. The inner array region is where device generated turbulence dominates and the influence of not including the support frame in the numerical model is less pronounced. Additionally, the calculation of turbulence flow characteristics from experiment is difficult in the near wake and where turbine structures interfere with the laser sheet. However, matching the turbulence intensity upstream of the last row turbine improves the prediction of the centreline velocity recovery downstream of the array. The wake downstream of the array is predicted well for the array configurations shown here in terms of velocity recovery and dissipation of turbulence between 14D and 20D.

4.2.4 Investigation of PIV Flow Field

Flow field measurements with PIV provide further insights into the resulting wake without the need for extensive point-by-point measurements along a pre-defined grid of measurement locations. This provides visualized wake data for inspection and determination of the processes occurring at the centreline of different array formations. For visualization, the individual measurements taken have been combined to provide continuous wake field for the inner array along the centreline (Distances of 2D - 9D) as well as the array wake downstream (14D - 20D).

Vectors are combined by averaging where both images have flow vectors within the overlapped area. Areas where no data has been recorded due to the PIV set-up (no access for laser sheet or reflections of device surface (refer to Section 2.3)) or where vectors were removed during post-processing remain visible in the resulting contour plots and show small inconsistencies of the flow field around this area as a product of the overlapping. Figure 4-20 shows individual measurements for each wake location in (a) and the combined wake plot for the wake field between 2D and 9D in (b). The array centreline from which data is presented for the velocity deficit and turbulence intensity is shown.

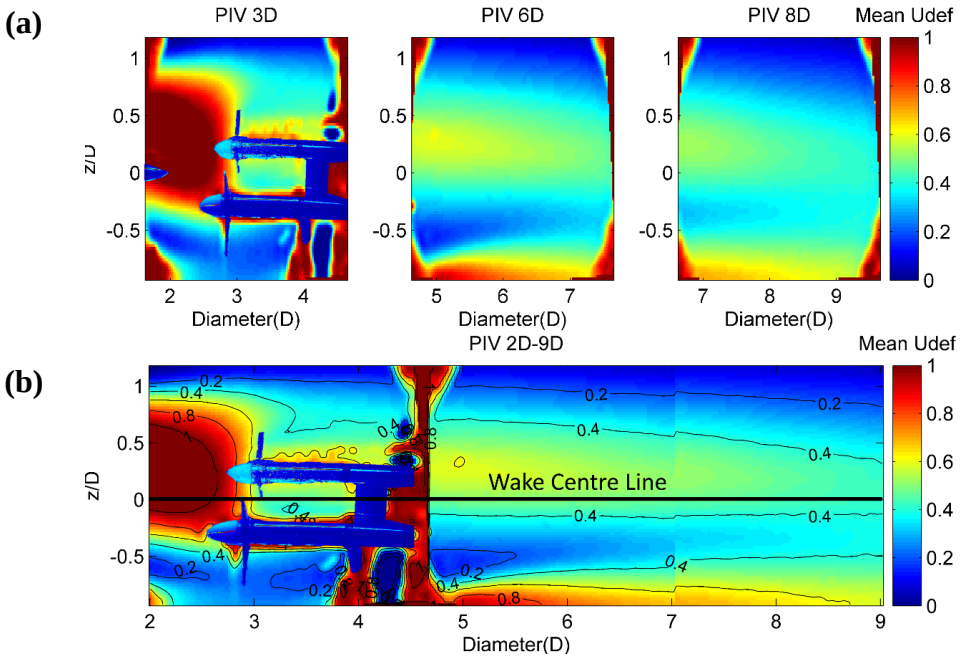

Figure 4-20 – (a) Individual and (b) Combined PIV Measurements Including the Position of Second Row Turbines for the Wake in Array L3T15 from 2D – 9D.

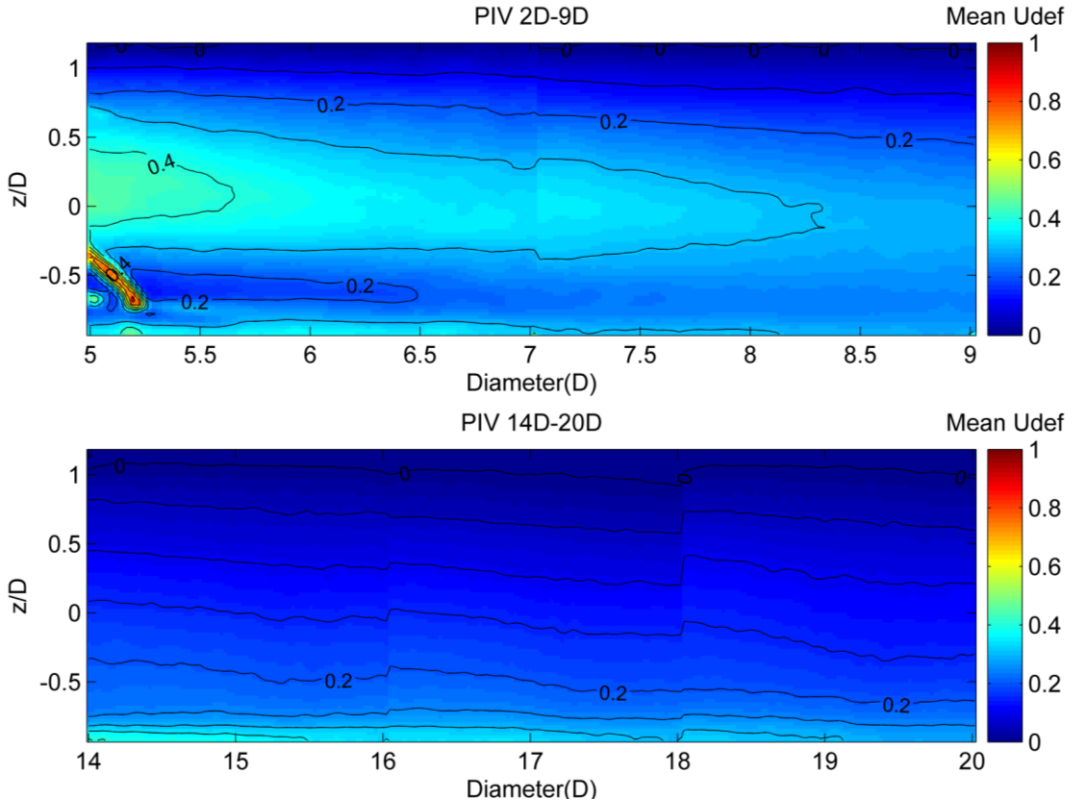

Figure 4-21 - Wake Velocity Deficit Contours of an Isolated Turbine in the CWC 0.52m/s Ambient Current.

The time averaged wake velocity contours presented in Figure 4-21 show the wake between 5D and 20D downstream of the rotor plane of a single turbine placed in the CWC. From the above plots, it can be seen that the wake centre is slightly shifted downwards and the centreline deficit remains above 30% up to 8D downstream. The vertical expansion of the wake beyond the rotor height can be seen between 5D and 9D with a deficit between 0% and 10% persisting at 0.5 < z/D < 1D and accelerated flow above the wake. The far wake downstream shows some discontinuities at the areas where the wakes have been merged from adjacent measurements which are arising due to the overlap of interrogation windows and areas of no data recording as detailed in Section 2.3.

The resulting array wake velocity deficit contours at the centreline are shown for a number of experimental array configurations (Figure 4-22 & Figure 4-23). The inner array wake (2D - 9D) and the array wake (14D - 20D) are shown to visualise areas of increased flow velocity, the wake shape, and characteristics as well as effects resulting from the presence of support structure and frame located on the test section floor. Comparison is made for the centreline flow field with longitudinal and transverse variation of the inter-device spacing.

The deficits exceeding unity shown in close proximity are a result of the PIV recording and analysis with very strong velocity gradients where very slow moving flow was observed and reflections of laser light off the turbine hub nacelle. An area of very slow moving fluid directly downstream of the first turbine can be clearly observed with the resulting wake further downstream in Figure 4-22, the close longitudinal (L3D) and transverse spacing (a) and is less pronounced for increased transverse spacing (b). Areas of ambient and slightly accelerated flow are identified above and below the wake. For increasing longitudinal spacing in Figure 4-23, similar trends of the centreline wake are observed. The wake of the upstream turbine develops further downstream before reaching the second row and an area of reduced velocity deficit is observed at about 1D as is shown in Section 3.3, however a slight reduction in vertical wake extent can be seen for increased spacing, both longitudinally and transversely.

For wide transverse and increased longitudinal spacing in L5T3 in Figure 4-23 a more noticeable shift of the wake towards the test section flow is observed than for close longitudinal spacing in Figure 4-22 and reduced wake extent is shown up to 20D. This indicates the effect of ambient flow to be stronger, when separation between the first two rows of the array is increased, thus the variations of the onset flow are causing increased mixing at the top of the wake.

The support structure wake is most pronounced in the L3T15 array in Figure 4-22(a) between 5D and 9D, indicating that increased blockage area of the three combined rotors at the array test section diverts the flow around the turbines and increases the presence of the support structure wake.

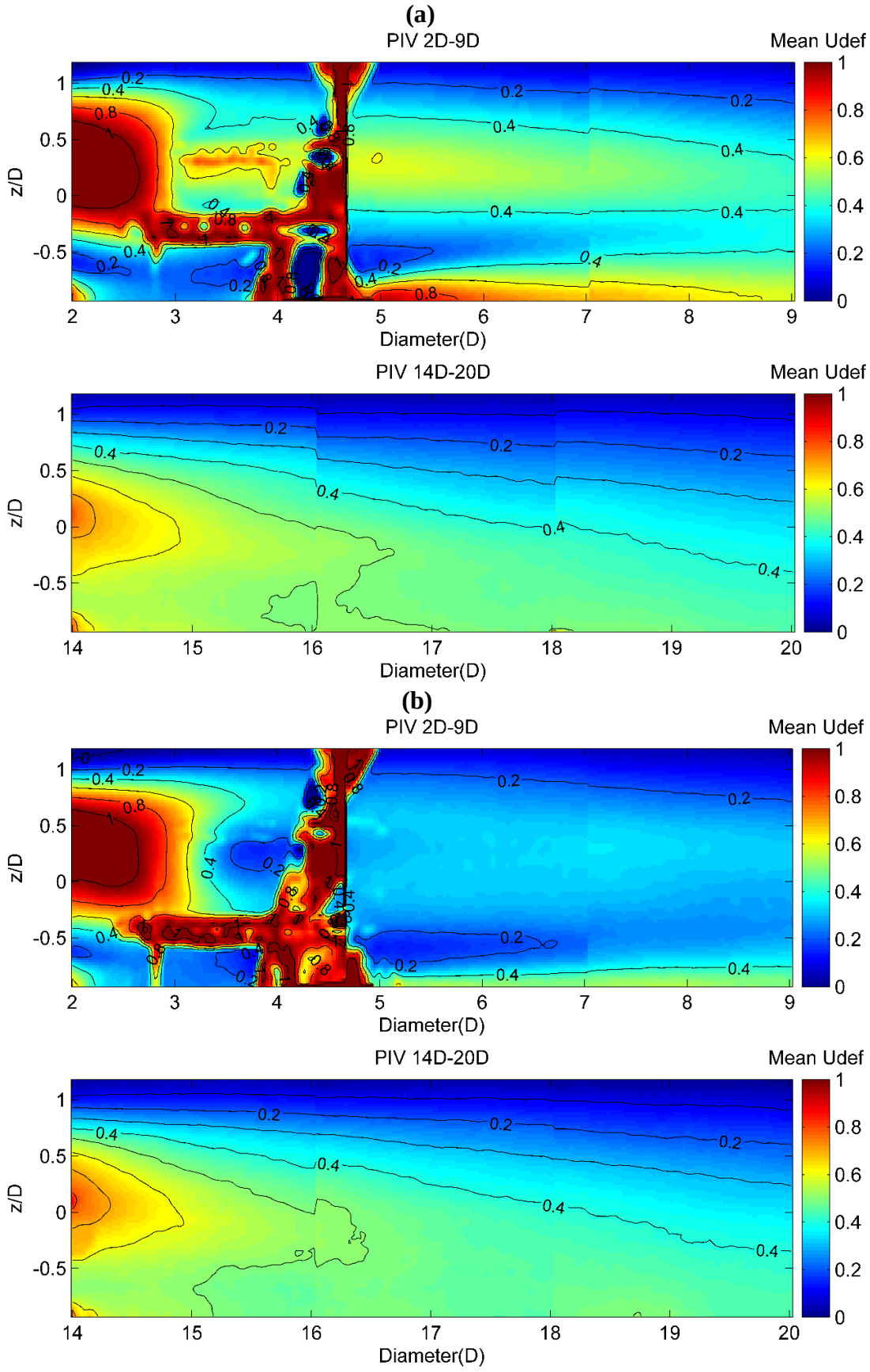

Figure 4-22 – Velocity Deficit for Array (a) L3T15 and (b) L3T2.

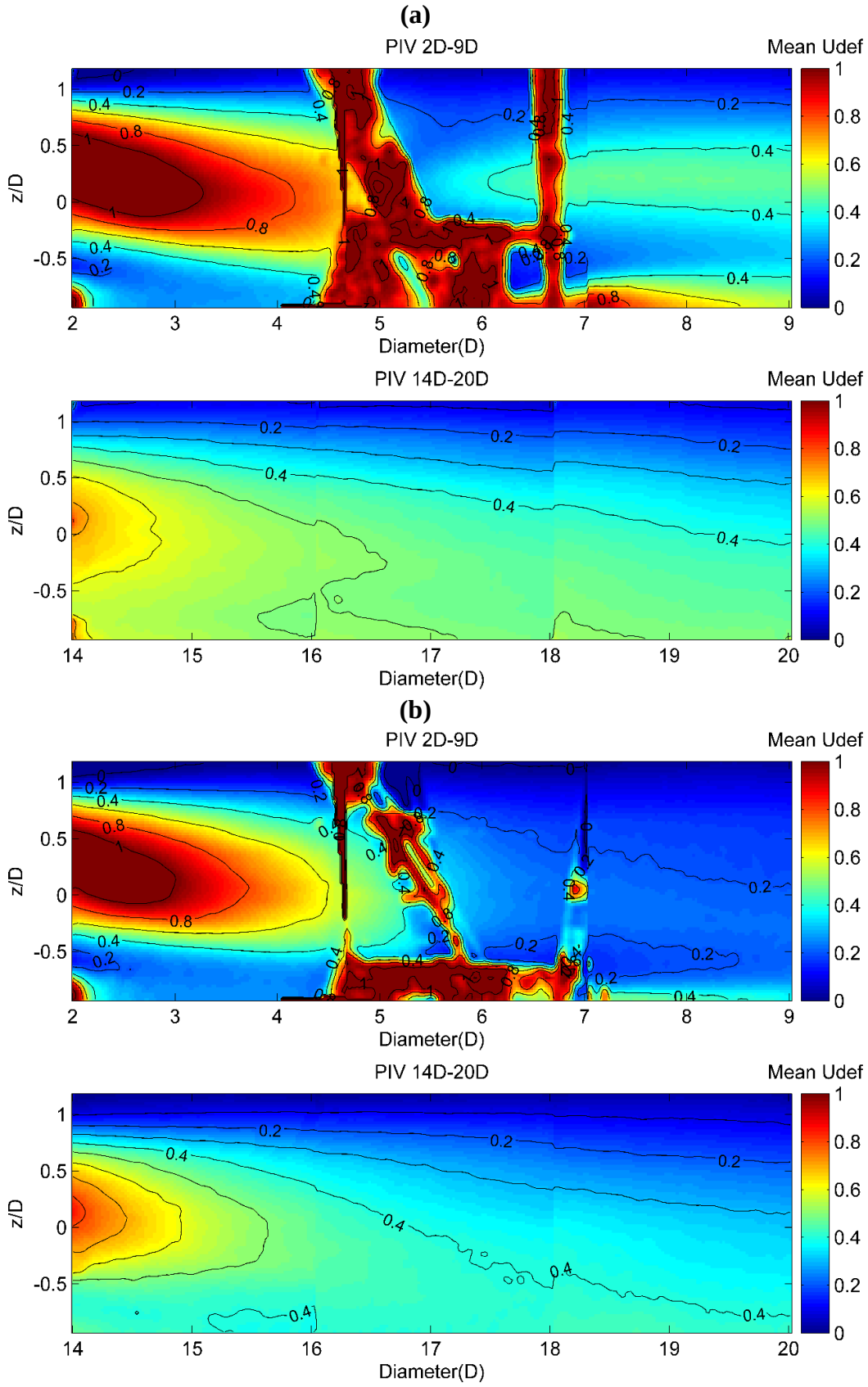

Figure 4-23 – Velocity Deficit for Array (a) L5T15 and (b) L5T3.

The recovery behind the second row of turbines is shown in Figure 4-24 (a) comparing the vertical velocity profile at 3D downstream of the second row for L3T15 and L5T3. Wake recovery, especially in the upper part, is accelerated for wide spacing. There is a layer of fluid with increased velocity present in close spacing between the support structure wake and turbine wake, aiding recovery of velocity in the lower half of the wake. The support structure wake is more pronounced in closer spacing as shown in Figure 4-22 (a) below -0.5 z/D. Downstream of the array however, at 3D and 8D distance from the last turbine, differences between the two formations are reduced, with smaller spacing showing slightly increased deficits at the bottom part of the wake in Figure 4-24 (b).

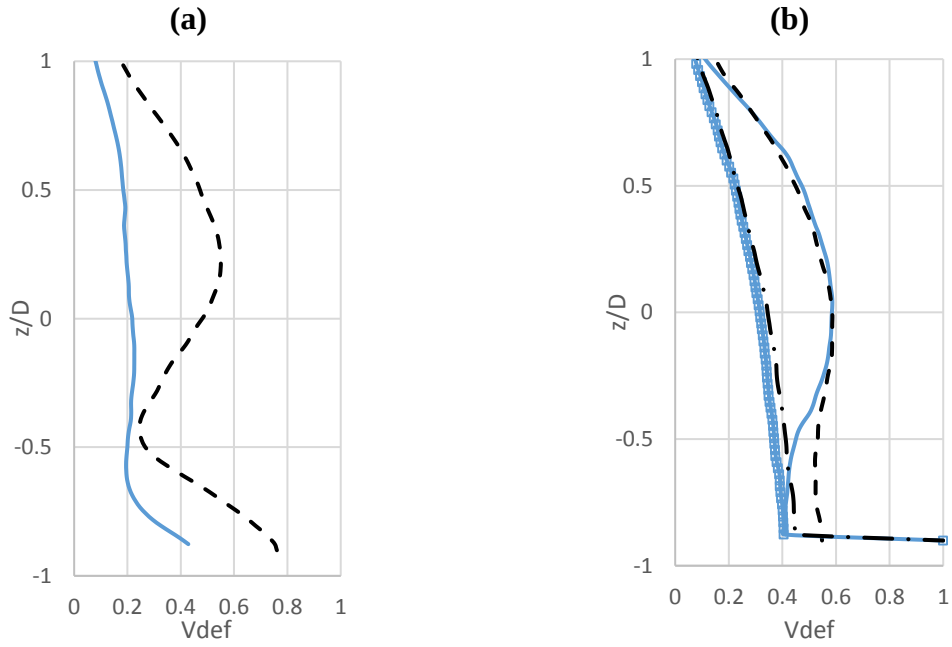

Figure 4-24 - Vertical Velocity Profiles at (a) 3D Downstream of the Second Row Turbines for L3T15 (Dash) and L5T3 (Solid) Respectively and (b) 3D (Dash L3T15, Solid L5T3) as well as 8D (Dash Dot L3T15, Square L5T3) Downstream of the Array.

4.2.5 Summary of Experimental Study in CWC

A comprehensive experimental study has been conducted to assess the influence of turbine spacings within a generic tidal turbine section of a staggered array design layout in addition to single and three turbine tests in the wide test section of the CWC. Multiple array sections were tested to assess the influence of longitudinal and transverse spacing in a three- row array in a staggered 1-2-1 configuration. First and last turbine were located on the array centreline, while the middle row turbines were varied in longitudinal location and transverse spacing.

The wake characteristics for a single turbine operating in a low ambient turbulence environment showed:

- Significantly slower wake recovery than in the Flume, with a wake velocity deficit of 12% persists at 20D downstream of the isolated device.
- Turbulence levels remain at approximately 8% compared to the 2% ambient turbulence.

The wake recovery at the centreline for a 3 turbine staggered set-up shows that:

- Initial wake recovery is sped-up due to more of the ambient flow being channelled around the downstream turbines and towards the array centreline.
- Further downstream areas of stagnating and increasing velocity deficit and turbulence intensity have been observed. This is within areas expected to see the expanded wake start merging towards the centreline wakes.
- The remaining turbulence intensity and wake recovery at 20D are very similar to that of a single turbine, thus showing the feasibility of a staggered arrangement in terms of velocity recovery prior to locating an additional turbine downstream.

Array experiments have shown the inner array wake recovery being significantly affected by the transverse spacing and similar wake recovery downstream of the array for configurations with different transverse and longitudinal spacings. Array centreline measurements at hub height showed that:

- Remaining velocity deficits are within 10% across all experiments at 20D downstream of the first turbine.
- Differences in the array wake recovery within the array and downstream of the array are attributed to varying transverse and longitudinal spacing and the altered flow field in and around the devices.
- Adding turbines in a staggered arrangement downstream of the first turbine increases initial flow recovery but also shows that very close spacing leads to large velocity deficits at the centreline while wide spacing of the second row shows inflow to the downstream turbine at lower velocity deficits, hence increasing the available power for downstream turbines.
- It is revealed that there are some benefits of locating turbines in close transverse spacing by increasing the wake recovery downstream of the array section (L3T15 recovering to lower velocity deficit than L3T2). However, the actual gain in performance would depend on tuning the downstream turbine to the occurring flow as in this experiment the perceived TSR differed from the upstream turbines due to the reduced velocity upstream of the turbine.
- Close spacing increased the effects of the support structure wake visualised by the PIV measurements which led to reduced velocity deficit on the lower part of the wake for the closely spaced arrays, whereas wider spacing saw increased velocity deficits towards the test section floor.

4.2.6 Further Discussion of Experimental Wake Characterisation

The single turbine wake characterisation has shown that a velocity deficit of 12% remained at 20D downstream of the turbine and a turbulence intensity of 7% was measured at the same position. The ambient turbulence in the CWC experiment facility was 2% and the wake of the tidal turbines in the array experiments shows velocity deficits between 30% and 40% with respect to the array inflow at the downstream end of the test section at 20D. The wake characteristics do not recover towards the low ambient turbulence and ambient current velocities due to the location of the last measurement station accessible during the experiment which is about 12D downstream of the last turbine arranged in array and the low ambient turbulence intensities. For array tests, the rate of wake recovery downstream of the array is higher due to the increased turbulence within the flow before reaching the downstream turbine. Further influences of the wake either side of the array centreline will be investigated numerically.

Comparison between the wake recovery of a single turbine operating in the low ambient turbulence intensity CWC with the WWC Flume experiments, with a turbulence intensity of 10%, shows that initial recovery is significantly accelerated for higher turbulence as well as showing recovery towards free stream velocities at 20D downstream where remaining velocity deficits of up to 5% were recorded.

Large differences observed between numerical and experimental wake characteristic in the near wake of the tidal turbine models highlight the drawbacks of large scale flow field recordings with high velocity shear and where structures are located within the recordings. The resulting wake deficits and turbulence intensities are affected by the time step used during experiments and reflections of the model surfaces. Where no obstructions are located within the recordings and with distances of 4D and more behind the turbine, the agreement between numerical and experimental wake characteristics is much improved.

The rotor centreline has been used across most tidal turbine studies for quick comparison of wake recovery and rotor performance characteristics. Centreline (or hub height) deficits have been used in previous studies where a vertical shift was observed (e.g. Chamorro *et al.*, 2013; Myers and Bahaj, 2010). The vertical shift of the wake centreline is observed in the present experiments, but is not predicted in the same manner in the numerical results shown here, hence the hub height was used for comparison to similar studies. For the investigation of array effects

with turbines operating axially aligned in the wake of an upstream turbine, the velocity deficit at the centreline is used because the inflow velocity is commonly determined at rotor centre height upstream of the individual turbine. Hence, in this study the hub height deficit is used for characterisation instead of the maximum deficit occurring at each position.

Visual inspection of the resulting flow field maps has shown that a vertical shift of the location of maximum velocity deficit can be observed, which is caused by a combination of the existing velocity shear in the ambient flow, though small, and the relatively low positioning of the turbine models in relation to the test section water depth. In combination with the array support structure, an additional wake was observed forming close to the test section floor that led to slow moving flow on the lower part of the wake, thus decreasing the re-energisation of the wake in comparison to the upper part which experiences mixing with the fast flowing ambient flow. The observed flow field thus shows similar characteristics to that observed with an increased roughness bed in the experiments by Myers and Bahaj (2010).

Visualisation of the flow field in the WWC Flume have shown accelerated flow around the turbine structure as well as giving a detailed insight into initial wake development and the influence of waves on the upper part of the near wake.

The most significant advantage of PIV measurements applied to wake characterisation is that undisturbed flow field recordings can be made. Depending on the required resolution of flow features under investigation, the size of the flow field can be adapted with relative ease. Difficulties in recording and processing measurements across highly sheared flows and flow where objects are present within the recordings introduce some challenges in terms of determining appropriate time stepping of the image recording as well as interrogation window size settings for post-processing and vector calculations.

4.3 Numerical Investigation of CWC Tidal Turbine Wake and Turbulence

Having characterised the hub-height wake for a single turbine and arrays of four turbines from experiment, and compared to the numerically obtained velocity deficit and turbulence intensity, further investigation of the three-dimensional flow field is presented in the following section. Additionally to the wake characterisation of a single turbine, a comparison of the wakes obtained with eddy-viscosity based (k - ω SST) and Reynolds stress transport based turbulence closure models is provided. Furthermore, a comparison of the resulting wakes using different turbulent mixing length scale definitions is included to stress the importance of correctly modelling the specific dissipation rate for tidal turbine flow simulations.

The numerically obtained flow field for the tidal turbine arrays is used to further examine and investigate the flow within and downstream of the array to determine the characteristics of the parameters governing the wake recovery and their specific evolution as shown in the experiments. For the simulation of array cases, a further investigation of the performance of individual turbines within the array is presented and time-averaged performance indicators, i.e. C_P and C_T, are provided.

Further flow insights such as vortex evolution and interaction with support structure and influence on the wake shape and flow recovery are sought using vortex identification criteria such as the Q-criterion. The Q-criterion is defined such that a positive Q value identifies a vortex as an area where the vorticity magnitude is greater than the magnitude of the strain rate (McNaughton, 2013) with the formulation shown in Equation (4-1).

$$Q = \frac{1}{2}[(tr(\nabla U))^2 - tr(\nabla U \cdot \nabla U)] = \frac{1}{2}\left(||\Omega||^2 + |S|^2\right) \qquad (4\text{-}1)$$

where Ω is the vorticity tensor and S the rate-of-strain tensor, tr() denotes the trace of the matrix.

4.3.1 Single Turbine Wake Characterisation

The wake of a single tidal turbine is further investigated and characterised numerically providing insights into the flow field and processes of wake recovery at a number of locations downstream of the rotor. Detailed flow characteristics are provided at several stations downstream of the turbine. A comparison of modelling aspects such as the turbulence closure model and characteristics of the wake using different specification of the turbulent mixing length defining the ambient inflow for the *k* - ω SST model is included for further reference. Brief comparison of the wake recovery for increased turbulence intensity of 10% has also been included from numerical simulations in the CWC with SST model and 10% turbulence intensity.

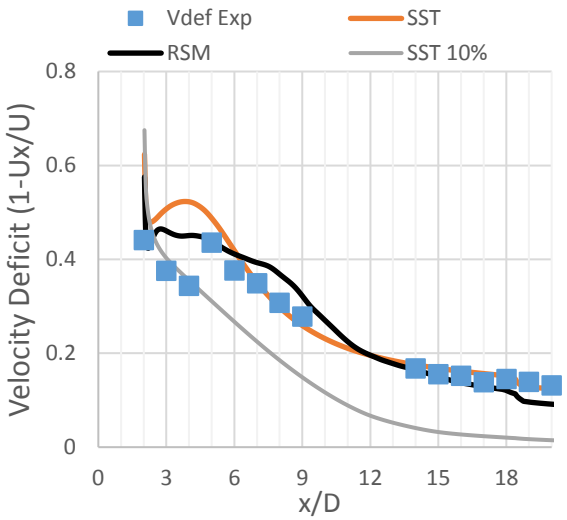

Figure 4-25 - Comparison of Wake Velocity Deficit with SST and RSM Turbulence Closure at 2% Ambient Turbulence and SST Turbulence Closure at High Ambient Turbulence Intensity of 10%.

Comparison of the wake evolution between the LRR RSM and *k* - ω SST model (Figure 4-25) shows similar wake velocity deficits over most of the numerical domain, especially in the far wake. Differences between the two models are most pronounced in the area just downstream of the turbine nacelle, between 3D and 5D. The RSM turbulence closure is expected to perform better in this area due to the isotropic turbulence assumption used to model the Reynolds stresses in the *k* - ω SST model. The wake recovery is slower at the centreline for the RSM case between 5D and 11D which can be attributed to the slower moving layer of fluid crossing towards the wake centreline as shown in Figure 4-26. Further downstream the two models perform very similar and agree well to the velocity deficit obtained from the experiments. Towards the downstream end of the domain, near 20D, the domain cell sizes increase which

shows different effects in the two turbulence models. From about 12D downstream, wake velocity deficit is lower for the higher order closure model towards the end of the computational domain. For increased ambient turbulence intensity (SST 10%), faster wake recovery is observed and velocity at the wake centreline recovers to within 1% of the ambient current velocity upstream of the turbine. Far wake recovery is similar to previous studies conducted at 8% - 10% ambient turbulence with similar remaining velocity deficits Stallard *et al.* (2013).

A comparison of the instantaneous and time-averaged flow field in Figure 4-26 shows for both types of turbulence closure model that the wake starts breaking down at approximately 10D downstream of the turbine and the ambient flow reaches towards the wake centreline. The effect of turbulence closure model is more pronounced in the instantaneous wake field compared to the time-averaged solution, showing slightly accelerated wake recovery far downstream of the turbine. Up to 10D the characteristics of the wakes are similar between the two closure models.

The differences in the near wake recovery (x/D < 5) are further investigated by examining the flow field in terms of the mean velocity fluctuations on the turbine hub height shown in Figure 4-27. The Reynolds stress model predicts a more turbulent flow field close to the turbine where high turbulence levels are expected and the rotational flow persists and shows its advantages over the eddy-viscosity models in handling anisotropic turbulence and rotational flows. However, as shown before, the effect on the wake characteristics is localised and the two models compared here predict similar wake characteristics with increasing distance from the turbine.

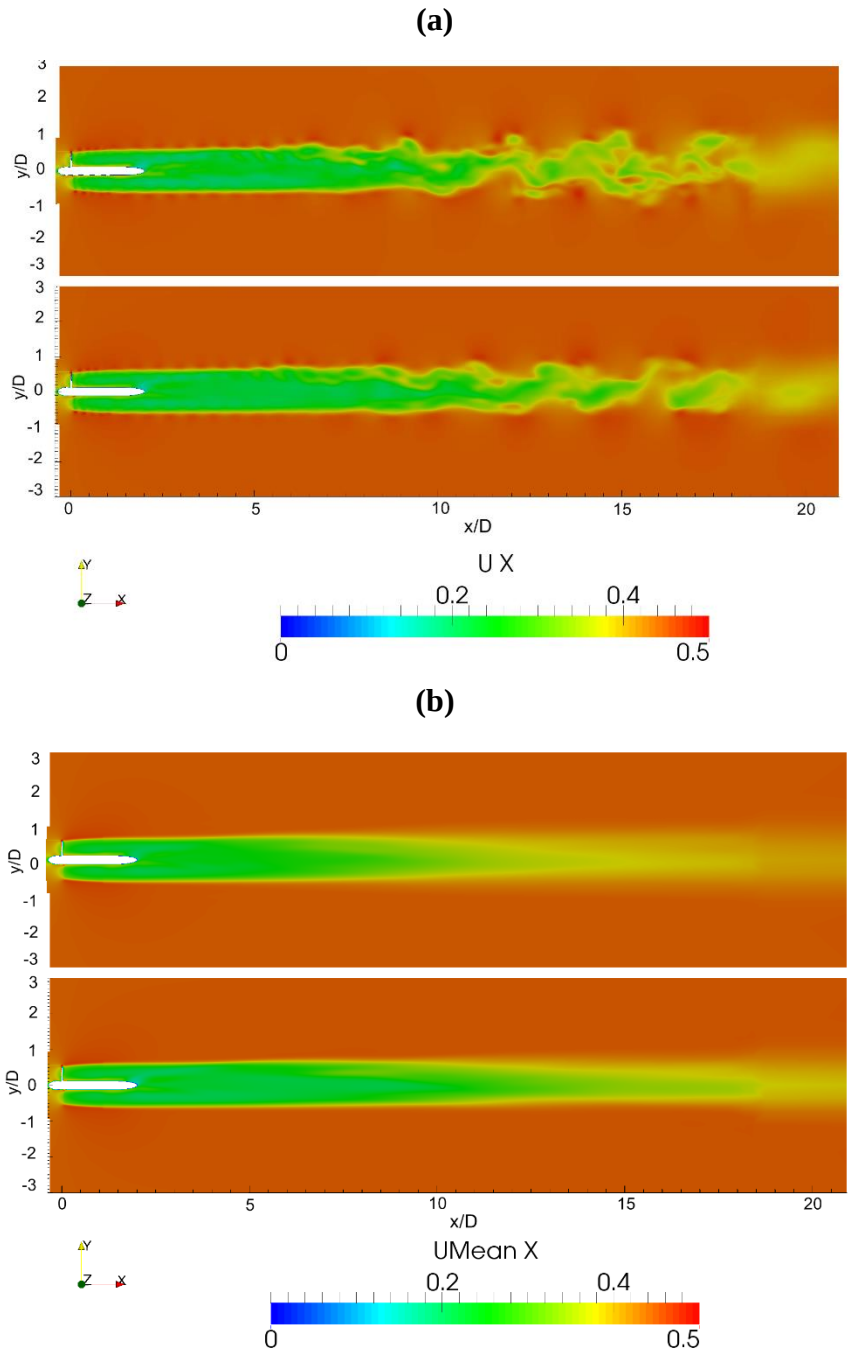

Figure 4-26 – Comparison between RSM (Top) and SST (Bottom) Turbulence Closure for (a) Instantaneous Wake and (b) Time Averaged Wake.

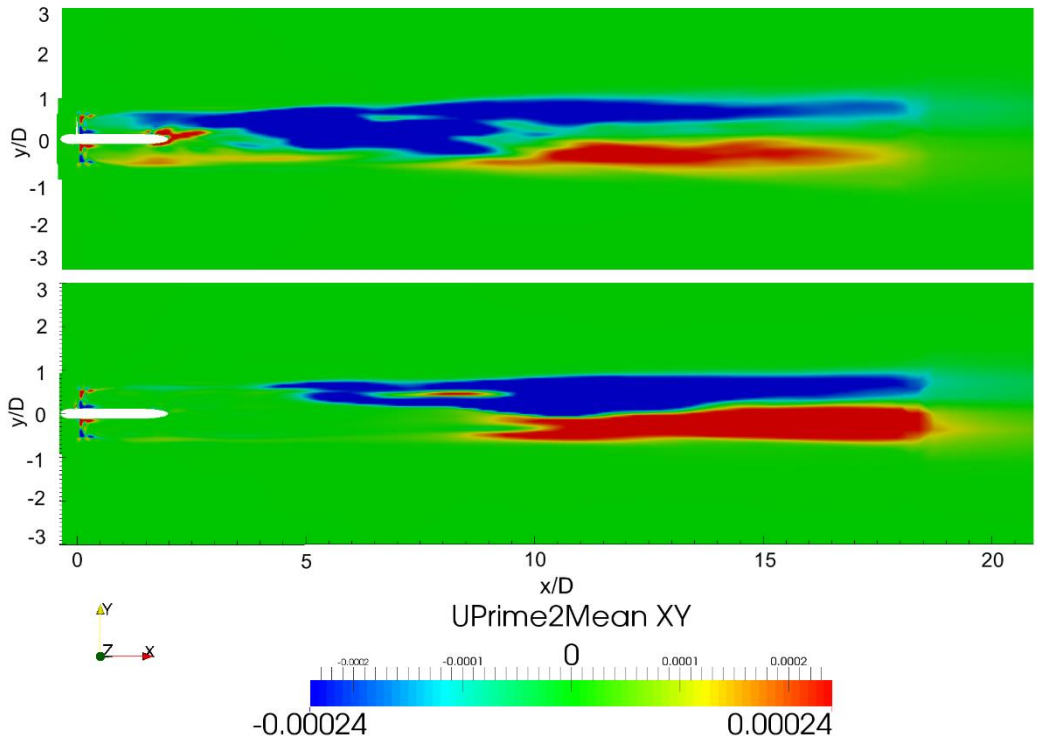

Figure 4-27 – Variance of Velocity (Uprime2Mean) Components (*uv*) Comparison of RSM (Top) and *k*-ω SST (Bottom) Turbulence Model.

Detailed characterisation of velocity deficit on the horizontal plane (Figure 4-28) and turbulence intensity (Figure 4-29) as well as vertical velocity deficit (Figure 4-30) for the various inflow parameters and turbulence models used are shown in the following. While the transverse and vertical velocity deficit at 2D just downstream of the nacelle shows little difference between the different modelling approaches and ambient turbulence intensities, the wake recovery further downstream reveals small differences in the wake shape and velocity deficit for both, transverse and vertical profiles.

A faster transition to bell-shaped velocity profile is observed with higher turbulence intensity for transverse and vertical profiles and at 20D the velocity deficit has almost recovered at the centreline of the wake with a remaining deficit of approximately 1.5%. The turbulence within the rotor height remains similar between both cases up to 10D where for the 10% case the wake turbulence has almost recovered to ambient levels. Closer to the turbine, turbulence intensity recovers to inlet levels at 15D and further recovers to below inlet levels at 20D.

The increased specific dissipation rate obtained by using a smaller reference length (L_2) when calculating the mixing length scale leads to a faster transition to the bell-shaped velocity deficit profile. The lower dissipation rate (L_1) and RSM velocity deficit show more asymmetric features and transition to bell-shaped profiles downstream of 10D only. The differences are most pronounced in the medium wake between 4D and 10D where the SST model with highest omega (ω) shows best agreement with the experiment in terms of the hub-height velocity deficit.

The vertical profiles show increased wake recovery at the top half of the wake (z/D = 0.5) compared to the lower part of the wake and recovery to ambient flow velocity by 20D while a deficit between 5% and 15% remains at the lower half and centreline respectively.

The transverse plots of Reynolds Stresses (*xy*) in Figure 4-31 show that most mixing occurs between 6D and 8D with the highest Reynolds stresses occurring at the rotor tip locations (z/D = ± 0.5). Further downstream where the wake flow has recovered to ambient flow velocity little mixing occurs across the wake.

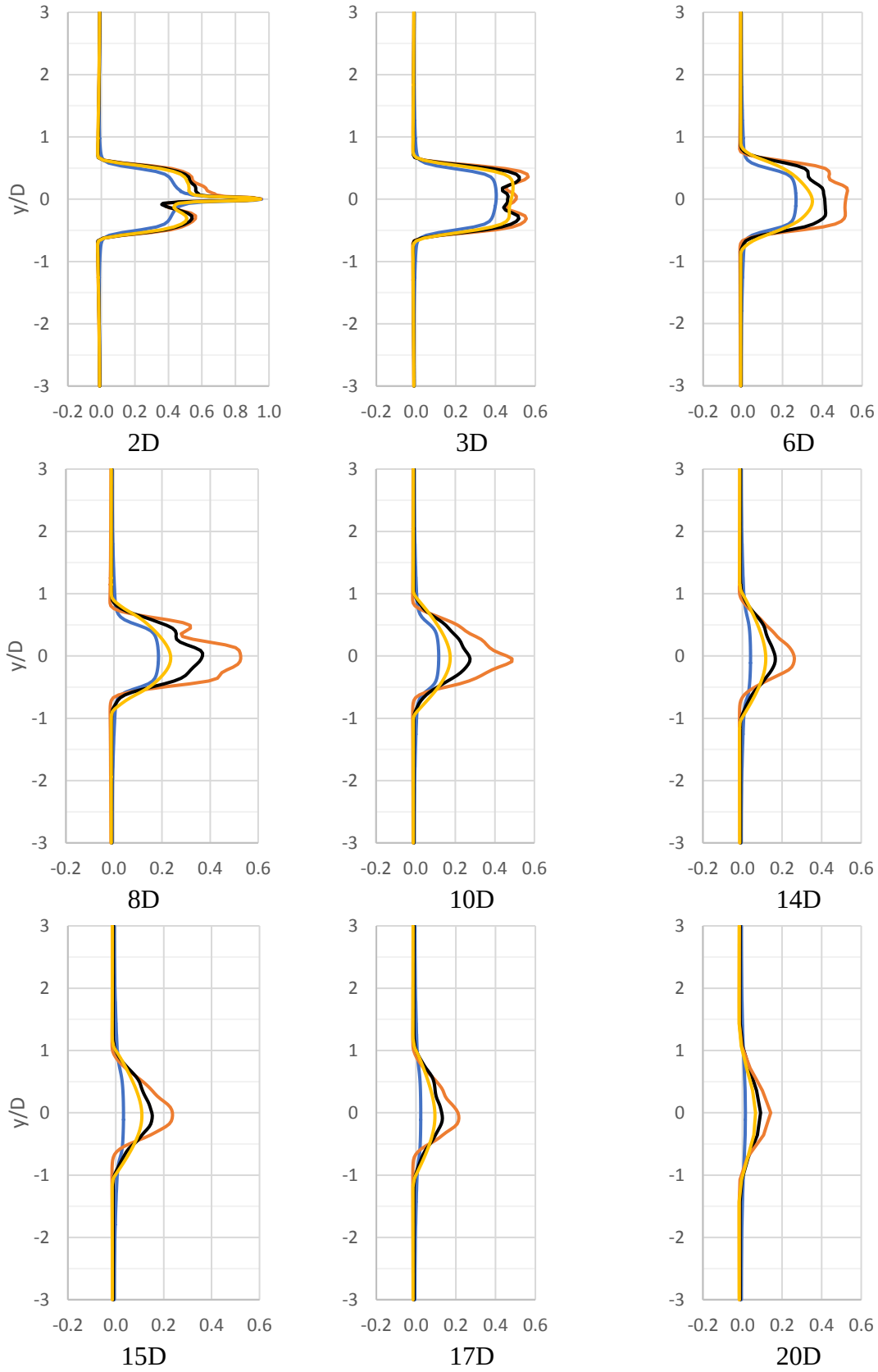

Figure 4-28 – Transverse Wake Velocity Deficit Comparison between RSM (Black) and *k* - ω SST Turbulence Model for L_1 (Orange), L_2 (Yellow) and Ti 10% (Blue).

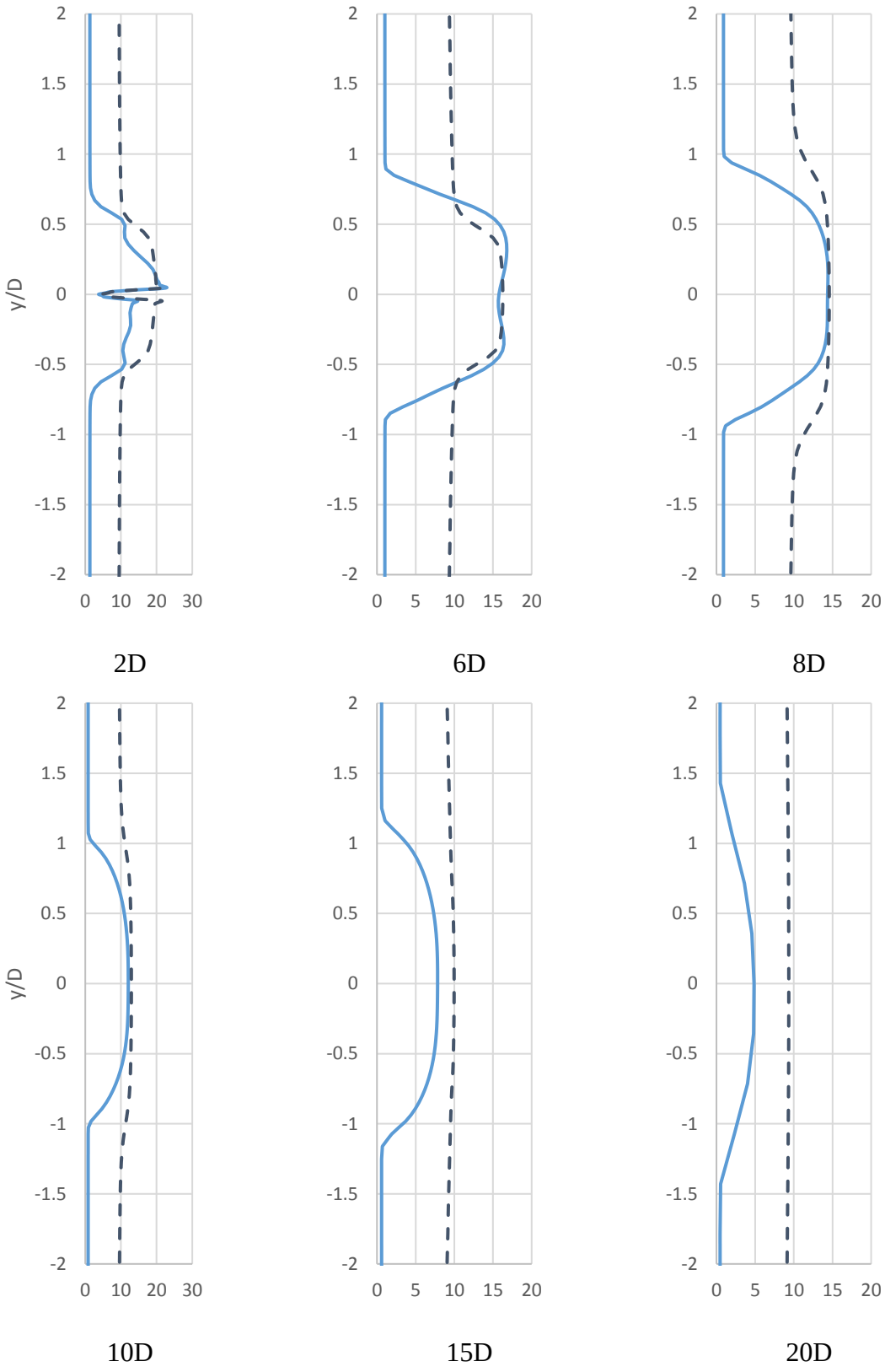

Figure 4-29 – Transverse Turbulence Intensity Comparison in Wake of A Single Turbine with Ambient Turbulence Levels of 2% (Solid) and 10% (Dashed).

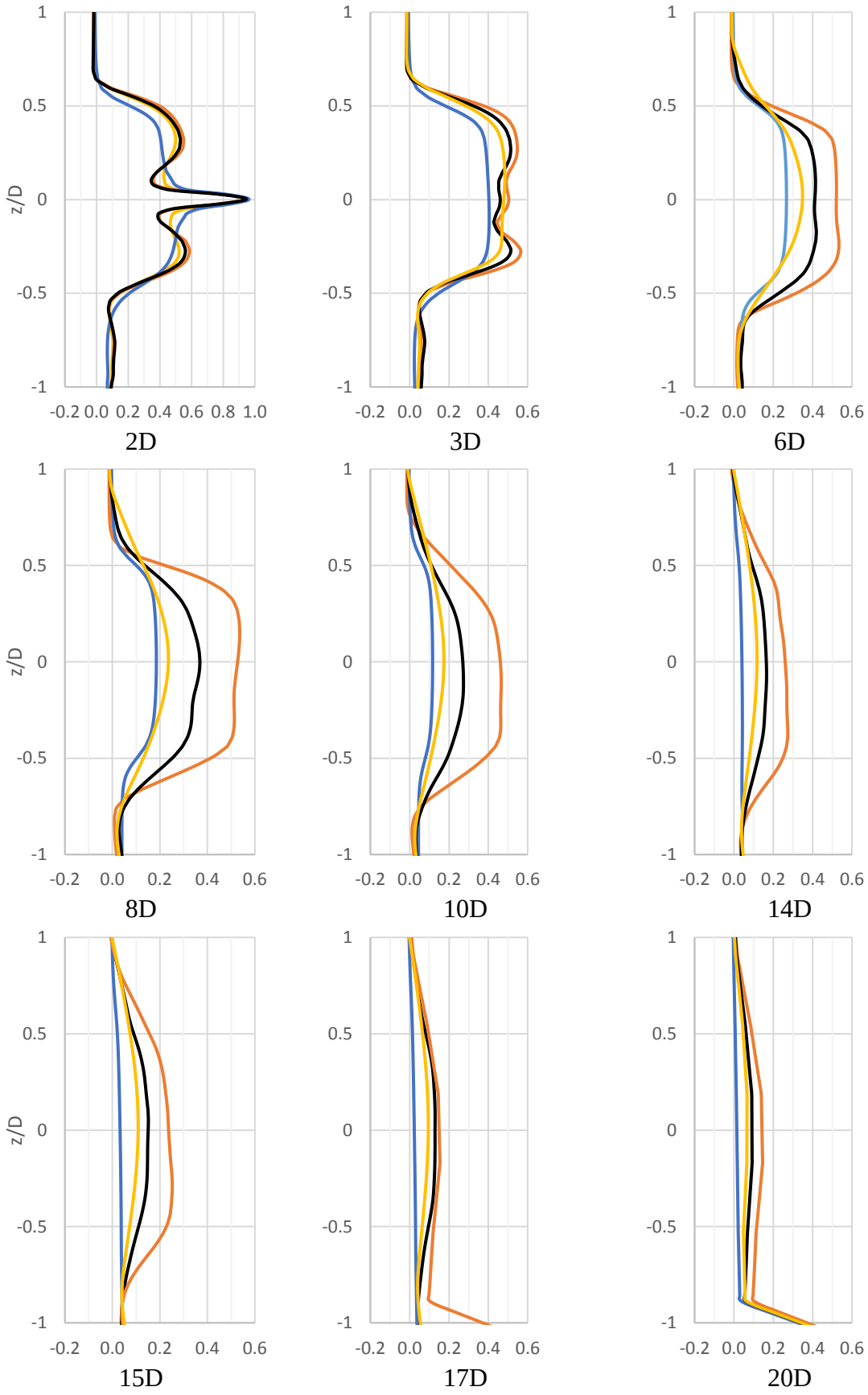

Figure 4-30 – Vertical Wake Velocity Deficit Comparison between RSM (Black) and *k* - ω SST Turbulence Model for L_1 (Orange), L_2 (Yellow) and Ti 10% (Blue).

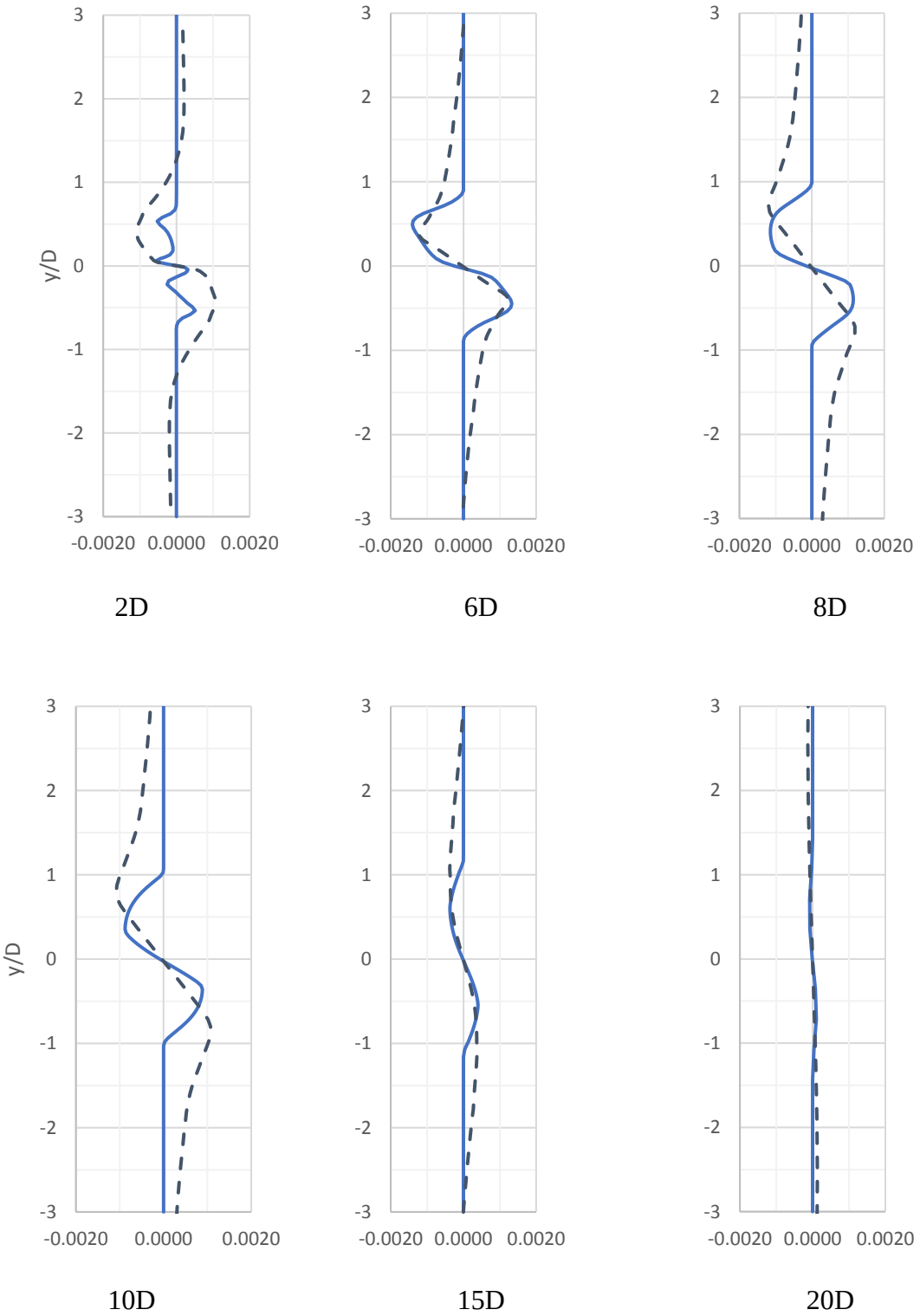

Figure 4-31 – Transverse Profile of Reynolds Stress (*xy*) for the Wake of a Single Turbine with Ambient Turbulence Levels of 2% (Solid) and 10% (Dashed).

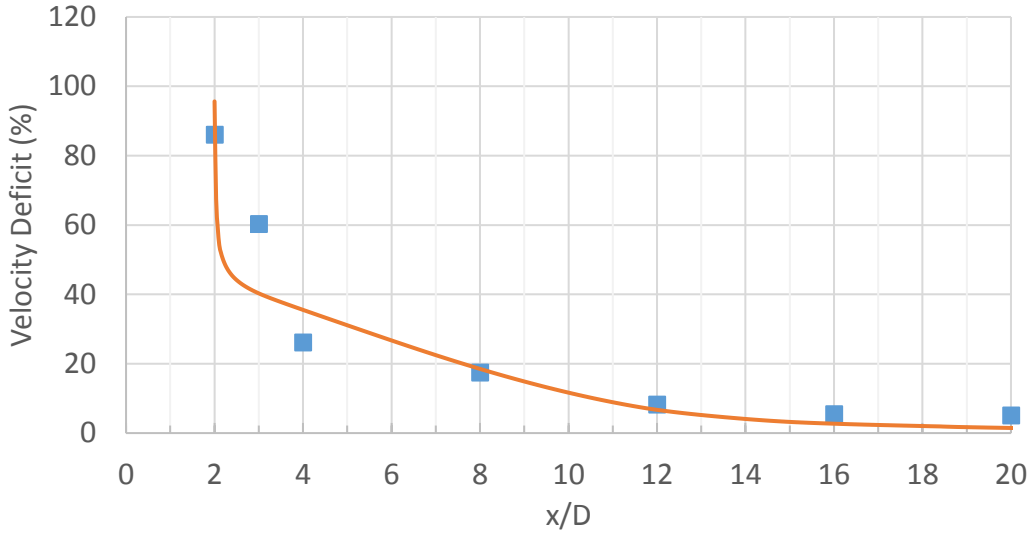

Figure 4-32 - Comparison of Single Turbine Wake Velocity Deficit from Experiment in WWC Flume (Box) with Single Turbine Numerical Simulation at 10% Ambient Turbulence Intensity in the CWC (Line).

The comparison of wake recovery between two single turbines in ambient turbulence intensities of 10% (Figure 4-32) shows very similar wake recovery and remaining deficits of approximately 1% at 20D. Agreement between numerical simulation and experiment is very good from 8D. Differences are expected due to the increased blockage ratio experienced during the experiments, however with high ambient turbulence levels wake recovery is largely dominated by the ambient flow conditions especially for the medium and far wake. The disagreement at 3D and 4D may be a result of ambient flow being diverted around the turbine and moving towards the wake centreline further downstream thus reducing the initial wake recovery but increasing it when the accelerated flow reaches the centreline. Further numerical simulations with the exact replication of the fluid domain are required to further assess the numerical wake recovery.

4.3.2 Array Wake

The centreline flow field within the array upstream of the last row turbine is shown in Figure 4-33 and compared between the array configurations. The close transverse spacings of L3T15 and L5T15 show increasing velocity deficits up to 2D downstream of the respective middle row turbines. Initially the recovery is accelerated for the L5T15 array between the two rotors located off the array centreline at 5D, indicating the ambient flow being directed towards the array centre. Further downstream the velocity deficits increase due to the influence of the second row turbines. The wide transverse cases show steadier wake recovery, although small increases are seen for L5T3 between 7D - 10D. Between 2D and 0.5D upstream of the last row turbine the velocity deficit increases for all cases ranging from 5% increase for the closely spaced arrays to 10% for wide transverse separation of the middle row turbines. 1D upstream of the downstream turbine inflow velocity deficit is 10% lower for the L5T3 case compared to L5T15 while the difference for the L3T15 to L3T3 array is about 6%.

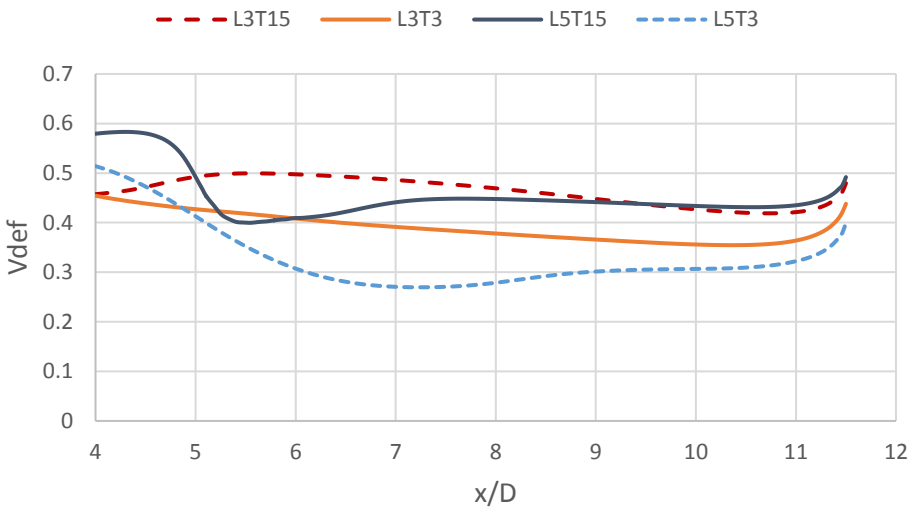

Figure 4-33 - Comparison of Velocity Deficit Evolution at Array Centreline Between Different Array Formations from Numerical Simulation.

Comparison of array wake characteristics across the two longitudinal spacings of L3 and L5 are shown in Figure 4-34 (a) and (b) respectively. Close transverse spacing (T15) showed a higher remaining velocity deficit for a longer distance downstream within the array section for both longitudinal spacings tested and an increase of velocity deficit 2D downstream of the second row followed by slow velocity recovery at the array centreline. Downstream of the array the rate of wake recovery is very similar with the T3 cases showing slightly accelerated recovery and little differences in the remaining velocity deficit are seen.

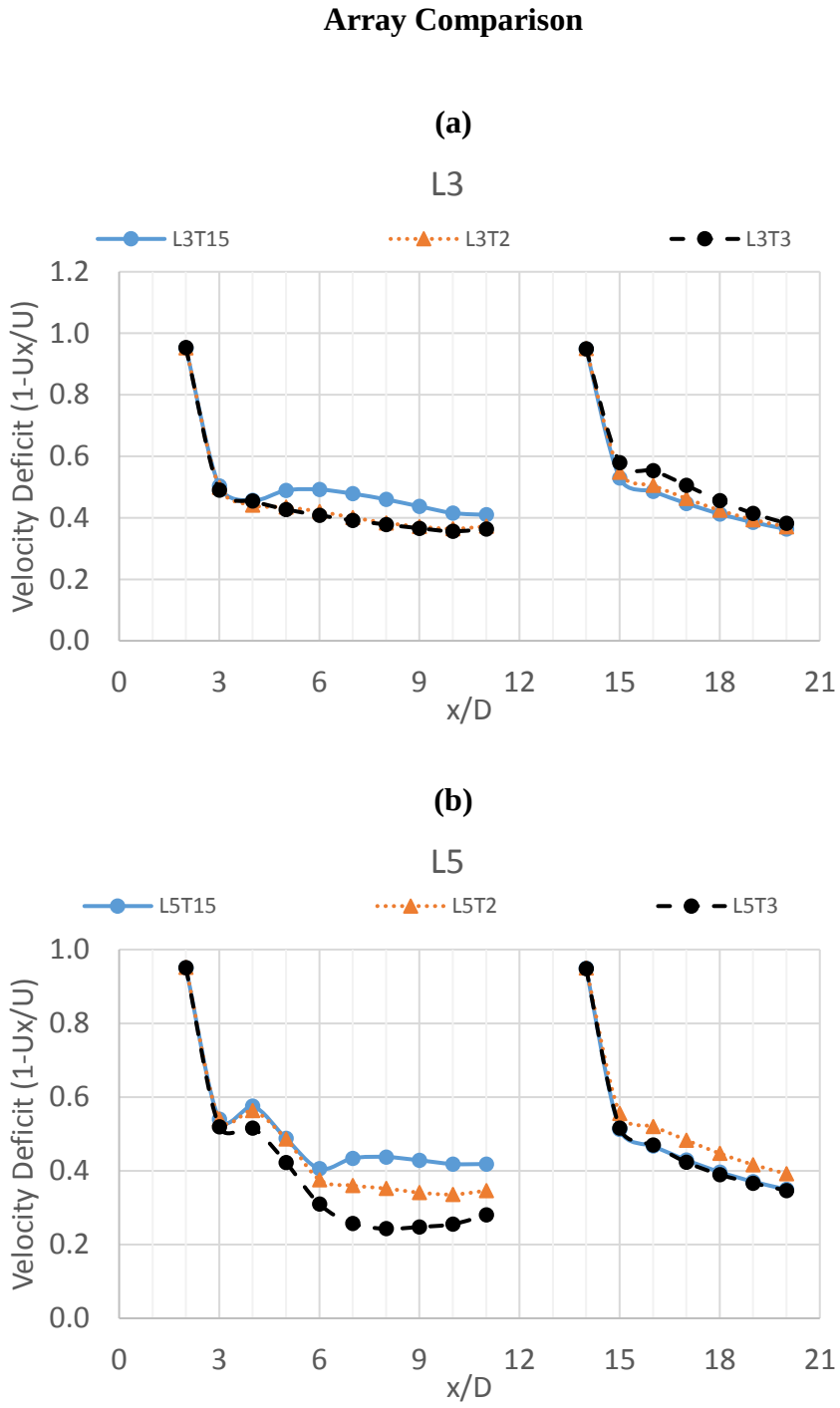

Figure 4-34 - Comparison of Wake Velocity Deficit for Arrays with Longitudinal Spacing of (a) L3 and (b) L5.

Comparison of the centreline velocity deficit on the vertical plane (*xz*) for L3 arrays (Figure 4-35) shows an area of reduced deficit just downstream of the second row rotors for T15 and T2 in (a) and (b) respectively, where the ambient current is flowing towards the array centreline due to the increased blockage of the two rotors thus reducing the velocity deficit. Downstream of the second row turbines, a stronger velocity deficit is seen. The vertical array centreline shows that the transverse spacing influences the vertical characteristics of the wake with a more pronounced area of slow moving fluid being present and larger variations of the velocity deficit across the rotor height ranging from 20% to 45%. This will influence the performance and optimum tuning of downstream turbines operating in a highly varying flow field across the rotors.

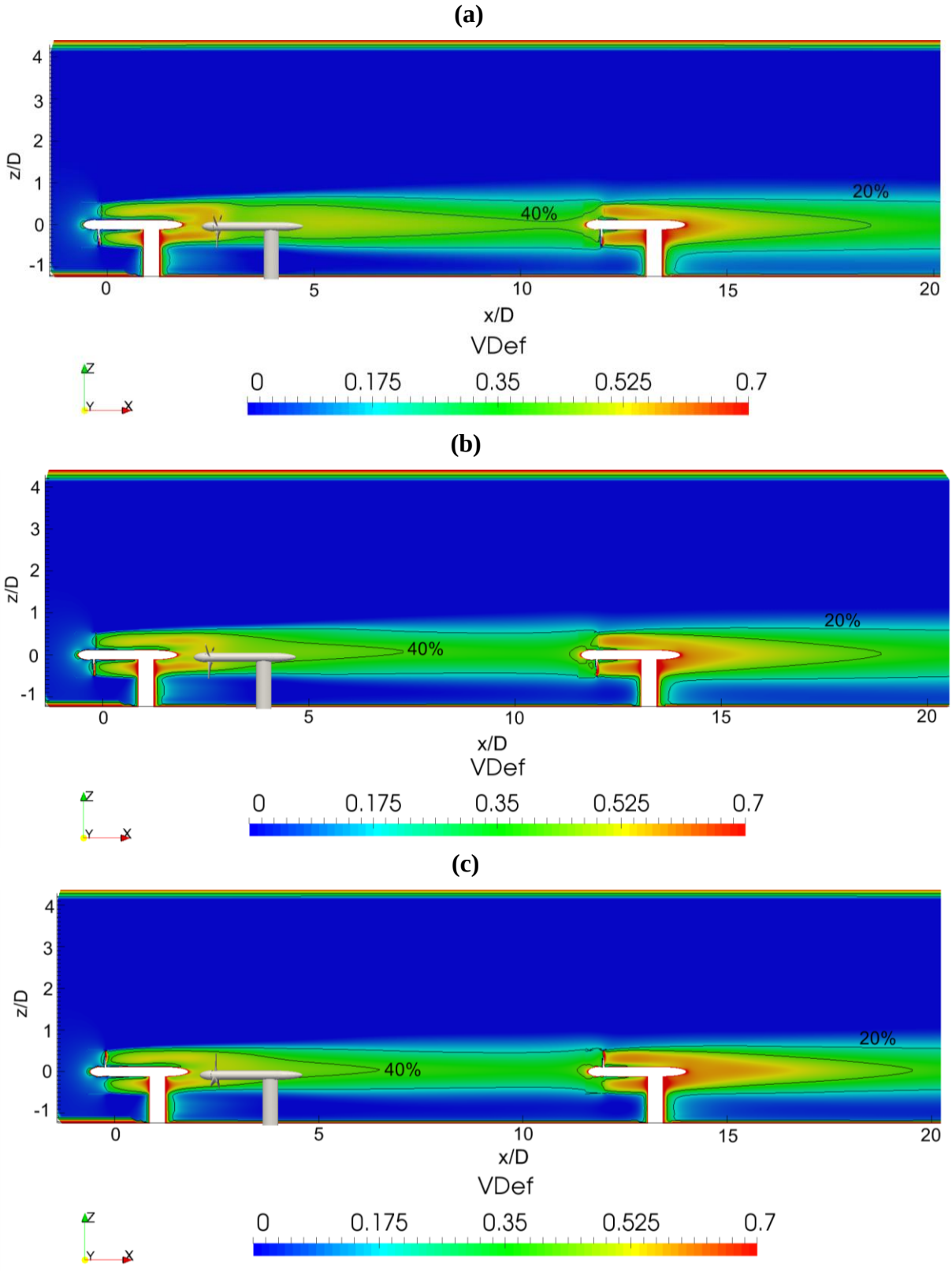

Figure 4-35 - Wake Velocity Deficit Contours for (a) L3T15, (b) L3T2 and (c) L3T3.

The differences in the resulting wake field within and downstream of the array can be observed in Figure 4-36. With closer transverse and longitudinal spacing of L3T15 in (a), the flow field shows a single combined wake without ambient flow penetrating between the adjacent turbine wakes. An area of slow moving fluid, spanning the entire area behind the three turbines, can be seen at the array centreline downstream of the second row. The initial wake of the first turbine reduces in deficit between the rotors of the second row and is less pronounced in the near wake behind the rotor blades for the second row turbines when compared to L5T3 in (b). However, the velocity deficit increases further downstream as shown previously in Figure 4-34 for close transverse spacing.

For the increased longitudinal spacing in Figure 4-36 (b), the initial wake develops behind the turbine structure showing an increased velocity deficit but faster recovery downstream of the second row turbines. The wake expands and then contracts between the two middle row turbines and wake expansion is observed again at 2D downstream of the second row turbines. The ambient flow separates the adjacent wakes and individual wakes can be clearly identified. Downstream of the array, a larger velocity deficit persists in the transverse direction, however flow of increased velocity can still be observed between the adjacent wakes. While downstream of the array the centreline wake is expanding, the outer wakes see asymmetrical recovery due to mixing with the accelerated fluid between the centre wake and the outer wake and slower mixing with the ambient flow outside the array sections. For the first and second row turbines, a wake at the downstream end of the nacelle can be observed where the vertical support interferes with the rotational flow, which is less pronounced for the structure of the downstream turbine operating in increased turbulent flow.

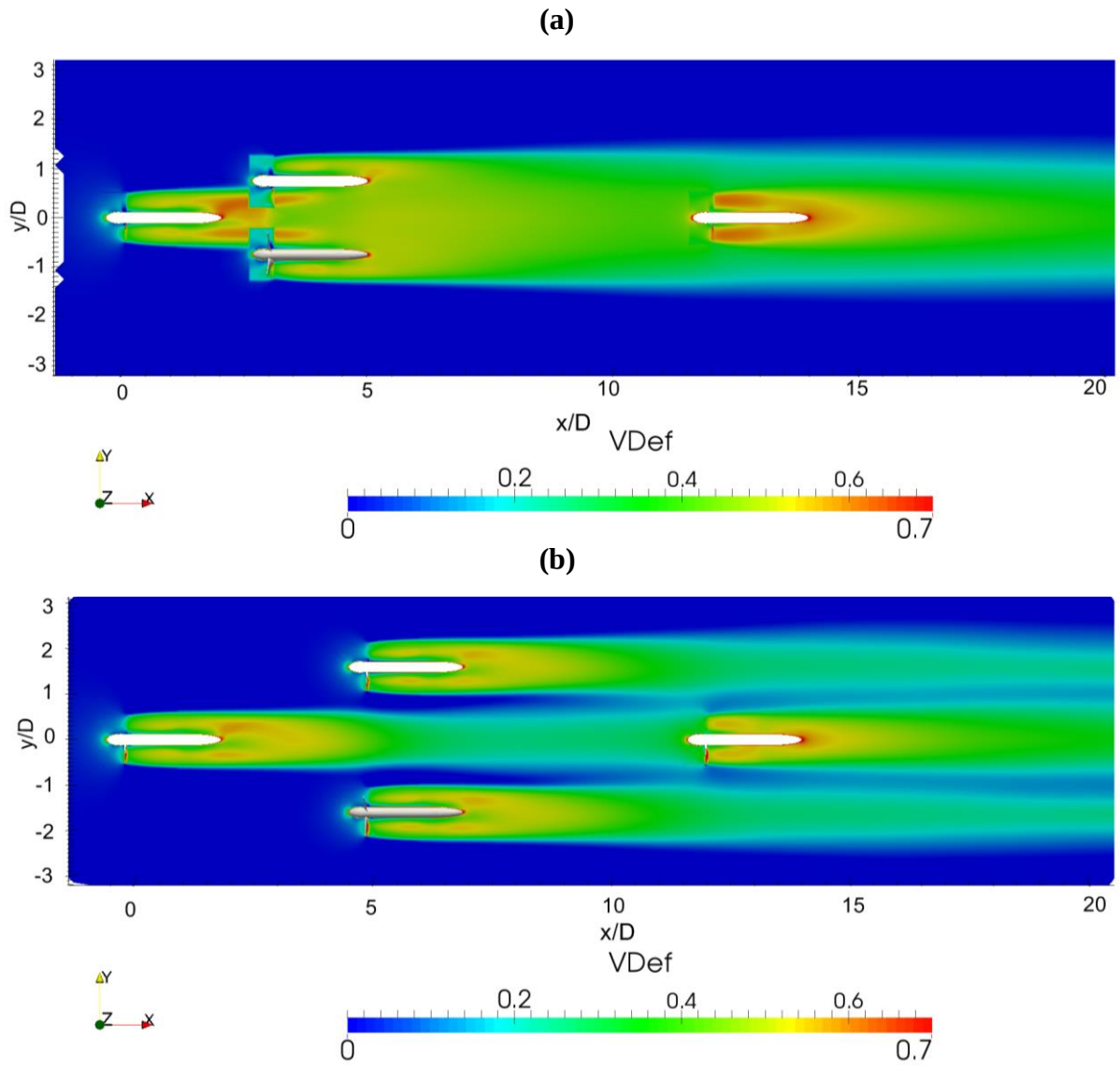

Figure 4-36 – Comparison of Velocity Deficit between (a) L3T15 and (b) L5T3.

The transverse wake velocity deficit profiles at three different stations for all 6 configurations are presented in Figure 4-37, showing wake development and dissipation across the transverse domain at hub height. With transverse spacing of T15 a single wake is identified for L3 at 8D and 10D with the highest velocity deficit at the centreline and the profile resembling a bell-shaped curve. For T2 and T3, individual wakes are identified. It can be seen that increased mixing with the ambient flow occurs in T3 up to 10D at $y/D > 0$ where the velocity deficit of the free stream between the wakes is increased compared to $y/D < 0$. This could indicate a slight movement of the wake towards the $y/D > 0$ side which is in the direction of wake rotation (the turbine blades are rotating anti-clockwise direction when looking from the upstream direction towards the array). Downstream of the array T15 and T2 transverse spacings result in a single,

combined wake where the T2 wake is wider in the L3 arrays than L5. For T3 spacing, three individual wakes exist downstream of the last turbine and increased velocity deficits can be observed in $y/D > 0$. The peak velocity deficits in the combined or individual wakes do not differ significantly in terms of velocity deficit. The similarities of the downstream wake recovery were observed in experiments as well.

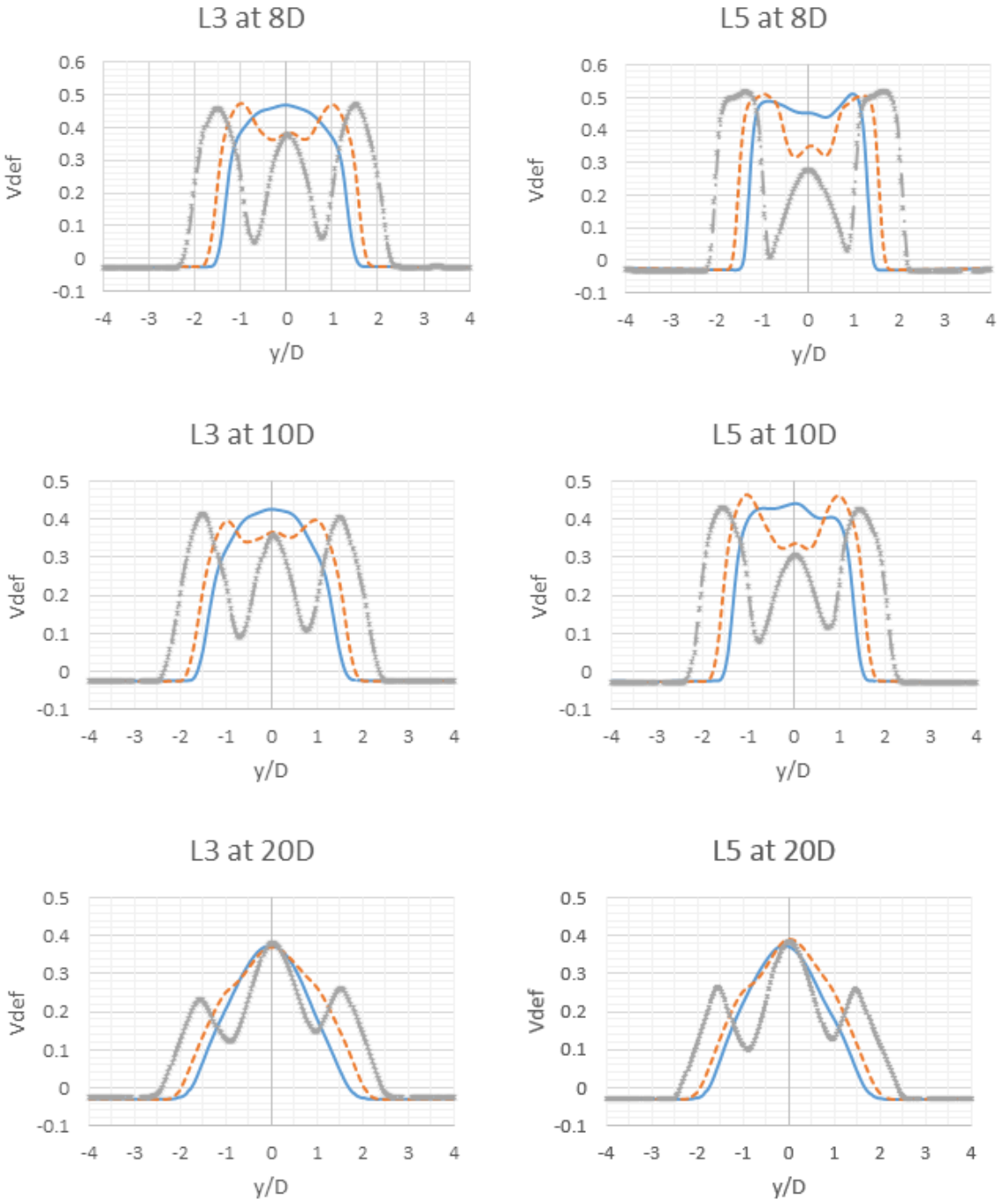

Figure 4-37 - Array Transverse Profiles of Velocity Deficit T15 (Solid), T2 (Dash) and T3 (Cross).

The transverse turbulence intensity contours in Figure 4-38 show a combined wake for the close longitudinal and transverse spacing in the L3T15 array, in (a). The large area downstream of the first and second row turbines shows turbulence levels between 20% and exceeding 30% in close proximity of the downstream rotor blades in the second row and around the support structure for the downstream turbine. However, while turbulence intensities are high, the velocity recovery is slow due to the confined wake of all three turbines acting as a large single wake where ambient flow does not mix with the volume of very slow moving fluid. Lower velocity deficits are seen for L5T3, in (b) and areas of ambient flow are present between the wakes of each turbine from the first two rows. As observed in Figure 4-36 (b), wake recovery is increased between 6D and 11D due to the mixing with ambient flow.

The slow and turbulent inflow to the downstream turbine causes a significantly increased turbulent wake around the turbine structure exceeding 40% turbulence intensity and persisting 2D downstream of the turbine (Figure 4-38). The flow fields of the downstream turbine are similar between the two cases which reflects the similarities in wake recovery observed downstream of the array section. Small areas of increased turbulence intensity are seen where the turbulent wakes are interacting about 10D downstream of the first turbine rotor. The transverse wake extent of 6D is increased for the L5T3 array compared to the transverse extent of approximately 4D seen for the L3T15 array.

(a)

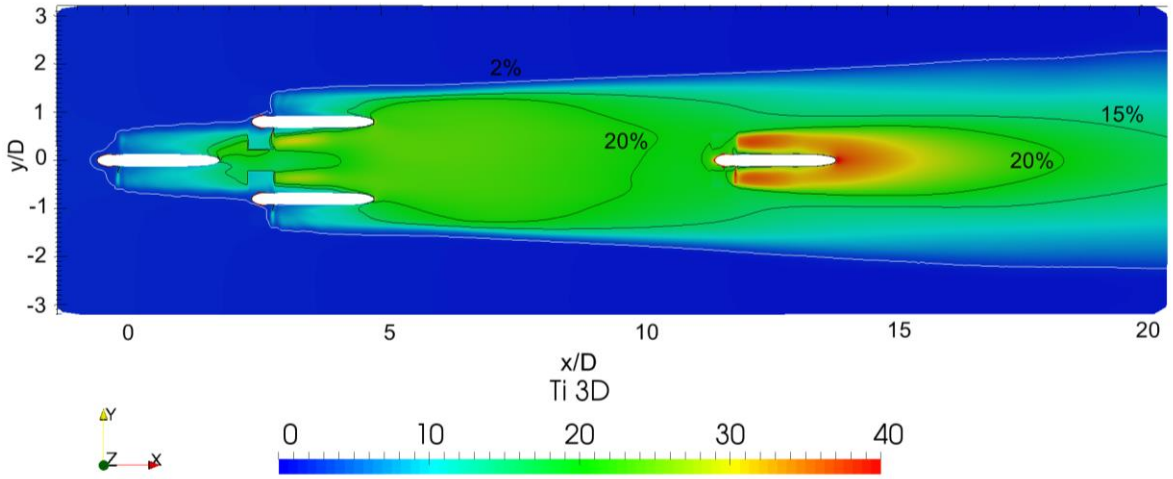

(b)

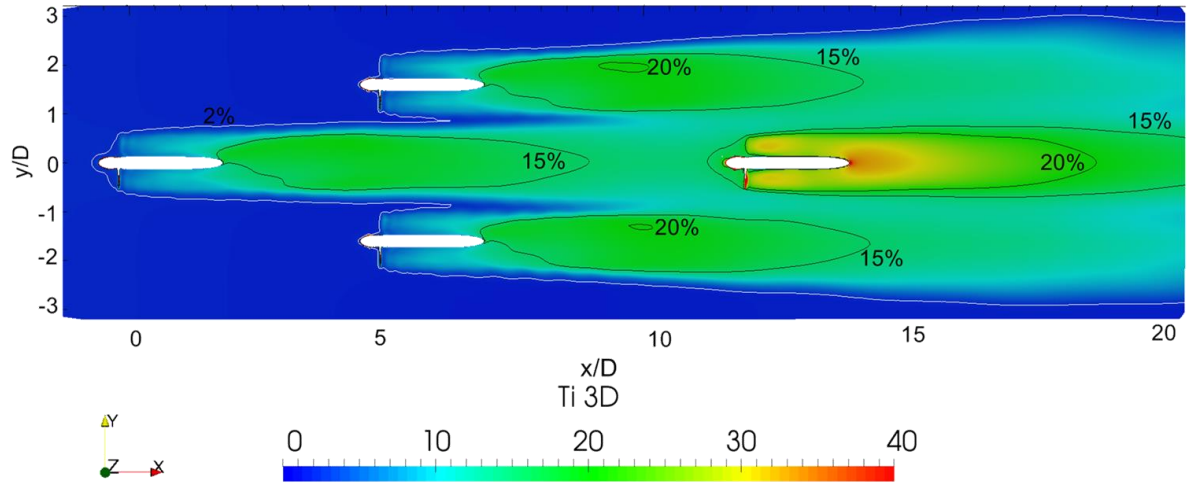

Figure 4-38 - Array Wake Turbulence Intensity Contours for (a) Horizontal Plane of L3T15 and (b) L5T3.

The Q-criterion is used to visualise vortices and shows the evolution of these downstream of the rotor. With low ambient turbulence, the breakdown of vortices shed of the turbine blades is delayed as can be seen in Figure 4-39 (a) and (b), showing a comparison between a single turbine at two different ambient turbulence levels (2% and 10%) in the near wake up to 6D. The upstream and the downstream array turbine vortices are shown for L3T15 in (c) and L5T3 in (d). The spacing between vortices increases around the area where the vertical support interferes and vortices begin to break down. The wake contracts between the second row turbines in L5T3 and where the shear layer starts expanding, about 2D downstream of the two rotors located at 5D, the vortices of the outer wakes break down and wake expansion is observed for the outer wakes. The vortices shed by the Far and Near turbine are significantly affected for L3T15 and break down within a distance of 1D downstream of the rotor due to being located in the turbulent wake of the upstream turbine. The downstream turbine shows the vortices to break down immediately downstream of the rotor due to the highly turbulent inflow. Wake expansion of the downstream turbine is more significant immediately downstream of the vortex break-down for the downstream turbine.

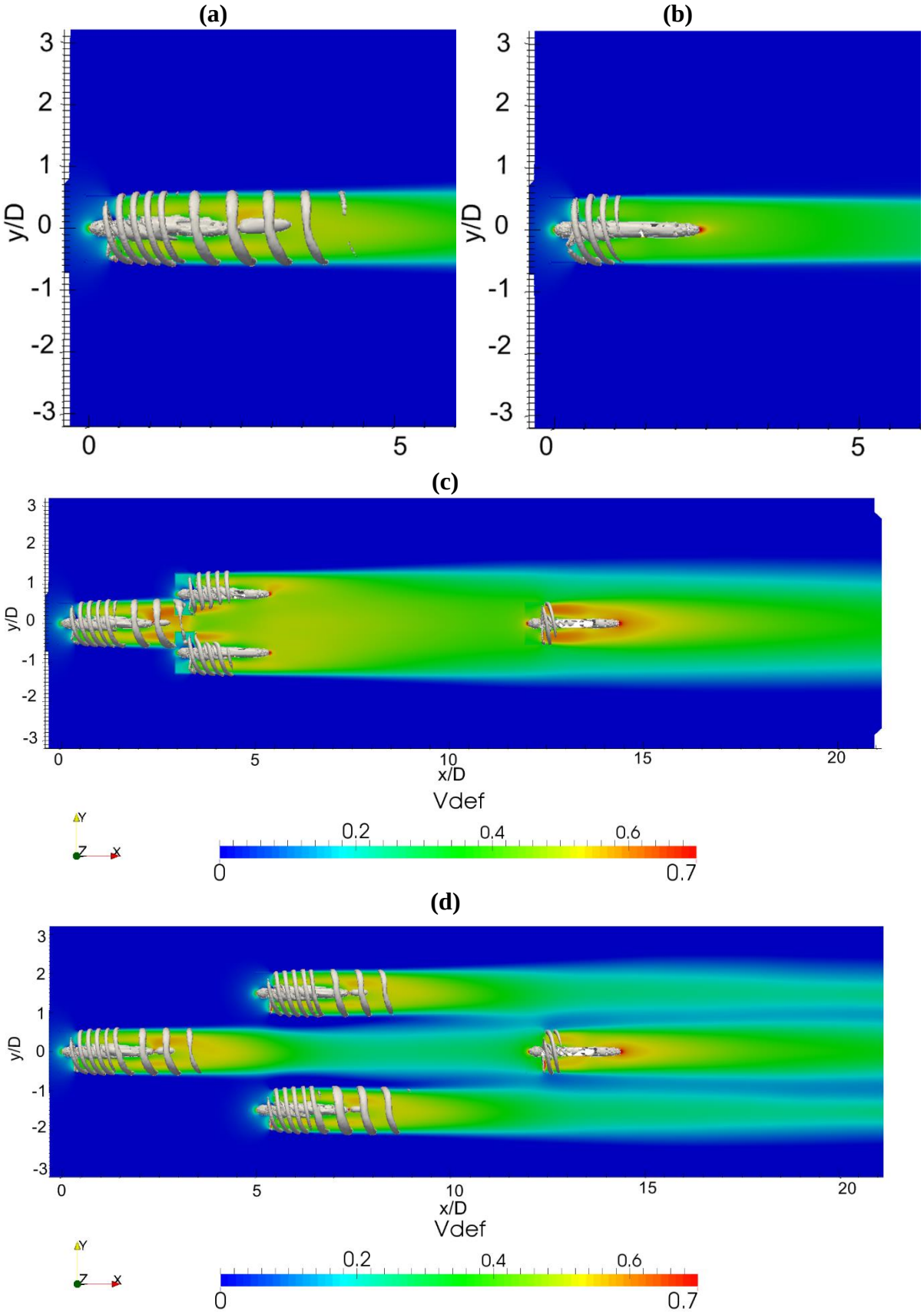

Figure 4-39 - Velocity Deficit and Q-criterion (Q=2) for Propagation of Vortices Around the Turbine Support Structure for (a) Single 2% (b) Single 10% (c) L3T15 and (d) L5T3 Array.

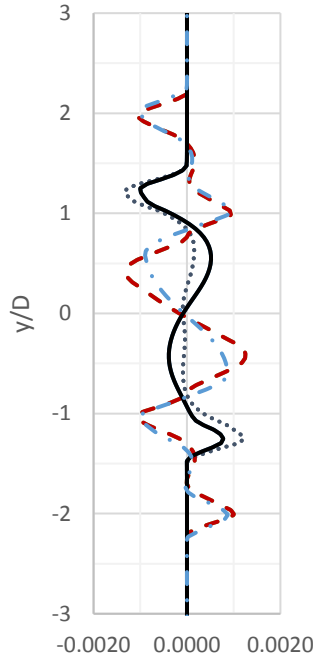

3D downstream of 2nd Row Rotor

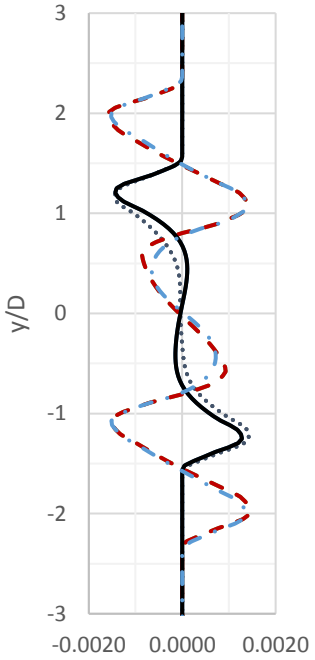

5D downstream of 2nd Row Rotor

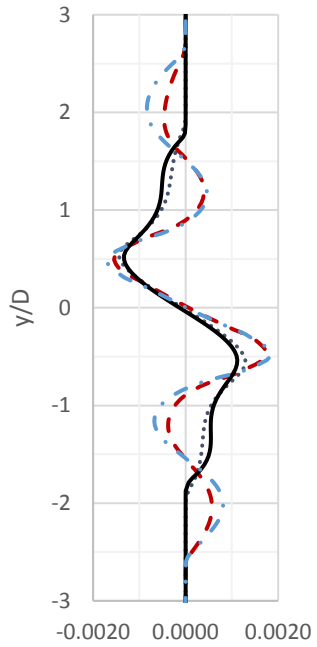

3D downstream of Last Turbine

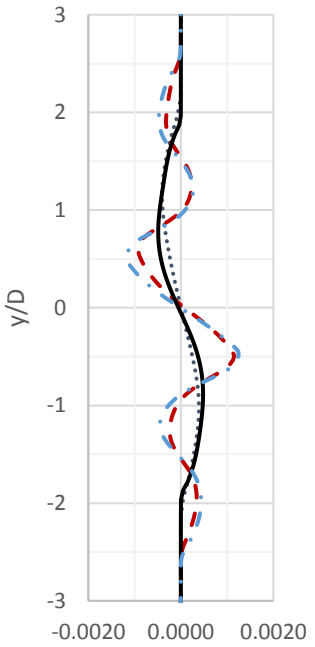

5D downstream of Last Turbine

Figure 4-40 - Transverse Profiles of Reynolds Stresses (*xy*) for L3T15 (Dot), L3T3 (Dash), L5T15 (Solid) and L5T3 (Dash Dot).

A comparison of the variation of Reynolds stresses in the *xy* plane at different downstream distances from the second row of turbines is shown in Figure 4-40. The existence of a large area of slow moving fluid in L3T15 as shown in Figure 4-36 (a) results of little mixing within the array wake from -1D to 1D transversely from the rotor centre at 3D downstream. At 5D downstream of the second row the mixing layers are wider and show only the outer mixing with ambient current around the array. For increased separation, increased mixing can be observed and individual peaks corresponding to the respective turbines located in the array are clearly shown. Downstream of the array (b) the differences are less pronounced, but for close transverse spacing a diffuse mixing layer is observed whereas individual layers can be seen for the wide transverse separation.

Further investigation of the transverse distribution of Reynolds stresses in the *xy* plane is presented in Figure 4-41, comparing the Reynolds stress field within the array among four different array configurations with minimum and maximum transverse spacing for both longitudinal configurations. The most significant observation is that with close transverse and longitudinal spacing for the L3T15 array in (a), very little mixing occurs at the centre part of the array downstream of the second row turbines. In comparison with L5T15 in (c), the flow re-energisation at the centreline is greatly reduced and mixing occurs mostly with the ambient flow either side of the array section. This corresponds to the existence of a large volume of very slow moving fluid identified in Figure 4-36 and shows the beneficial effects of longitudinal spacing increasing the wake mixing. For both close transverse spacing arrays the mixing downstream of the array section shows similar characteristics with an increase in mixing around the turbine and a more diffused field of increased Reynolds stresses further downstream.

With wide transverse spacing, mixing can be observed on each individual wake as well as downstream of the array section. The ambient flow between adjacent wakes can clearly be seen as a small volume where little mixing occurs. This persists through the entire array section. From the obtained data it can also be seen that the wakes of the two outer turbines of the middle row are diverted around the centre wake of the downstream turbine. Increased mixing for a longer distance is observed downstream of the array section.

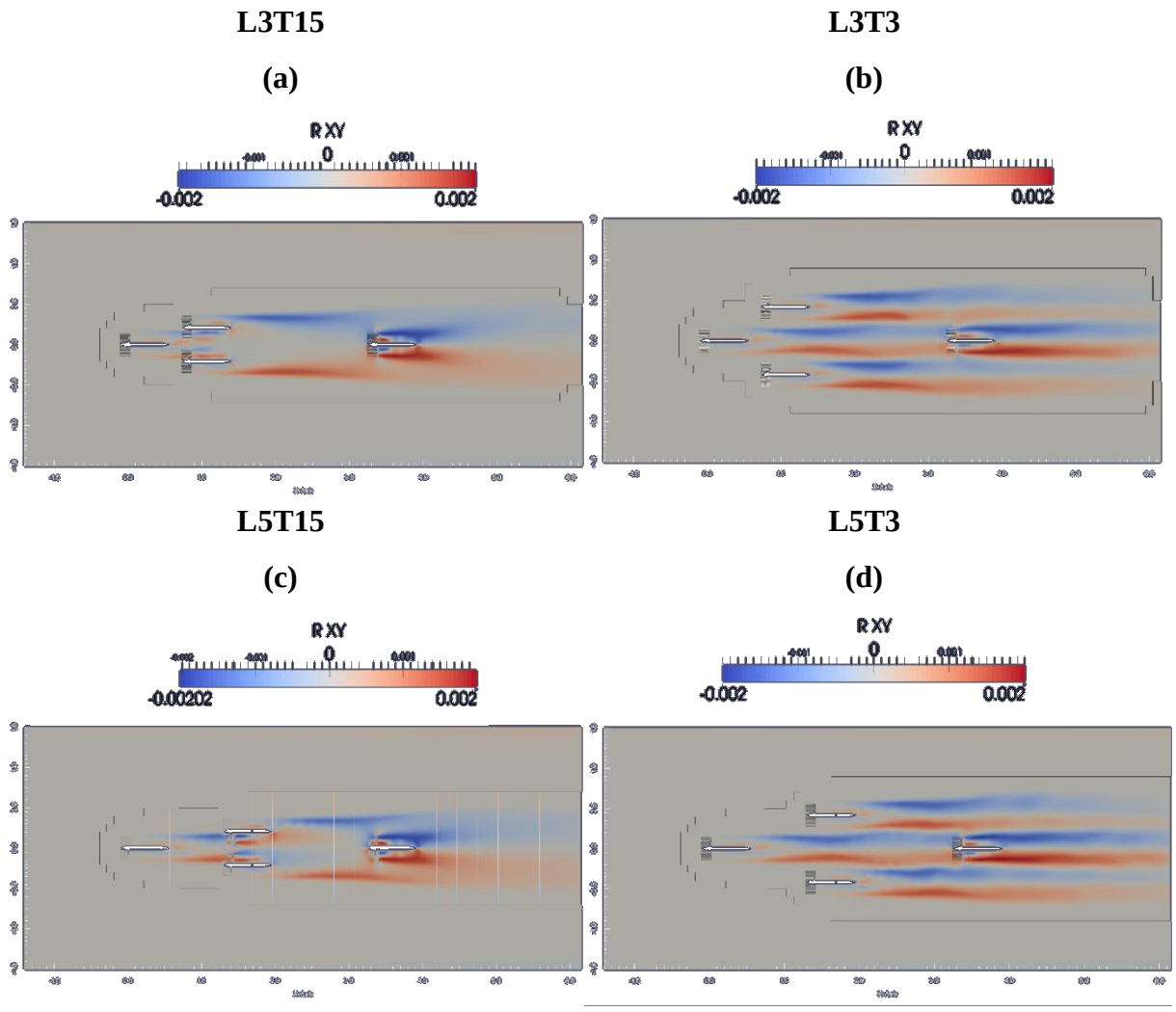

Figure 4-41 – Comparison of Reynolds Stresses in (*xy*) Plane Between Different Array Configurations Showing the Mixing with Ambient Flow.

A comparison of the wake recovery for the two turbines located off the centreline is shown in Figure 4-42. Turbines are referred to as "Far" corresponding to the turbine located for $y/D > 0$ (top turbine in Figure 4-41) and "Near" for the turbine located in $y/D < 0$ (bottom turbine in Figure 4-41). For close transverse spacing shown in Figure 4-42 (a), the differences between the two turbines are slightly larger for the increased longitudinal separation of L5. For both cases, the Far turbine sees slightly increased wake recovery at the centreline of the turbine. For wide transverse spacing of the middle row turbines (b) the differences are less pronounced for the large longitudinal spacings tested and for L3T3 the Near turbine wake recovers faster between 9D and 18D. In (c) and (d), for close spacing, the influence of the last row turbine can be seen at 9D and 7D downstream of the middle row turbines respectively, increasing wake

recovery where flow accelerated around the rotor and an increase in velocity deficit further downstream due to the combined wake of the entire array as shown in Figure 4-36.

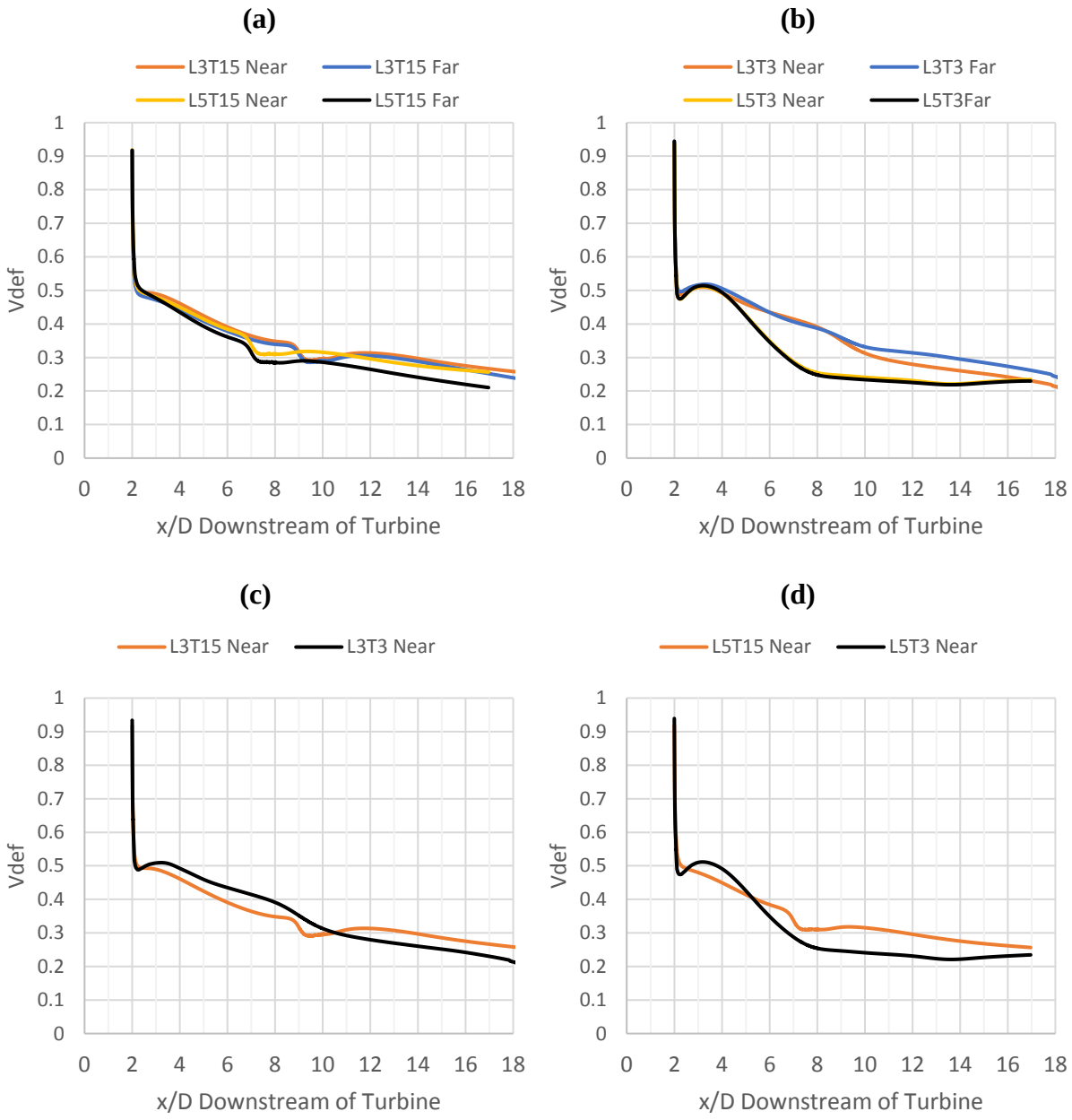

Figure 4-42 – Wake Recovery of Near and Far Turbine for Different Longitudinal and Transverse Array Spacing.

4.3.3 Array Turbine Performance

While the main focus of the project was to determine the influences of array spacing on the resulting flow field, and little performance characterisation of turbines operating in array has been conducted experimentally, the numerical simulations allow for comparisons of performance of individual turbines in array. Ultimately, power producing performance is the final indicator of an arrays commercial performance thus a brief summary of the achieved performance of each turbine is presented in the following. Additionally, the performance of an isolated tidal turbine operating in a higher ambient turbulence flow is included as well.

The thrust and power coefficients for all turbines are presented in Table 4-1. Performance data for the downstream turbine has been calculated based on the array inflow conditions (U_∞) and the numerically predicted inflow velocity one diameter upstream of the turbine, averaged across circular elements along the turbine diameter. Data is presented for all four turbines, the second row turbines are denoted as “Near” and “Far”.

It can be seen that while the operation of the first turbine is constant across all configuration, the second row turbines operate similar to an isolated turbine with large transverse spacing and show lower power coefficients when close to or operating in part of the upstream wake for arrays with transverse spacing of T15. The performance of the downstream turbine is significantly reduced, as expected due to operating off design point (TSR = 4) with an effective TSR of 5.4 to 6.5 due to the slowed inflow conditions.

For increased turbulence intensity of 10% the thrust acting on the turbine structure is increased while the average power coefficient is equivalent to that at 2% ambient turbulence intensity. The loading on the tidal turbine structure is thus increased but performance of the specific rotor design tested here is not affected significantly by the increasingly turbulent flow.

Table 4-1 - Comparison of Operating Conditions of Turbines in Array, Velocity Upstream of Array (U_∞) and 1D Upstream of Last Turbine are Used for Calculation of TSR, Thrust and Power Coefficient of Downstream Turbine. The TSR is 4 for All Turbines in Ambient Flow, and the Effective TSR for the Downstream Turbine has been Included.

	Single 2%		**Single 10%**		**L3T15**		**L3T3**		**L5T15**		**L5T3**	
Turbine	**C_T**	**C_P**	**C_T**	**C_P**	**C_T**	**C_P**	**C_T**	**C_P**	**C_T**	**C_P**	**C_T**	**C_P**
Upstream	0.70	0.34	0.73	0.34	0.70	0.33	0.70	0.32	0.70	0.33	0.70	0.33
Far					0.62	0.27	0.71	0.30	0.64	0.29	0.74	0.38
Near					0.63	0.25	0.70	0.32	0.65	0.29	0.74	0.35
Downstream	Effective TSR				6.3		5.4		6.5		5.4	
	Array (U_∞)				0.36	0.04	0.43	0.09	0.34	0.02	0.46	0.11
	U_{1D} Upstream				0.9	0.13	0.79	0.19	0.95	0.08	0.65	0.23

4.3.4 Summary Numerical Investigation

The comprehensive CFD study presented here showed the applicability of transient RANS simulations with a rotor-stator interface to account for the effects of rotating tidal turbine blades and the flow field characterisation in tidal turbine arrays. Three-dimensional RANS simulations with the $k-\omega$ SST turbulence model and RSM closure model have been compared to data from experimental measurements and show good agreement for a single turbine and with the array sections tested. Further improvements to the numerical set-up are required to achieve better agreement at locations close to the turbines.

Further analysis of the numerical flow field and individual turbine performance has shown that:

- Definition of the specific dissipation rate is vital for achieving matching wake predictions and best results are achieved when the turbulence mixing length is based on turbine blade characteristics rather than depending on the operating environment.
- RSM and $k-\omega$ SST turbulence closure models showed similar predictions of wake velocity deficit. The RSM model performed better closer to the turbine, where the effect of rotating flows and increased turbulence are significant.
- Investigation of the transverse mixing has provided explanations for the stagnating flow observed in experiments and numerical simulations for close transverse spacing within the inner array section. Mixing with surrounding flow is significantly reduced and no wake re-energization occurs at the centerline of the array. High turbulence intensity alone does not lead to increased recovery if no mixing with faster moving fluid is possible.
- Vertical shifts of the wake are less pronounced than in experiments, the main reason for this is the omission of the array support frame which was used in the experiments to locate and move the turbine models on and showed development of an additional wake between the turbine wake and test section floor, especially for close transverse spacing.
- Performance of the second row turbines is slightly reduced for close transverse spacing where part of the rotor is located within the wake of the upstream turbine. With large transverse spacing the first and second row turbines show similar thrust and power coefficients.

- The downstream turbine is significantly affected by the position in the wake of the upstream turbines with the lowest performance for increased longitudinal and close transverse spacing (L5T15) with a reduction of approximately 60% compared to the single turbine and upstream turbines. For wide transverse spacing the power coefficients are reduced by 43% and 31% for L3T3 and L5T3 respectively.

Chapter 5. Conclusion and Future Works

The work presented in this thesis has described the design of a scaled tidal turbine model intended to be used for the wake characterisation of turbines operating in a number of multi-turbine arrangements. The experiments conducted with the model turbine include the wake characterisation of single turbines in two different operating conditions for ambient turbulence intensity and proximity to bounding surfaces. The WWC Flume experiments further investigated the effects of multi-turbine arrangements for up to three turbines axially aligned. The CWC experiments investigated the effects of longitudinal and transverse inter-device spacing in a staggered array configuration of four tidal turbine models. The comprehensive numerical modelling for single and staggered array cases is presented and the resulting flow field predictions are validated against experimental measurements and used to further investigate the complex flow field around tidal turbine devices. Further comparison of numerical methodologies is included for additional insight into the turbulence model parameters and their influence on the wake modelling. The following section presents the conclusions that are drawn:

5.1 Conclusions

A comprehensive analysis of single turbine and multiple turbine arrangements has been presented with the aim to investigate the wake characteristics and turbulence effects in tidal turbine arrays. By conducting a combined experimental and numerical study, focusing on the wake recovery in tidal turbine arrays, several important contributions have been made to the existing body of knowledge.

Multiple scaled tidal turbine devices have been designed and tested in configurations that represent likely first and second generation deployment. It was shown that for tidal turbines operating in increased ambient turbulence levels and in axially aligned configurations with up to three turbines, the wake recovery is dominated by the ambient flow conditions and little difference was observed between different spacing configurations. Slightly increased wake recovery is observed in the near wake and lower velocity deficits remain at a downstream distance of 20D compared to the wake of a single turbine. A brief investigation of the effects of surface waves on the near wake flow field is presented showing slightly accelerated wake recovery.

The use of non-intrusive flow field recordings has been presented for the wake characterisation of tidal turbine arrays. The advantages and disadvantages of such measurements have been discussed and it was shown that PIV measurements provide beneficial insight into the flow field characteristics at significantly reduced complexity of measurement when compared to point measurements previously adopted.

The comprehensive array wake measurements conducted within and downstream of a staggered tidal turbine array provide valuable guidance on the effects of longitudinal and transverse device spacing for closely spaced tidal stream turbine arrays. While the inner array section was strongly influenced by the transverse spacing between turbines, the wake recovery downstream of the array was shown to be less affected by the spacing of upstream turbines in this low ambient turbulence intensity case. The experiments have highlighted the importance of wake re-energisation through mixing with ambient flow for accelerated wake recovery and shown that turbulence intensity in the wake alone does not provide an accurate insight into the wake recovery in closely spaced arrays. In addition, the wake characteristics presented here provide a first attempt to validate the numerical methodologies presented herein for the wake modelling in staggered turbine arrangements.

Comprehensive numerical modelling using fully resolved turbine devices and dynamic mesh capabilities within the open source software package OpenFOAM has been validated against the experimentally obtained wake data. The agreement between numerical and experimental wake characterisation was shown to be good and it was also highlighted that definition of turbulence inflow parameters is vital for achieving good agreement. Comparison of different length scale definitions has shown that for the bottom fixed turbines utilised here, mixing length scale definitions based on turbine characteristics such as the chord length produced significantly better agreement with experiments than mixing length scales defined by the operating environment, i.e. the turbine immersion or water depth. The three dimensional numerical simulations provided further explanation for the results of the experimental study and allowed investigation of the array flow field and wake developments away from the array centreline.

The present approach showed that utilising automated mesh generation simplifies the mesh generation process for complex three dimensional structures while providing accurate results in terms of turbine performance and wake characteristics. A detailed validation of the automatically generated meshes provides further contributions to the scarce body of literature

concerning the numerical modelling of tidal stream turbines. Accounting for the resolved blade shape and rotation showed good agreement with the experimental measurements and is important for predicting the accelerated near wake recovery when compared to simplified methods such as actuator disk modelling. Additional investigation into the breakdown of complex three dimensional flow phenomena and the performance of individual turbines in array is presented to highlight the capabilities of applying validated numerical models to array modelling.

The use of open source software, which has significant benefits for complex flow simulations utilising multi-core processing, has shown good agreement for the performance and wake characteristics of the tidal turbine model presented herein. This can have significant impact on the future research developments as large scale, and computationally expensive numerical modelling can be conducted without incurring excessive multi-core licensing fees.

5.2 Further Work

The presented work has focused on the wake characterisation for multi-turbine arrays using experimental and numerical methods. The insight presented here aims to provide an initial characterisation of the influences of multi-turbine spacing on the resulting flow field and has not included a detailed characterisation of the power performance of individual turbine devices arranged in arrays. Further work, both numerically and experimentally, to be undertaken in order to fully account for the effects of closely spaced tidal turbine arrays is outlined in the following.

5.2.1 Experimental Work

The wake characterisation presented here focuses on the main statistics used to quantify the effect of energy removal from tidal currents and determining appropriate spacing between turbines for the deployment of multi-turbine arrays. Wake recovery is investigated in terms of the turbine hub height velocity recovery. Further insights are to be sought to fully understand and explain the resulting wake behaviour, ideally by combining flow measurements on the vertical and horizontal plane of tidal turbine arrays to determine the extent of transverse mixing in more detail. In addition, PIV can be used to conduct detailed investigations of three-dimensional flow features by reducing the area of interest and adjusting the analysis to specific flow phenomena under investigation. Determining and optimising the actual power

performance of tidal turbines in array requires tuning individual turbines to their occurring inflow conditions and will provide further guidance on the spacing of array sections to optimise electricity generation.

5.2.2 Numerical Work

The immediate work following the presented project is to further investigate flow physics within the tidal turbine array with a specific focus on wake dynamics. Further investigation and validation of numerical array modelling with advanced modelling such detached eddy simulations (DES) or improved combination of simplified methods that reduce the meshing requirements can be performed to improve the computational efficiency and accuracy of simulations. Further numerical simulations investigating a wider range of operating conditions such as ambient turbulence and TSRs are required to gain insights into the flow field development under the complex environmental conditions faced by tidal turbine arrays. More realistic operating conditions should include modelling the tidal turbine rotation through the fluid imposed forces instead of specifying a constant rotation. Further analysis of the fluctuating forces due to the turbulent inflow in arrays will aid developers for structural design and control mechanism to optimise turbine performance and lifecycle management.

References

Abolghasemi, M.A., Piggott, M.D., Spinneken, J., Viré, A., Cotter, C.J. and Crammond, S. (2016) 'Simulating tidal turbines with multi-scale mesh optimisation techniques', *Journal of Fluids and Structures*, 66, pp. 69-90.

Afgan, I., McNaughton, J., Rolfo, S., Apsley, D.D., Stallard, T. and Stansby, P. (2013) 'Turbulent flow and loading on a tidal stream turbine by LES and RANS', *International Journal of Heat and Fluid Flow*, 43(0), pp. 96-108.

Ahmadian, R. and Falconer, R.A. (2012) 'Assessment of array shape of tidal stream turbines on hydro-environmental impacts and power output', *Renewable Energy*, 44, pp. 318-327.

Apsley, D.D. and Leschziner, M.A. (2000) 'Advanced Turbulence Modelling of Separated Flow in a Diffuser', *Flow, Turbulence and Combustion*, 63(1), p. 81.

Argyropoulos, C.D. and Markatos, N.C. (2015) 'Recent advances on the numerical modelling of turbulent flows', *Applied Mathematical Modelling*, 39(2), pp. 693-732.

Atcheson, M., MacKinnon, P. and Elsaesser, B. (2015) 'A large scale model experimental study of a tidal turbine in uniform steady flow', *Ocean Engineering*, 110, Part A, pp. 51-61.

Atlantis Resources Ltd (2017) *Meygen Project Development & Operation*. Available at: https://www.atlantisresourcesltd.com/projects/meygen/ (Accessed: 31/05/17).

Bahaj, A.S., Batten, W.M.J. and McCann, G. (2007a) 'Experimental verifications of numerical predictions for the hydrodynamic performance of horizontal axis marine current turbines', *Renewable Energy*, 32(15), pp. 2479-2490.

Bahaj, A.S., Molland, A.F., Chaplin, J.R. and Batten, W.M.J. (2007b) 'Power and thrust measurements of marine current turbines under various hydrodynamic flow conditions in a cavitation tunnel and a towing tank', *Renewable Energy*, 32(3), pp. 407-426.

Bahaj, A.S. and Myers, L.E. (2003) 'Fundamentals applicable to the utilisation of marine current turbines for energy production', *Renewable Energy*, 28(14), pp. 2205-2211.

Bahaj, A.S. and Myers, L.E. (2013) 'Shaping array design of marine current energy converters through scaled experimental analysis', *Energy*, 59(0), pp. 83-94.

Bahaj, A.S., Myers, L.E., Thomson, M.D. and Jorge, N. (2007c) 'Characterising the wake of horizontal axis marine current turbines', *Proc. 7th EWTEC*.

Barthelmie, R.J., Hansen, K., Frandsen, S.T., Rathmann, O., Schepers, J.G., Schlez, W., Phillips, J., Rados, K., Zervos, A., Politis, E.S. and Chaviaropoulos, P.K. (2009) 'Modelling and measuring flow and wind turbine wakes in large wind farms offshore', *Wind Energy*, 12(5), pp. 431-444.

Batten, W.M., Harrison, M.E. and Bahaj, A.S. (2013) 'Accuracy of the actuator disc-RANS approach for predicting the performance and wake of tidal turbines', *Philos Trans A Math Phys Eng Sci*, 371(1985), p. 20120293.

Batten, W.M.J., Bahaj, A.S., Molland, A.F. and Chaplin, J.R. (2007) 'Experimentally validated numerical method for the hydrodynamic design of horizontal axis tidal turbines', *Ocean Engineering*, 34(7), pp. 1013-1020.

Batten, W.M.J., Bahaj, A.S., Molland, A.F. and Chaplin, J.R. (2008) 'The prediction of the hydrodynamic performance of marine current turbines', *Renewable Energy*, 33(5), pp. 1085-1096.

Beaudoin, M. and Jasak, H. (2008) 'Development of a generalized grid interface for turbomachinery simulations with OpenFOAM', *Open source CFD International conference*. Berlin.

BP (2017) *Energy Outlook 2017*. [Online]. Available at: http://www.bp.com/content/dam/bp/pdf/energy-economics/energy-outlook-2017/bp-energy-outlook-2017.pdf (Accessed: 02/06/2017).

Carbon Trust (2011a) *Accelerating Marine Energy*. [Online]. Available at: https://www.carbontrust.com/media/5675/ctc797.pdf (Accessed: 30/10/2013).

Carbon Trust (2011b) *UK Tidal Current Resource & Economics* [Online]. Available at: https://www.carbontrust.com/media/77264/ctc799_uk_tidal_current_resource_and_economics.pdf (Accessed: 10/10/2013).

Catalano, P. and Amato, M. (2003) 'An evaluation of RANS turbulence modelling for aerodynamic applications', *Aerospace Science and Technology*, 7(7), pp. 493-509.

Celik, I., Ghia, U., Roache, P., Freitas, C., Coleman, H. and Raad, P. (2008) 'Procedure for Estimation and Reporting of Uncertainty Due to Discretization in CFD Applications', *Journal of Fluids Engineering*, 130(7), pp. 078001-078001-4.

CFD Direct (2017) *OpenFOAM User Guide*. Available at: https://cfd.direct/openfoam/user-guide/v3-snappyHexMesh/#x26-1520005.4.

Chamorro, L.P., Arndt, R.E.A. and Sotiropoulos, F. (2012) 'Reynolds number dependence of turbulence statistics in the wake of wind turbines', *Wind Energy*, 15(5), pp. 733-742.

Chamorro, L.P., Hill, C., Morton, S., Ellis, C., Arndt, R.E.A. and Sotiropoulos, F. (2013a) 'On the interaction between a turbulent open channel flow and an axial-flow turbine', *Journal of Fluid Mechanics*, 716, pp. 658-670.

Chamorro, L.P., Troolin, D.R., Lee, S.J., Arndt, R.E.A. and Sotiropoulos, F. (2013b) 'Three-dimensional flow visualization in the wake of a miniature axial-flow hydrokinetic turbine', *Experiments in Fluids*, 54(2), pp. 1-12.

Churchfield, M.J., Li, Y. and Moriarty, P.J. (2013) 'A large-eddy simulation study of wake propagation and power production in an array of tidal-current turbines', *Philos Trans A Math Phys Eng Sci*, 371(1985), p. 20120421.

Clarke, J.A., Connor, G., Grant, A.D. and Johnstone, C.M. (2007) 'Design and testing of a contra-rotating tidal current turbine', *Proceedings of the Institution of Mechanical Engineers, Part A: Journal of Power and Energy*, 221(2), pp. 171-179.

Coiro, D.P., Maisto, U., Scherillo, F., Melone, S. and Grasso, F. (2006) 'Horizontal axis tidal current turbine: numerical and experimental investigations', *Proceedings of the OWEMES*. pp. 20-22.

Daly, T., Myers, L.E. and Bahaj, A.S. (2013) 'Modelling of the flow field surrounding tidal turbine arrays for varying positions in a channel', *Philos Trans A Math Phys Eng Sci*, 371(1985), p. 20120246.

DECC (2011) *Renewable Energy Roadmap 2011*. Department of Energy and Climate Change, London, UK. [Online]. Available at: https://www.gov.uk/government/uploads/system/uploads/attachment_data/file/48128/2167-uk-renewable-energy-roadmap.pdf (Accessed: 25/10/2013).

Dobrev, I., Maalouf, B., Troldborg, N. and Massouh, F. (2008) 'Investigation of the wind turbine vortex structure', *14th international symposium on applications of laser techniques to fluid mechanics, Lisbon, Portugal*. pp. 07-10.

Doman, D.A., Murray, R.E., Pegg, M.J., Gracie, K., Johnstone, C.M. and Nevalainen, T. (2015) 'Tow-tank testing of a 1/20th scale horizontal axis tidal turbine with uncertainty analysis', *International Journal of Marine Energy*, 11, pp. 105-119.

Draper, S. and Nishino, T. (2013) 'Centred and staggered arrangements of tidal turbines', *Journal of Fluid Mechanics*, 739, pp. 72-93.

EIA (2016) 'International Energy Outlook 2016'. U.S. Energy Information Administration. Available at: https://www.eia.gov/outlooks/ieo/pdf/0484(2016).pdf (Accessed: 29/10/2016).

European Commission (2014) *Blue Energy - Action needed to deliver on the potential of ocean energy in European seas and oceans by 2020 and beyond* [Online]. Available at: http://eur-lex.europa.eu/legal-content/EN/TXT/PDF/?uri=CELEX:52014DC0008&from=EN (Accessed: 18/08/2014).

European Commission (2017a) *2020 Climate and Energy Package*. Available at: https://ec.europa.eu/clima/policies/strategies/2020_en (Accessed: 05/06/2017).

European Commission (2017b) *Renewable Energy Progress Report 2017*. [Online]. Available at: https://ec.europa.eu/commission/sites/beta-political/files/report-renewable-energy_en.pdf (Accessed: 05/06/2017).

Farrell, P.E. and Maddison, J.R. (2011) 'Conservative interpolation between volume meshes by local Galerkin projection', *Computer Methods in Applied Mechanics and Engineering*, 200(1), pp. 89-100.

Ferziger, J.H. and Peric, M. (2012) *Computational methods for fluid dynamics*. Springer Science & Business Media.

Frost, C., Morris, C.E., Mason-Jones, A., O'Doherty, D.M. and O'Doherty, T. (2015) 'The effect of tidal flow directionality on tidal turbine performance characteristics', *Renewable Energy*, 78, pp. 609-620.

Funke, S.W., Farrell, P.E. and Piggott, M.D. (2014) 'Tidal turbine array optimisation using the adjoint approach', *Renewable Energy*, 63, pp. 658-673.

Galloway, P.W., Myers, L.E. and Bahaj, A.S. (2014) 'Quantifying wave and yaw effects on a scale tidal stream turbine', *Renewable Energy*, 63(0), pp. 297-307.

Garrett, C. and Cummins, P. (2005) 'The power potential of tidal currents in channels', *Proceedings of the Royal Society A: Mathematical, Physical and Engineering Science*, 461(2060), pp. 2563-2572.

Garrett, C. and Cummins, P. (2007) 'The efficiency of a turbine in a tidal channel', *Journal of Fluid Mechanics*, 588, pp. 243-251.

Giles, J., Myers, L., Bahaj, A., Nians, J.O. and Shelmerdine, B. (2011) 'Foundation-based flow acceleration structures for marine current energy converters', *IET Renewable Power Generation*, 5(4), pp. 287-298.

Giles, J.W. (2013) *Energy extraction from shallow tidal flows*. EngD thesis. University of Southampton.

Good, A., Hamill, G., Whittaker, T. and Robinson, D. (2011) 'PIV analysis of the near wake of a tidal turbine', *Proc. ISOPE*. Maui, Hawaii, June 19-24.

Harrison, M.E., Batten, W.M.J., Myers, L.E. and Bahaj, A.S. (2010) 'Comparison between CFD simulations and experiments for predicting the far wake of horizontal axis tidal turbines', *Renewable Power Generation, IET*, 4(6), pp. 613-627.

Issa, R.I. (1986) 'Solution of the implicitly discretised fluid flow equations by operator-splitting', *Journal of Computational Physics*, 62(1), pp. 40-65.

Janiszewska, J.M., Ramsay, R.R., Hoffmann, M.J. and Gregorek, G.M. (1996) *Effects of grit roughness and pitch oscillations on the S814 airfoil*. National Renewable Energy Lab., Golden, CO (United States).

Jasak, H. (1996) *Error analysis and estimation for finite volume method with applications to fluid flow*. PhD thesis. Imperial College London, University of London.

Jasak, H., Jemcov, A. and Tukovic, Z. (2007) 'OpenFOAM: A C++ library for complex physics simulations', *International workshop on coupled methods in numerical dynamics*. IUC Dubrovnik, Croatia, pp. 1-20.

Javaherchi, T., Stelzenmuller, N. and Aliseda, A. (2013) 'Experimental and numerical analysis of the doe reference model 1 horizontal axis hydrokinetic turbine', *Proceedings of the 1st Marine Energy Technology Symposium*.

Jeffcoate, P., Starzmann, R., Elsaesser, B., Scholl, S. and Bischoff, S. (2015) 'Field measurements of a full scale tidal turbine', *International Journal of Marine Energy*, 12, pp. 3-20.

Jeffcoate, P., Whittaker, T., Boake, C. and Elsaesser, B. (2016) 'Field tests of multiple 1/10 scale tidal turbines in steady flows', *Renewable Energy*, 87, pp. 240-252.

Jo, C.h., Yim, J.y., Lee, K.h. and Rho, Y.h. (2012) 'Performance of horizontal axis tidal current turbine by blade configuration', *Renewable Energy*, 42(0), pp. 195-206.

Johansen, J. and Sørensen, N.N. (2004) 'Aerofoil characteristics from 3D CFD rotor computations', *Wind Energy*, 7(4), pp. 283-294.

Kang, S., Borazjani, I., Colby, J.A. and Sotiropoulos, F. (2012) 'Numerical simulation of 3D flow past a real-life marine hydrokinetic turbine', *Advances in Water Resources*, 39(0), pp. 33-43.

Kim, W.-W. and Menon, S. (1995) 'A new dynamic one-equation subgrid-scale model for large eddy simulations', *33rd Aerospace Sciences Meeting and Exhibit*. American Institute of Aeronautics and Astronautics. Available at: https://doi.org/10.2514/6.1995-356 (Accessed: 2017/08/18).

Krishnaswami, C. (2013) *Experimental Analysis of Near and Transitional Wind Turbine Wake Using Stereo Particle Image Velocimetry*. MSc thesis. Delft University of Technology [Online]. Available at: http://www.lr.tudelft.nl/fileadmin/Faculteit/LR/Organisatie/Afdelingen_en_Leerstoelen/Afdeling_AEWE/Wind_Energy/Education/Masters_Projects/Finished_Master_projects/doc/Chidam_r2.pdf (Accessed: 23/07/2014).

Lartiga, C. and Crawford, C. (2010) 'Actuator disk modeling in support of tidal turbine rotor testing', *Proceedings 3rd International Conference on Ocean Energy*. Available at: https://www.icoe-conference.com/publication/actuator_disk_modeling_in_support_of_tidal_turbine_rotor_testing/ (Accessed: 04/02/2014).

Launder, B.E., Reece, G.J. and Rodi, W. (1975) 'Progress in the development of a Reynolds-stress turbulence closure', *Journal of Fluid Mechanics*, 68(3), pp. 537-566.

Launder, B.E. and Spalding, D.B. (1974) 'The numerical computation of turbulent flows', *Computer Methods in Applied Mechanics and Engineering*, 3(2), pp. 269-289.

LaVision GmbH (2014a) 'Davis 8.2 Software Manual'.

LaVision GmbH (2014b) 'Flow Master - Getting Started'.

LaVision GmbH (2014c) 'Imaging Tools'.

Lee, S.H., Lee, S.H., Jang, K., Lee, J. and Hur, N. (2010) 'A numerical study for the optimal arrangement of ocean current turbine generators in the ocean current power parks', *Current Applied Physics*, 10(2, Supplement), pp. S137-S141.

Liu, J., Lin, H. and Purimitla, S.R. (2016) 'Wake field studies of tidal current turbines with different numerical methods', *Ocean Engineering*, 117, pp. 383-397.

Liu, Y., Xiao, Q., Incecik, A., Peyrard, C. and Wan, D. (2017) 'Establishing a fully coupled CFD analysis tool for floating offshore wind turbines', *Renewable Energy*, 112, pp. 280-301.

MacLeod, A.J., Barnes, S., Rados, K.G. and Bryden, I.G. (2002) 'Wake effects in tidal current turbine farms', *International Conference on Marine Renewable Energy-Conference Proceedings*. Newcastle Upon Tyne. Available at: http://mickpeterson.org/Classes/Design/2007_8/Project_webs/Tidal_test/pdf/MacLeod%202002%20MAREC%20-%20wake%20effects%20in%20tidal%20current%20turbines.pdf (Accessed: 12/12/2013).

Maganga, F., Germain, G., King, J., Pinon, G. and Rivoalen, E. (2010) 'Experimental characterisation of flow effects on marine current turbine behaviour and on its wake properties', *Iet Renewable Power Generation*, 4(6), pp. 498-509.

Malki, R., Williams, A.J., Croft, T.N., Togneri, M. and Masters, I. (2013) 'A coupled blade element momentum - Computational fluid dynamics model for evaluating tidal stream turbine performance', *Applied Mathematical Modelling*, 37(5), pp. 3006-3020.

Marine Current Turbines (2008) *World's first commercial-scale tidal power system feeds electricity to the National Grid*. Available at: http://www.marineturbines.com/3/news/article/10/world_s_first_commercial_scale_tidal_power_system_feeds_electricity_to_the_national_grid__ (Accessed: 04/06/2014).

MARINET (2017) *Tidal Energy DeviceL Support Structure Wake Impact on Performance*. Available at: http://www.marinet2.eu/wp-content/uploads/2017/04/TEDSSWIP_UNIFI-CRIACIV_Infrastructure_Access_Report.pdf (Accessed: 10/08/2017).

Mason-Jones, A. (2010) *Performance Assessment of a Horizontal Axis Tidal Turbine in a High Velocity Shear Environment*. PhD thesis. Cardiff University.

Mason-Jones, A., O'Doherty, D.M., Morris, C.E. and O'Doherty, T. (2013) 'Influence of a velocity profile & support structure on tidal stream turbine performance', *Renewable Energy*, 52(0), pp. 23-30.

Mason-Jones, A., O'Doherty, D.M., Morris, C.E., O'Doherty, T., Byrne, C.B., Prickett, P.W., Grosvenor, R.I., Owen, I., Tedds, S. and Poole, R.J. (2012) 'Non-dimensional scaling of tidal stream turbines', *Energy*, 44(1), pp. 820-829.

McNaughton, J. (2013) *Turbulence modelling in the near-field of an axial flow tidal turbine in Code_Saturne*. PhD thesis. University of Manchester [Online]. Available at: https://www.escholar.manchester.ac.uk/api/datastream?publicationPid=uk-ac-man-scw:200650&datastreamId=FULL-TEXT.PDF (Accessed: 13/08/2016).

McNaughton, J., Afgan, I., Apsley, D.D., Rolfo, S., Stallard, T. and Stansby, P.K. (2014) 'A simple sliding-mesh interface procedure and its application to the CFD simulation of a tidal-stream turbine', *International Journal for Numerical Methods in Fluids*, 74(4), pp. 250-269.

McTavish, S., Feszty, D. and Nitzsche, F. (2014) 'An experimental and computational assessment of blockage effects on wind turbine wake development', *Wind Energy*, 17(10), pp. 1515-1529.

Menter, F.R. (1994) 'Two-equation eddy-viscosity turbulence models for engineering applications', *AIAA Journal*, 32(8), pp. 1598-1605.

Menter, F.R. and Esch, T. (2001) 'Elements of industrial heat transfer predictions', *16th Brazilian Congress of Mechanical Engineering (COBEM)*.

Menter, F.R., Kuntz, M. and Langtry, R. (2003) 'Ten years of industrial experience with the SST turbulence model', *Turbulence, heat and mass transfer*, 4(1), pp. 625-632.

Milne, I.A., Day, A.H., Sharma, R.N. and Flay, R.G.J. (2013) 'Blade loads on tidal turbines in planar oscillatory flow', *Ocean Engineering*, 60, pp. 163-174.

Milne, I.A., Day, A.H., Sharma, R.N. and Flay, R.G.J. (2015) 'Blade loading on tidal turbines for uniform unsteady flow', *Renewable Energy*, 77, pp. 338-350.

Minesto (2017) *Holyhead Deep Project*. Available at: http://minesto.com/projects/holyhead-deep (Accessed: 12/07/207).

Mycek, P., Gaurier, B., Germain, G., Pinon, G. and Rivoalen, E. (2014a) 'Experimental study of the turbulence intensity effects on marine current turbines behaviour. Part I: One single turbine', *Renewable Energy*, 66(0), pp. 729-746.

Mycek, P., Gaurier, B., Germain, G., Pinon, G. and Rivoalen, E. (2014b) 'Experimental study of the turbulence intensity effects on marine current turbines behaviour. Part II: Two interacting turbines', *Renewable Energy*, 68, pp. 876-892.

Mycek, P., Gaurier, B.t., Germain, G., Pinon, G. and Rivoalen, E. (2013) 'Numerical and experimental study of the interaction between two marine current turbines', *International Journal of Marine Energy*, 1(0), pp. 70-83.

Myers, L. and Bahaj, A.S. (2007) 'Wake studies of a 1/30th scale horizontal axis marine current turbine', *Ocean Engineering*, 34(5-6), pp. 758-762.

Myers, L. and Bahaj, A.S. (2009) 'Near wake properties of horizontal axis marine current turbines', *Proceedings of the 8th European Wave and Tidal Energy Conference*. Uppsala, Sweden.

Myers, L.E. and Bahaj, A.S. (2010) 'Experimental analysis of the flow field around horizontal axis tidal turbines by use of scale mesh disk rotor simulators', *Ocean Engineering*, 37(2-3), pp. 218-227.

Myers, L.E. and Bahaj, A.S. (2012) 'An experimental investigation simulating flow effects in first generation marine current energy converter arrays', *Renewable Energy*, 37(1), pp. 28-36.

Neary, V.S., Gunawan, B., Hill, C. and Chamorro, L.P. (2013) 'Near and far field flow disturbances induced by model hydrokinetic turbine: ADV and ADP comparison', *Renewable Energy*, 60(0), pp. 1-6.

NERC (2013) *Marine Mammal Impacts*. Natural Environment Research Council. [Online]. Available at: http://www.nerc.ac.uk/innovation/activities/infrastructure/offshore/marine-mammal-impacts/ (Accessed: 05/06/2017).

Nishino, T. and Willden, R.H.J. (2012) 'The efficiency of an array of tidal turbines partially blocking a wide channel', *Journal of Fluid Mechanics*, 708, pp. 596-606.

Nuernberg, M. and Tao, L. (2016) *Proceedings of the International Conference on Offshore Mechanics and Arctic Engineering - OMAE*. Available at: https://www.scopus.com/inward/record.uri?eid=2-s2.0-84996552007&doi=10.1115%2fOMAE2016-54516&partnerID=40&md5=f7f63eb714a9e581fd9de8f1706cd457.

Nuernberg, M. and Tao, L. (2017) 'Three dimensional tidal turbine array simulations using OpenFOAM with dynamic mesh', *Ocean Engineering*.

Nuernberg, M. and Tao, L. (2017, Submitted for Publication) 'Wake Characterisation of Tidal Turbines in Arrays'.

O'Doherty, T., Mason-Jones, A., O'Doherty, D.M. and Byrne, C.B. (2009) 'Experimental and Computational Analysis of a Model Horizontal Axis Tidal Turbine', *8th European Wave and Tidal Energy Conference*. Uppsala, Sweden.

OEE (2017) *Ocean Energy Project Spotlight*. Ocean Energy Europe. [Online]. Available at: https://www.oceanenergy-europe.eu/images/Documents/Publications/170228-Ocean-energy-spotlight-final.pdf (Accessed: 13/06/2017).

OffshoreWIND.biz (2017) 'Image of Hywind from Statoil Video', *First Hywind Turbine Arrives in Scottish Waters*. Available at: http://www.offshorewind.biz/2017/07/24/first-hywind-turbine-arrives-in-scottish-waters/ (Accessed: 28/07/2017).

Olczak, A., Stallard, T., Feng, T. and Stansby, P.K. (2016) 'Comparison of a RANS blade element model for tidal turbine arrays with laboratory scale measurements of wake velocity and rotor thrust', *Journal of Fluids and Structures*, 64, pp. 87-106.

OPEN CASCADE (2013) 'SALOME 7.2.0'. Available at: http://files.salome-platform.org/Salome/Salome7.2.0/SALOME_7_2_0_Release_Notes.pdf (Accessed: 07/08/2017).

OpenCFD Ltd. (2017) 'OpenFOAM Extended Code Guide'. http://www.openfoam.com/documentation/cpp-guide/html/. Available at: http://www.openfoam.com/documentation/cpp-guide/html/ (Accessed: 13/06/2017).

OpenFOAM 2.3.0 (2014) *SnappyHexMesh Mesh Generation*.

ORE CATAPULT (2016) *Cost Reduction Monitoring Framework 2016*. Offshore Renewable Energy Catapult. [Online]. Available at: http://crmfreport.com/wp-content/uploads/2017/01/crmf-report-2016.pdf (Accessed: 15/05/2017).

Panasonic (2014) 'Panasonic MINAS 15 II Series Manual'. Available at: https://industrial.panasonic.com/content/data/MT/PDF/manual/en/acs/minas-a5-2_manu_e.pdf.

Patankar, S.V. and Spalding, D.B. (1972) 'A calculation procedure for heat, mass and momentum transfer in three-dimensional parabolic flows', *International Journal of Heat and Mass Transfer*, 15(10), pp. 1787-1806.

Pérez, B., Mínguez, R. and Guanche, R. (2013) 'Offshore wind farm layout optimization using mathematical programming techniques', *Renewable Energy*, 53(Supplement C), pp. 389-399.

Raffel, M., Willert, C.E., Wereley, S. and Kompenhans, J. (2013) *Particle image velocimetry: a practical guide*. Springer.

Raúl Bayoán, C., José, L., Luciano, C., Hyung Suk, K. and Charles, M. (2010) 'Experimental study of the horizontally averaged flow structure in a model wind-turbine array boundary layer', *Journal of Renewable and Sustainable Energy*, 2(1), p. 013106.

Sanderse, B. (2009) 'Aerodynamics of wind turbine wakes', *Energy Research Center of the Netherlands (ECN), ECN-E–09-016, Petten, The Netherlands, Tech. Rep*.

Sanderse, B., van der Pijl, S.P. and Koren, B. (2011) 'Review of computational fluid dynamics for wind turbine wake aerodynamics', *Wind Energy*, 14(7), pp. 799-819.

Schmitt, F.G. (2007) 'About Boussinesq's turbulent viscosity hypothesis: historical remarks and a direct evaluation of its validity', *Comptes Rendus Mécanique*, 335(9-10), pp. 617-627.

Shi, W., Atlar, M. and Norman, R. (2017) 'Detailed flow measurement of the field around tidal turbines with and without biomimetic leading-edge tubercles', *Renewable Energy*, 111, pp. 688-707.

Shi, W.C., Wang, D., Atlar, M. and Seo, K.C. (2013) 'Flow separation impacts on the hydrodynamic performance analysis of a marine current turbine using CFD', *Proceedings of the Institution of Mechanical Engineers Part a-Journal of Power and Energy*, 227(8), pp. 833-846.

Shives, M. and Crawford, C. (2016) 'Adapted two-equation turbulence closures for actuator disk RANS simulations of wind & tidal turbine wakes', *Renewable Energy*, 92, pp. 273-292.

Smagorinsky, J. (1963) 'GENERAL CIRCULATION EXPERIMENTS WITH THE PRIMITIVE EQUATIONS', *Monthly Weather Review*, 91(3), pp. 99-164.

Somers, D.M. (1992) *The S814 and S815 Airfoils.* Airfoils Inc., State College, PA. [Online]. Available at: http://citeseerx.ist.psu.edu/viewdoc/download?doi=10.1.1.602.9855&rep=rep1&type=pdf (Accessed: 18/07/2017).

Somers, D.M. and Tangler, J.L. (1996) 'Wind Tunnel Test of the S814 Thick Root Airfoil', *Journal of Solar Energy Engineering*, 118(4), pp. 217-221.

Spalart, P.R. (2000) 'Strategies for turbulence modelling and simulations', *International Journal of Heat and Fluid Flow*, 21(3), pp. 252-263.

Spalding, D.B. (1961) 'A Single Formula for the "Law of the Wall"', *Journal of Applied Mechanics*, 28(3), pp. 455-458.

Speziale, C.G., Sarkar, S. and Gatski, T.B. (1991) 'Modelling the pressure–strain correlation of turbulence: an invariant dynamical systems approach', *Journal of Fluid Mechanics*, 227, pp. 245-272.

Stallard, T., Collings, R., Feng, T. and Whelan, J. (2013) 'Interactions between tidal turbine wakes: experimental study of a group of three-bladed rotors', *Philos Trans A Math Phys Eng Sci*, 371(1985), p. 20120159.

Stallard, T., Feng, T. and Stansby, P.K. (2015) 'Experimental study of the mean wake of a tidal stream rotor in a shallow turbulent flow', *Journal of Fluids and Structures*, 54, pp. 235-246.

Statoil (2017) *Hywind Scotland*. Available at: https://www.statoil.com/en/news/hywindscotland.html (Accessed: 15/06/2017).

Stelzenmuller, N. (2013) *Marine Hydrokinetic Turbine Array Performance and Wake Characteristics*. Msc thesis. University of Washington.

Tedds, S.C., Owen, I. and Poole, R.J. (2014) 'Near-wake characteristics of a model horizontal axis tidal stream turbine', *Renewable Energy*, 63(0), pp. 222-235.

The Crown Estate (2012) *Project Distribution Map*. Uk Wave and Tidakl Key Resource Areas Project. Available at: https://www.thecrownestate.co.uk/media/5476/uk-wave-and-tidal-key-resource-areas-project.pdf (Accessed: 30/06/2017).

The OpenFOAM Foundation (2014) *OpenFOAM 2.3.0*. Available at: https://openfoam.org/release/2-3-0/ (Accessed: 1/03/2014).

The OpenFOAM Foundation (2015) 'Programmer's Guide' 3.0.1.

Thielicke, W. (2016) *PIVlab1.41*. Available at: http://pivlab.blogspot.co.uk/ (Accessed: 13/03/2016).

Thielicke, W. and Stamhuis, E. (2014) 'PIVlab–towards user-friendly, affordable and accurate digital particle image velocimetry in MATLAB', *Journal of Open Research Software*, 2(1).

Tidal Lagoon Power (2017) *Cardiff Tidal Lagoon*. Available at: http://www.tidallagoonpower.com/projects/cardiff/ (Accessed: 10/06/2017).

Turnock, S.R., Phillips, A.B., Banks, J. and Nicholls-Lee, R. (2011) 'Modelling tidal current turbine wakes using a coupled RANS-BEMT approach as a tool for analysing power capture of arrays of turbines', *Ocean Engineering*, 38(11-12), pp. 1300-1307.

United Nations (2017a) *The Paris Agreement*. Available at: http://unfccc.int/paris_agreement/items/9485.php (Accessed: 04/08/2017).

United Nations (2017b) *Status of Ratification of the Kyoto Protocol*. Available at: http://unfccc.int/kyoto_protocol/status_of_ratification/items/2613.php (Accessed: 04/08/2017).

Untrakdrover (2012) *Agucadoura, WindFloat Prototype*. Wikimedia Commons. Available at: https://upload.wikimedia.org/wikipedia/commons/7/76/Agucadoura_WindFloat_Prototype.jpg (Accessed: 04/07/2017).

Vennell, R. (2010) 'Tuning turbines in a tidal channel', *Journal of Fluid Mechanics*, 663, pp. 253-267.

Vennell, R. (2011a) 'Estimating the power potential of tidal currents and the impact of power extraction on flow speeds', *Renewable Energy*, 36(12), pp. 3558-3565.

Vennell, R. (2011b) 'Tuning tidal turbines in-concert to maximise farm efficiency', *Journal of Fluid Mechanics*, 671, pp. 587-604.

Vennell, R., Funke, S.W., Draper, S., Stevens, C. and Divett, T. (2015) 'Designing large arrays of tidal turbines: A synthesis and review', *Renewable and Sustainable Energy Reviews*, 41, pp. 454-472.

Vermeer, L.J., Sorensen, J.N. and Crespo, A. (2003) 'Wind turbine wake aerodynamics', *Progress in Aerospace Sciences*, 39(6-7), pp. 467-510.

Versteeg, H.K. and Malalasekera, W. (2007) *An introduction to computational fluid dynamics: the finite volume method*. Pearson Education.

Walker, S. (2014a) *Hydrodynamic interactions of a tidal stream turbine and support structure*. PhD thesis. University of Sheffield.

Walker, S. (2014b) *Hydrodynamic interactions of a tidal stream turbine and support structure.* . University of Sheffield.

Weller, H.G., Tabor, G., Jasak, H. and Fureby, C. (1998) 'A tensorial approach to computational continuum mechanics using object-oriented techniques', *Computers in physics*, 12(6), pp. 620-631.

Westerweel, J. (1997) 'Fundamentals of digital particle image velocimetry', *Measurement Science and Technology*, 8(12), p. 1379.

Whale, J., Anderson, C.G., Bareiss, R. and Wagner, S. (2000) 'An experimental and numerical study of the vortex structure in the wake of a wind turbine', *Journal of Wind Engineering and Industrial Aerodynamics*, 84(1), pp. 1-21.

Whelan, J.I., Graham, J.M.R. and Peiro, J. (2009) 'A free-surface and blockage correction for tidal turbines', *Journal of Fluid Mechanics*, 624, pp. 281-291.

Whelan, J.I. and Stallard, T. (2011) 'Arguments for modifying the geometry of a scale model rotor', *9th European Wave and Tidal Energy Conference*. Available at: http://www.gl-garradhassan.com/assets/downloads/Arguments_for_Modifying_the_Geometry_of_a_Scale_Model_Rotor.pdf (Accessed: 08/05/2014).

Wilcox, D.C. (2010) 'Turbulence modelling for CFD,' *DCW Industries*, (Third Edition).

WindEurope (2016a) *The European Offshore Wind Industry*. [Online]. Available at: https://windeurope.org/wp-content/uploads/files/about-wind/statistics/WindEurope-Annual-Offshore-Statistics-2016.pdf (Accessed: 08/05/2017).

WindEurope (2016b) *Making Transition Work*. [Online]. Available at: https://windeurope.org/wp-content/uploads/files/about-wind/reports/WindEurope-Making-transition-work.pdf (Accessed: 08/05/2017).

WindEurope (2017) *Floating Offshore Wind Vision Statement* [Online]. Available at: https://windeurope.org/wp-content/uploads/files/about-wind/reports/Floating-offshore-statement.pdf (Accessed: 04/07/2017).